

AFOSR-TR- 85-0004

## FINAL TECHNICAL REPORT

5

1 OCTOBER 1982 - 30 SEPTEMBER 1984

## REGIONAL SEISMIC WAVE PROPAGATION



30 NOVEMBER 1984



RONDOUT ASSOCIATES, INCORPORATED

P.O. BOX 224

STONE RIDGE, NEW YORK 12484

(914) 687-9150

DISTRIBUTION STATEMENT A

Approved for public release  
Distribution Unlimited

Sponsored by

Advanced Research Projects Agency (DOD)

ARPA Order No. 4493, 4669, 4451

Monitored by AFOSR/NP under Contract #F49620-83-C-0017

The views and conclusions contained in this document are those of the authors and should not be interpreted as necessarily representing the official policies, either expressed or implied, of the Defense Advanced Research Projects Agency or the U.S. Government.

85 02 05 026

AD-A150 801

MIC FILE COPY

UNCLASSIFIED

SECURITY CLASSIFICATION OF THIS PAGE

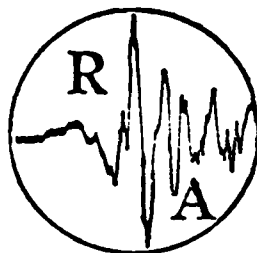
## REPORT DOCUMENTATION PAGE

1a. REPORT SECURITY CLASSIFICATION Unclassified		1b. RESTRICTIVE MARKINGS None	
2a. SECURITY CLASSIFICATION AUTHORITY N.A.		3. DISTRIBUTION/AVAILABILITY OF REPORT  Approved for public release; Distribution unlimited.	
2b. DECLASSIFICATION/DOWNGRADING SCHEDULE N.A.			
4. PERFORMING ORGANIZATION REPORT NUMBER(S)		5. MONITORING ORGANIZATION REPORT NUMBER(S)  AFOSR-TR- 85-0004	
6a. NAME OF PERFORMING ORGANIZATION Rondout Associates, Inc.	6b. OFFICE SYMBOL (If applicable) N.A.	7a. NAME OF MONITORING ORGANIZATION Air Force Office of Scientific Research	
6c. ADDRESS (City, State and ZIP Code) P.O. Box 224 Stone Ridge, New York 12484		7b. ADDRESS (City, State and ZIP Code) Building 410 / N.P. Bolling Air Force Base, DC 20332	
8a. NAME OF FUNDING/SPONSORING ORGANIZATION DARPA/AFOSR	8b. OFFICE SYMBOL (If applicable)	9. PROCUREMENT INSTRUMENT IDENTIFICATION NUMBER F49620-83-C-0017	
8c. ADDRESS (City, State and ZIP Code) 1400 Wilson Boulevard Arlington, VA 22209		10. SOURCE OF FUNDING NOS.	
11. TITLE (Include Security Classification) Regional Seismic Wave Propagation (U)		PROGRAM ELEMENT NO. 62714E	TASK NO. 4493
12. PERSONAL AUTHOR(S) J.A. Carter, L.L. Peseckis, P.W. Pomeroy, and G.H. Sutton		WORK UNIT NO. 01	
13a. TYPE OF REPORT Final	13b. TIME COVERED FROM 10-1-82 TO 9-30-84	14. DATE OF REPORT (Yr., Mo., Day) 30 November 1984	15. PAGE COUNT 250
16. SUPPLEMENTARY NOTATION			
17. COSATI CODES		18. SUBJECT TERMS (Continue on reverse if necessary and identify by block number)	
FIELD	GROUP	SUB. GR.	
			Regional seismic waves Lg Pn and Sn Yield determination Depth discrimination
1. ABSTRACT (Continue on reverse if necessary and identify by block number) Work has involved evaluation of methodologies for using regional seismic waves, particularly Lg for yield determination. The Wake Island Hydrophone Array digital recording continues to provide high quality data. Polarization and array analyses have been made of Catskill Seismic Array and Regional Seismic Test Network data. For continental models, whole waveform synthetics demonstrate clearly the large dependence of the amplitude and spectral shape on the focal depth and the smaller dependence of these factors on focal mechanism. The broad band digital seismic station, SRNY has been in operation since 16 May 1984. Digital data are recorded magnetic cartridge tapes each capable of holding 67 Megabytes or 38 hours of data. Many programs have been developed for data handling and analysis. Keywords include: Pn and Sn, Yield determination, and Depth discrimination.			
20. DISTRIBUTION/AVAILABILITY OF ABSTRACT UNCLASSIFIED/UNLIMITED <input checked="" type="checkbox"/> SAME AS RPT. <input type="checkbox"/> DTIC USERS <input type="checkbox"/>		21. ABSTRACT SECURITY CLASSIFICATION Unclassified	
22a. NAME OF RESPONSIBLE INDIVIDUAL Dr Henry R. Radoski		22b. TELEPHONE NUMBER (Include Area Code) 202/767-4906	22c. OFFICE SYMBOL NP

# FINAL TECHNICAL REPORT

1 OCTOBER 1982 - 30 SEPTEMBER 1984

## REGIONAL SEISMIC WAVE PROPAGATION



30 NOVEMBER 1984

RONDOUT ASSOCIATES, INCORPORATED

P.O. BOX 224

STONE RIDGE, NEW YORK 12484

(914) 687-9150

*Approved for public release;  
distribution unlimited.*

Sponsored by

Advanced Research Projects Agency (DOD)

ARPA Order No. 4493, 4669, 4451

Monitored by AFOSR/NP under Contract #F49620-83-C-0017

The views and conclusions contained in this document are those of the authors and should not be interpreted as necessarily representing the official policies, either expressed or implied, of the Defense Advanced Research Projects Agency or the U.S. Government.

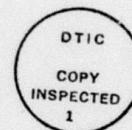
# Table of Contents

	Page
Executive Summary-----	i
TASK A	
Introduction-----	1
Methodology-----	2
Problems in Lg Yield Determination-----	3
Determination of $Q(f)$ -----	4
$m_{bLg}$ Yield Calculation-----	7
Determination of Yield Using $m_{bLg}$ -----	8
Calculated Yields-----	10
References-----	12
Figures-----	13
TASK B	
Introduction-----	70
Data Sources-----	71
Wake Island Hydrophone Array (WHA) Analyses-----	73
Teleseismic P Waves-----	73
Comparisons of Pn and Sn ( $P_0$ and $S_0$ ) with Lg-----	75
Attenuation-----	77
$Q(f)$ and Source Spectra for Pn and Sn ( $P_0$ and $S_0$ )-----	79
Catskill Seismic Array (CSA) and RSTN Analyses-----	82
Polarization and Array Analyses of CSA data-----	82
The Goodnow, New York and Related Earthquakes-----	85
Modeling with "Whole Seismogram" Synthetics-----	87
Continental Models-----	87
Effects of Focal Depth, Focal Mechanism, and Velocity Structure-----	87
Effects of $Q(f)$ -----	89
Comparison with Data-----	90
Oceanic Models-----	91
Effects of Low Velocity Sediment and Water-----	92
Comparison with Data-----	94
References-----	96
Figures-----	101
TASK C	
Introduction-----	151
Broad Band Seismic Station-----	151
Analysis Techniques-----	153
Polarization Analysis-----	153
Instantaneous Polarization-----	154
Adaptive Polarization-----	157
Beam Forming-----	162
Slowness Stacking-----	163
Synthetic Seismograms-----	163
Applications-----	165
Long Island Earthquake-----	165
Rhode Island Earthquake-----	167
Description of Analysis Software-----	168



# Table of Contents continued

	<u>Page</u>
References-----	183
Figures-----	185
APPENDICES	
Appendix A-----	A1
Appendix B-----	B1
Appendix C-----	C1
Appendix D-----	D1



Accession For	
NTIS GRA&I	<input checked="checked" type="checkbox"/>
DTIC TAB	<input type="checkbox"/>
Unannounced	<input type="checkbox"/>
Justification	
By	
Distribution/	
Availability Codes	
Dist	Avail and/or Special
A-1	

## Executive Summary

### Task A

Under this portion of the contract, the principal effort has involved the evaluation of methodologies for using regional seismic waves, particularly Lg, for yield determination. Following Nuttli's methodology, RAI has determined attenuation (Q) for paths between the Nevada Test Site (NTS) and the WWSSN stations BKS, TUC, DUG, GOL, and COR. For an exponential model of the frequency dependence of Q i.e.  $Q=Q_0 f^\zeta$ , values obtained are:

NTS-BKS	$Q_0=225$	$\zeta=.2$
NTS-TUC	$Q_0=300$	$\zeta=.2$
NTS-DUG	$Q_0=230$	$\zeta=.3$
NTS-GOL	$Q_0=345$	$\zeta=.3$
NTS-COR	$Q_0=220$	$\zeta=.4$

These values as well as those derived from a linear attenuation model ( $Q=Q_0+\alpha f$ ) are significantly different than those proposed by Nuttli for the same path. Using all of these Q values, RAI analysts have determined  $m_{bLg}$ 's for three data sets. One of these consists of events of announced yield and the other two are composed of events with classified yields. The latter determinations are discussed in the classified section of this report. Using these  $m_{bLg}$  values for the first data set and announced yields,  $m_{bLg}$  versus yield curves have been developed for a three (BKS, TUC, and DUG) and a five (BKS, TUC, DUG, GOL, and COR) station network and for the individual stations BKS, GOL, and DUG.

For the three station network (BKS, TUC, DUG)  $m_{bLg} = .65 \log Y + 4.02$   
 $\sigma = .043$  assuming all the error is in the  $m_{bLg}$  measurement, not the yield. When GOL is added to the data set, the relationship  $m_{bLg} = .65 \log Y + 3.85$   
 $\sigma = .050$  is obtained. Given the size of the change in these relationships and the small number of events in this sample (7), neither relationship should be used to calculate yield. A more accurate and comprehensive curve can be found in the classified section of this report. Using that curve, yields for "unknown" NTS events can be determined with an accuracy of  $\pm 50\%$ .

Task B

AIR FORCE OFFICE OF SCIENTIFIC RESEARCH (AFSC)  
NOTICE OF TRANSMITTAL TO DTIC  
This technical report has been reviewed and is  
approved for public release IAW AFR 190-12.  
Distribution is unlimited.  
MATTHEW J. KERPER  
Chief, Technical Information Division

The principal accomplishments under this Task can be listed in three (3) segments.

1. Analysis of Wake Island Hydrophone Array (WHA) Data: The upgraded digital recording at WHA continues to provide high quality data. Teleseismic P waves from explosions and earthquakes are recorded with high coherence across the 40 km aperture array with a detection threshold of approximately  $m_b=4.5$ . A comparison of the Pn and Sn ( $P_0$  and  $S_0$ ) propagation in the oceans with the propagation of Lg on the continents demonstrates a similar mode of propagation for these wave types through vastly different crustal structures. The demonstrated high Q of the oceanic lithosphere which allows the propagation of high frequency Pn and Sn increases rapidly, approximately proportional to frequency ( $\sim f^1$ ), above one (1) Hz.
2. Analysis of Catskill Seismic Array (CSA) and Regional Seismic Test Network (RSTN) Data: Polarization and array analyses of the CSA data reveals that P and S phase velocities can be well determined with this triangular array with approximately two (2) km aperture. Polarization analysis demonstrates the ability to accurately determine the azimuth of the event. The Goodnow, New York earthquake sequence provided a unique data set to examine the capabilities of the RSTN network particularly the RSNY station. A comparison of the amplitude spectrum of the main event with aftershock spectra demonstrates the major spectral differences between different size events in a restricted focal region. In particular, the aftershock spectrum peaks at 10 Hz with energy above the noise background between 2 and 20 Hz while the mainshock has information at frequencies from .1 to 20 Hz.
3. Modeling with "Whole Seismogram" Synthetics: For continental models, whole waveform synthetics demonstrate clearly the large dependence of the amplitude and spectral shape on the focal depth and the smaller dependence of these factors on focal mechanism. In particular, for one data set, a set of curves for focal depths between .1 km and 3 km shows a shift of spectral peak of more than one (1) octave in frequency. The

effects of the frequency dependence of  $Q$  as well as constant  $Q$  have been examined. In a comparison with observed data from two local events in Rhode Island and Long Island Sound, the whole waveform synthetics demonstrated a depth resolution of  $\pm 1$  km at short regional distances.

A comparison study of oceanic model, whole-waveform synthetics demonstrates the effects of low velocity sediments and water, particularly that much of the dominant prolonged character of the high frequency teleseismic oceanic  $P_n$  and  $S_n$  results from reverberations in the sediment and water layers. A comparison of the whole waveform synthetics with observational data recorded on an OBS ( $\Delta=6.15^\circ$ ) from an  $m_b=4.8$  Marianas earthquake demonstrates the power of full waveform modeling.

Full waveform modeling of the entire observed seismogram (in contrast to the first few cycles of the  $P$  wave), allows the utilization of all the information on the seismogram for determination of focal parameters, discrimination parameters, and yield determination. RAI is actively investigating these uses in its ongoing research program.

#### Task C

The broad band digital seismic station, SRNY, installed at  $41.849^\circ N$ ,  $74.151^\circ W$  has been in operation since 16 May 1984. Digital data are recorded at 60 samples/second/channel on 1/4" magnetic cartridge tapes each capable of holding 67 megabytes or 38 hours of data.

Many programs have been developed for data handling and analysis. These include programs to read the data from the cartridges onto a SUN microcomputer (raisun) putting it into Center for Seismic Studies (CSS) format, spectral analysis programs, a display program for the SUN, a filter program, and an adaptive polarization analysis program. All of these programs have been installed on CSS-SUN at the CSS and are available for general use. Data transfer from raisun to the CSS is accomplished through simple copy commands over the network of which raisun is now a part.

The adaptive polarization method has shown great promise as a tool for earthquake location using a single station. Array methods such as beam forming and slowness stacking have also been tested and applied to CSA and WHA data.

## TASK A

### Introduction

The purpose of this work is to determine the usefulness of regional seismic waves, particularly Lg, to estimate the yield of Eurasian events. The use of regional waves, recorded outside the USSR, can provide important measurements of the yield which can supplement those based on  $m_b$  and  $M_s$  measurements.

The Work Statement for this Task reads as follows:

1. Evaluate the usefulness of Pg and Lg to estimate yield for Eurasian and Africa events.
2. Investigate possible causes of amplitude variation (i.e., source and recording site geology).
3. Analyze the regional phases for use in discrimination and yield estimation.

The following report outlines the results of this work.

The Nuttli methodology (Nuttli, preprints 1, 2, 3) for estimating yield from short period regional Lg waves has held exciting promise as a method to determine the yield of USSR underground nuclear explosions without the need for calibration events of known yield from the USSR test site or seismic stations inside the Soviet Union.

The method consists of several steps: 1)) determination of Q for source-receiver paths using the predominant frequency versus time method (Herrmann, 1980); 2) measurement of the sustained amplitude of short period Lg waves in the velocity range 3.3-3.6 km/sec.; 3) calculation of  $m_{bLg}$  using 1) and 2); and 4) construction of an  $m_{bLg}$ -yield calibration curve for NTS events which would be transportable to other areas of the world once  $m_{bLg}$ 's are calculated using the appropriate Q corrections.

The purpose of RAI's study is to evaluate this method using a larger data set than previous studies, to determine any problems and to quantify the

errors resulting from each step.

### Methodology

To determine  $Q$ , data of predominant frequency as a function of time in the  $L_g$  coda are collected for each source-receiver path. These data are compared to sets of master curves predicting the frequency behavior with time as a function of the parameters in the  $Q$  model assumed. Using this method, RAI has determined the  $Q$ 's for five paths assuming both an exponential ( $Q=Q_0 f^\zeta$ ) and a linear ( $Q=Q_0 + \alpha f$ ) model of frequency dependence. These paths are from NTS to the WWSSN stations DUG, BKS, TUC, GOL, COR (see Table I in the following section). A good fit to the data can be found using either model.

With the  $Q$ 's from the exponential model, we calculated  $m_{bLg}$ 's for three data sets. One of these consists of events of announced yield and the other two are composed of events with classified yields which are discussed in the classified section of this report. Calibration curves for each data set have been developed as well as a curve for all the data. In addition, we have found calibration curves for the stations BKS, DUG and GOL.

The dependence of these network curves on stations included in the data set was examined. For the data set with announced yields, we found the least squares fit to data from stations BKS, DUG and TUC:

$$m_{bLg} = .65 \log y + 4.02$$

with a standard deviation of  $\sigma=.043$  assuming all the error is in the  $m_{bLg}$  measurement, not the yield. When station GOL is included, the calibration curve becomes

$$m_{bLg} = .65 \log y + 3.84 \text{ with } \sigma=.050.$$

Given the size of the change in these curves from adding one station and that there are only seven events in this data set, neither should be used to calculate yield. A more accurate curve can be found in the classified section of this report.



These calibration curves differ since GOL has a characteristically lower  $m_{bLg}$  than the other stations. After Q corrections are made, each station has characteristically high or low  $m_{bLg}$ 's compared to the others. Several methods to minimize this problem have been tried but all leave some displacement in the two curves.

RAI has also examined the effect of adding more events to the curve which results are reported in the classified section.

In that section, we also show the accuracy of determining the yield of events in one data set using the calibration curve obtained from a different data set. For the best case, we were able to determine yield to  $\pm 50\%$ .

#### Problems in Lg Yield Determination

The largest problem that we have found lies in the Q determination. This is crucially important in that the transportability of this curve to other areas of the world totally depends on making the right Q correction to  $m_{bLg}$ .

The values of  $Q_0$  we find from our predominant frequency versus time data are significantly higher than those used by Nuttli (preprints 1 and 2). Nuttli chooses his exponential dependence ( $\zeta$  in  $Q = Q_0 f^\zeta$ ) on frequency from other studies (private communication). He uses  $\zeta = 0.6$  compared to our finding  $\zeta = 0.2-0.3$  for the three stations our studies have in common. The value he chooses agrees with the results of other studies (e.g. Mitchell, 1980) using 1 Hz Lg waves and determining amplitude attenuation with distance.  $\zeta = 0.6$ , however, does not fit our data.

A possible reason for this discrepancy is that the  $\zeta$  value is changing from  $\zeta = 0.4-0.6$  at 1 Hz to  $\zeta = 0-0.2$  at .2 Hz (Mitchell, 1980). This frequency range is precisely the one in which the predominant frequency versus time data is collected. In this method, the lower frequencies are critical to uniquely defining  $\zeta$ .

A potential solution to this problem is to develop master curves using a varying exponential dependence:

$$Q = Q_0 f^{\zeta(f)}.$$

We must emphasize that without the resolution of this problem, calibration curves are not transportable.

In the following sections, we discuss each step separately.

### Determination of $Q(f)$

To determine  $Q(f)$ , predominant frequency in the short period codas of  $L_g$  is plotted as a function of time. This plot is then compared to sets of master curves (Herrmann, 1980) which depend on the model of frequency dependence assumed and the parameters in that model. We used two models of frequency dependence: 1) an exponential model (Mitchell, 1980)  $Q=Q_0 f^\zeta$  and 2) a linear model,  $Q=Q_0+\alpha f$ . For each  $\zeta$  or  $\alpha$ , we obtain a set of curves with different  $Q_0$ 's. (These are shown with one data set superimposed in Figures 1-7.)

We determined  $Q$  for paths from NTS to five WWSSN stations. The stations, their distances to NTS as well as their instrument magnifications are given in Table I.

Because of its low gain and large distance, COR recorded only two clear  $L_g$  arrivals (for the two largest events) out of 14 events examined.  $m_{bLg}$ 's were not calculated for this station.  $Q$  was determined for this path by taking predominant frequencies at times after  $L_g$  should have arrived, assuming a velocity of 3.5 km/sec.

Thirteen events recorded by WWSSN station LUB, 1300 km from NTS, were also examined. Most of these had a large amplitude .8 Hz arrival in our velocity window of 3.3-3.6 km/sec. This station was not used in our study because of the lack of a 1 Hz arrival.

Table I

<u>STATION</u>	<u>DISTANCE TO NTS</u>	<u>MAGNIFICATIONS</u>
DUG	450 km	100k or 200k (sometimes lowered for NTS events)
BKS	530 km	25k
TUC	730 km	200k
GOL	980 km	200k or 400k
COR	1000 km	12.5k or 25k

The predominant frequency versus time data from BKS is shown superimposed on master curves for the exponential model with  $\zeta=0, .2, .4, .6, .8$  and for the linear model with  $\alpha=50$  and 100 in Figures 1-7. Similarly, DUG data superimposed on master curves is given in Figure 8-14, TUC in Figures 15-21, GOL in Figures 22-28 and COR in Figures 29-35. Notice that for the exponential models as  $\zeta$  increases the slope of the fall-off increases. In addition, the intercept of a given  $Q_0$  curve with the time axis decreases with increasing  $\zeta$ . For the linear models, the slope also increase with increasing  $\alpha$  but the time intercept of the different curves remains the same.

The slope of the fall-off of the data determines the  $\zeta$  or  $\alpha$ . For each station, the master curves for higher  $\zeta$ 's or  $\alpha$ 's than the best model are steeper than the data and those lower have less steep slopes.

A computer program was developed to find both the exponential and linear models from which the data has the lowest standard deviation. These "best" models are listed in Table II. The standard deviations are calculated assuming all the error is in the predominant frequency measurement, not the travel time. A  $\sigma=.1$  corresponds approximately to  $\pm 25$  in  $Q_0$ . Note that at COR where the clear  $L_g$  arrival is not usually present, the  $\zeta=.4$  of the exponential model is higher than the others.

The best fit curves for both Q models for each station are shown with the data in Figures 36-45. It must be noted that with this data, we can not distinguish between the exponential and linear Q models.

Table II  
BEST MODELS TO FIT DATA  
(LOWEST STANDARD DEVIATION)

EXPONENTIAL

NTS-BKS:	$\zeta = .2$	$Q_0 = 225$	$(\sigma = .085)$
NTS-DUG:	$\zeta = .3$	$Q_0 = 230$	$(\sigma = .105)$
NTS-TUC:	$\zeta = .2$	$Q_0 = 300$	$(\sigma = .089)$
NTS-GOL:	$\zeta = .3$	$Q_0 = 345$	$(\sigma = .099)$
NTS-COR:	$\zeta = .4$	$Q_0 = 220$	$(\sigma = .096)$

LINEAR

NTS-BKS:	$\alpha = 50$	$Q_0 = 175$	$(\sigma = .083)$
NTS-DUG:	$\alpha = 50$	$Q_0 = 210$	$(\sigma = .110)$
NTS-TUC:	$\alpha = 50$	$Q_0 = 265$	$(\sigma = .085)$
NTS-GOL:	$\alpha = 50$	$Q_0 = 370$	$(\sigma = .100)$
NTS-COR:	$\alpha = 50$	$Q_0 = 235$	$(\sigma = .100)$

Problems

The  $Q$ 's we obtain differ substantially from those found by Nuttli (1973) for the three paths our studies have in common. He uses an exponential model and, from other data (Nuttli, private communication), chooses  $\zeta = .6$  for the paths from NTS to BKS, DUG and TUC. Figures 46-48 show our data at these stations with the  $Q_0, \zeta$  curve used by Nuttli. The standard deviations of our data from his curve are also given. Clearly, the curves fall off too steeply for the data. His smaller data set, however, falls within the scatter of ours and is consistent with our choice of  $Q$  (Figures 49-52).

Nuttli's choice of  $\zeta$  is consistent with that found by other studies (Nuttli, 1973; Street, 1976; Pomeroy, 1977; Bollinger, 1974; Mitchell, 1980) in which amplitude attenuation with distance is measured for  $L_g$  at 1 Hz. As shown by Mitchell (1980), these and other studies indicate that a choice of  $\zeta = .4-.8$  is appropriate at 1 Hz while  $\zeta = 0-.2$  is a better choice at frequencies

less than about .2 Hz. The predominant frequency versus time data are collected precisely in this frequency range. The lower frequency data is needed to uniquely define the slope of the fall off and thus,  $\zeta$ . The  $\zeta$ 's found by this method are an average, then, of the  $\zeta$ 's over this frequency range.

Although it can be argued that the solution to this problem is to take the  $\zeta$  as determined in other ways from 1 Hz waves, this would defeat one of the main advantages of using this method, i.e. no stations needed inside the country of interest.

A potential solution to this problem is to develop master curves using a variable  $\zeta$ , i.e. using  $Q=Q_0 f^{\zeta(f)}$ . This method might also produce different  $Q_0$ 's than assuming a constant value of  $\zeta$ .

Without resolution of this problem, calibration curves are not transportable and this method, like others, will have to rely on USSR events of known yield to calibrate and internal stations to determine  $Q$ .

#### $m_{bLg}$ Calculation

Sustained amplitude of  $Lg$  is measured at velocities between 3.3 and 3.6 km/sec and frequencies of  $1 \pm 0.15$  Hz. We choose the sustained amplitude to be the amplitude level in the desired velocity range at or above which are three or more peaks. The formulas to calculate  $m_{bLg}$  are given by Nuttli (pre-print 1):

$$A(10) = A(\Delta) \left( \frac{\Delta}{10} \right)^{1/3} \left( \frac{\sin \frac{\Delta}{111}}{\sin \frac{10}{111}} \right)^{1/2} e^{\frac{\pi f(\Delta-10)}{QU}}$$

$$m_{bLg} = 5.0 + \log_{10} \left( \frac{A(10)}{110} \right)$$

where  $A(\Delta)$  is the measured sustained amplitude of ground motion in microns,  $\Delta$  is the epicentral distance in km,  $f$  is the frequency and  $U$  is the group velocity of the wave packet measured. For the exponential model  $Q=Q_0 f^{\zeta}$

$$A(10) = A(\Delta) \left( \frac{\Delta}{10} \right)^{1/3} \left( \frac{\sin \frac{\Delta}{111}}{\sin \frac{10}{111}} \right)^{1/2} e^{\frac{\pi f^{1-\zeta} (\Delta-10)}{Q_0 U}}$$

and for the linear model  $Q=Q_0+\alpha f$

$$A(10) = A(\Delta) \left( \frac{\Delta}{10} \right)^{1/3} \left( \frac{\sin \frac{\Delta}{111}}{\sin \frac{10}{111}} \right)^{1/2} e^{\frac{\pi f (\Delta-10)}{U(Q_0 + \alpha f)}}$$

These formulas are accurate assuming that  $m_{bLg}$  and  $m_b$  of teleseismic P waves scale in the same way (Nuttli, preprint 1) and that Lg is an airy phase.

$m_{bLg}$ 's were calculated for three data sets. One has announced yields and will be discussed here. The other two have classified yields and will be discussed in the classified section of this report.

All together,  $m_{bLg}$ 's were calculated for 45 events recorded by BKS, 15 by DUG, eight by TUC and 32 by GOL. The classified data set consists of the seven events listed in Table III with their announced yields (Springer and Kinnaman, 1971 and 1975). All events occurred in hard rock below the water table (Springer and Kinnaman, 1971). We obtained six  $m_{bLg}$ 's for BKS, three each for DUG and GOL and one at TUC.

#### Determination of Yield Using $m_{bLg}$

There are two options when relating  $m_{bLg}$  and yield. One is to calculate network  $m_{bLg}$ 's and plot these versus log yield to get a network calibration curve. Otherwise, a station calibration curve can be obtained by plotting individual station  $m_{bLg}$ 's against log yield. Both of these options are discussed below.



Table III

<u>EVENT</u>	<u>DATE</u>	<u>ANNOUNCED YIELD(kt)</u>	$m_{bLg}$ <u>(without GOL)</u>	$m_{bLg}$ <u>(with GOL)</u>
Bilby	9/13/63	235	5.58	5.41
Rex	2/24/66	19	4.87	4.71
Chartreuse	5/6/66	70	5.23	5.02
Commodore	5/20/67	250	5.51	5.34
Scotch	5/23/67	150	5.38	5.23
Benham	12/19/68	1100	6.04	5.88
Starwart	4/26/73	85	5.30	5.16

After Q corrections are made, each station has characteristically higher or lower  $m_{bLg}$ 's than the others. DUG is on average .27 magnitude units higher than BKS. TUC is .39 magnitude units lower than BKS on average, and GOL averages .55 magnitude units lower.

To eliminate these biases, we calculate network  $m_{bLg}$ 's using the CSS program LSMF (Least Squares Matrix Factorization). Originally, we used the same three stations as Nuttli (preprints 1-3) but with fewer events because we restricted all our events to be below the water table. The resulting  $m_{bLg}$  versus log yield curve is shown in Figure 53. The error bars are the 95% confidence limits and are so large because of the paucity of data. The calibration curve calculated by a linear least squares fit to the data is  $m_{bLg} = .65 \log y + 4.02$ . The standard deviation is  $\sigma = .043$  assuming all the error is in the  $m_{bLg}$ , not the yield.

We added station GOL data to decrease the error bars. The result  $m_{bLg} = .65 \log y + 3.84$  is plotted in Figure 54. Note that the two curves have the same slope but the second is displaced downward by .18 magnitude units from the first. This results from GOL having characteristically lower  $m_{bLg}$ 's than the other stations and thus pulls the network  $m_{bLg}$  down. The data are given in Table III. Just as adding stations changes the calibration curve significantly, adding events also changes the curve. As an example, our original  $m_{bLg}$  versus log yield curve (Semi-Annual Report) was derived from network  $m_{bLg}$ 's calculated by LSMF using several more events which were subsequently

discarded since they occurred above the water table. This original curve was  $m_{bLg} = .69 \log y + 3.69$  which differs in both slope and intercept from the later curve.

Since there are so few events on any of these curves, they should not be used to calculate yields. A more accurate curve can be found in the classified section of this report.

We also calculated a station calibration curve for BKS as shown in Figure 55.  $m_{bLg} = .61 \log y + 4.13$  with  $\sigma = .030$ , again assuming all error is in the  $m_{bLg}$  measurement.

### Calculated Yields

Yields of these events are calculated using the calibration curve in Figure 54. These are shown in Table IV. On average, these values overestimate the announced values by 6%.

Since our  $Q$ 's differ from Nuttli's, our calibration curves also differ. Figure 56 shows his data (preprint 2) with some events edited out. The equation of the linear least squares fit is  $m_{bLg} = .73 \log y + 4.4$  with  $\sigma = .049$ . The curve is displaced upwards from ours because of Nuttli's lower  $Q$ 's. Using our  $m_{bLg}$ 's and his curve, yields are severely underestimated, just as using his  $m_{bLg}$ 's and our curve grossly overestimates the yields (see Table V). His calibration curve with his  $m_{bLg}$ 's underestimates the calculated yields by 6% on average. The ability of our curve to calculate the yields of events not included in the data set is examined in the classified section of this report.

A  $m_{bLg}$  versus log yield curve was also determined for the  $m_{bLg}$ 's derived from the linearly frequency dependent  $Q$  (Figure 57). Note that it is almost identical to our exponential model calibration curve.

Table IV

<u>EVENT</u>	<u>ANNOUNCED YIELD</u>	<u>NETWORK <math>\underline{m}_{bLq}</math></u>	<u>CALCULATED YIELD</u> $(\underline{m}_{bLq} = .65 \log y + 3.84)$
Bilby	235	5.41	260
Rex	19	4.71	22
Chartreuse	70	5.02	65
Commodore	250	5.34	203
Scotch	150	5.23	138
Benham	1100	5.88	1376
Starwart	85	5.16	107

Table V

<u>EVENT</u>	<u>ANNOUNCED YIELD</u>	<u>RAI'S <math>\underline{m}_{bLq}</math></u>	<u>NUTTLI'S <math>\underline{m}_{bLq}</math></u>	<u>CALCULATED YIELD RAI-NUTTLI</u>	<u>CALCULATED YIELD NUTTLI-RAI</u>	<u>CALCULATED YIELD NUTTLI-NUTTLI</u>
Bilby	235	5.41	6.10	24kt	2999	213
Rex	19	4.71	5.28	3	164	16
Chartreuse	70	5.02	5.76	7	899	73
Commodore	250	5.34	6.04	19	2425	176
Scotch	150	5.23	6.00	14	2104	156
Benham	1100	5.88	6.65	107	21042	1208
Starwart	85	5.16	5.85	11	1237	97

## References

- Bollinger, G.A., 1979, Attenuation of the Lg Phase and the Determination of  $m_0$  in the Southeastern United States, Bull. Seis. Soc. Am., v. 69, pp. 45-63.
- Herrmann, R.B., 1980, Q Estimates Using Coda of Local Earthquakes, B.S.S.A., v. 70, no. 2, pp. 447-468.
- Mitchell, B.J., 1980, Frequency Dependence of Shear Wave Internal Friction in the Continental Crust of Eastern North America, Jour. Geophys. Res., v. 85, no. B10, pp. 5212-5218.
- Mitchell, B.J. and O.W. Nuttli, 1982, Attenuation of Seismic Waves at Regional Distances, Semi-Annual Report Contract F49620-79-C-0025.
- Mitchell, B.J. and O.W. Nuttli, 1983, Attenuation of Seismic Waves at Regional Distances, Semi-Annual Report Contract F49620-83-C-0015.
- Nuttli, O.W., 1973, Seismic Wave Attenuation and Magnitude Relations for Eastern North America, J. Geophys. Res., v. 78, pp. 876-885.
- Nuttli, O.W., Seismic Yield Determination For NTS Events Using Regional Lg Waves (preprint 1; also contained in Mitchell and Nuttli, 1982).
- Nuttli, O.W., A Methodology for Obtaining Seismic Yield Estimates of Underground Explosions Using Short Period Lg Waves (Preprint 2).
- Nuttli, O.W., Illustration of Use of Coda Q Method to Obtain Anelastic Attenuation Values for Paths from Salmon (Mississippi) and NTS Events (Preprint 3; also contained in Mitchell and Nuttli, 1983).
- Pomeroy, P.W., 1977, Aspects of Seismic Wave Propagation in Eastern North America, Preliminary Report, Rondout Associates, Incorporated, Stone Ridge, New York.
- Springer, D.L. and R.L. Kinnaman, 1971, Seismic Source Summary for U.S. Underground Nuclear Explosions, 1961-1970, Bull. Seism. Soc. Am., 61, 1073-1098.
- Springer, D.L. and R.L. Kinnaman, 1975, Seismic Source Summary for U.S. Underground Nuclear Explosions, 1971-1973, Bull. Seism. Soc. Am., 65, 343-349.
- Street, R.L., 1976, Scaling Northeastern United States/Southeastern Canada Earthquakes by their Lg Waves, Bull. Seis. Soc. Am., v. 66, pp. 1525-1537.

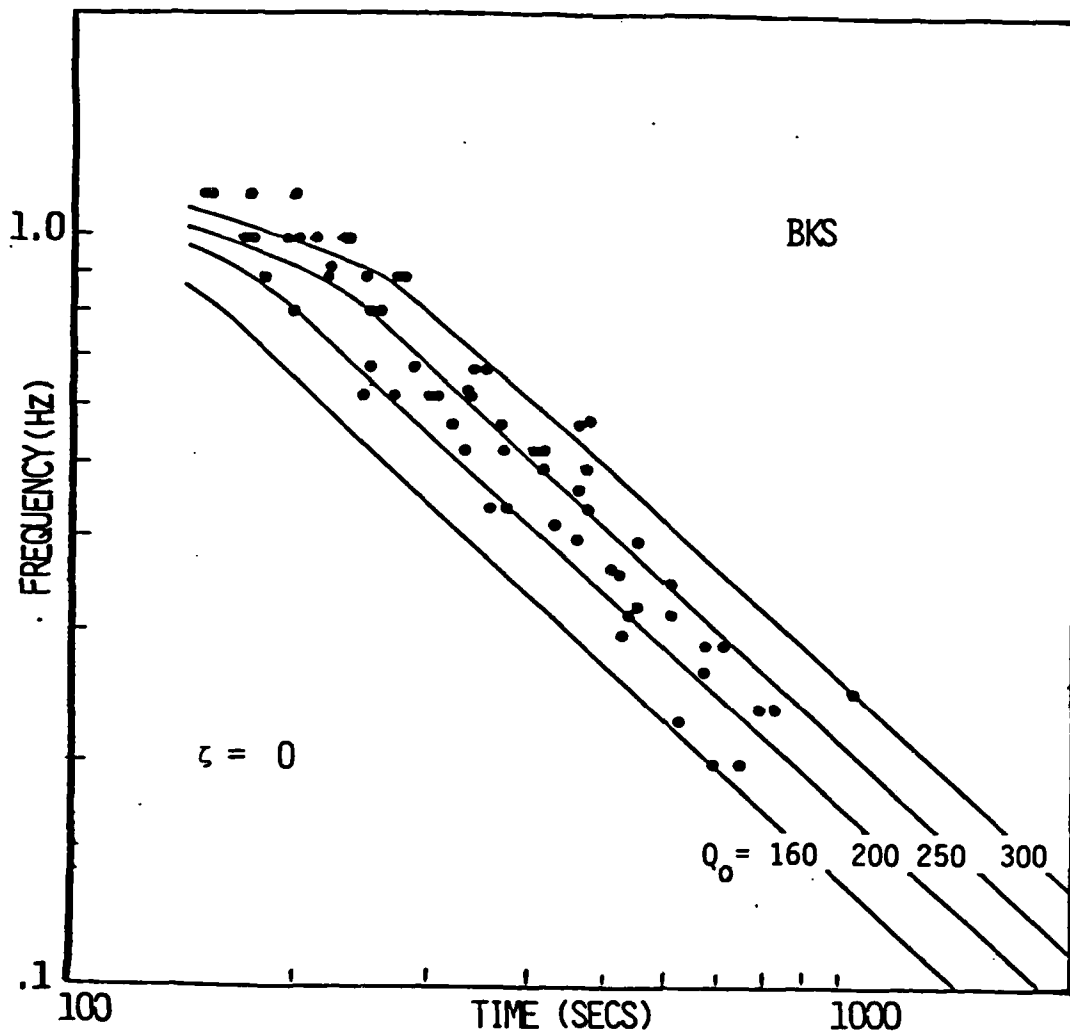


Figure 1.  $f_p$  versus  $t$  data at BKS with theoretical curves generated using a  $Q$  model with  $p$  no frequency dependence. That is,  $Q=Q_0 f_p^\zeta$  with  $\zeta=0$ . Note that the data trend down across the different  $Q_0$  curves indicating a higher slope than these curves.

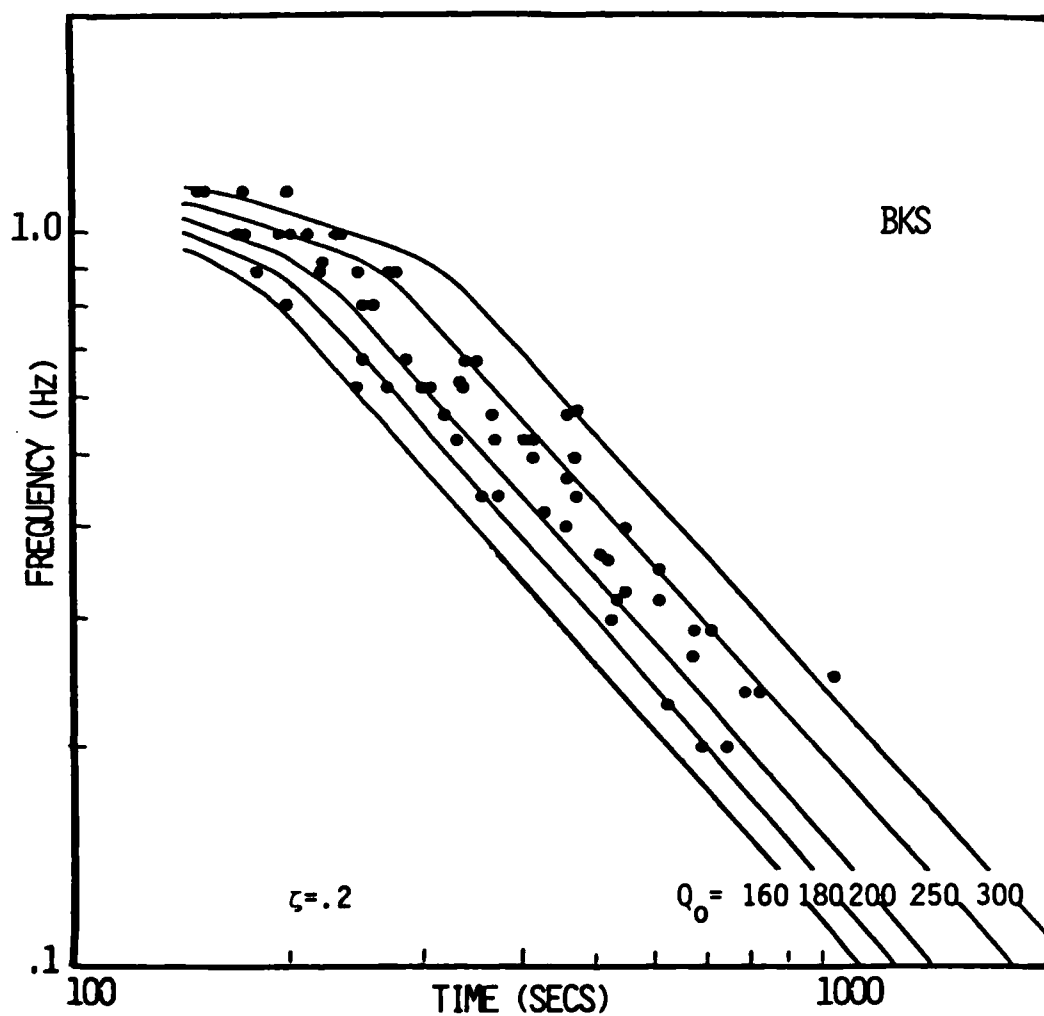


Figure 2.  $f$  versus  $t$  data at BKS with theoretical curves generated using an exponential  $P$  model of frequency dependence  $Q = Q_0 f^\zeta$  with  $\zeta = .2$ . The data appear to have the same slope as the curves and  $Q_0 \approx 225$  appears to fit the data.



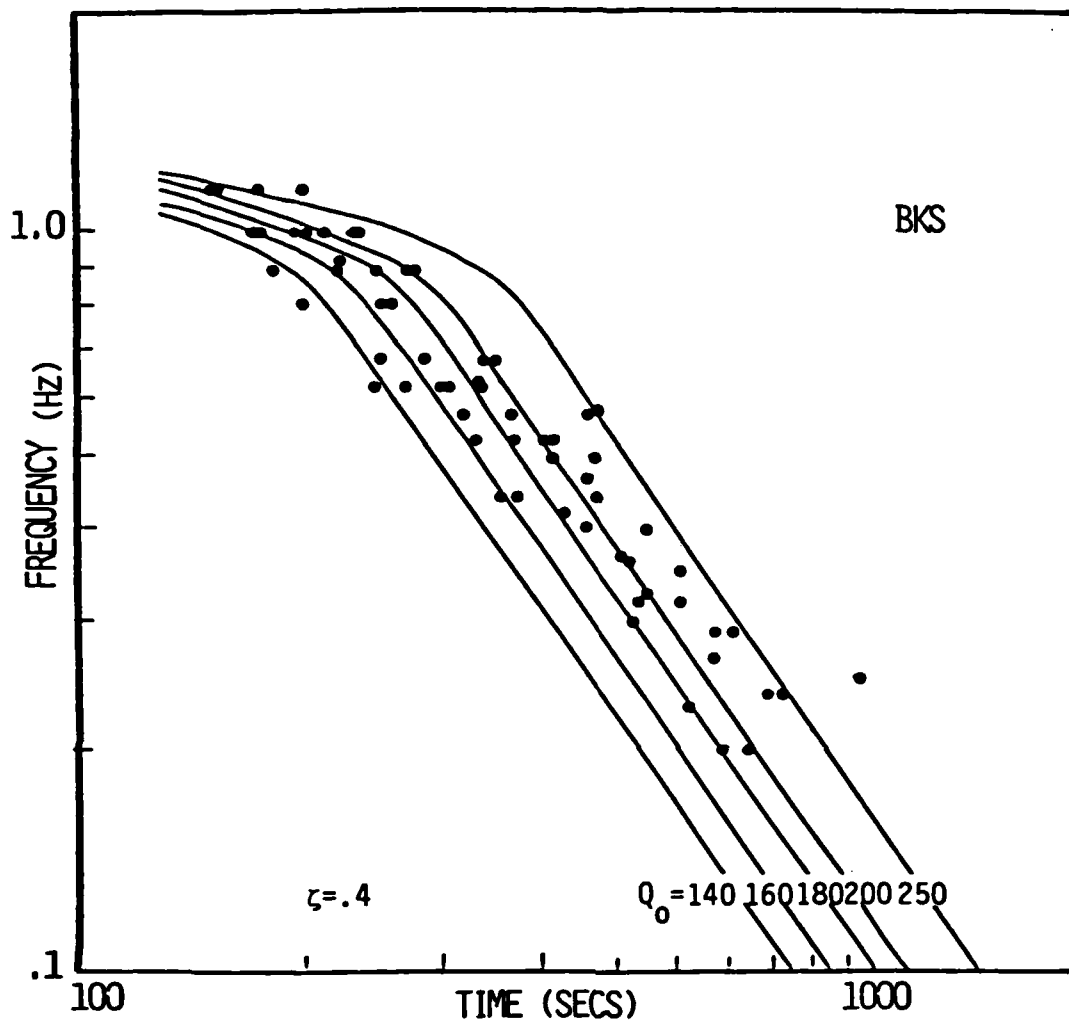


Figure 3.  $f_p$  versus  $t$  data at BKS with  $\zeta = .4$ ,  $Q = Q_0 f_p^\zeta$  theoretical curves. Here the data  $f_p$  seem to cut upwards across the curves, indicating a lower slope than the curves.

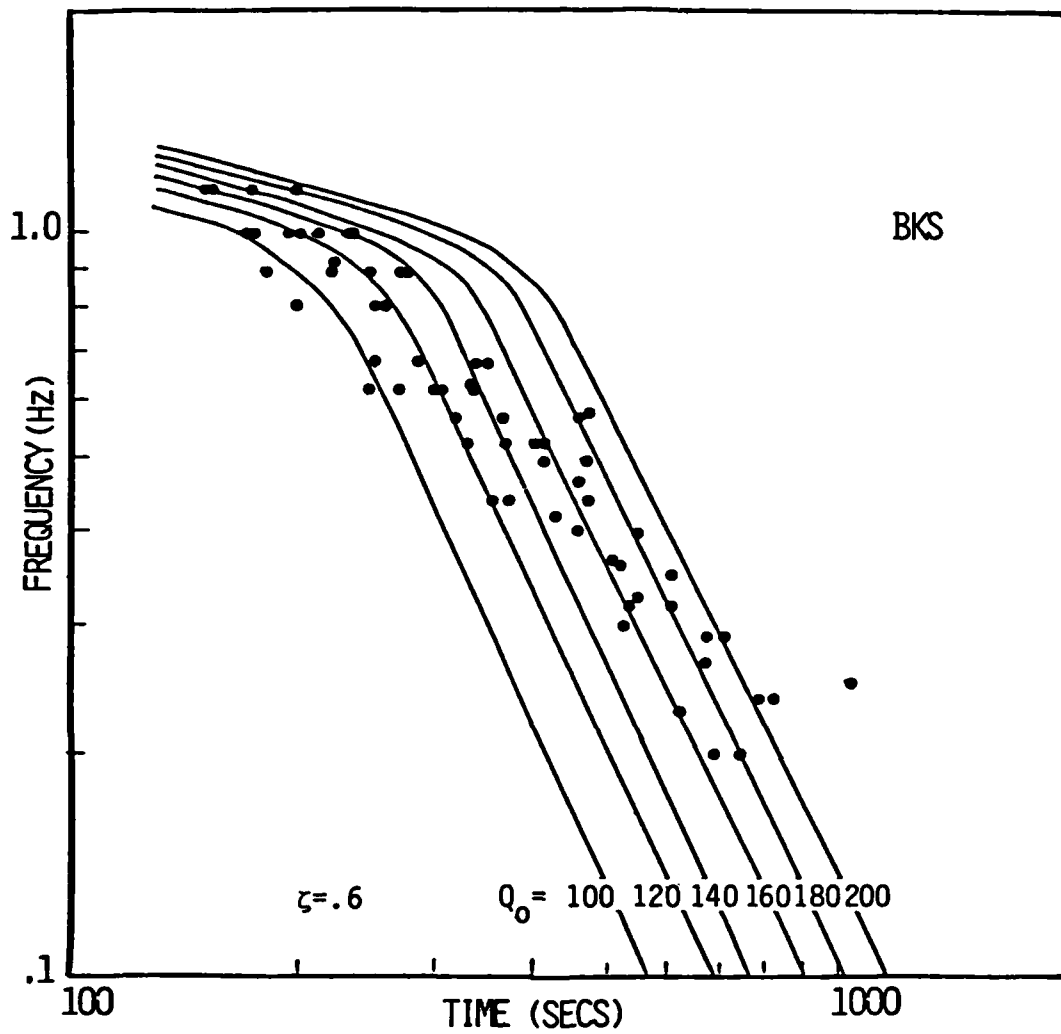


Figure 4.  $f$  versus  $t$  data at BKS with  $\zeta = 0.6$ . As the  $\zeta$  increases, the slope increases. Here the data cut across the theoretical curves more severely than in Figure 3 for  $\zeta = 0.4$ .

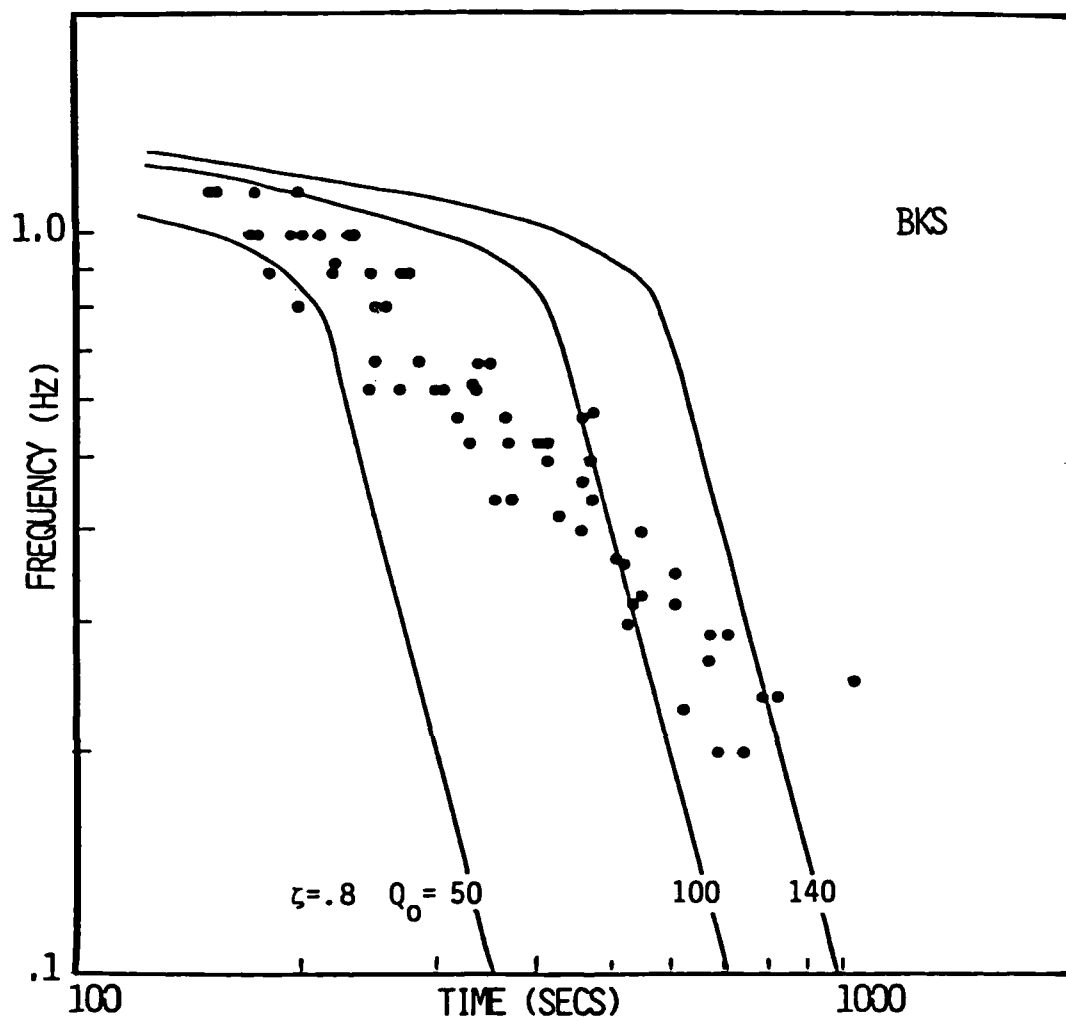


Figure 5.  $f_p$  versus  $t$  data at BKS with  $\zeta = 0.8$ . The data seem to have a totally different  $P$  slope than these theoretical curves.

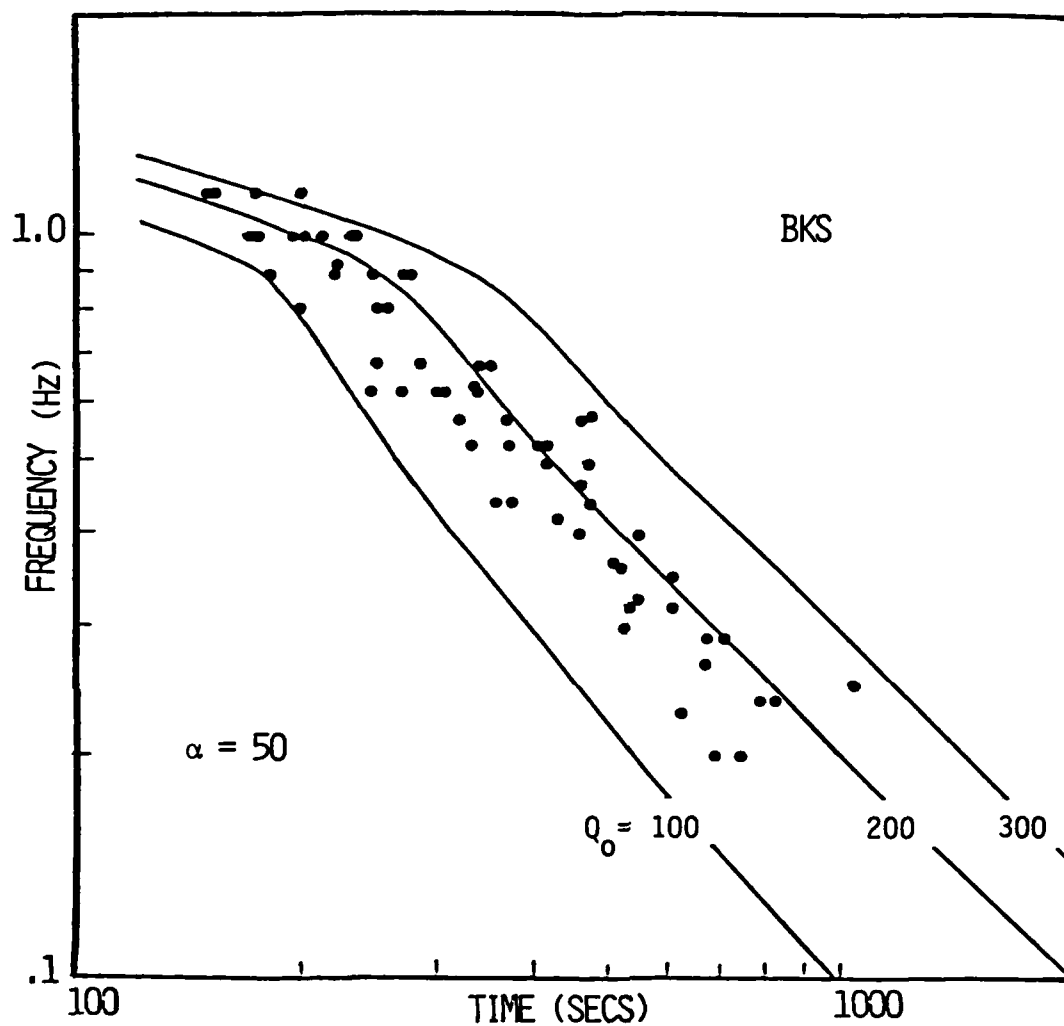


Figure 6.  $f_p$  versus  $t$  data at BKS with theoretical curves generated using a  $Q$  model with a  $p$  linear dependence on frequency ( $Q=Q_0 + \alpha f$ ).  $\alpha=50$ . A curve of  $Q_0 \approx 175$  seems to fit the data fairly well.

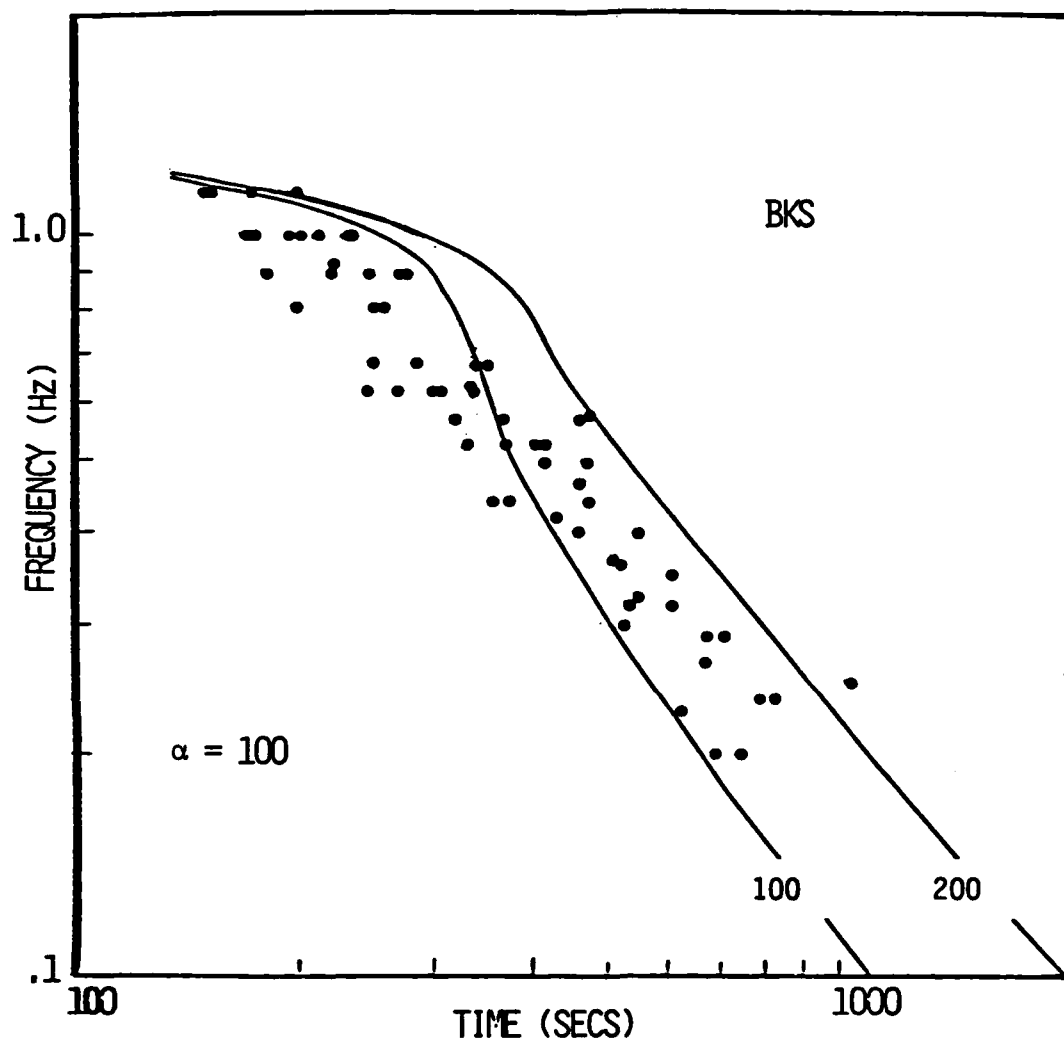


Figure 7.  $f_p$  versus  $t$  data at BKS with theoretical curves for  $\alpha=100$ . The data  $f_p$  seem to have a lower slope than the theoretical curves.

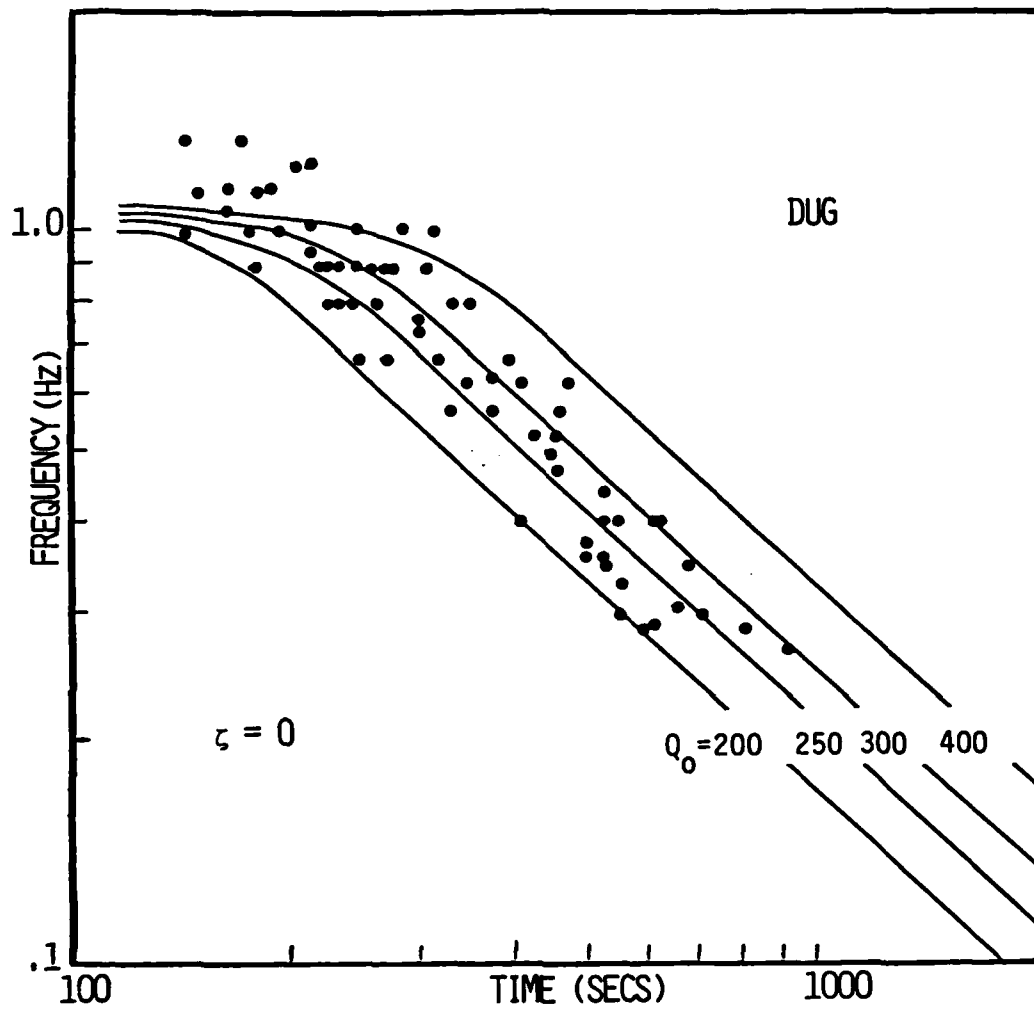


Figure 8.  $f_p$  versus  $t$  data at WSSN station DUG with theoretical curves from a  $Q$  model  $P$  with no frequency dependence. That is,  $Q=Q_0 f^\zeta$  with  $\zeta=0$ . The data trend down across the different  $Q_0$  curves indicating a  $Q_0$  steeper slope than these curves.



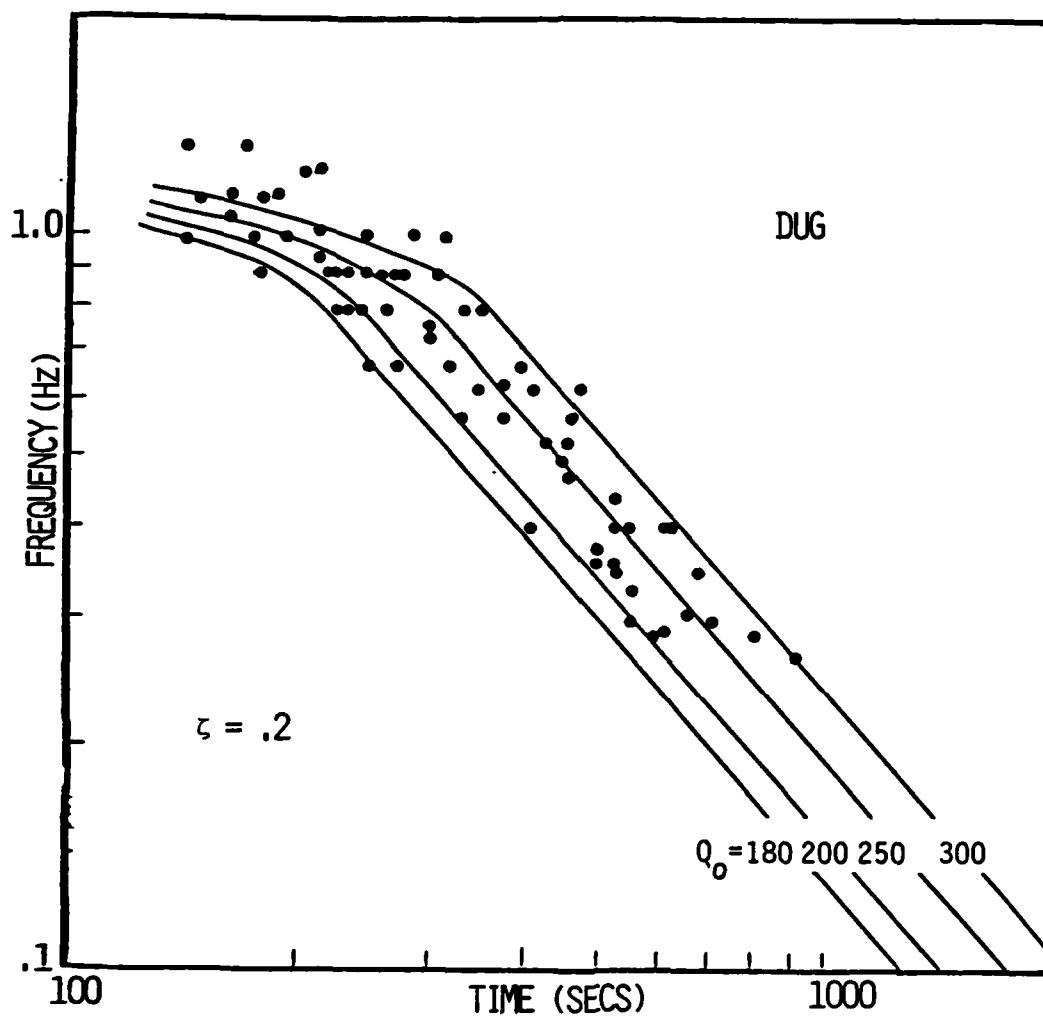


Figure 9.  $f_p$  versus  $t$  data at DUG with the  $\zeta=0.2$  theoretical curves. The slope of the  $f_p$  data is close to that of these curves. The RAI choice for best exponential  $Q$  model is  $\zeta=0.3$ ,  $Q_0=230$ .

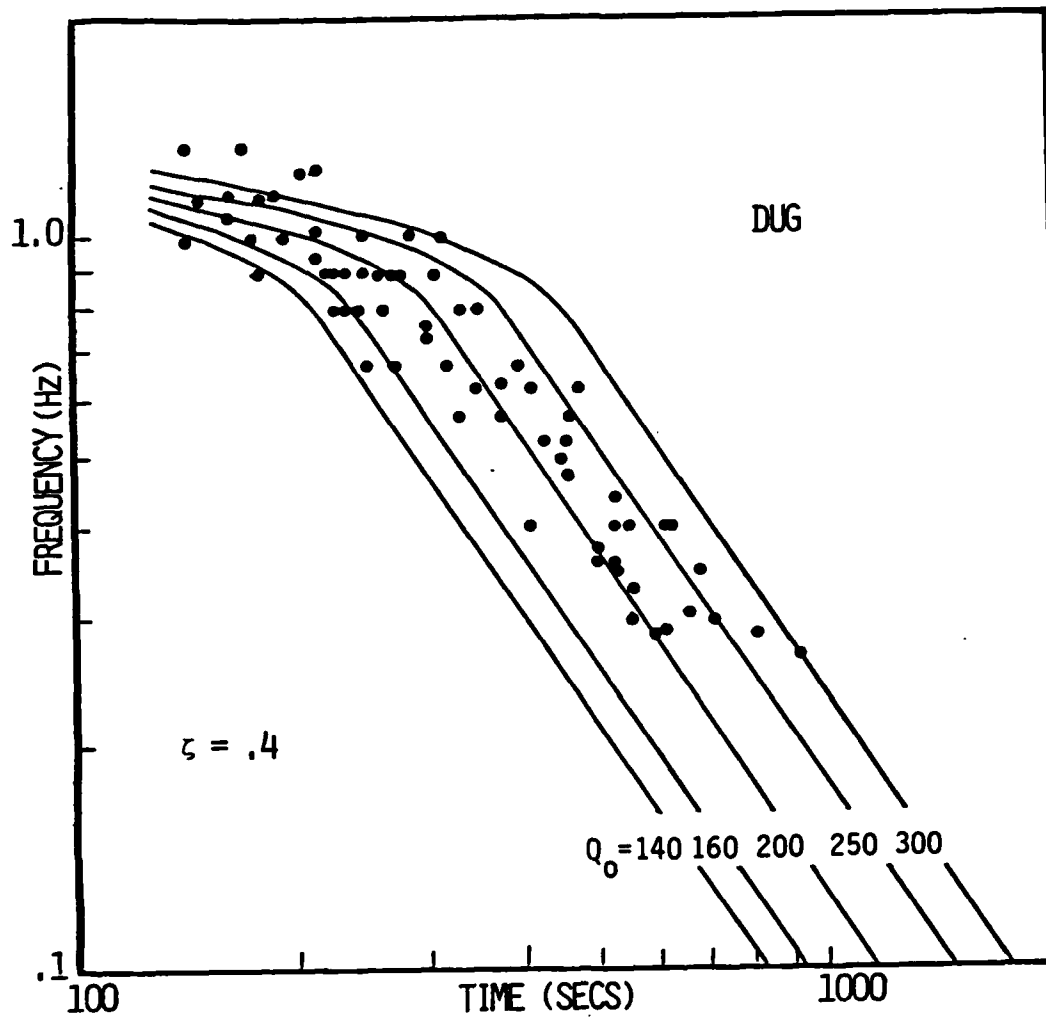


Figure 10.  $f_p$  versus  $t$  data at DUG with the  $\zeta=.4$  theoretical curves.

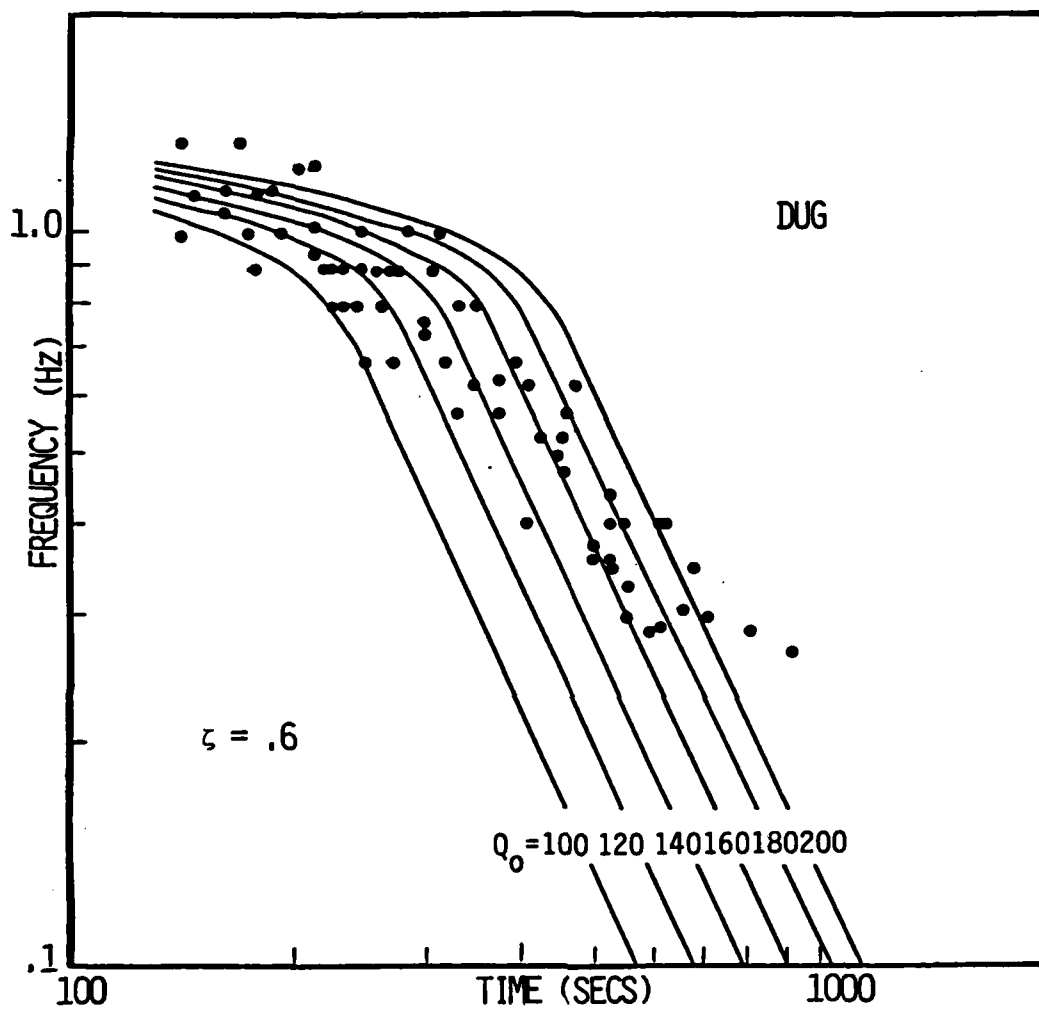


Figure 11.  $f_p$  versus  $t$  data at DUG with the  $\zeta=.6$  theoretical curves. The slope of  $f_p$  these curves appears much steeper than that of the data.

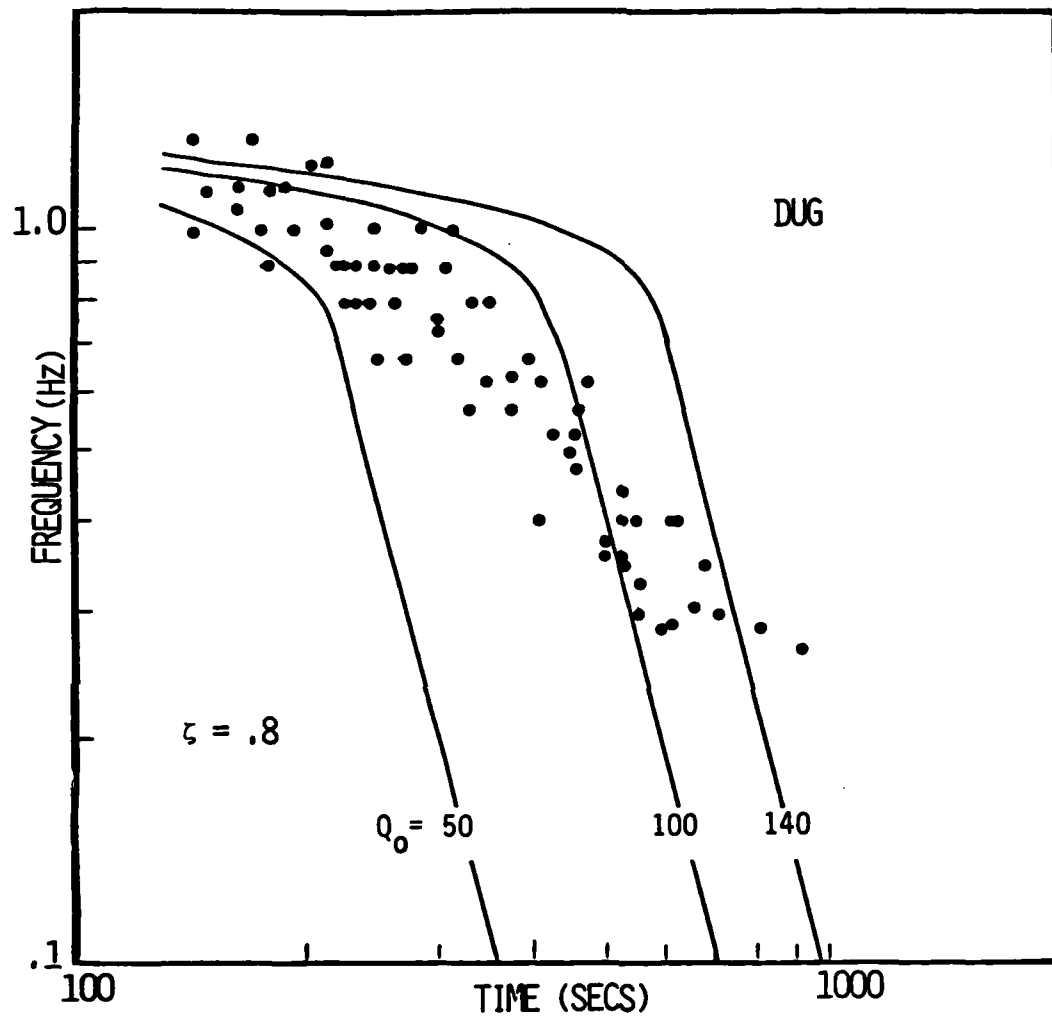


Figure 12.  $f_p$  versus  $t$  data at DUG with the  $\zeta=.8$  theoretical curves. The slope of these curves appears to be much steeper than that of the data.

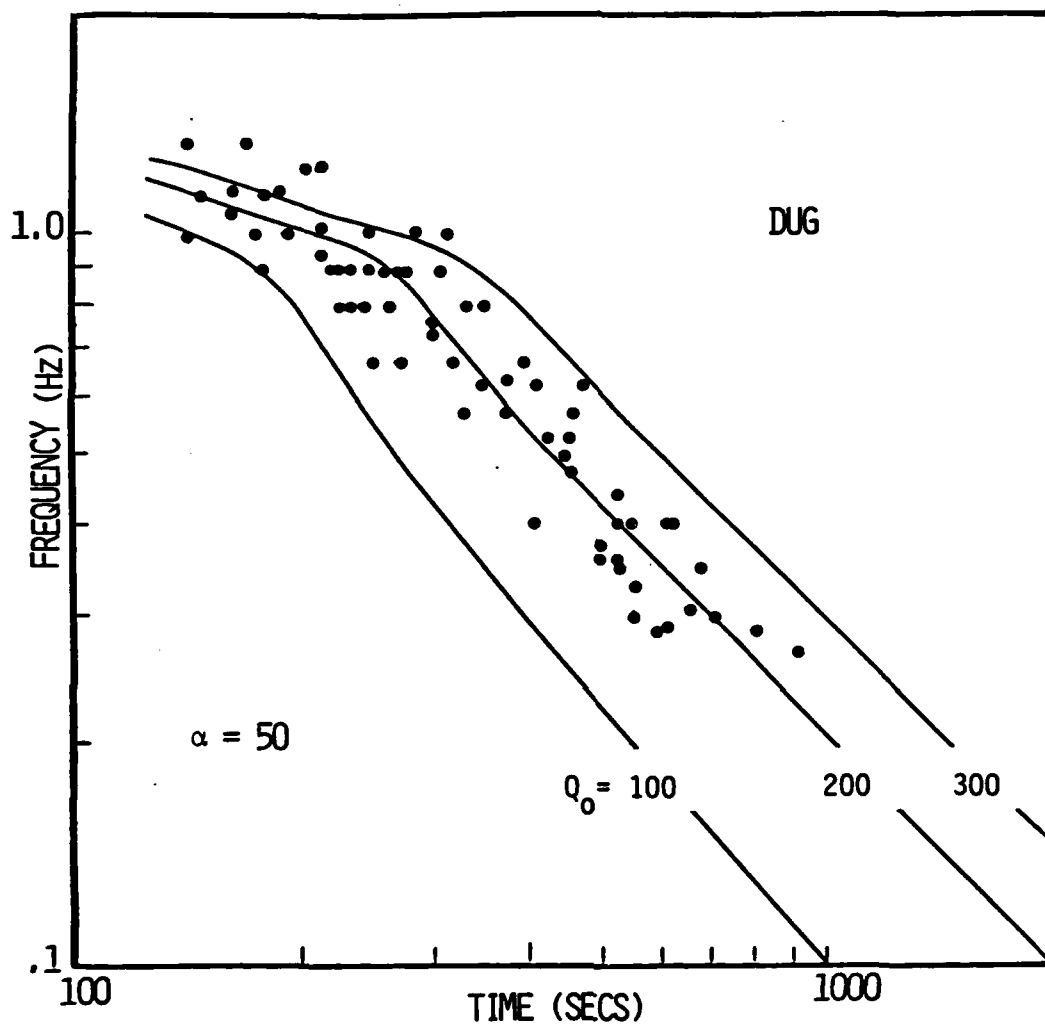


Figure 13.  $f_p$  versus  $t$  data at DUG on theoretical curves generated using a linearly  $P$  frequency dependent  $Q$  model ( $Q=Q_0 + \alpha f$ ) with  $\alpha=50$ . The slope of the data seems to be close to that of these curves.

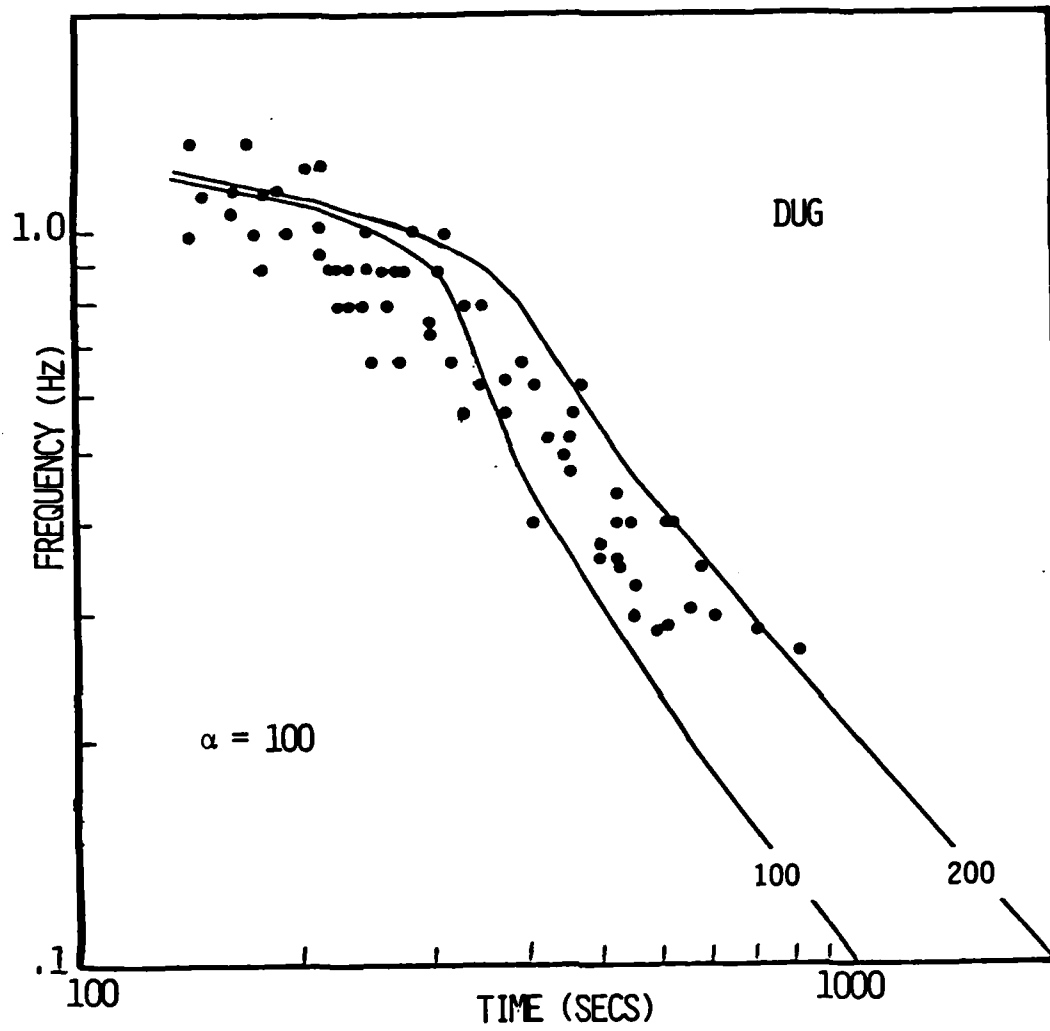


Figure 14.  $f_p$  versus  $t$  data at DUG with  $\alpha=100$  in the linear Q model.

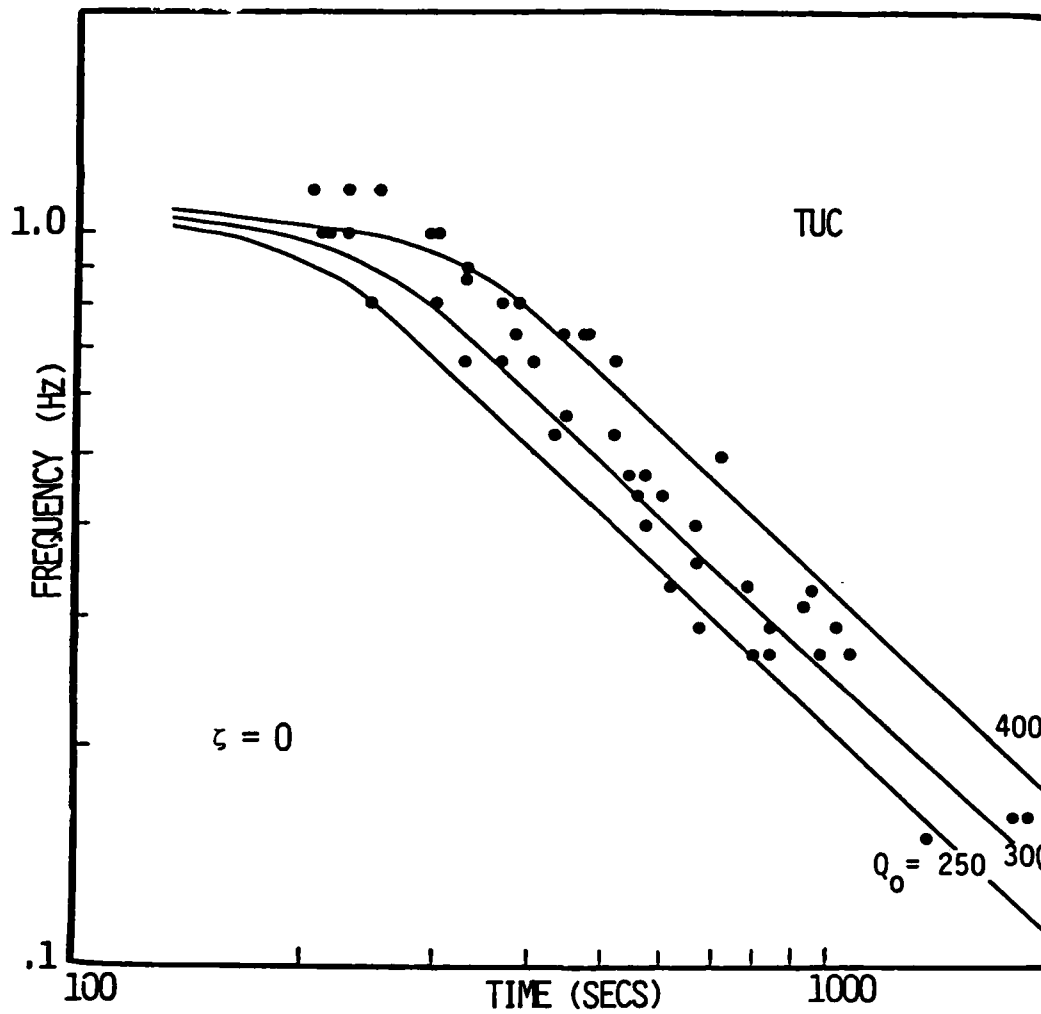


Figure 15.  $f$  versus  $t$  data at TUC with a frequency dependent model  $Q=Q_0 f^\zeta$  with  $\zeta=0$ . As in Figures 1 and 8 for BKS and DUG, the data have a steeper slope than these theoretical curves indicating the need for a frequency dependent model ( $\zeta \neq 0$ ).

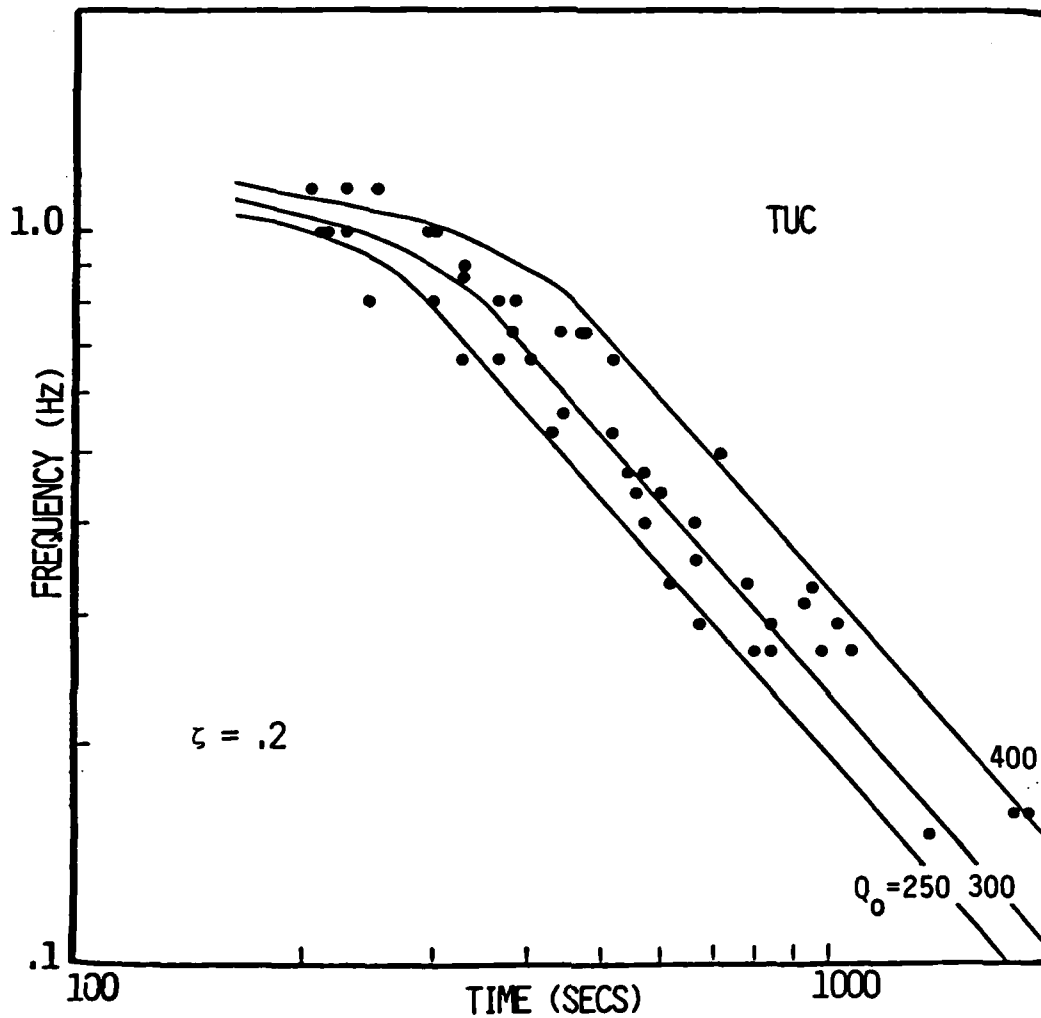


Figure 16.  $f$  versus  $t$  data at TUC with an exponential frequency dependent model  $PQ = Q_0 f^\zeta$  with  $\zeta = .2$ . These curves appear to fit the slope of the data. The RAI choice of best exponential fit to the data is  $\zeta = .2$ ,  $Q_0 = 300$ .



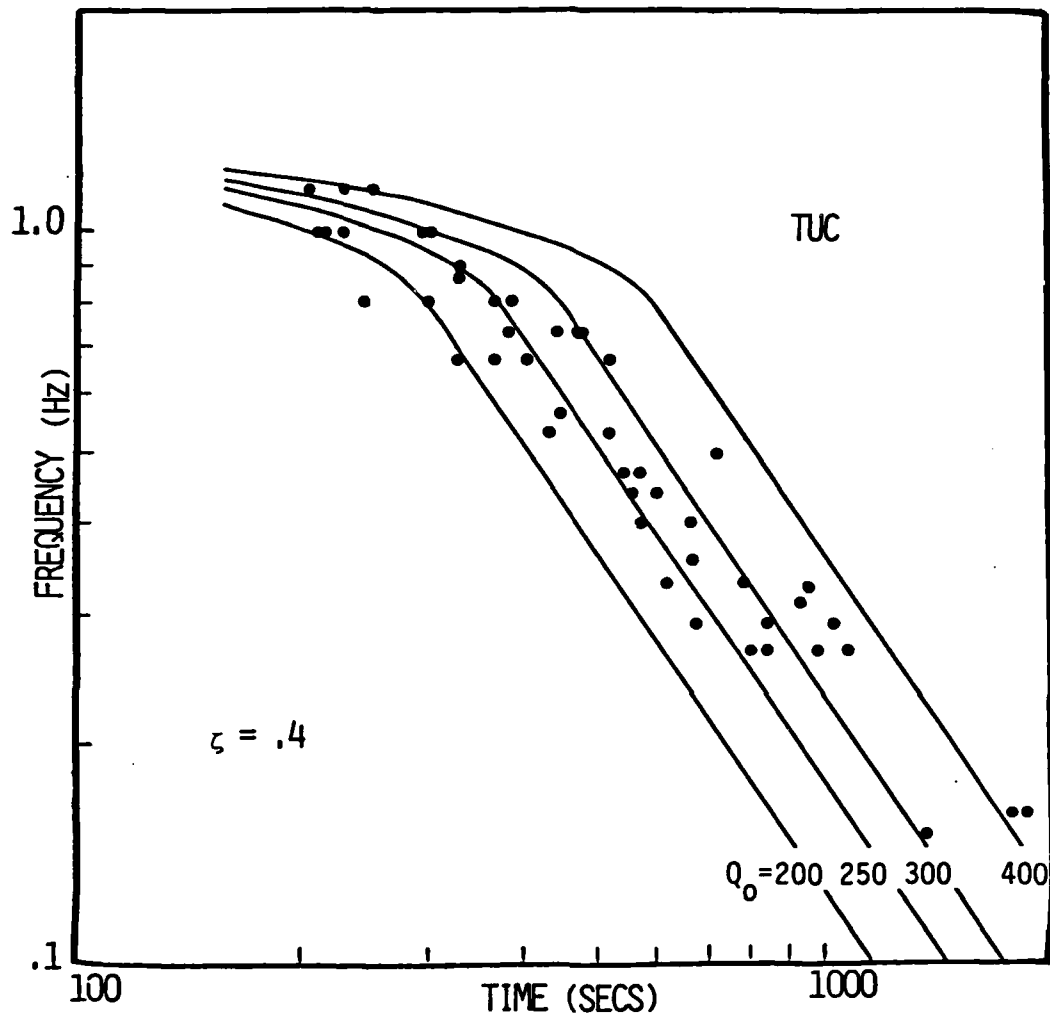


Figure 17.  $f_p$  versus  $t$  data at TUC for the  $\zeta=.4$  theoretical curves. The curves have a  $p$  somewhat steeper slope than the data.

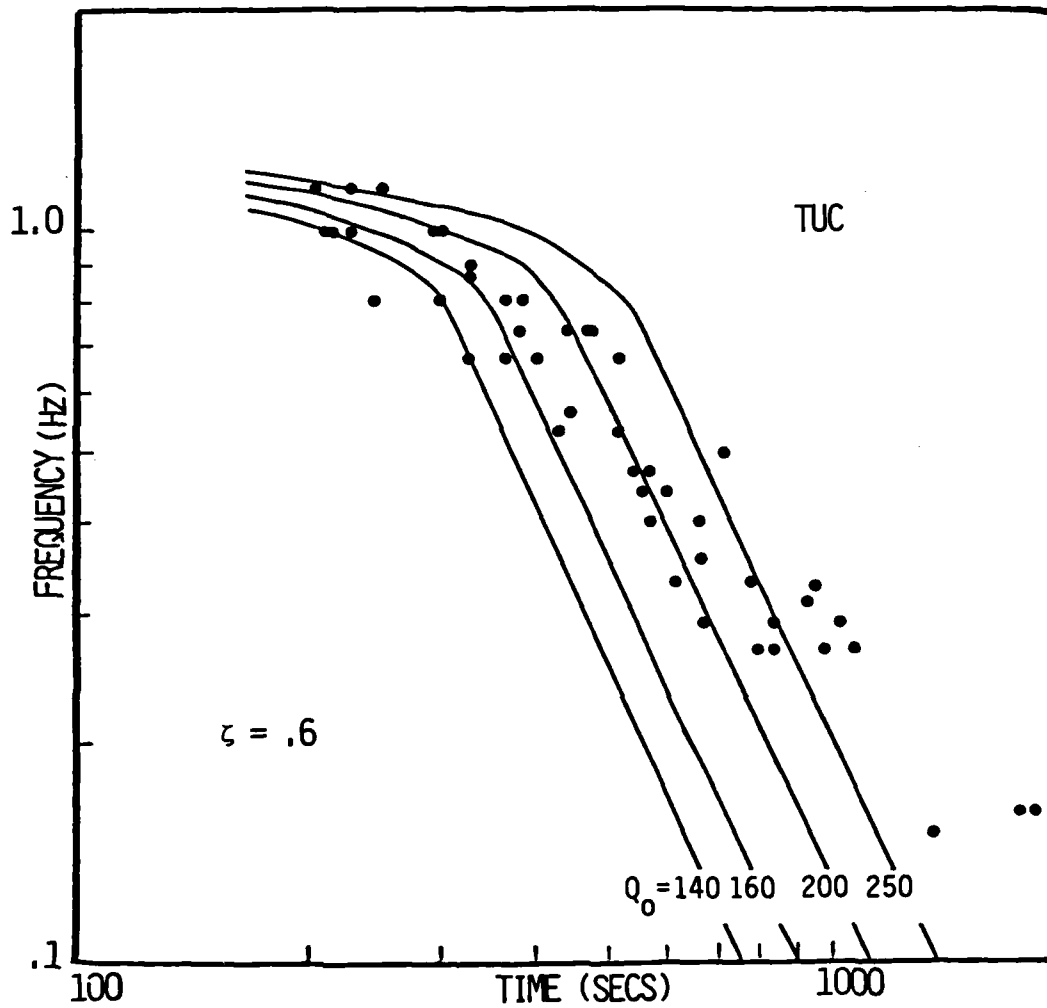


Figure 18.  $f$  versus  $t$  data at TUC with  $\zeta=.6$  theoretical curves. As in Figure 4 and 11 for PBKS and DUG, the curves have a steeper slope than the data.

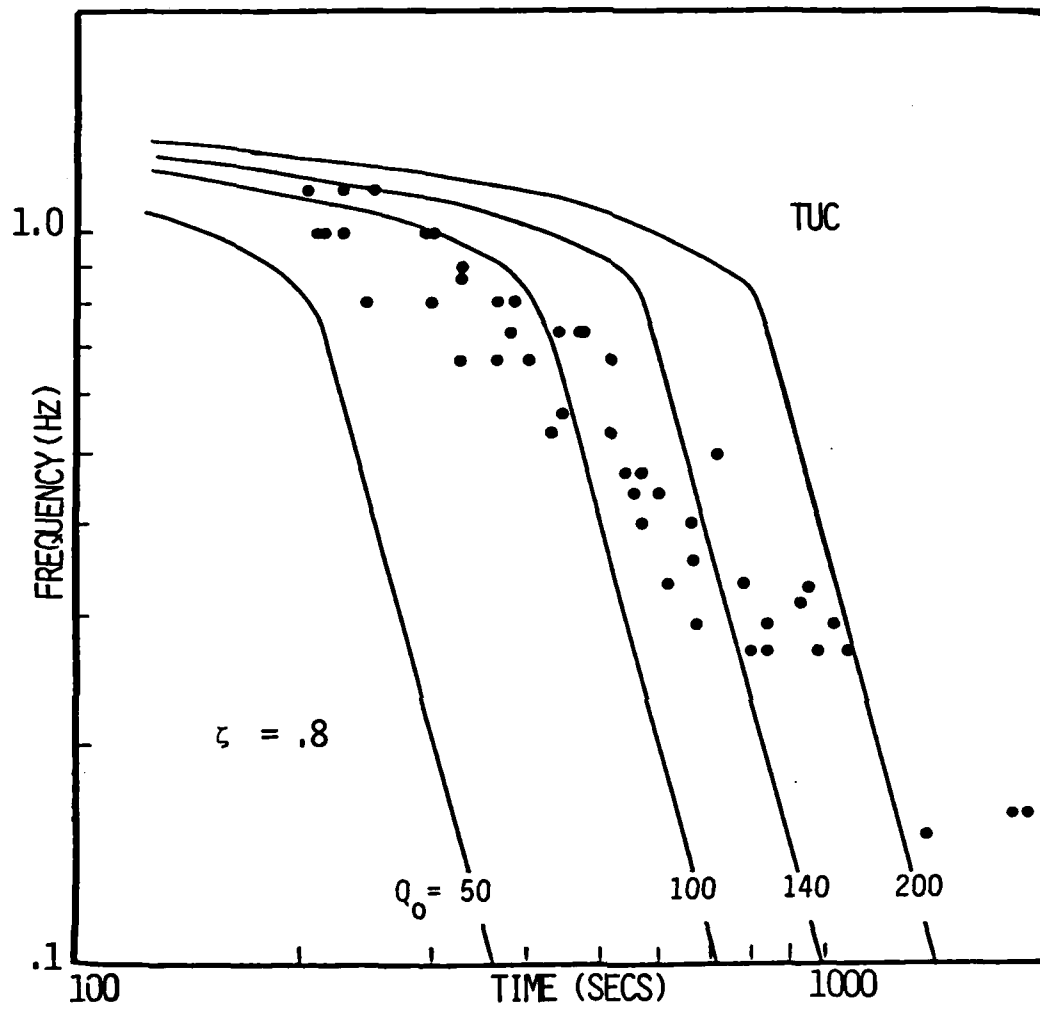


Figure 19.  $f_p$  versus  $t$  data at TUC for  $\zeta = .8$ .

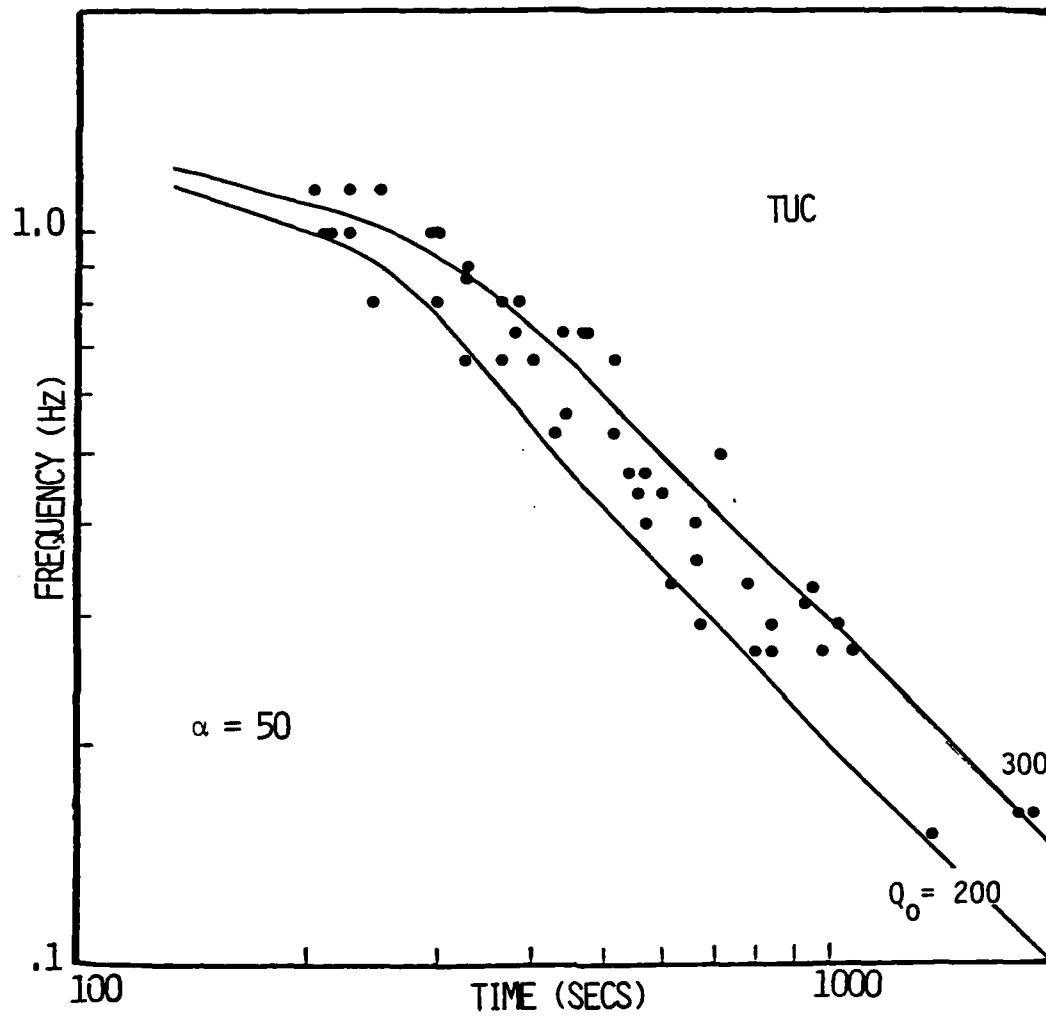


Figure 20.  $f_p$  versus  $t$  data at TUC with a linear frequency dependent  $Q$  model  $Q = Q_0 + \alpha f_p$  with  $\alpha = 50$ . The RAI choice for best linear model fit to the data is  $\alpha = 50$ ,  $Q_0 = 275$ .

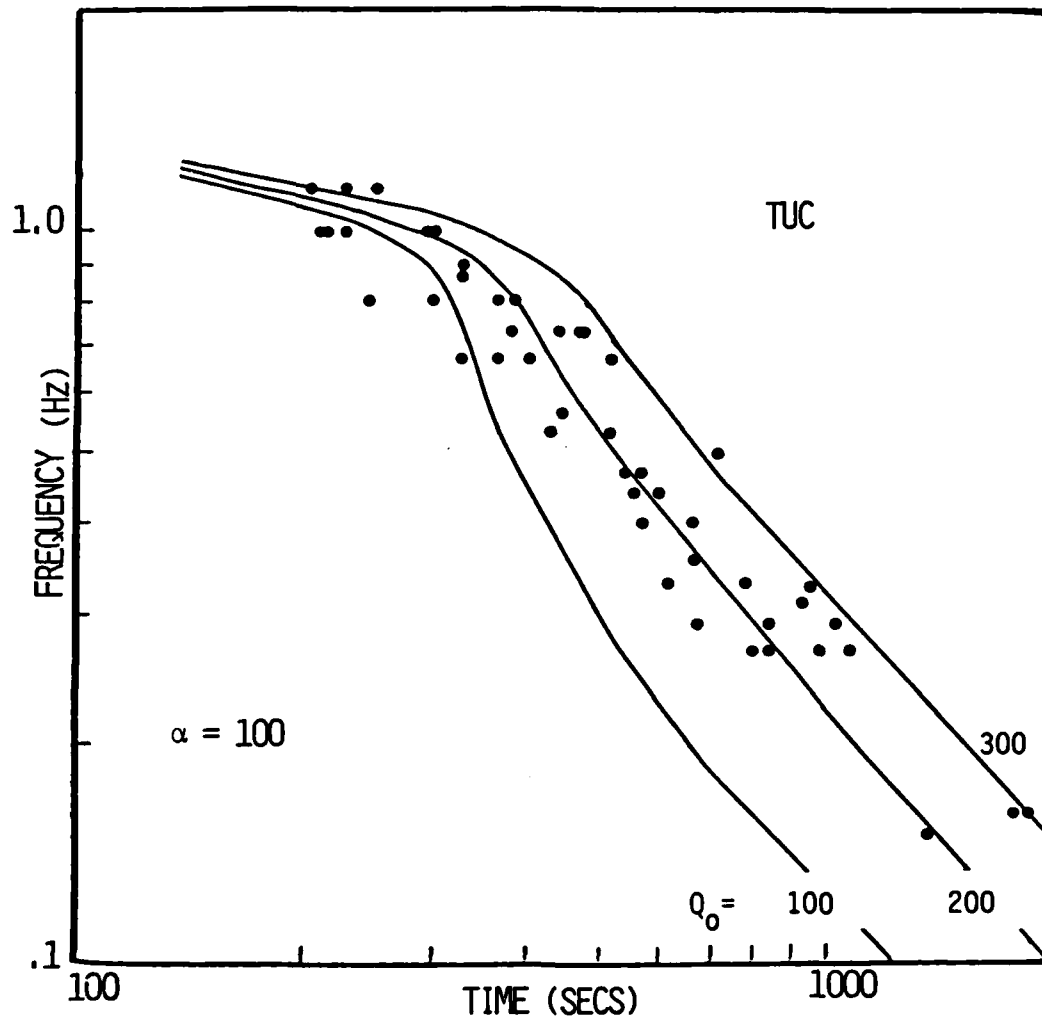


Figure 21.  $f_p$  versus  $t$  data at TUC with the  $\alpha=100$  linear theoretical curves.

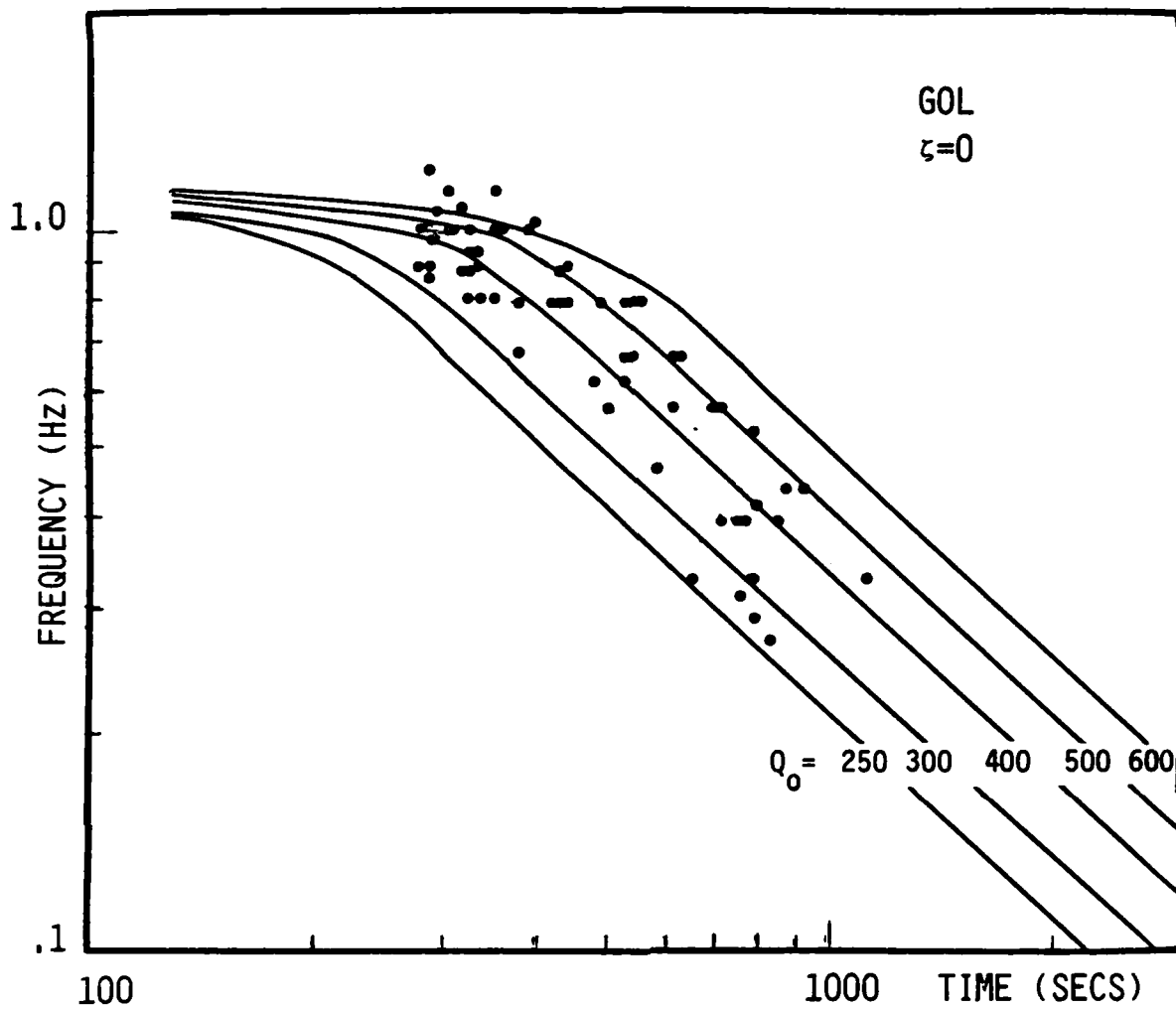


Figure 22. GOL predominant frequency ( $f_p$ ) versus time data on master curves with  $\zeta=0$ . Note the data's steeper slope than the curves.

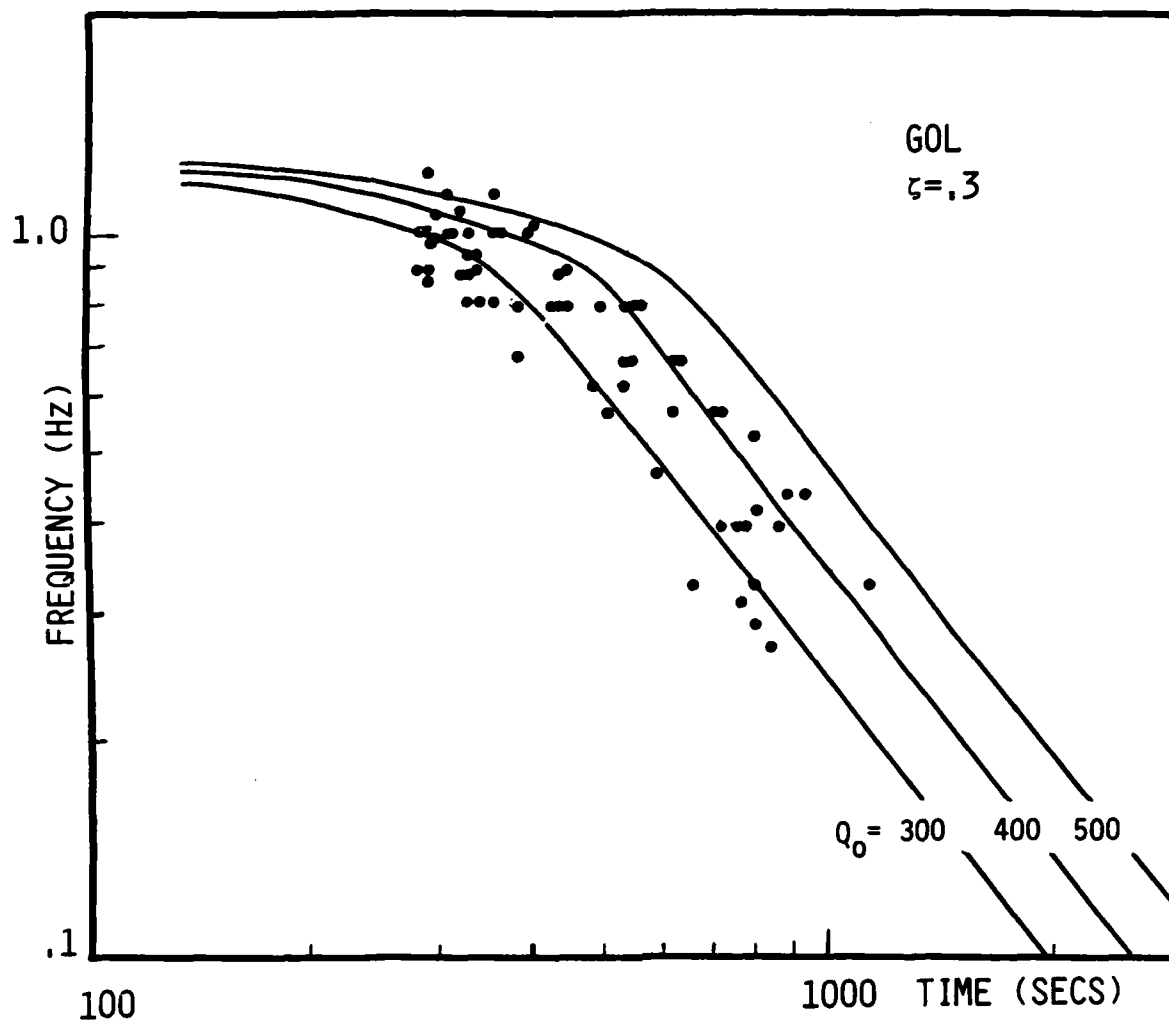


Figure 23. GOL  $f_p$  versus time data on master curves with  $\zeta = 0.3$ . Our best fit is  $\zeta = 0.3$   $Q_0 = 345$ .

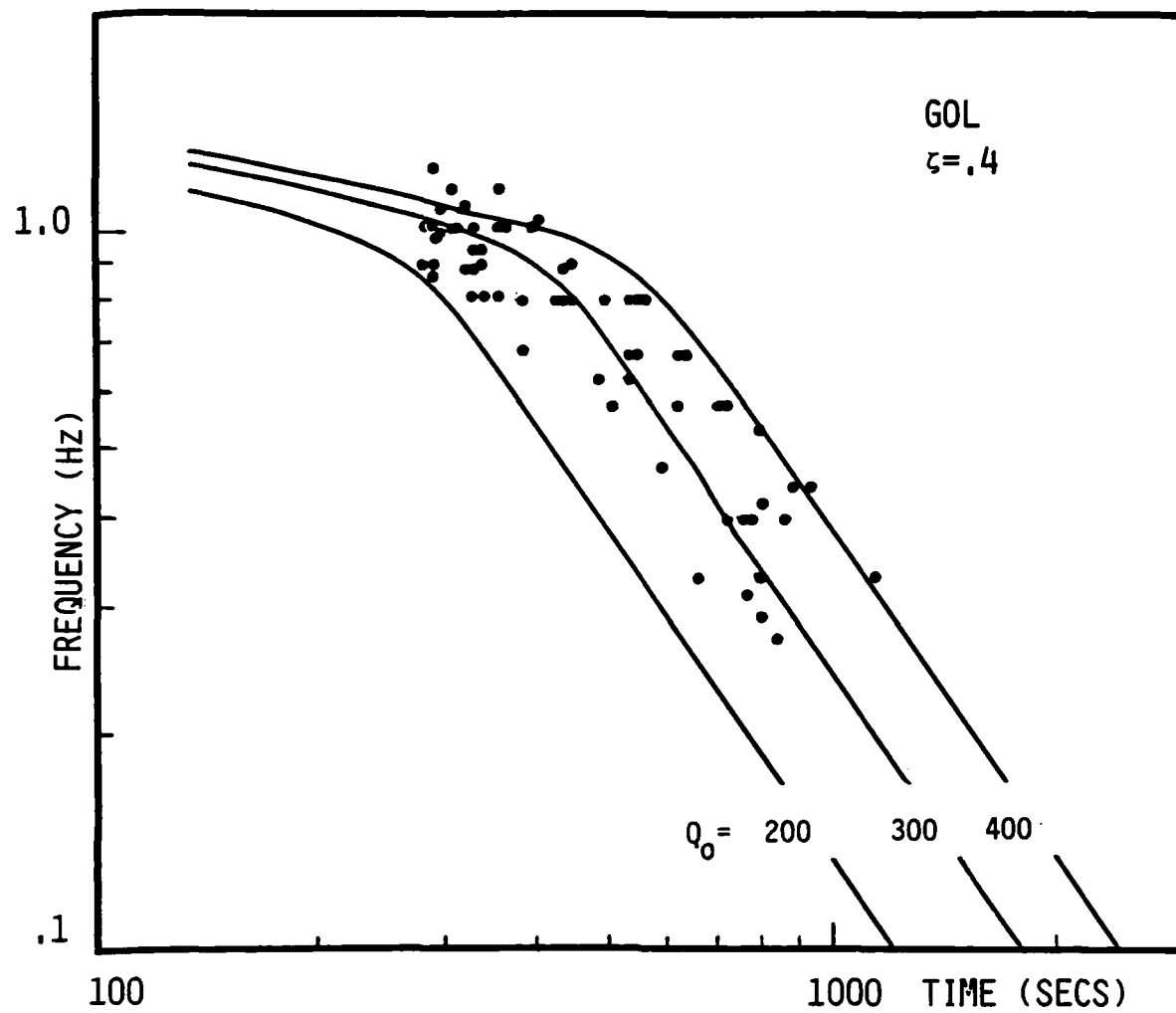


Figure 24. GOL  $f$  versus time data on master curves with  $\zeta = .4$ . Note the data's slightly 'less steep slope than the curves'.



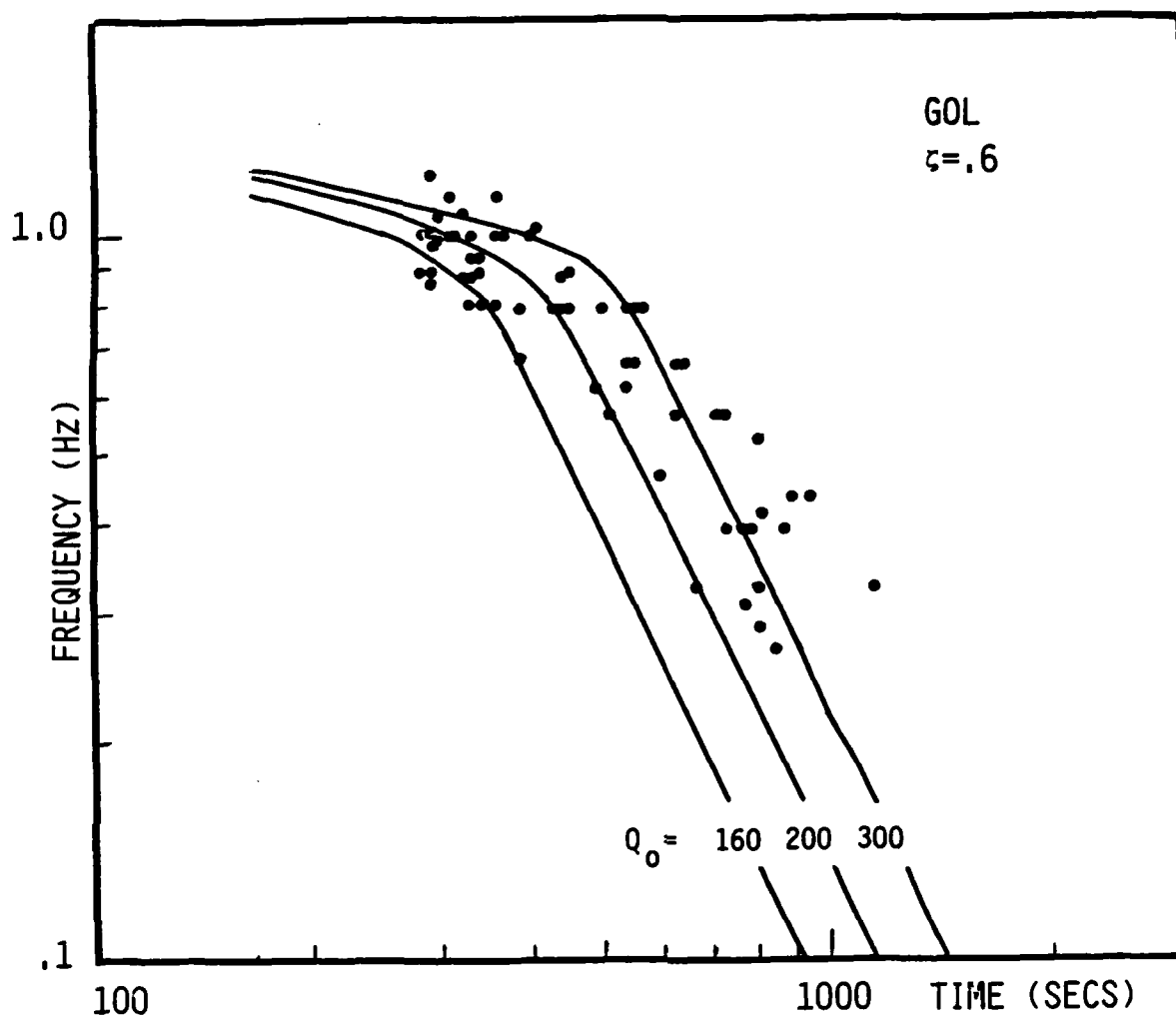


Figure 25. GOL  $f$  versus time data on master curves with  $\zeta = .6$ . The slope of the data is much less steep than that of the  $Q_0$  curves.

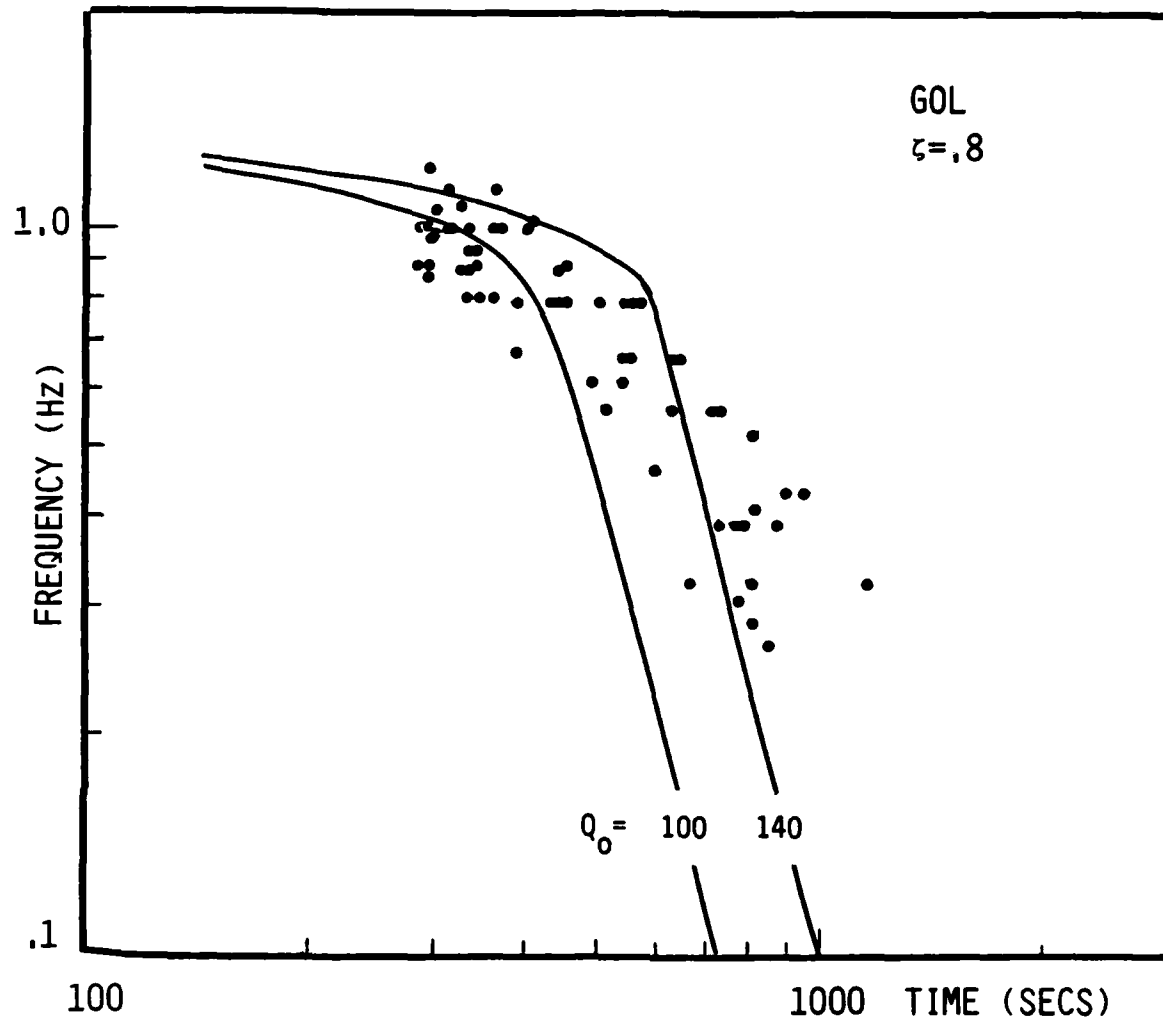


Figure 26. GOL  $f_p$  versus time data on master curves with  $\zeta = .8$ .

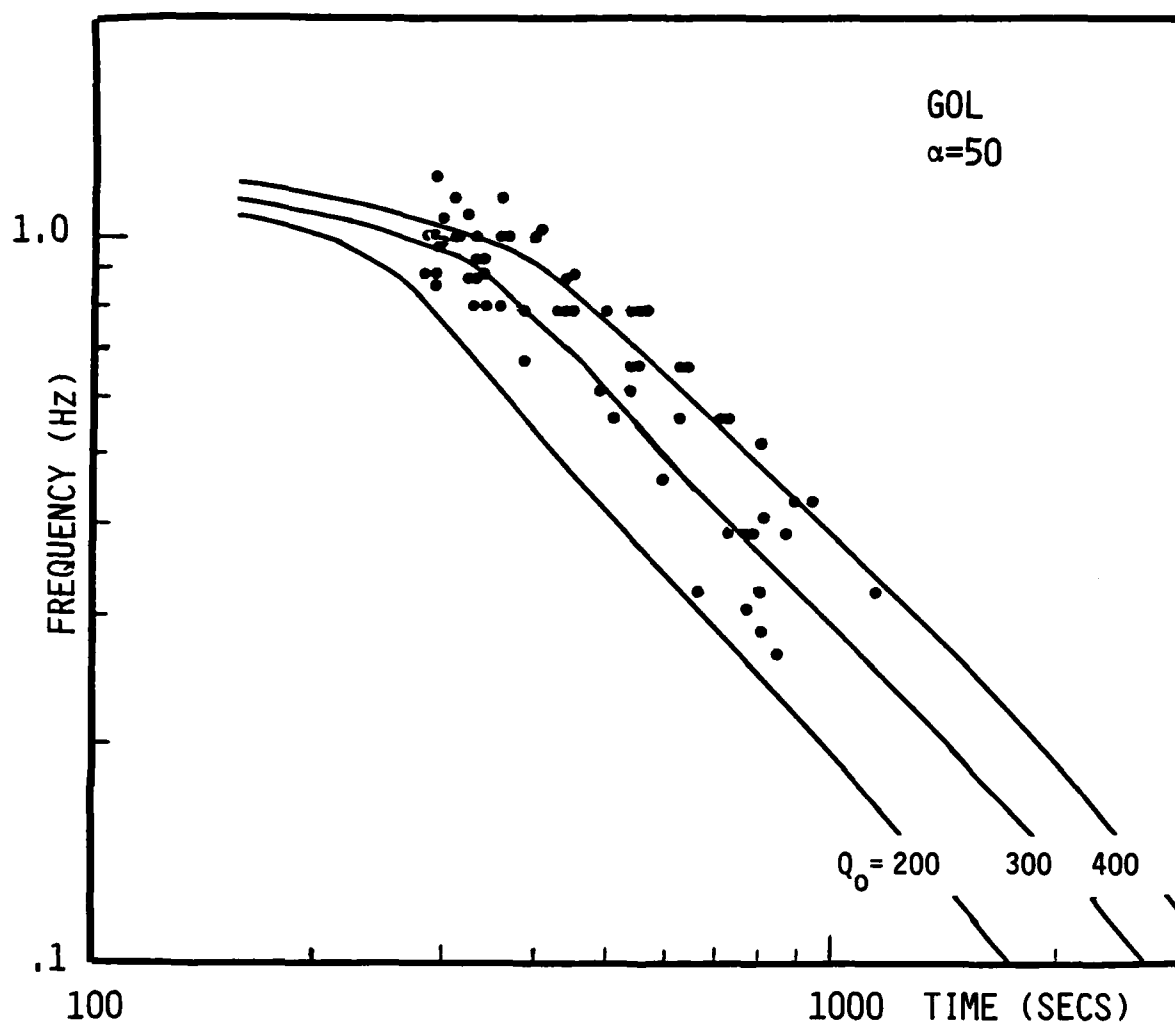


Figure 27. GOL  $f$  versus time data on master curves of a linearly frequency dependent  $Q$ .  $PQ=Q_0+\alpha f$ .  $\alpha=50$ . The RAI best linear model fit is  $\alpha=50$   $Q_0=370$ .

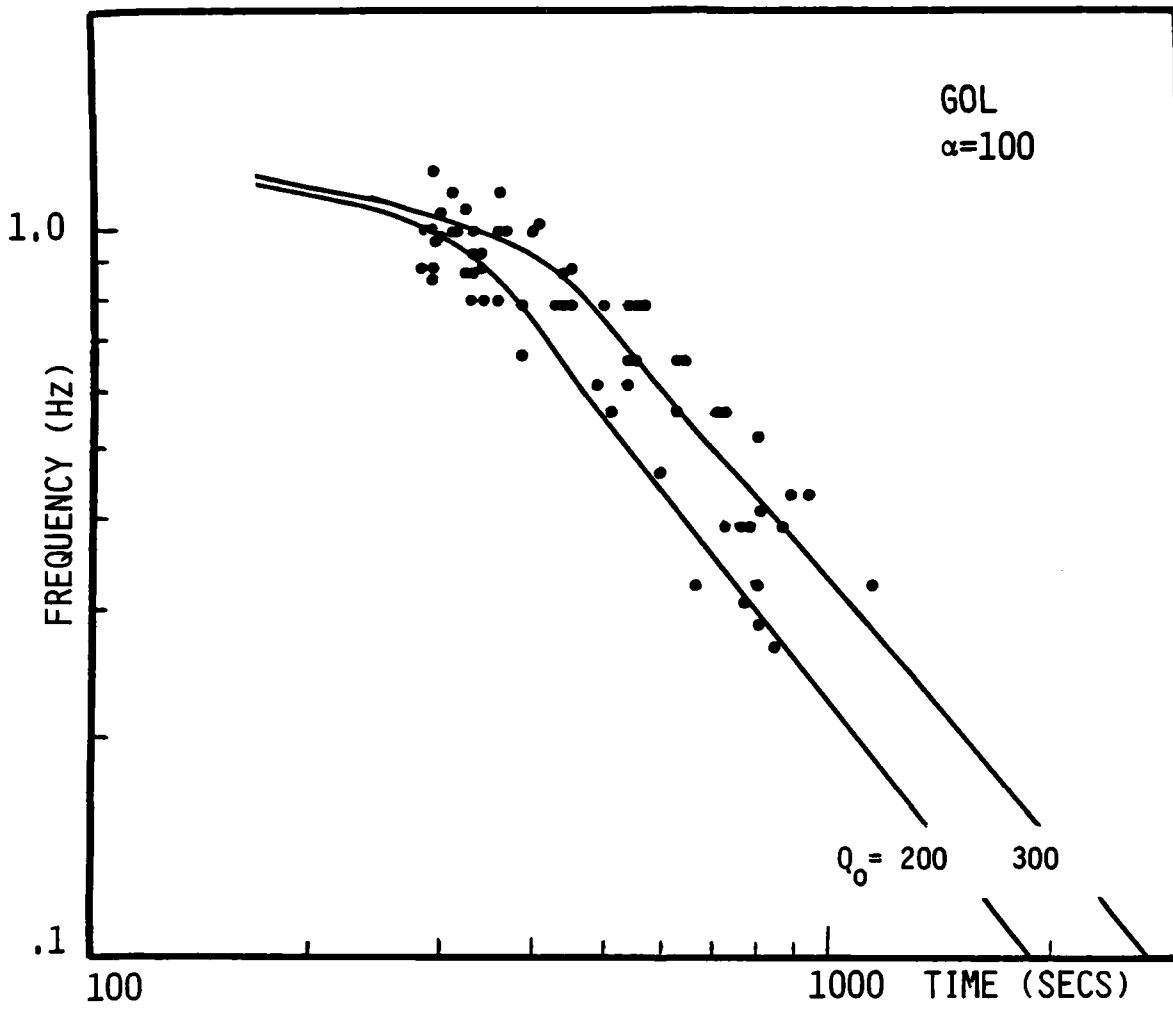


Figure 28. GOL  $f_p$  versus time data on linear master curves with  $\alpha=100$ .

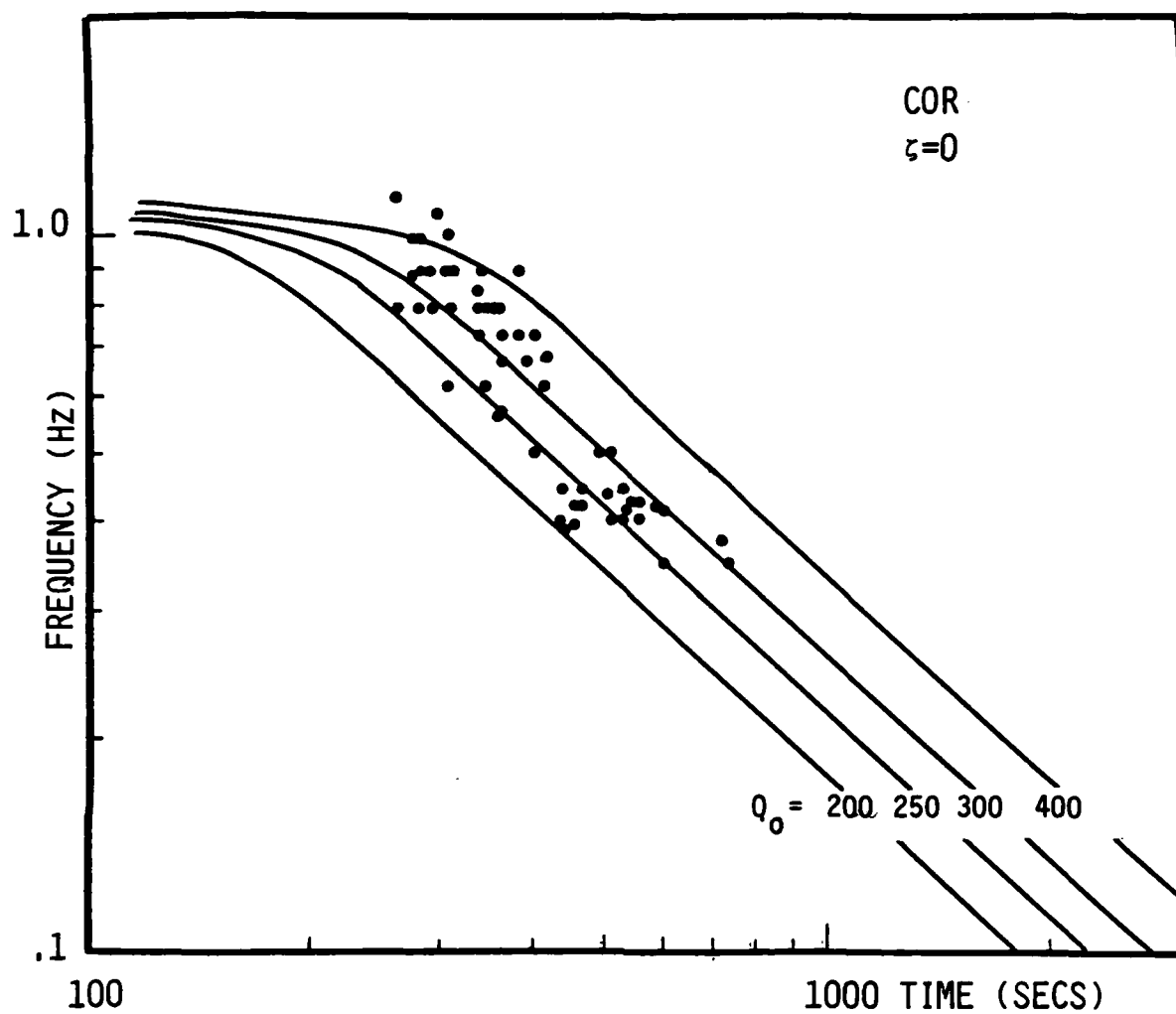


Figure 29. COR predominant frequency ( $f_p$ ) versus time data on master curves with  $\zeta=0$ . The slope of the data is  $P$  steeper than that of the curves.

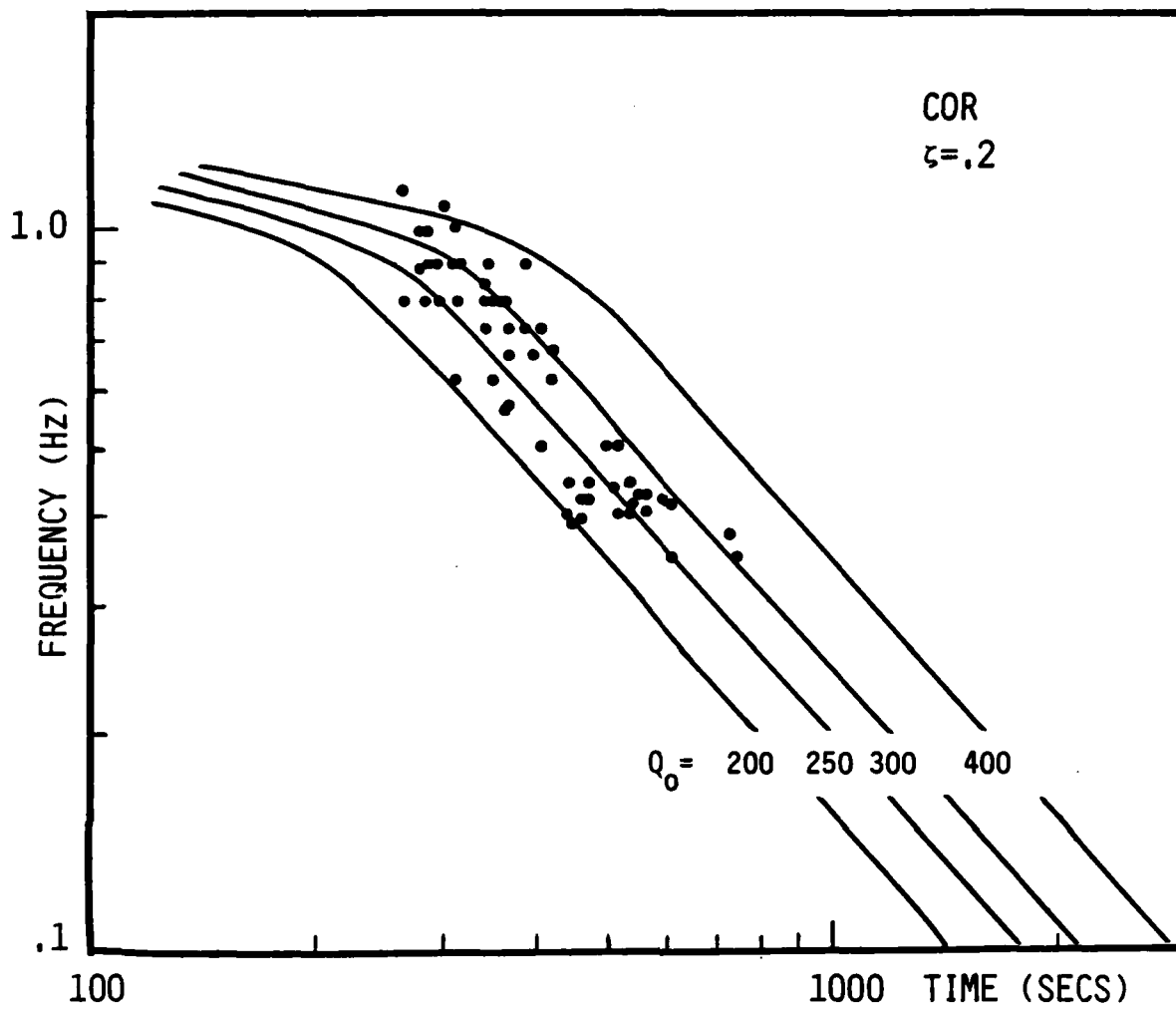


Figure 30. COR  $f_p$  versus time data on master curves with  $\zeta = .2$

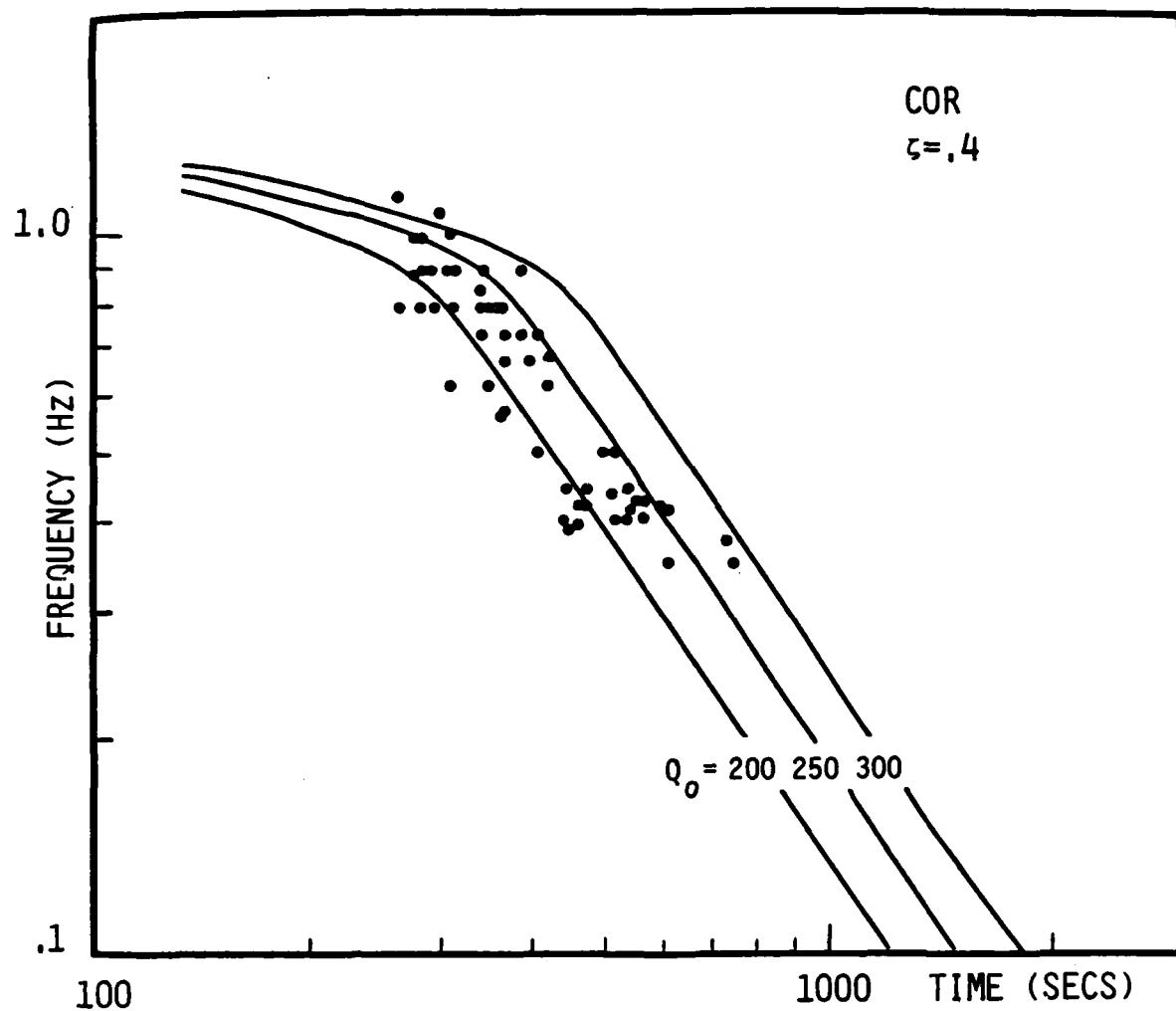


Figure 31. COR  $f$  versus time data on master curves with  $\zeta = .4$ . The RAI best fit is  $\zeta = .4$   $P_{Q_0 = 220}$ .

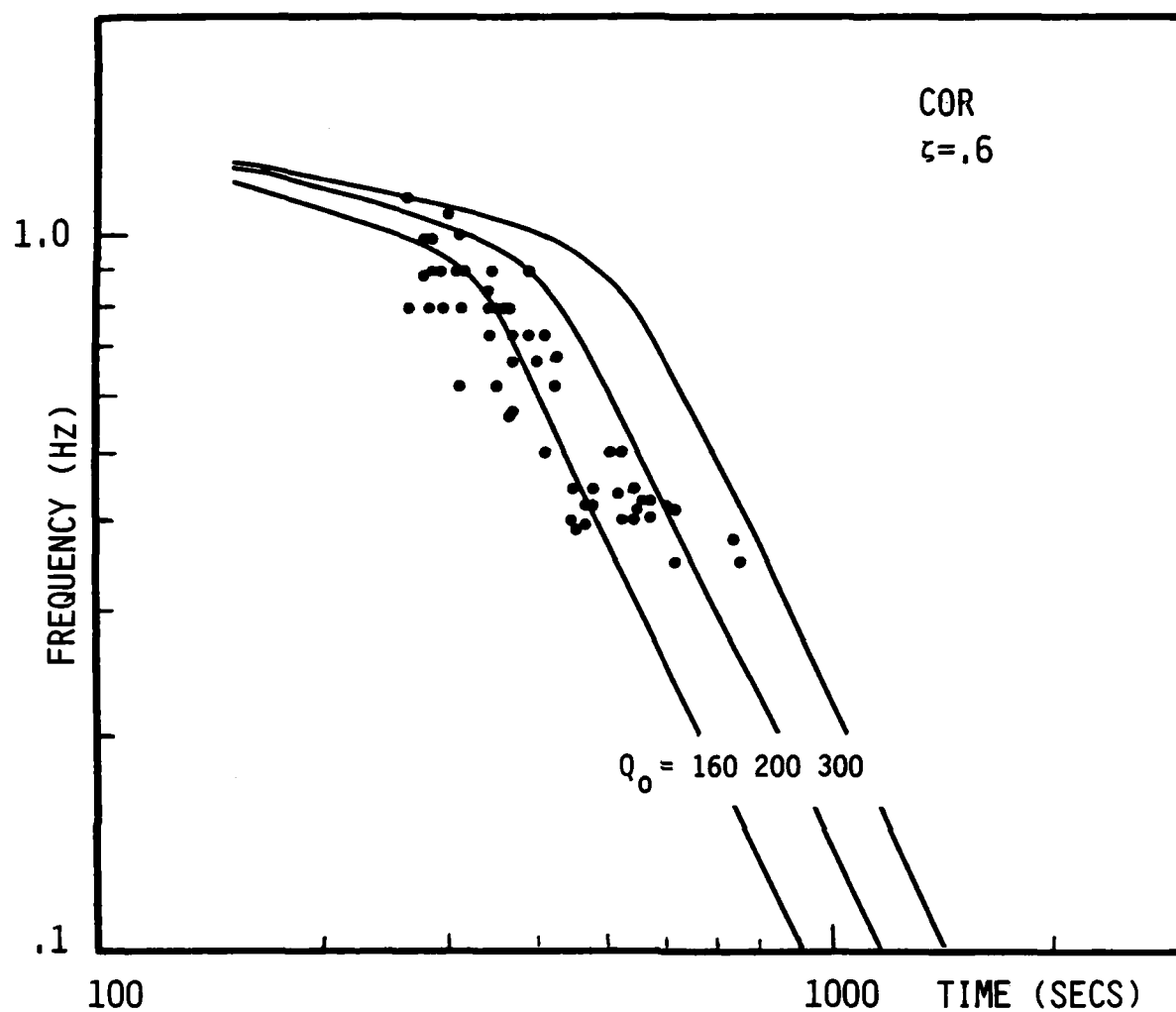


Figure 32. COR  $f$  versus time data on master curves with  $\zeta = .6$ . The data has a less steep slope than these curves.



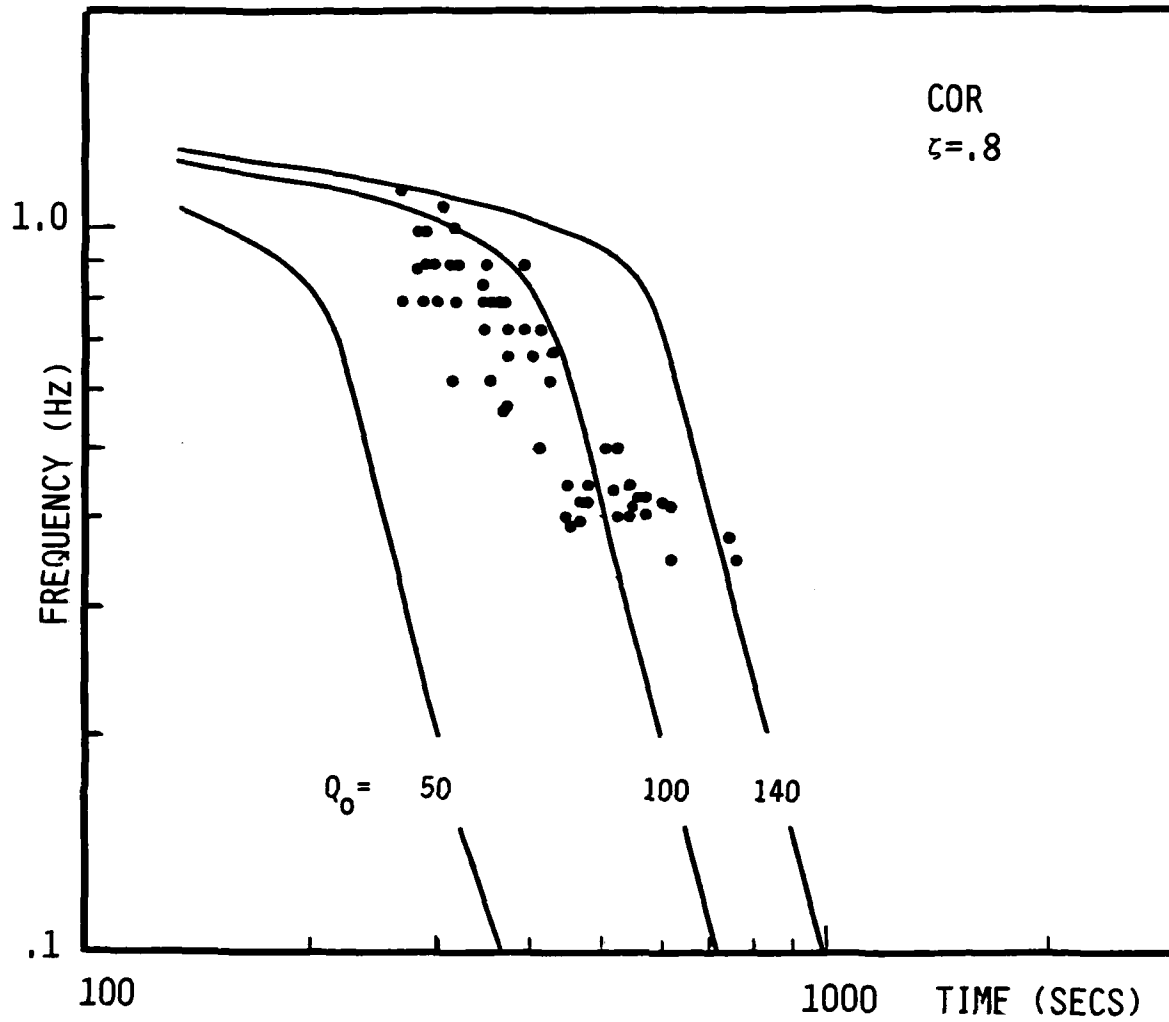


Figure 33. COR  $f_p$  versus time data on master curves with  $\zeta = .8$ .

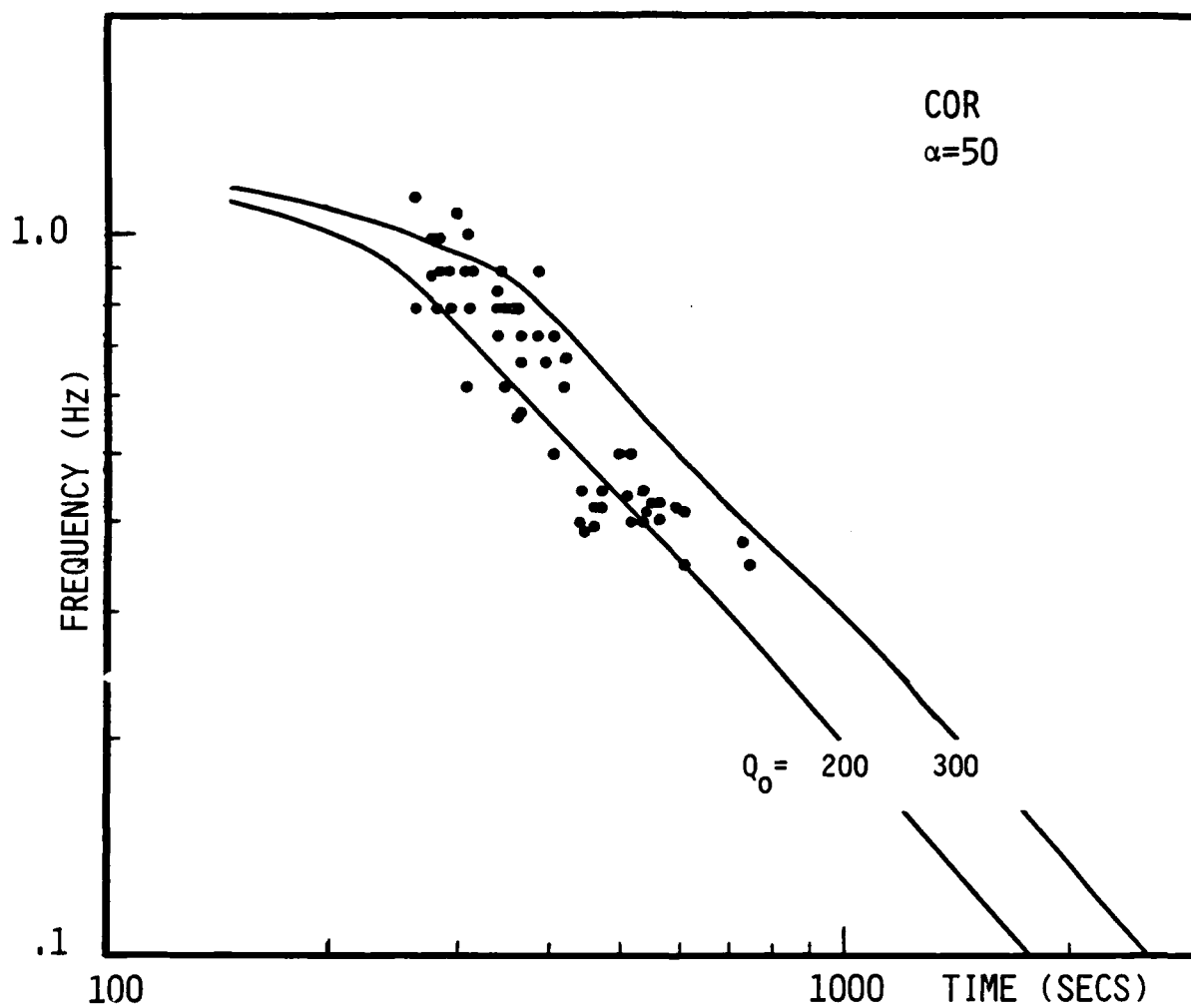


Figure 34. COR  $f_0$  versus time data on master curves from the linear Q model with  $\alpha=50$ . The  $P_{RAI}$  best linear model fit is  $\alpha=50$   $Q_0=235$ .

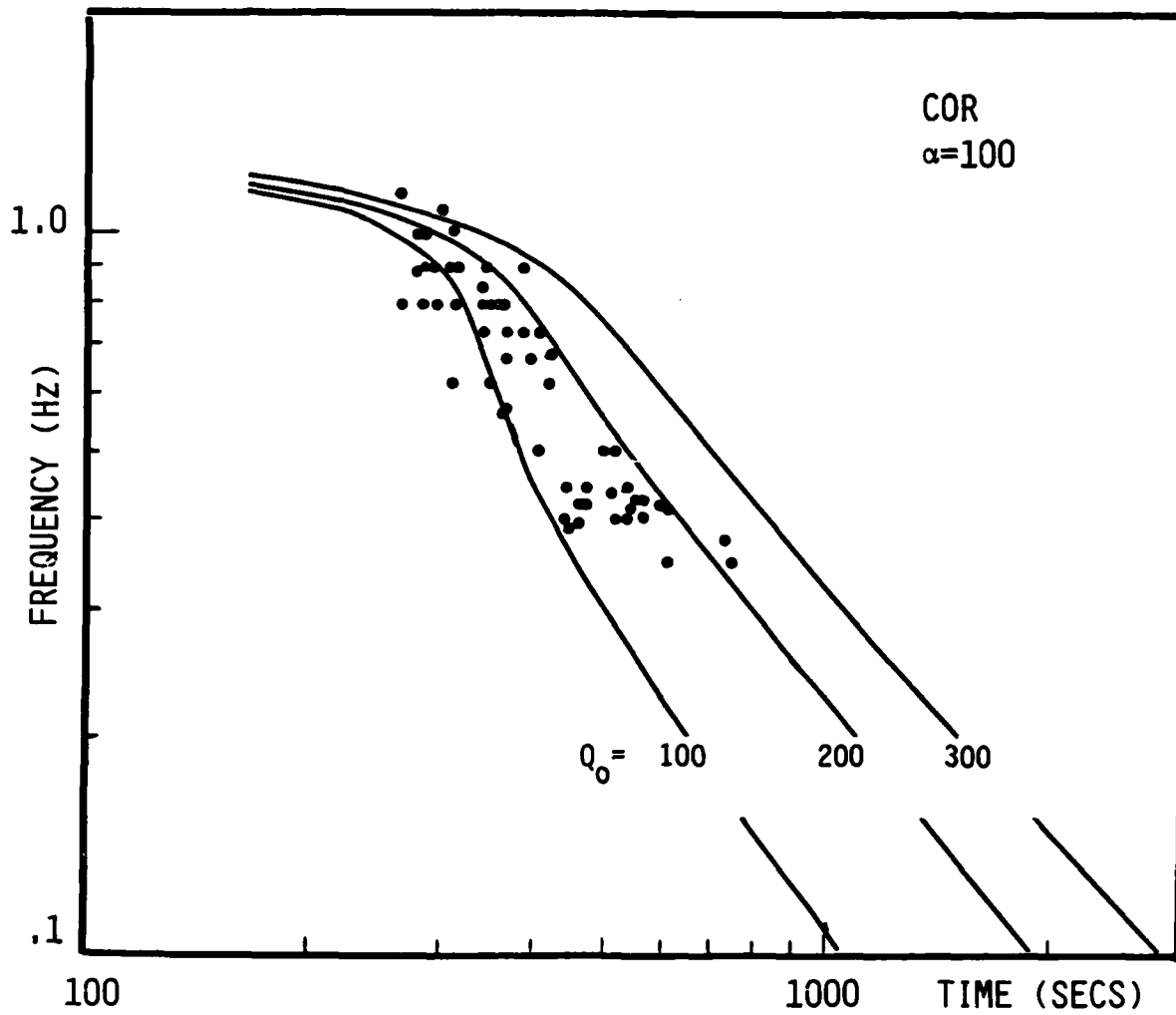


Figure 35. COR  $f_p$  versus time data on master curves with  $\alpha=100$ .

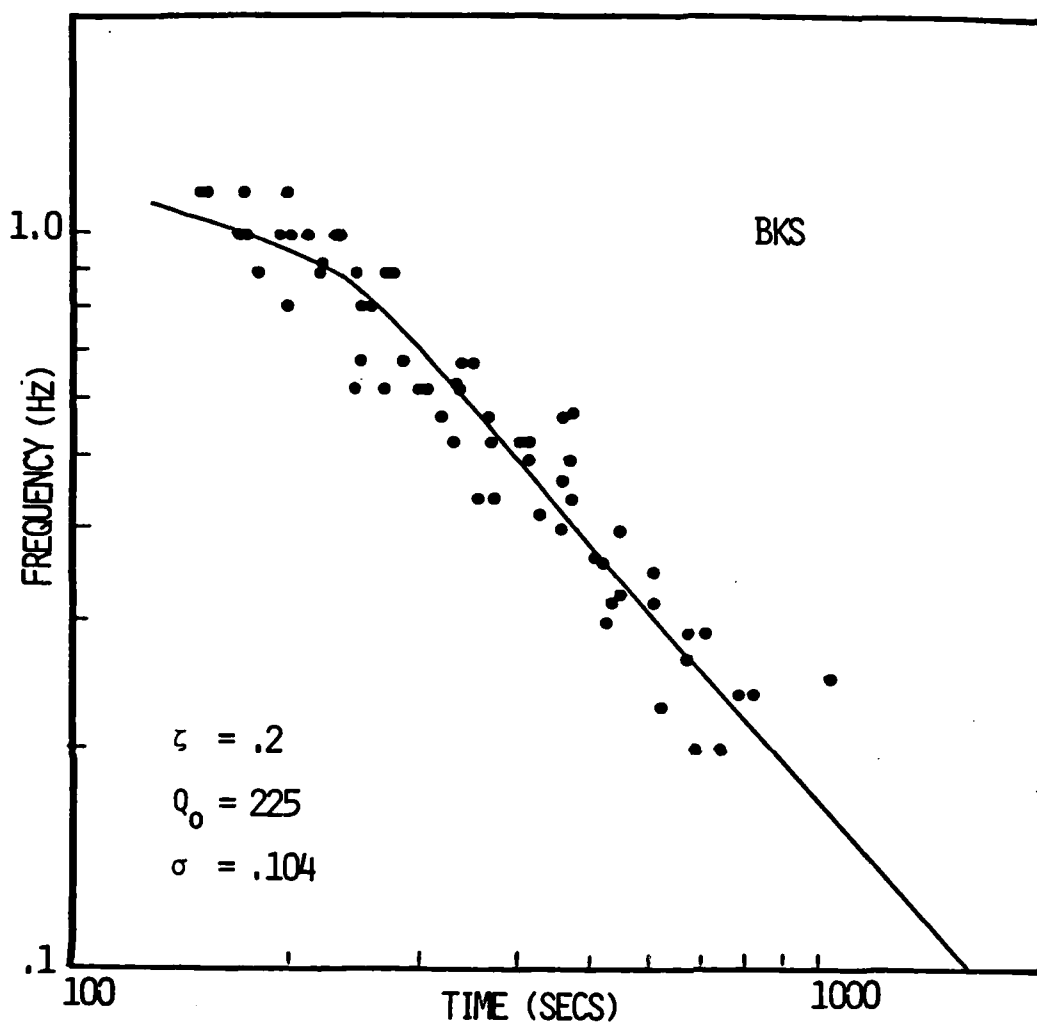


Figure 36. The RAI best fit for our data at WWSSN station BKS for an exponential model of frequency dependence of  $Q$  ( $Q=Q_0 f^z$ ).  $Q_0$  and  $z$  are shown. The standard deviation ( $\sigma$ ) of the data from this curve is also given.

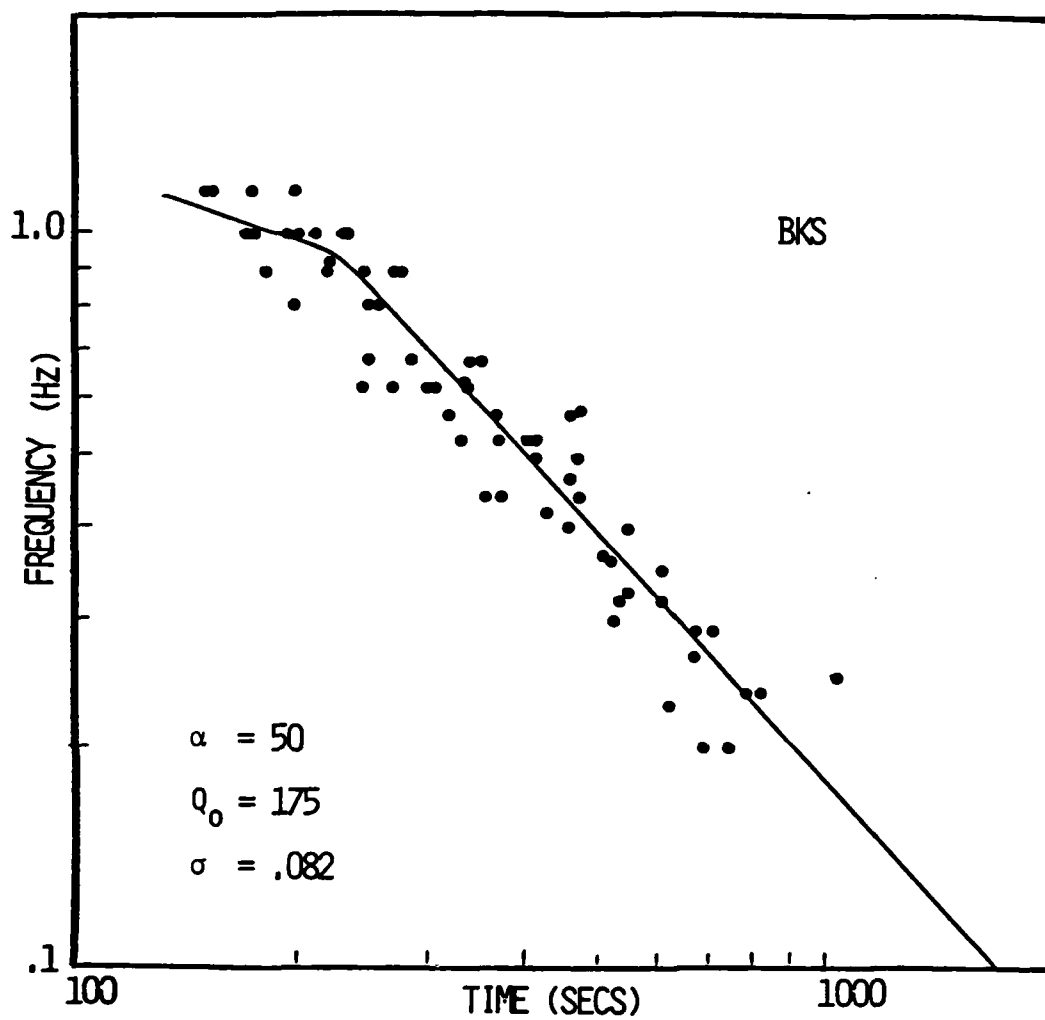


Figure 37. The RAI best linear ( $Q=Q_0 + \alpha f$ ) fit to our data at BKS.  $Q_0$  and  $\alpha$  are shown along with the standard deviation ( $\sigma$ ) of the data from this curve. Note that  $\sigma$  is lower here than in Figures 8 and 10.

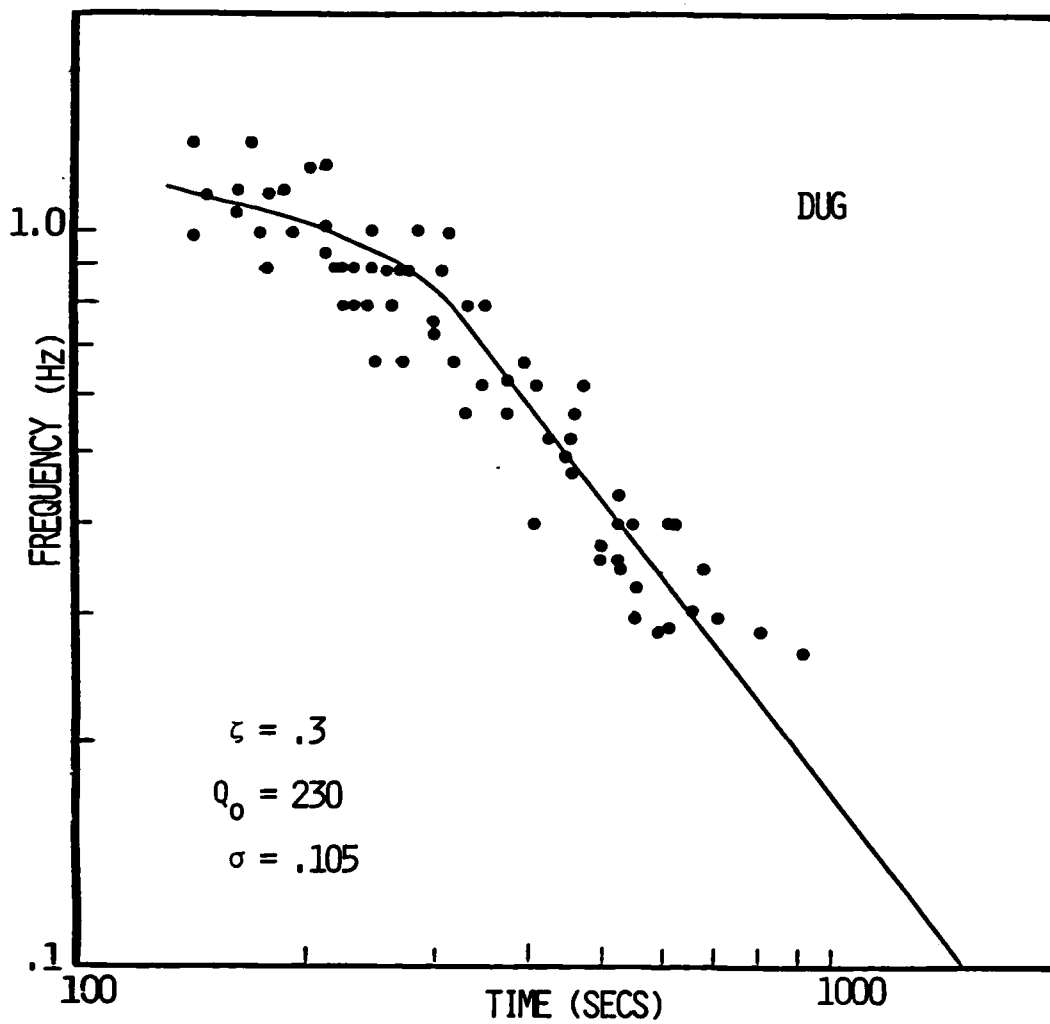


Figure 38. The RAI best exponential ( $Q=Q_0 f^z$ ) fit to our data is shown for WSSN station DUG. The parameters in the  $Q_0$  model  $z$  and  $Q_0$  are given along with the standard deviation of the data from this model.  $\sigma$  is the lowest of those in Figures 11-14.

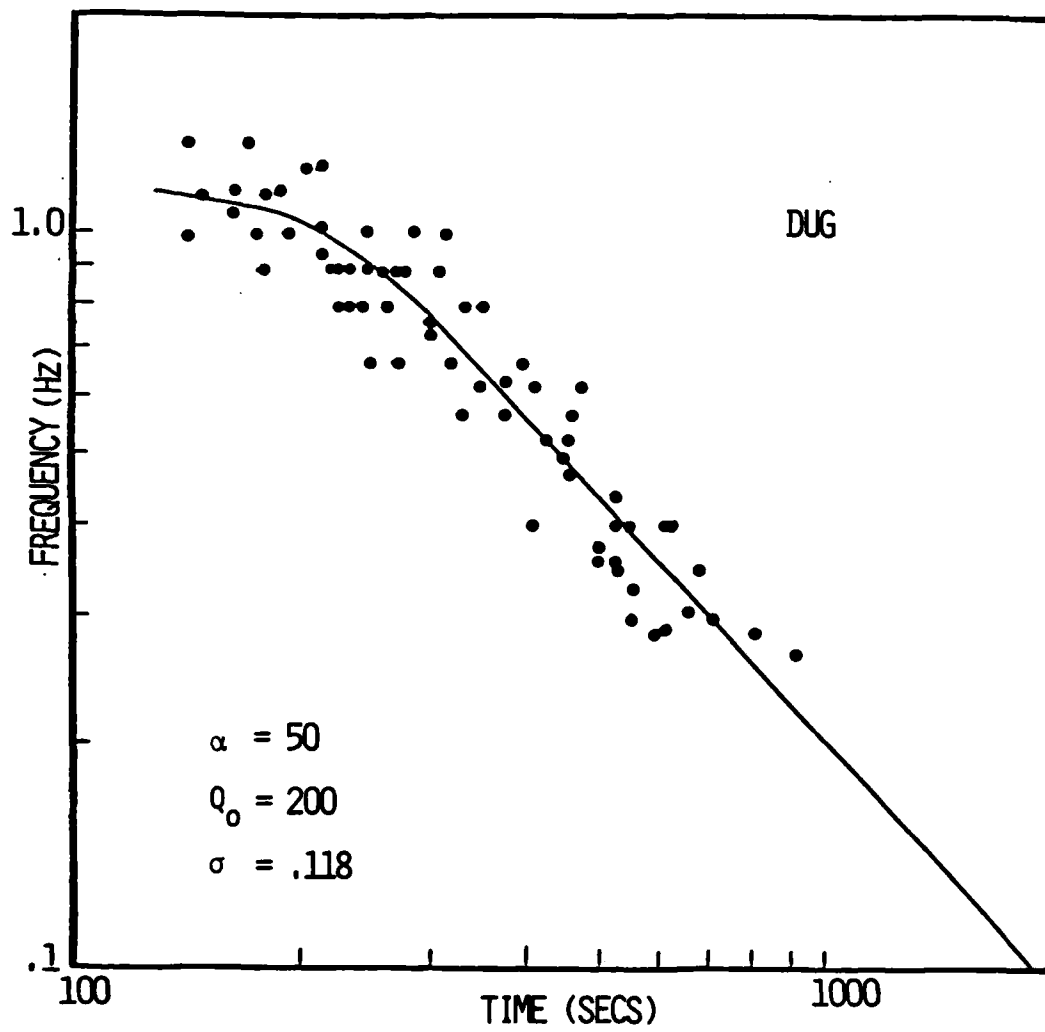


Figure 39. The RAI best linear ( $Q=Q_0 + \alpha f$ ) fit to our data is shown for DUG.  $\zeta$ ,  $Q_0$  and  $\sigma$  are also given.

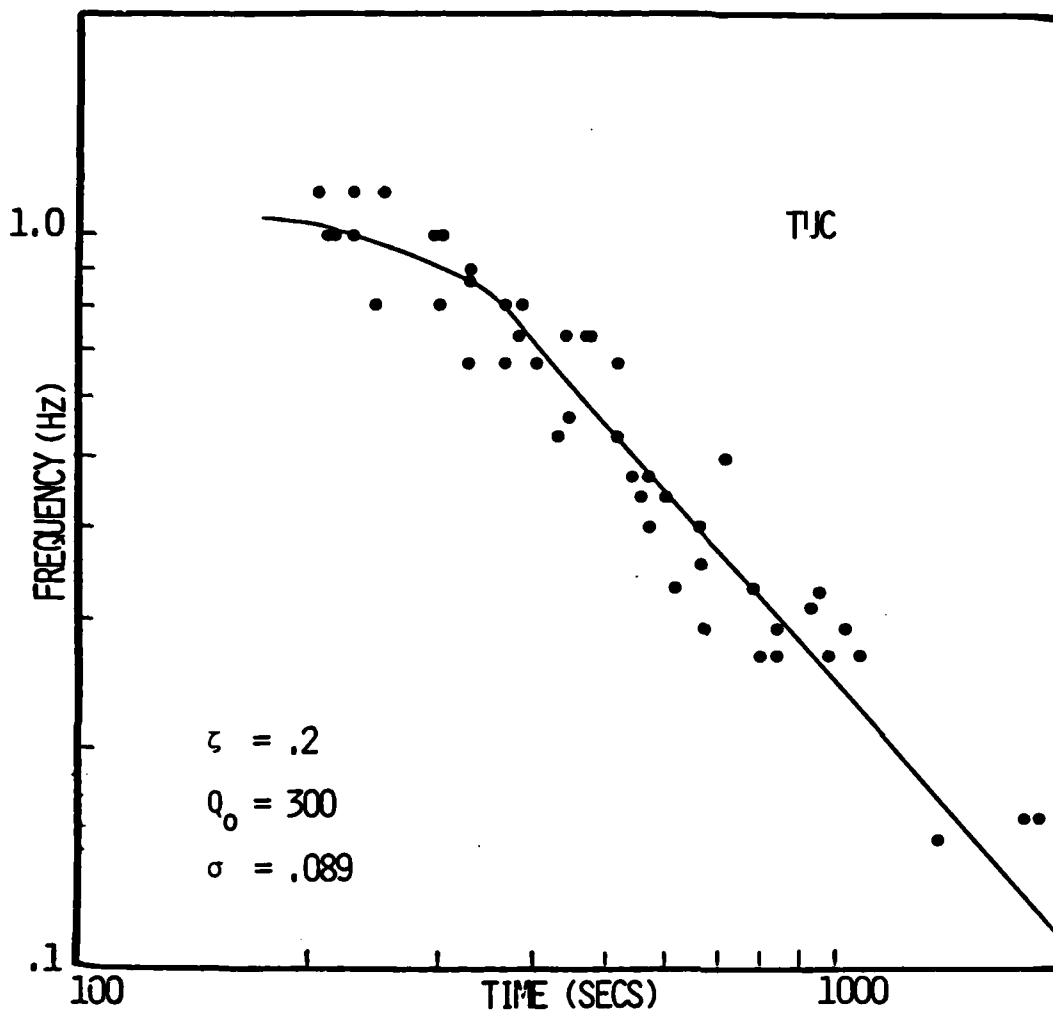


Figure 40. The RAI best exponential Q model fit to the data at WWSSN station TUC.  $\zeta$ ,  $Q_0$ , and the standard deviation ( $\sigma$ ) of the data from this curve are also presented.



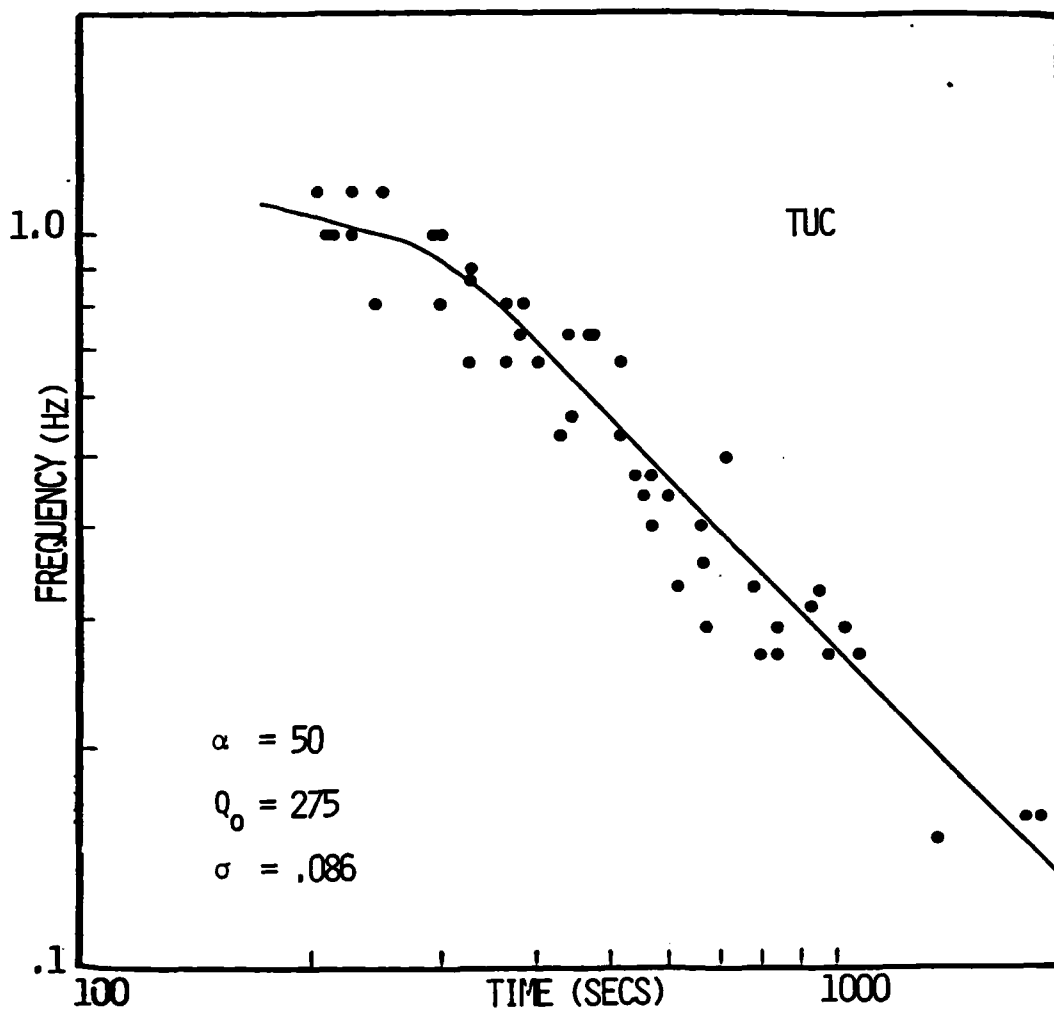


Figure 41. The RAI best linear Q model fit to our TUC data.  $\alpha$ ,  $Q_0$  are shown with the standard deviation,  $\sigma$ , which is lower than that in Figure 16 and lower than but close to that in Figure 14.

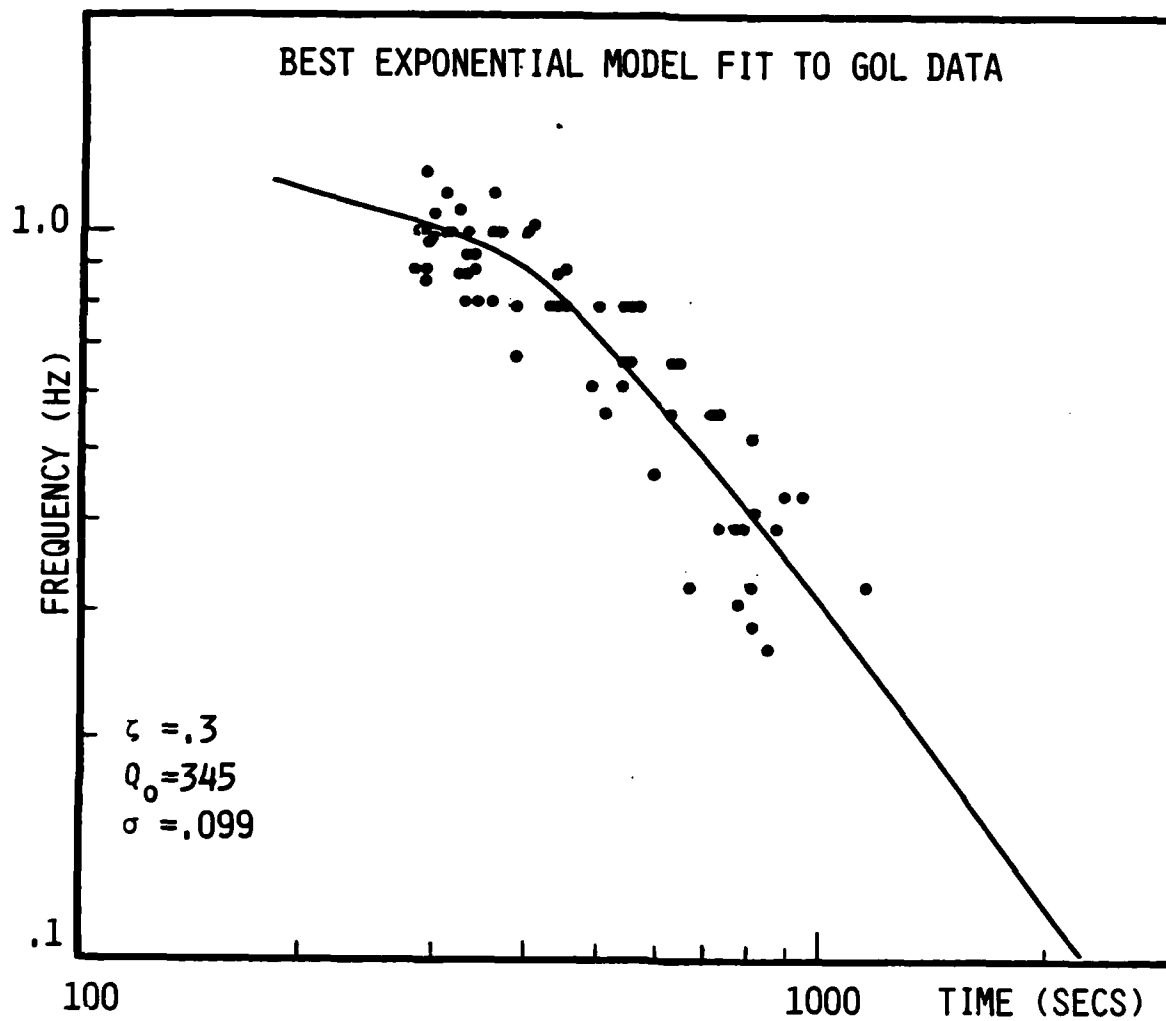


Figure 42. GOL data with the RAI best fit using an exponential model of frequency dependent  $Q$ . The standard deviation ( $\sigma$ ) is calculated assuming no error in the time measurement and all the error in the frequency measurement.

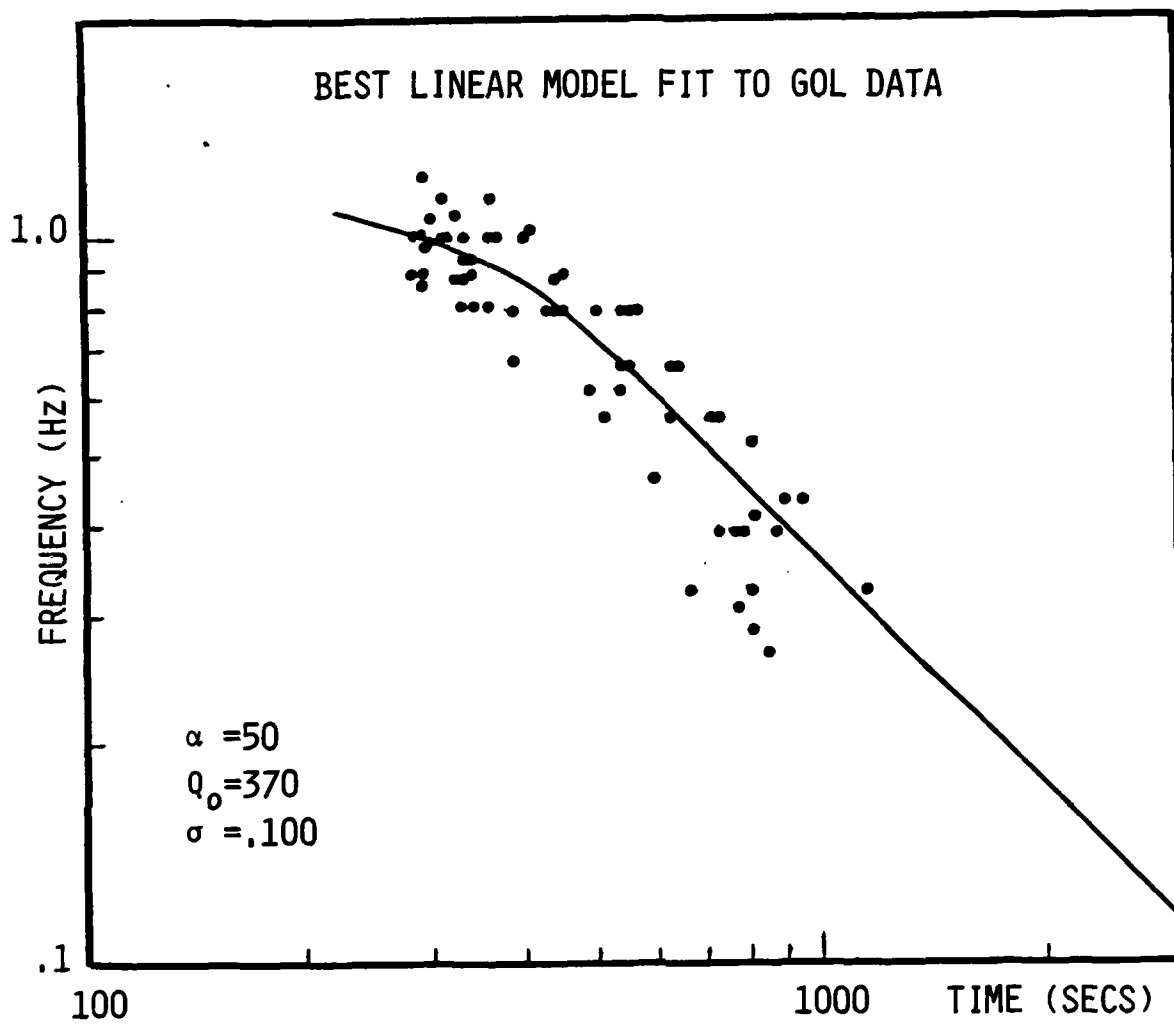


Figure 43. GOL data with the RAI best fit using a linear model of frequency dependent  $Q$ .

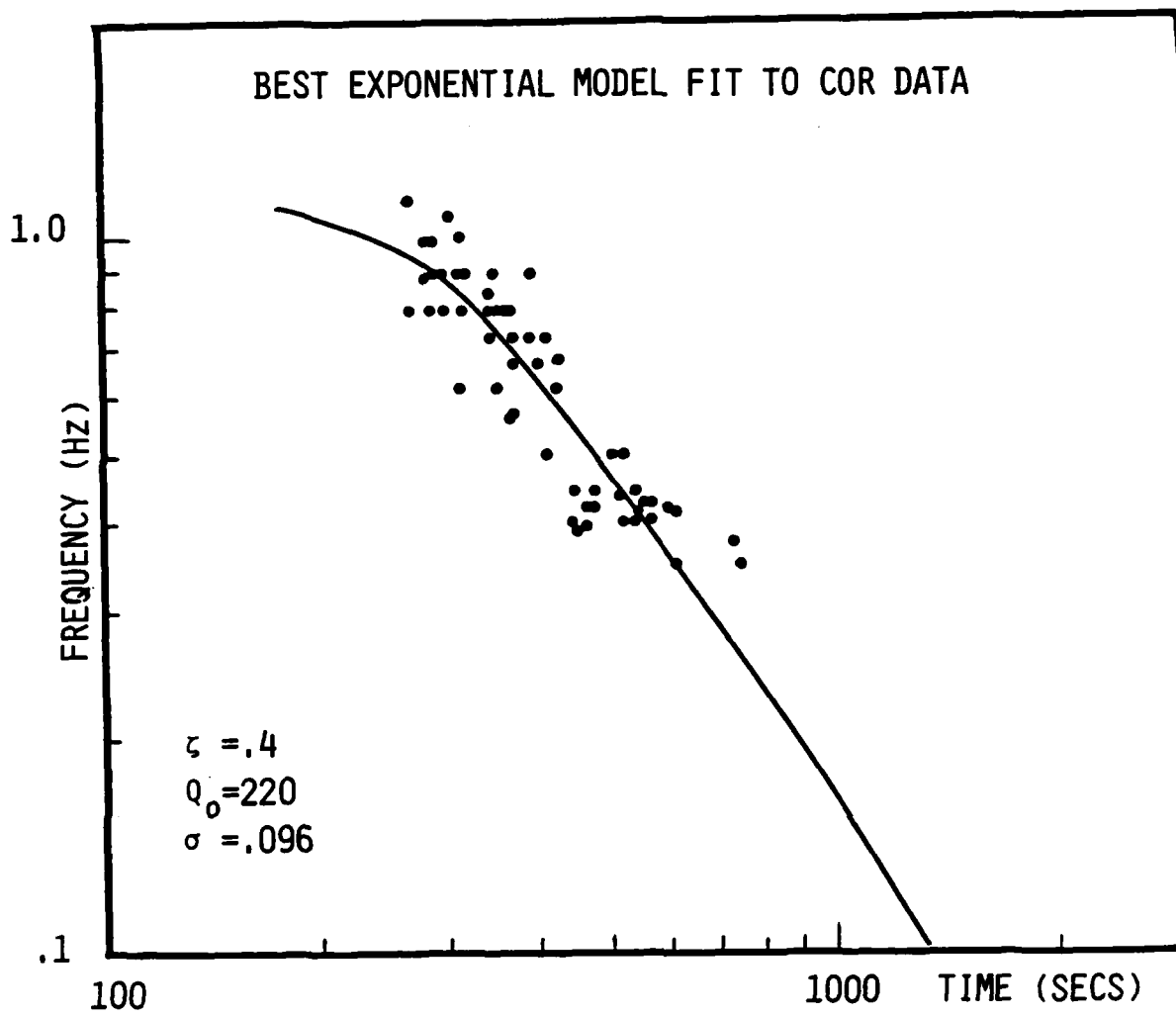


Figure 44. COR data with the RAI best exponential model fit.

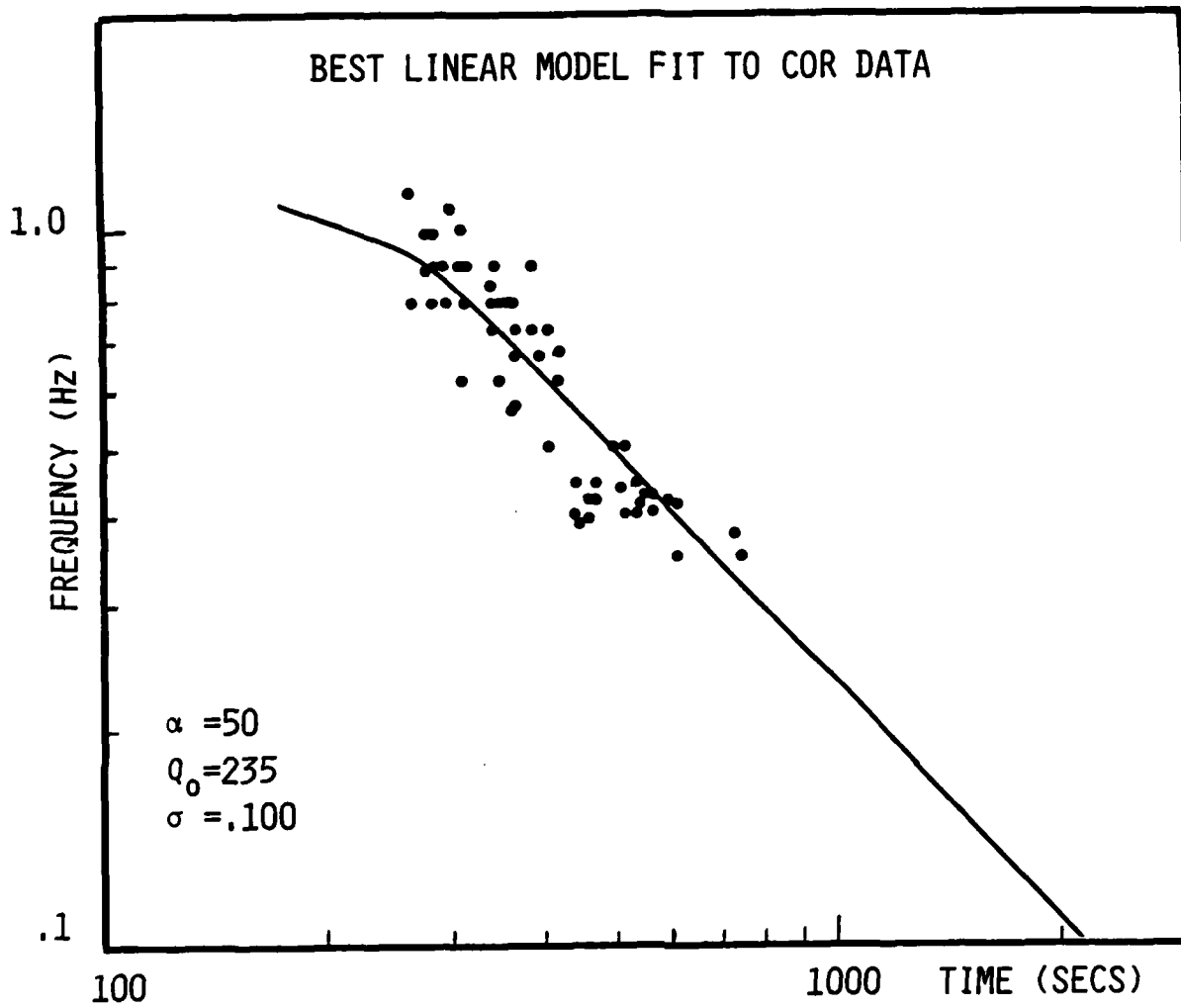


Figure 45. COR data with the RAI best linear model fit.

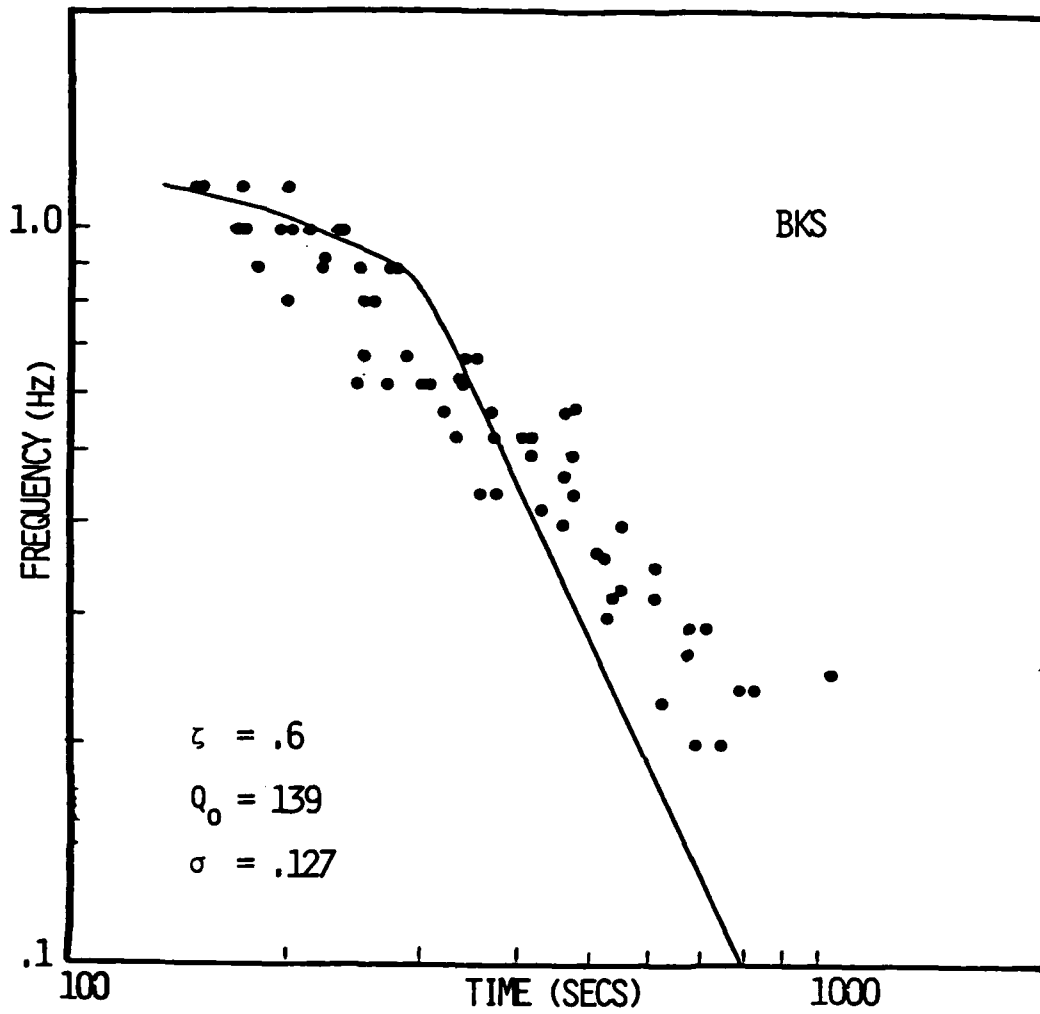


Figure 46. Nuttli's choice of Q model to fit his data at BKS is shown with our data along with the standard deviation ( $\sigma$ ).  $\sigma$  is larger than those in Figures 8 and 9.

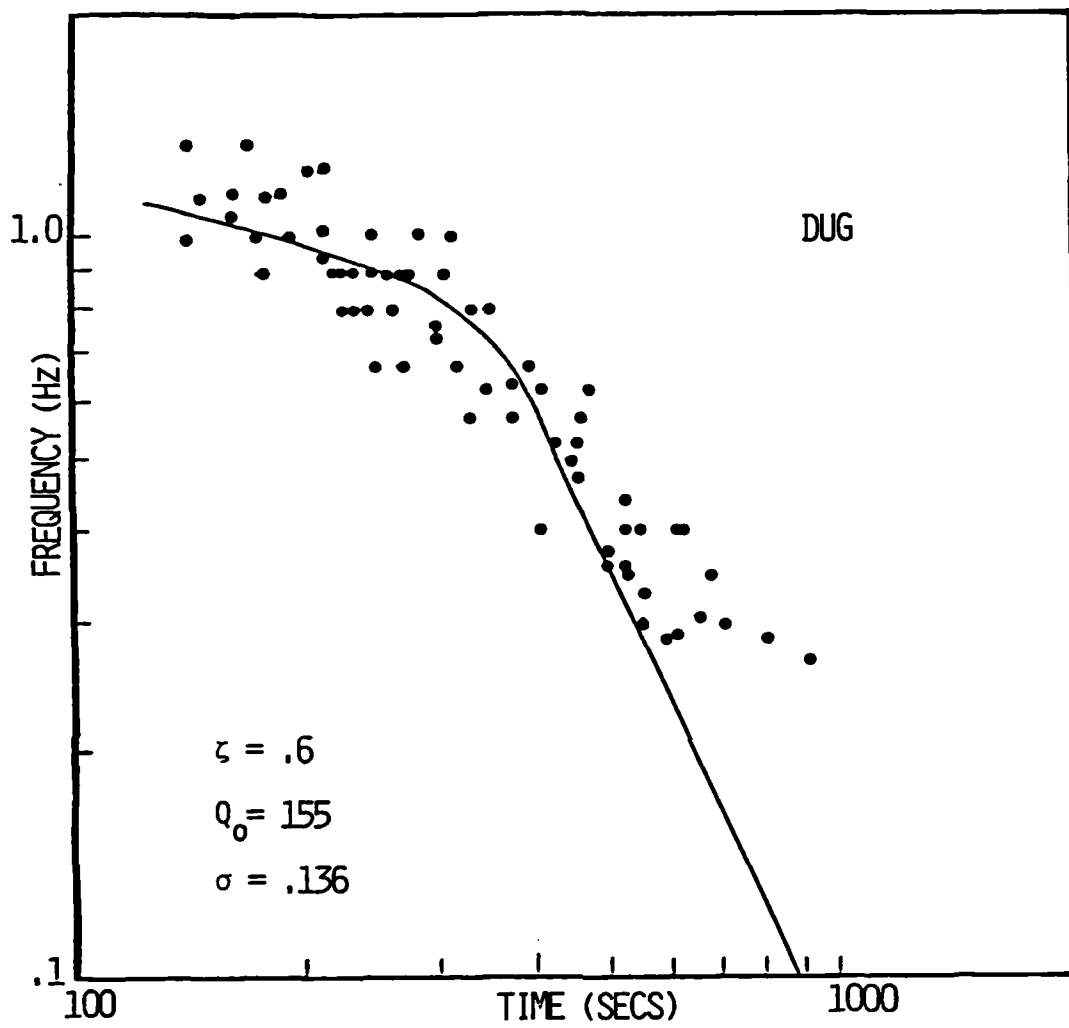


Figure 47. Nuttli's model for DUG is shown on our data. The standard deviation ( $\sigma$ ) is the largest of those in Figures 11-13.

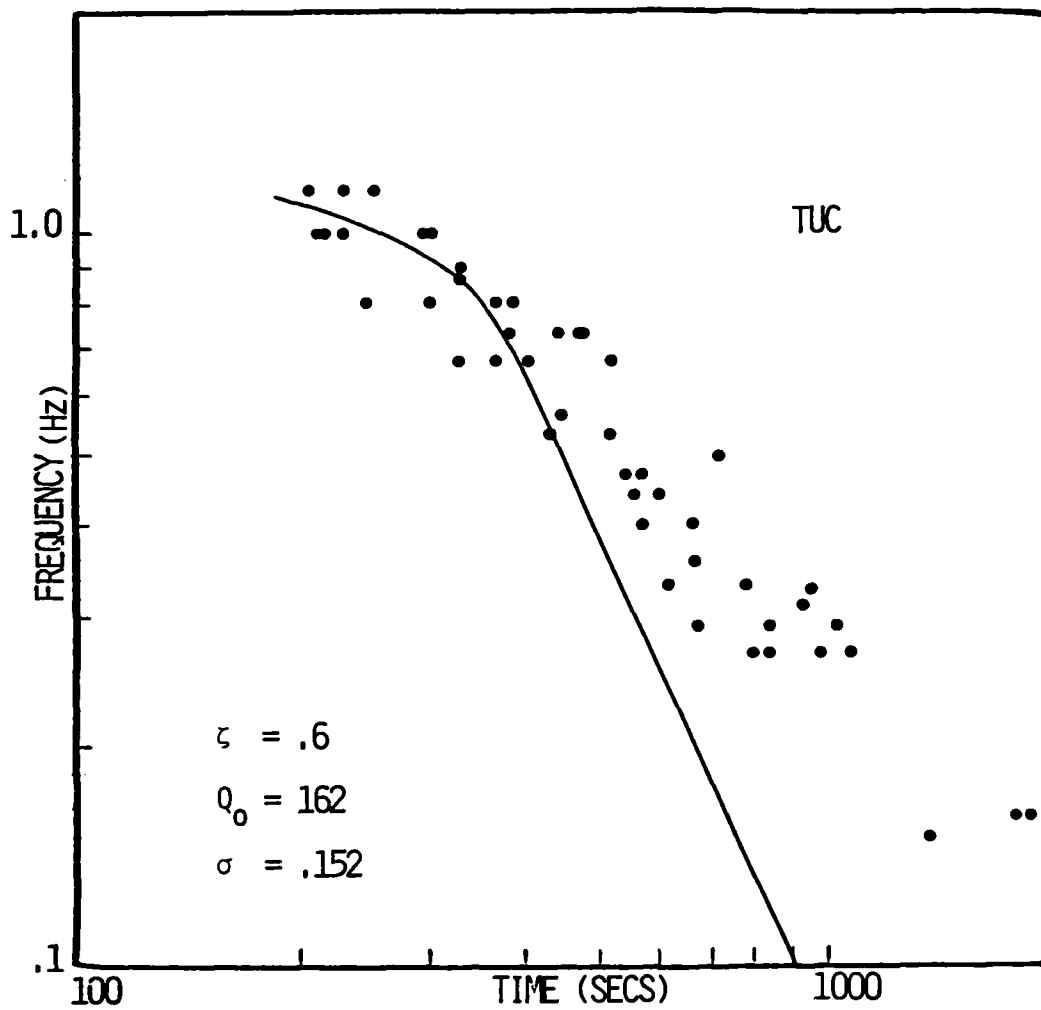


Figure 48. RAI's TUC data with Nuttli's model for TUC. The standard deviation is much larger than those in Figures 14 and 15.



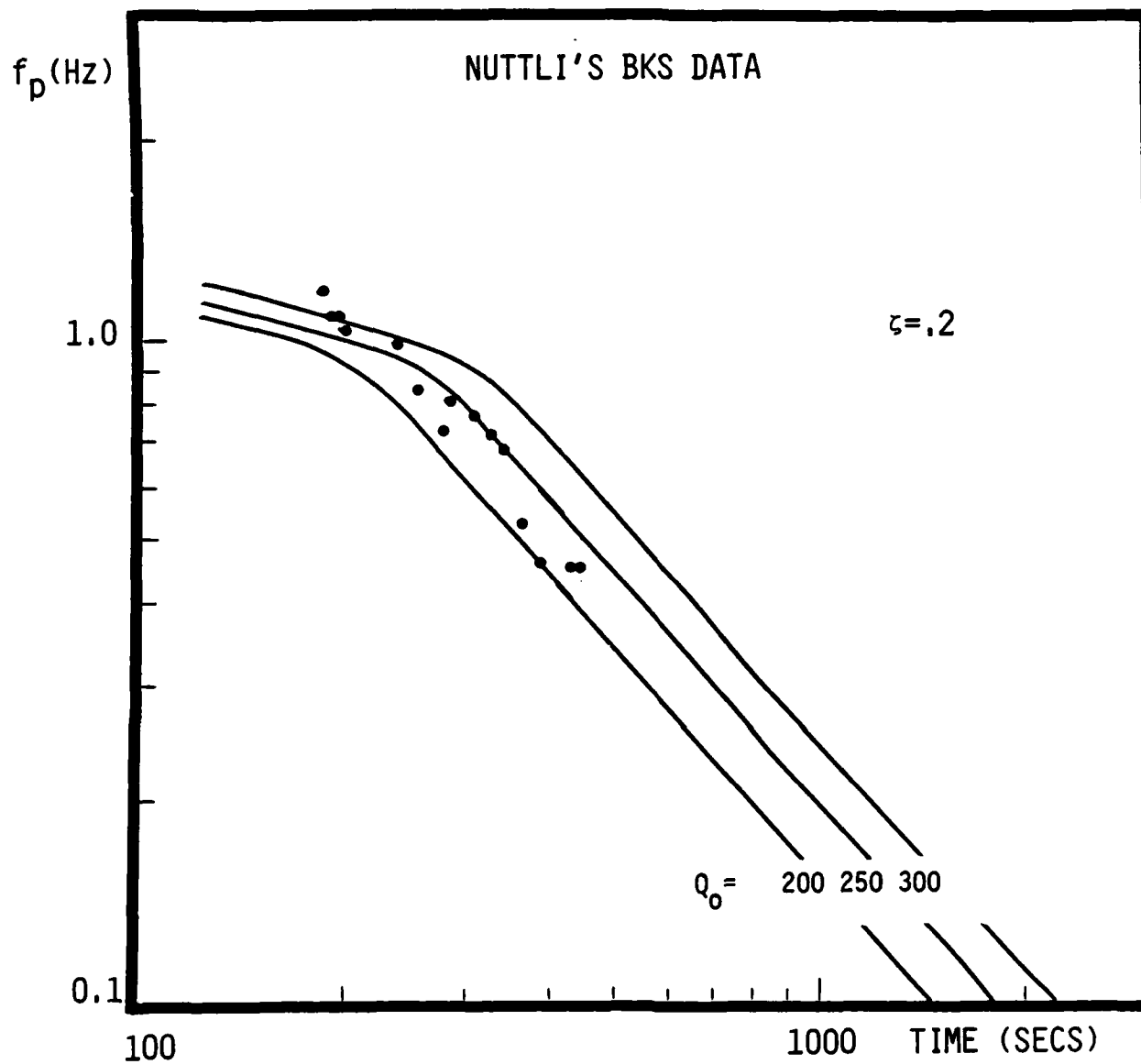


Figure 49. The best fit to our BKS data is  $Q_0 = 225$   $\zeta = .2$ . The standard deviation of Nuttli's data from our best fit is  $\sigma = .080$  assuming all the error is in the frequency measurement not the time.

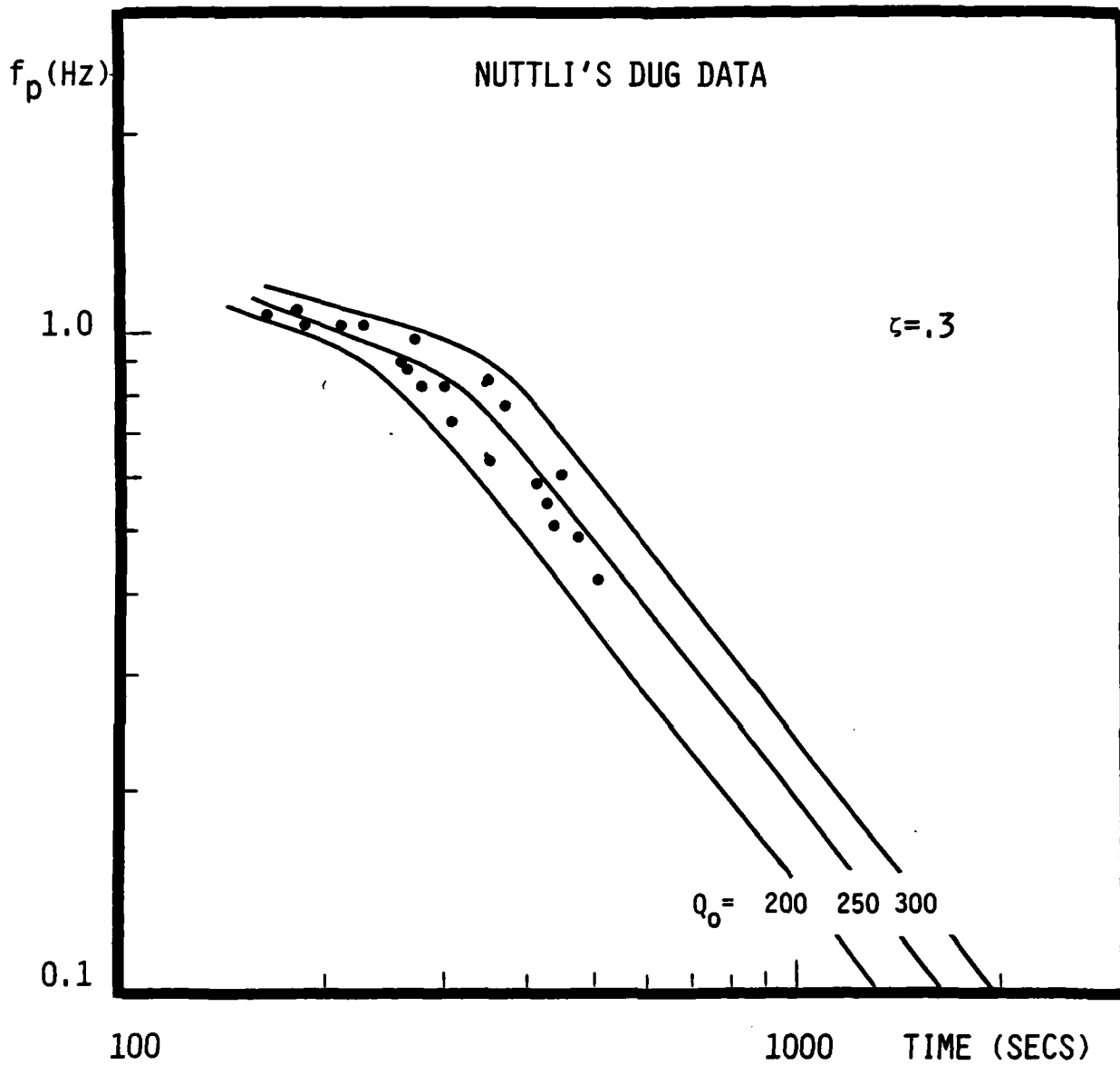


Figure 50. The best fit to our data is  $Q_0 = 230$   $\zeta = .3$ . The standard deviation of Nuttli's data from our best fit is  $\sigma = .063$  assuming no error in the time measurement.

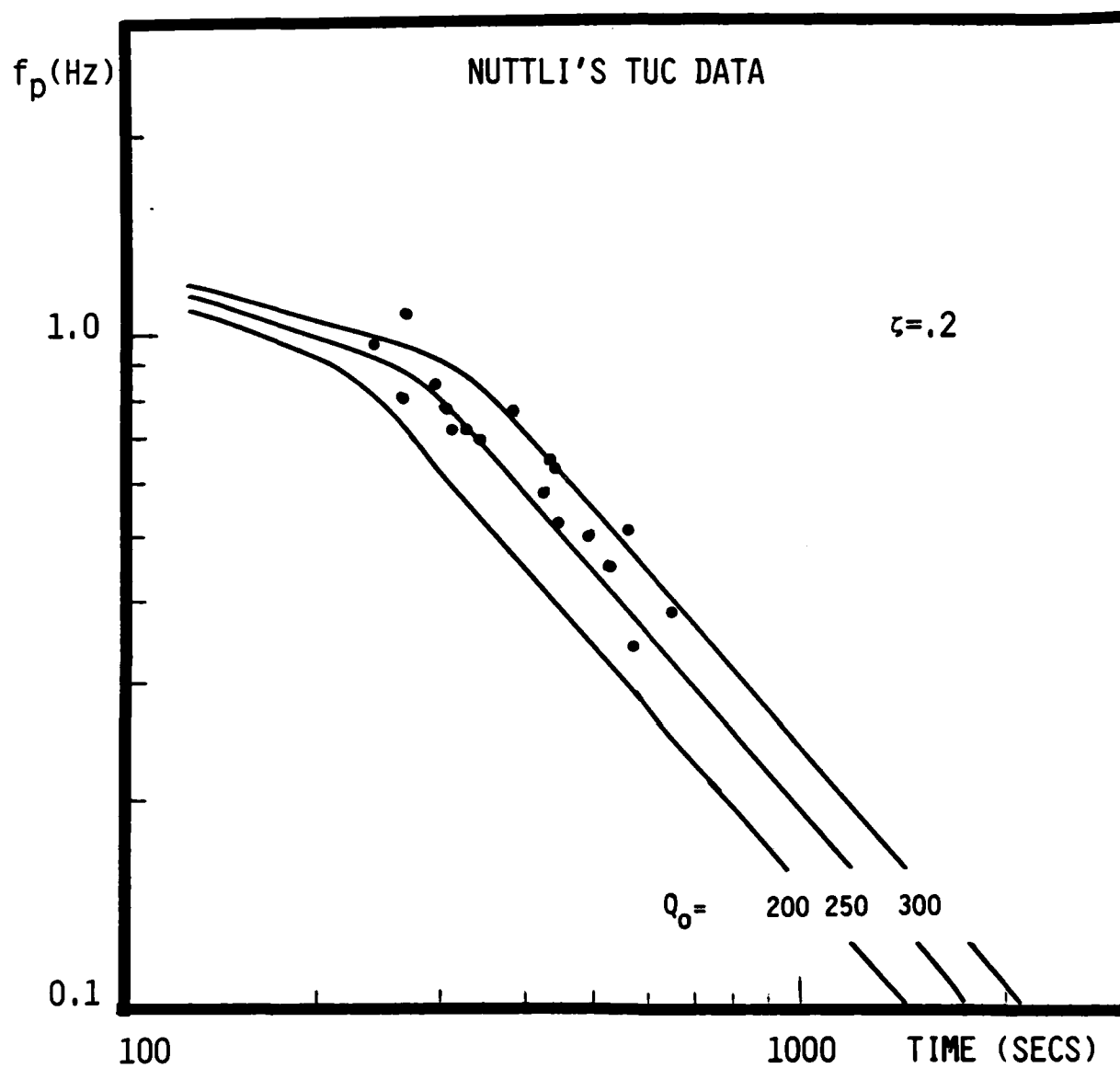


Figure 51. The best fit to our TUC data is  $Q_0 = 300$   $\zeta = .2$ . The standard deviation of Nuttli's data from our best fit is  $\sigma = .102$ .

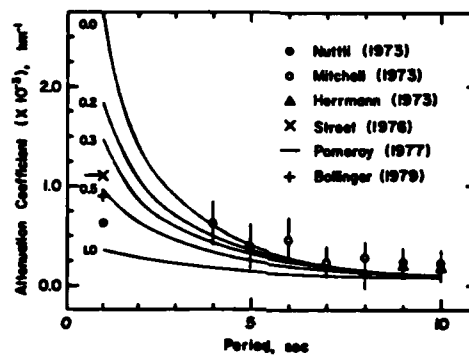


Figure 52. Higher-mode Rayleigh wave attenuation coefficient data and theoretical values obtained for various frequency-dependent internal friction models for which the exponent of frequency ( $\zeta$ ) is assumed to be uniform over the entire frequency range.

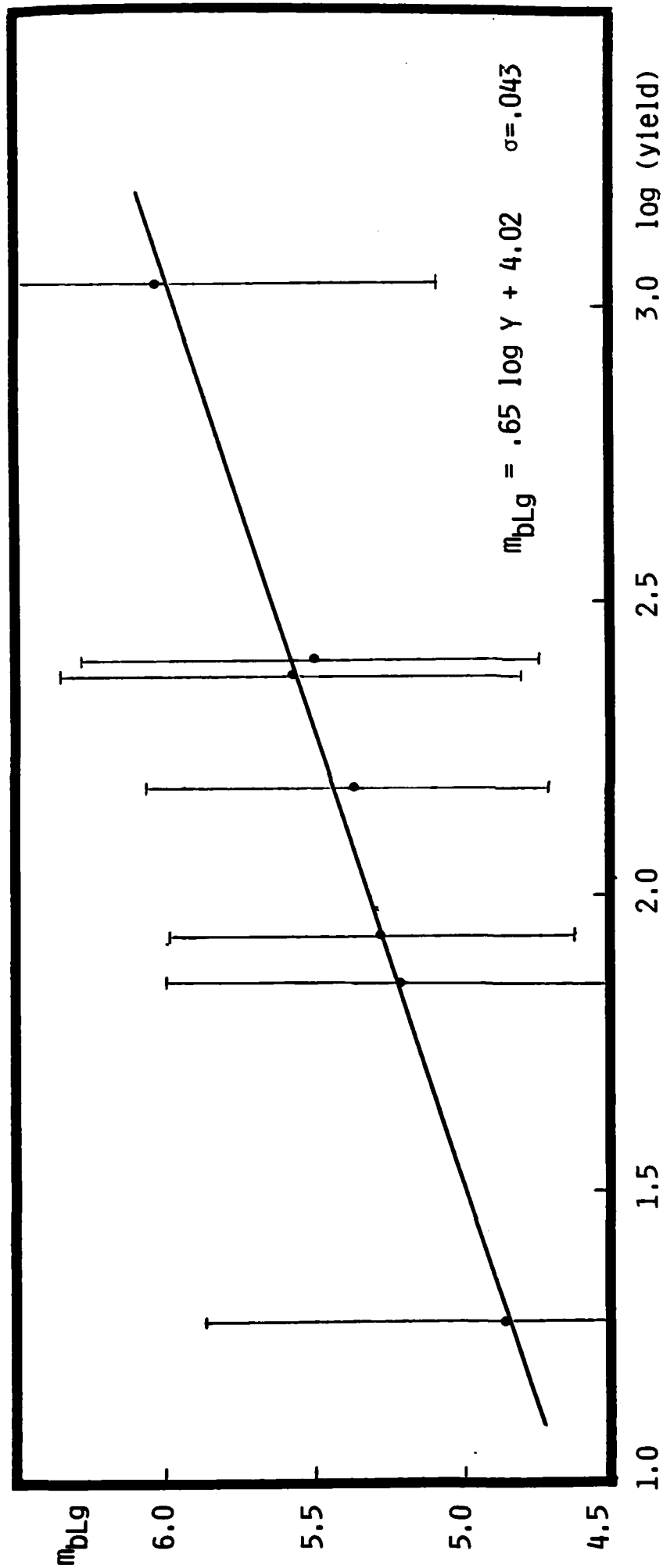


Figure 53. RAI original network  $m_{bLg}$  versus log (yield) data using stations BKS, DUG, TUC to calculate the  $m_{bLg}$ . The best linear fit is shown with  $\sigma$  the standard deviation ( $\sigma$ ).  $\sigma$  is calculated assuming all the error is in the  $m_{bLg}$  measurement. The error bars are the  $\pm 95\%$  confidence limits set by the CSS program LSMF.

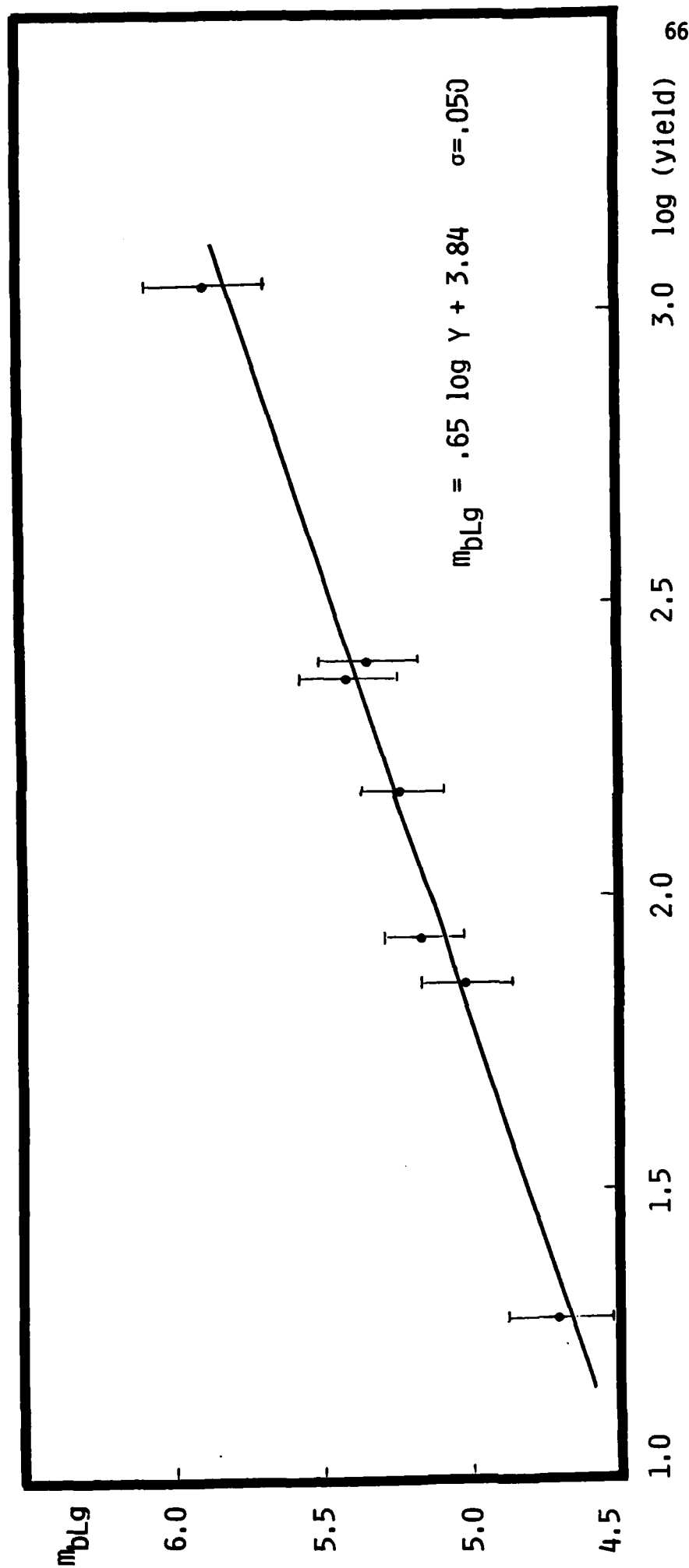


Figure 54. Network  $m_{bLg}$  versus  $\log$  yield with stations BKS, DUG, TUC and GOL contributing to the  $m_{bLg}$ . The best linear fit is shown with the standard deviation. The  $\pm 95\%$  confidence limits are shown as error bars.

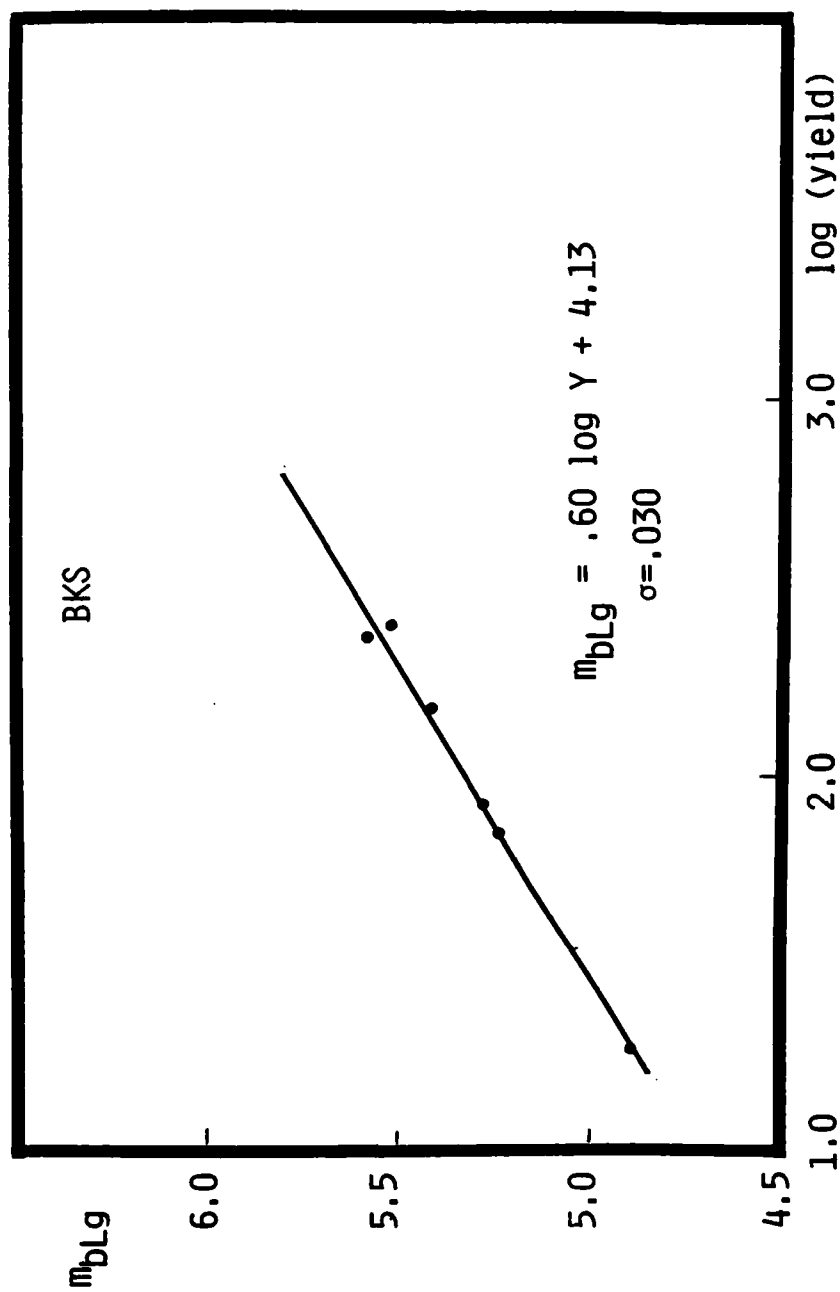


Figure 55. The BKS calibration curve. The best linear fit is shown.

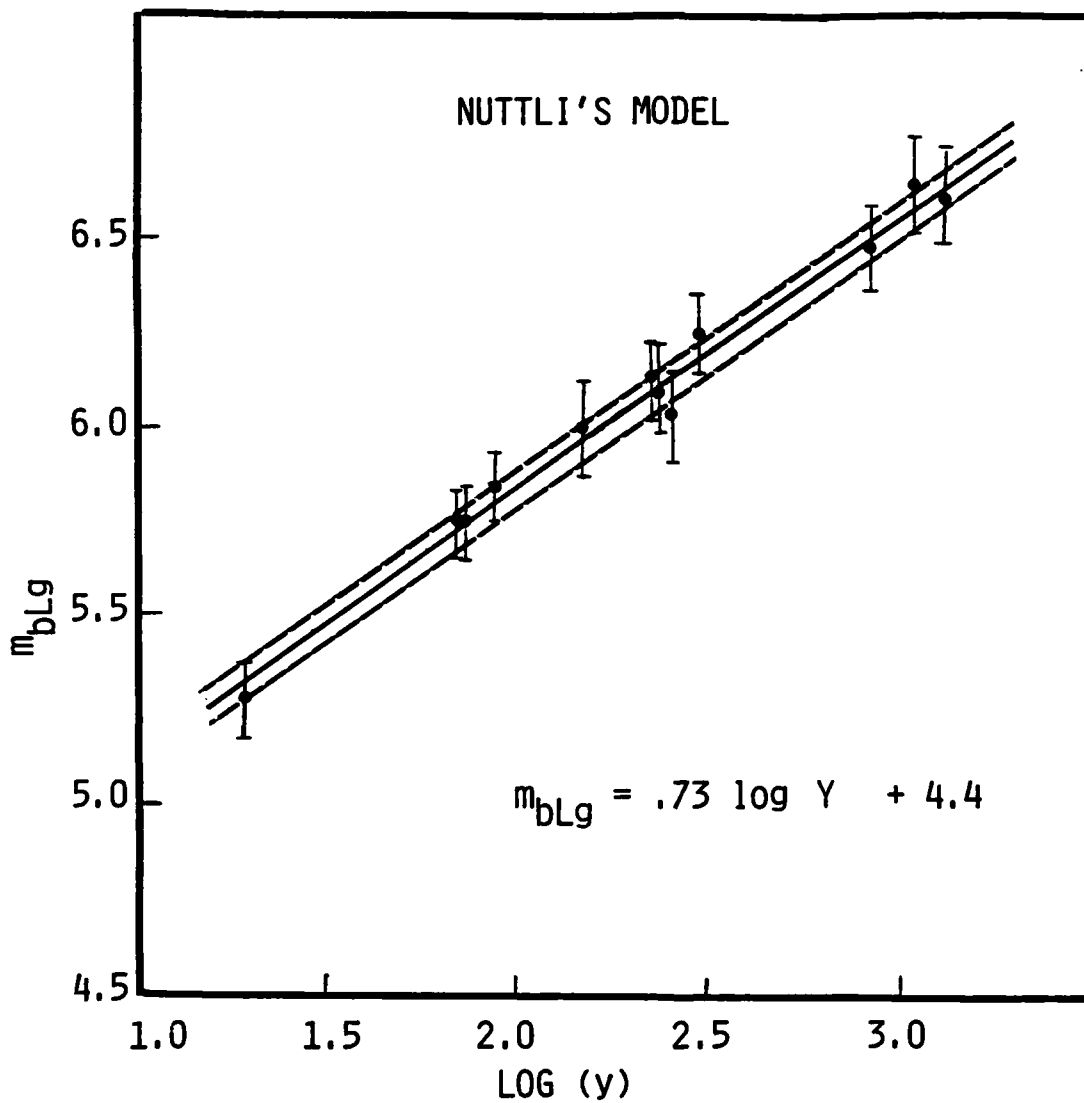


Figure 56. Network  $m_{bLg}$  versus log yield for Nuttli's hard rock data. Network  $m_{bLg}$ 's were calculated by submitting Nuttli's data to LSMF. The best least squares fit is shown by the solid line with the equation given below the curve. The dashed lines are the  $\pm 1\sigma$  curves. The error bars on the data points are the 95% confidence levels calculated by LSMF.  $\sigma = .049$ .



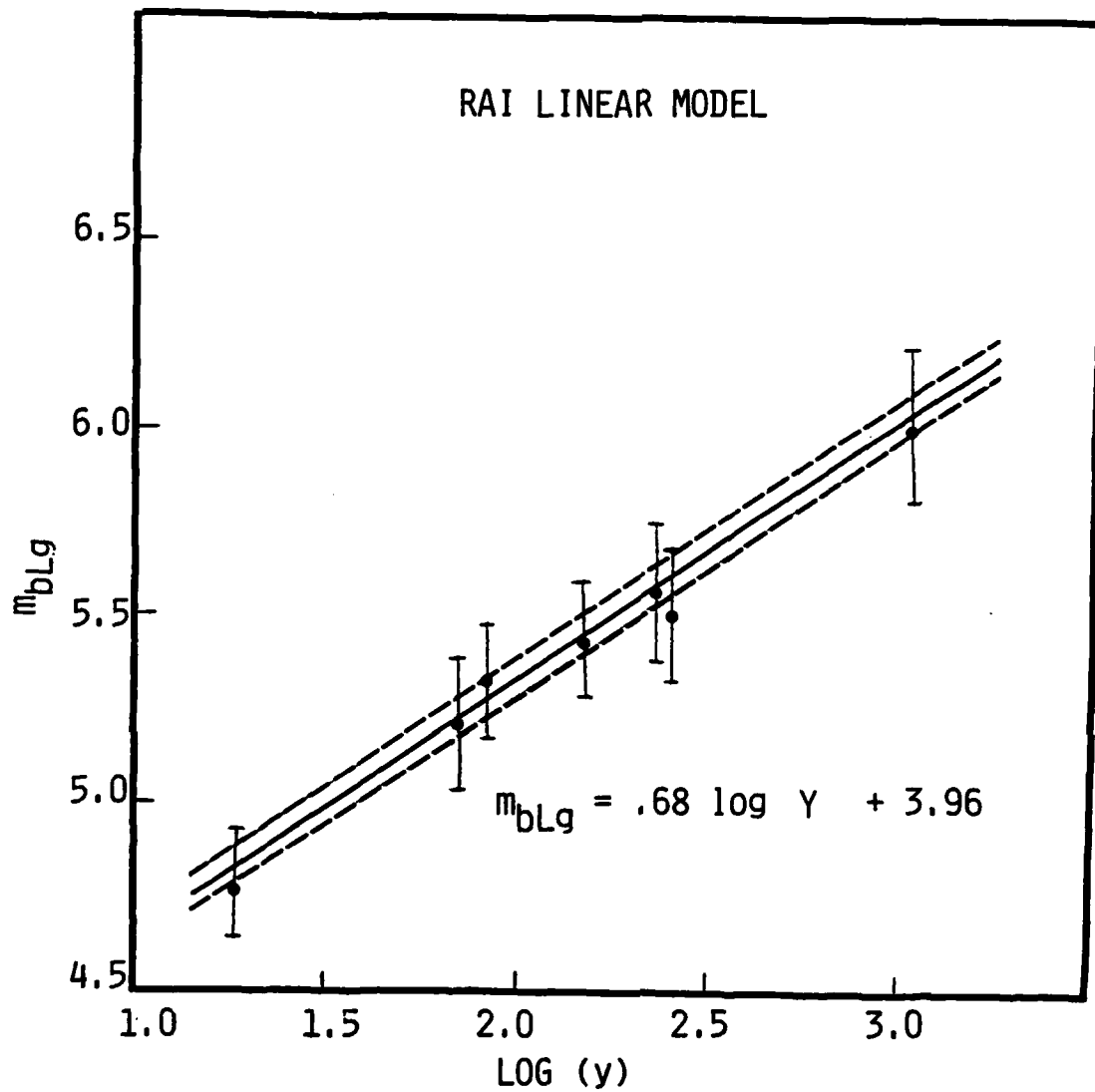


Figure 57. Network  $m_{bLg}$  versus log yield. Network  $m_{bLg}$ 's were calculated as in Figure 17 but using the RAI best linear Q models  $m_{bLg}$  instead of the exponential models. Error bars on the data points are the 95% confidence levels calculated by LSMF. The solid line is the least squares fit to the data. The equation of this line is shown. The dashed lines are the  $\pm 1\sigma$  curves.  $\sigma = .049$ .

## TASK B

### Introduction

The objectives of the research summarized in this report are to determine the utility of short-period (less than about 3 sec) oceanic and continental guided waves and body waves in resolving depth and of short-period spectra for discrimination and yield determination. The research primarily has involved analysis of digital data from the Wake Island ocean bottom hydrophone array (WHA) and from the Catskill Seismic Array (CSA). More recently, we also have used data archived at the Center for Seismic Studies (CSS) from RSTN stations and other stations of the GDSN. In this report, we shall summarize some results using RSTN, WHA, and CSA data and their comparison with synthetic data.

The WHA broadband digital recording system is producing unique seismic data continuously from an oceanic environment. It happens to be at a favorable distance for the reception of teleseismic P waves from known nuclear explosion test sites. In addition, it is a very quiet location for frequencies above about 2.5 Hz (McCreery et al., 1983). In the McCreery et al. paper (Appendix A), we presented and compared spectra of nuclear explosions, shallow earthquakes and background noise as recorded at WHA. Significant differences were found between the spectra of P phases from explosions and shallow focus earthquakes of similar magnitude at 61-71° distance.

Coherent signals across the WHA bottom array (40 km across) enable reliable determination of P wave phase velocities for earthquakes and nuclear explosions. The phase velocities are clearly resolved and agree with expected values for the given epicentral distances. Spectral characteristics of high-frequency oceanic guided waves Pn and Sn are discussed in Walker et al., 1983 (Appendix B). Estimates of  $Q(f)$  of the oceanic lithosphere have been obtained using these waves and are presented in this report.

An array of bottom hydrophones is an excellent receiver for short period components of teleseismic P waves, and oceanic guided waves Pn and Sn. The unique WHA data were used to study attenuation as a function of frequency needed for better estimation of yield, and the short period characteristics of explosion and earthquake signals that are useful in discrimination. Further

research along these lines would be rewarding.

Most of the regional earthquakes from the eastern United States recorded on the Catskill Seismic Array (CSA) have been analyzed to some extent including frequency and polarization filtering, beam forming, and slowness stacking, and generation of various spectra.

The data, for both continental and oceanic paths, are compared to synthetic seismograms using various velocity/attenuation models. Using one of the models, good fits have been obtained for two local continental earthquakes indicating a depth resolution for these shallow events of less than  $\pm 1$  km. Not only the details of individual arrival times but the entire character of the "whole" seismogram changes markedly with depth in the synthetics. Low velocity sediments and the oceanic water layer have a profound effect on the character of high-frequency, teleseismic Pn/Sn ( $P_0$  and  $S_0$ ). Various  $Q(f)$  functions also produce strong effects on synthetics.

RSTN data from the Goodnow, New York earthquake (10/7/83,  $m_b=5.2$ ) and its aftershocks also were studied.

The analysis techniques mentioned above (beam forming, instantaneous and adaptive polarization filtering, and slowness stacking) were developed for use at CSS and have been implemented on the SUN computer. Other programs available for use on the SUN include spectral analysis, spectrogram (frequency versus time versus dB), and waveform operations (addition, subtraction, multiplication, or division of waveforms) and take full advantage of the available interactive graphics. Data transfer between "seismo" at CSS and "raisun" at RAI through the leased phone line is routine and even large files are easily transferred overnight. Large, computer intensive programs such as synthetic seismograms are run directly on seismo at CSS. A detailed description of these techniques and additional examples of their performance are presented in Section C of this report.

### Data Sources

The Center for Seismic Studies (CSS) has archived digital waveform data from the following elements of the Global Digital Seismic Network (GDSN): SRO (Seismic Research Observatories); RSTN (Regional Seismic Test Network); ASRO

(Abbreviated Seismic Research Observatories); and DWWSSN (Digital World-Wide Seismic Station Network). These stations are located in Figures 1C and 24. The data quality from RSTN and SRO generally are generally excellent since the stations contain specially designed digital borehole instrumentation. A number of examples of data from RSTN stations are included in this report. The ASRO and DWWSSN data are of varying quality.

Data from CSA (Catskill Seismic Array, Figures 1B and 24) and WHA (Wake Hydrophone Array, Figures 1A and 1C) are also available from CSS. CSA was the only tripartite, three component, fully digital broad-band seismic array operated in the region east of the Rocky Mountain Front. The array, located near the Catskill Mountains about midway between New York City and Albany, was operated by Rondout Associates, Incorporated under contract from the Air Force Office of Scientific Research from 6 September 1980 to 18 November 1981. CSA data are recorded flat to velocity from about .07 to 10 Hz. Nyquist frequencies for the SP-RSTN and CSA data are 20 and 12.5 Hz, respectively. Many examples of data from CSA are presented in this report.

The WHA broadband digital recording system is producing unique seismic data continuously from an oceanic environment. It happens to be at a favorable distance for the reception of teleseismic P waves from known nuclear explosion test sites. In addition, it is a very quiet location for frequencies above about 2.5 Hz (McCreery et al., 1983, Appendix A). In the McCreery et al. paper, we presented and compared spectra of nuclear explosions, shallow earthquakes and background noise as recorded at WHA. Significant differences were found between the spectra of P phases from explosions and shallow focus earthquakes of similar magnitude at 61-71° distance.

WHA was put into operation 29 June 1979 by Hawaii Institute of Geophysics (HIG) under funding from AFOSR and ONR (current support is principally from AFOSR with a small supplement from ACDA). WHA consists of six hydrophones (71 to 76), bottom mounted, in a water depth of 5.5 km in an array 40 km across and an additional five pairs of hydrophones at a considerably larger array spacing, suspended at SOFAR depth (900m) (Figure 1A). The bottom array lies in a relatively flat area centered 20.5°N-116.5°E, on high Q oceanic lithosphere greater than 100MY old. Currently all the deep hydrophones and five of the SOFAR hydrophones (at sites 1, 2, and 4) are operational. For the period

before September 1982, only a small amount of data are available from the whole 11 element array. Generally only three phones were recorded, on a slow speed analog tape cassette recorder. A complete description and evaluation of that recording system is contained in Walker et al. (1981). An efficient system is available at HIG for digitizing the analog tape data.

In September 1982, the Wake Array was upgraded by HIG in cooperation with RAI, to digital recording of up to 12 hydrophones at 80 samples/sec and 16 bits/sample, with other recording configurations obtainable under software control. The new system is working well (currently recording eight hydrophones); event tapes, about one for every two or three days, and separate tapes containing randomly selected samples of background noise are now being generated routinely at HIG for use at HIG, RAI, and the Center for Seismic Studies (CSS). Examples of WHA data are shown in Figures 2-5, 7, and 11.

#### Wake Island Hydrophone Array (WHA) Analyses

Teleseismic P Waves: Figures 2 and 3 illustrate spectra and spectral ratios, respectively, for explosions at NTS, Tuamotus, and Eastern Kazakh recorded at WHA. The events are of similar magnitude and similar distance (Table I). Also shown in Figure 3 is a seismogram and its spectrogram from the Eastern Kazakh event. Note that the signal is well above background at 10 Hz, the limit of the figure. The record shown includes the direct P and the first water surface reflection of P, PsP1. Although the amplitude of the first cycle and a half is greater than three times the following coda, the signal remains well above background to beyond PsP2 and a time interval of 20 sec, including P though PsP2, was used to produce the spectral ratios. (Amplitudes were corrected by 2 dB per 0.1 difference in magnitude before taking ratios.)

The spectral ratios EK-TU and EK-NTS (dB) increase fairly regularly from 0.6 to 2.8 Hz; the EK-TU ratio being the greater with more than 20 dB increase. Above 3.4 Hz the ratios both generally decrease with frequency until cut off by noise at 4.0 and 5.6 Hz for NTS and TU, respectively.

Previously reported results using explosion P wave spectra to obtain path-averaged  $t^*$  as a function of frequency for paths from NTS and three

TABLE I  
EXPLOSION SOURCE DATA

LOCATION	DATE	$m_b$	DISTANCE TO WHA
Eastern Kazakh	8/4/79	6.1	73 <sup>0</sup>
Tuamotu	7/25/79	6.0	68 <sup>0</sup>
NTS	9/06/79	5.8	68 <sup>0</sup>

Russian sites to WHA and CSA are given in Table II.

Coherent signals across the WHA bottom array (40 km across) enable reliable determination of P wave phase velocities for earthquakes and nuclear explosions. This is demonstrated in Figures 4 and 5 where seismograms and slowness (reciprocal velocity) stacks for the Eastern Kazakh explosion (Figure 4) and a deep Philippine Islands earthquake,  $m_b=5.1$  (Figure 5) are shown. The slowness stacks are produced by delay-sum of the array elements at each value of slowness. (Traces are at equal intervals of slowness.) The phase velocities are clearly resolved and agree with expected values for the given epicentral distances. Figure 5 also demonstrates the high correlation between P and PsP1. Further results from WHA data are given in Appendices A and B.

Comparisons of Pn and Sn ( $P_0$  and  $S_0$ ) with Lq: Figure 6A from Sutton et al., 1978, is an example of long-range high-frequency Pn and Sn ( $P_0$  and  $S_0$ ) along with a T phase, recorded from a Marianas earthquake over a  $60^\circ$  oceanic path on an HIG-OBS in the East Mariana Basin. This record illustrates the emergent beginning and long duration of Pn and Sn (comparable to T, whose propagation is fairly well understood). Figure 6B is a broad-band monitor record from the Catskill Seismic Array showing an intermediate depth Puerto Rico earthquake ( $h=189$  km,  $m_b=5.7$ ,  $\Delta=27.8^\circ$ ) recorded from the vertical component of station 2 of the array. On this record, in addition to impulsive P and S phases, high frequency Pn and Sn and the fundamental mode Rayleigh wave are well recorded. Ground velocity spectra for the Puerto Rico earthquake are shown in Figure 6C. The Pn and Sn spectra are from one minute of data around the respective amplitude maxima; the noise spectrum is from one half minute of data before the first P arrival and should be raised by factor 1.4 for comparison. Signal is well above noise to the Nyquist frequency (12.5 Hz). The Pn and Sn spectra fall off at about -14 dB/oct between 2 and 10 Hz.

A considerable number of regional and teleseismic Pn and Sn arrivals have been recorded by (components of) WHA. Figure 7 shows the rectified signal and spectra recorded, with the up-graded digital system, from hydrophone 74 for a large, intermediate depth earthquake south of Honshu, Japan. Note that although Pn and Sn phases start near 8.2 and 4.7 km/sec, respectively, the maxima occur at considerably lower velocity and the signals die off slowly after the maxima. In this case, the signal remains well above background

TABLE II

$t^*(f)$  FOR EXPLOSION P WAVES TO CSA AND WHA ( $t^*=t/\bar{Q}$ )

PATH	DISTANCE	t (sec)	$m_b$	$t^*$		
				1 Hz	5 Hz	10 Hz
NZ-CSA	60 <sup>0</sup>	611	5.8	.49	.33	.24
NZ-WHA	77 <sup>0</sup>	716	5.8	.65	.42	.29
EK-CSA	85 <sup>0</sup>	759	6.1	.69	.45	.31
WS-WHA	77 <sup>0</sup>	716	4.5	.72 $\pm$	.48 $\pm$	.29 $\pm$
EK-WHA	73 <sup>0</sup>	693	6.1	.82	.48	.32
NTS-WHA	68 <sup>0</sup>	663	5.8	1.02	.53	.33
NTS-CSA	33 <sup>0</sup>	399	5.6	1.60	.67 $\pm$	.40 $\pm$



continuously, through the T phase, for more than 30 minutes; also, except for the mantle P wave, which falls to noise level near 8 Hz, the spectra show signal to noise 30 to 40 dB between about 2.5 and 10 Hz. The maximum signal to noise and dynamic range of interest approach 50 dB. The Sn and T phase spectra are strikingly similar; Pn starts higher and falls off slightly more rapidly with increasing frequency; Pn, Sn, and T are all well above background beyond 20 Hz. The spectrum of the background noise shows that the specially designed pre-whitening filter in the hydrophone preamplifiers has flattened the noise above 5 Hz and reduced the rise expected at low frequencies to a moderate 15 to 18 dB. The mantle P has a maximum at 2.5 Hz and little energy above 7.5 Hz; whereas, Pn and Sn have maxima near 3.5 to 6 Hz and contain significant energy near 20 Hz with Sn being relatively somewhat richer in high frequencies than Pn.

More complete descriptions of long-range high-frequency Pn/Sn recorded on the ocean floor can be found in Sutton et al., 1978; Walker et al., 1978; McCreery and Sutton, 1980; and McCreery and Sutton, 1981. Talandier and Bouchon, 1979, describe similar observations from high-gain high-frequency island-based seismographs. Synthetic Pn/Sn are compared with an OBS seismogram later in this report.

Figure 8-10 show examples of Lg recorded over continental paths in eastern North America. Comparison of Figures 6-10 illustrate the superficial similarities among these phases.

Figures 8 and 10 show spectra of the vertical component of ground velocity of Lg at CSA for five events ranging in distance from  $32.6^\circ$  to  $1.4^\circ$  and in  $m_b$  from 5.6 to 2.7. The straight lines are 6 dB/oct, with an additional line at -12 dB/oct for Harzer. The dashed lines are for background before the signal. The observed maxima, representing the source corner frequency, possibly modified by attenuation, range from less than 0.3 Hz for Harzer to greater than 3 Hz for the Rhode Island earthquake.

Attenuation: The attenuation of seismic wave provides a means for observing the anelastic properties of the earth's interior. Conversely, adequate knowledge of the attenuation of the seismic waves is required in order to use them with confidence to infer dynamic conditions at the earthquake source.

Using a unique data set of high-frequency, teleseismic Pn and Sn wave trains recorded at WHA from circum-Pacific earthquakes (Figure 11), we have been able to estimate apparent Q as a function of frequency between about 1 and 10 to 15 Hz for the lithospheric waveguide.

The lithosphere of the northwest Pacific is an extremely efficient seismic waveguide, passing frequencies as high as 30 and 35 Hz to 2000 km (for Pn and Sn, respectively) and as high as 15 and 20 Hz to 3300 km (for Pn and Sn, respectively) (Walker et al., 1983). Although details of the generation and propagation of Pn/Sn are not well understood, it is generally agreed that they are guided waves propagating within the lithosphere. Recent theoretical work involving the generation of synthetic seismograms (Menke and Richard, 1980; Gettrust and Frazer, 1981; and Sutton and Harvey, 1981) is beginning to improve our understanding of these phases. However, work is still required in several areas. As an example, there still seems to be disagreement concerning the relative importance of scattering as opposed to some laterally uniform velocity-depth function in producing the drawn-out character of Pn and Sn. In addition, little theoretical work has been done on the effects of focal depth and sediment velocity structure near the receiver. Use of synthetic seismograms will be discussed further below.

Our observational studies of Pn/Sn across the northwestern Pacific have shown that the apparent Q of the lithosphere is high, higher for Sn than for Pn, and that Q increases strongly with frequency above about 1 Hz (Walker et al., 1978; McCreery and Sutton, 1981).

Attenuation as a function of depth within the earth, for frequencies lower than 1 Hz, has been investigated with considerable success for many years (e.g. Anderson and Hart, 1978). Regional variations of attenuation in the continental crust and upper mantle have also been investigated (e.g. Sutton et al., 1967; Cheng and Mitchell, 1981).

Recently, there has been an increase of interest in the frequency dependence of Q (e.g. Aki and Chouet, 1975; Aki, 1980a and b, 1981; Mitchell, 1981). Especially for frequencies above 1 Hz, scattering appears to make an important contribution to attenuation within the continental crust and upper mantle (Aki and Chouet, 1975; Aki, 1980a and b, 1981; Dainty, 1981; Dainty and Toksoz, 1981; Wu, 1982). Attenuation from scattering ( $Q_s$ ) takes the same

exponential form as that from internal dissipation ( $Q_i$ ) and the two mechanisms can be difficult to differentiate, i.e.  $1/Q = 1/Q_i + 1/Q_s$ .

The estimates of  $Q$  obtained for the western Pacific lithosphere from high-frequency teleseismic Pn and Sn, in agreement with the continental studies referenced above, show a strong increase with frequency. However, the values of  $Q$  are considerably larger (Walker et al., 1978; McCreery and Sutton, 1981).

$Q(f)$  and Source Spectra for Pn and Sn ( $P_0$  and  $S_0$ ): Averaged spectra for Pn and Sn are plotted in Figure 11 for two distance ranges; from 10 and six earthquakes for the  $17^\circ$  to  $22^\circ$  and  $26^\circ$  to  $33^\circ$  spectra, respectively. Average magnitudes are  $m_b=5.3$  and 5.8. The very slight change in spectral fall off with distance is a combined result of high  $Q$  and of increase in  $Q$  with increasing frequency.

Figure 12A summarized estimates of apparent  $Q$  as a function of frequency obtained for Pn and Sn by three methods. The circles and squares were obtained using Wake data; the triangles in the middle are preliminary results recently obtained by McCreery and Walker from a single event recorded along a 1500 km linear array of OBS's deployed across the location of the Wake Array. The OBS experiment was supported by ONR and designed to study Pn and Sn propagation. The circle method, which produced the lowest values, was employed to reduce effects of uncertainty in the Pn and Sn amplitude dependence on magnitude and spreading law. The procedure is described in the RAI Final Report cited before (Pomeroy et al., 1983). It should be emphasized that these lower  $Q$  values are similar to those obtained by others for continental propagation. The square method, which produced the highest  $Q$  values, is a more common technique that requires a correction of amplitudes for spreading and for magnitude differences. Note that all three methods yield a strong frequency dependence from about 2 to greater than 10 Hz and that the OBS (triangle) method and square method yield significantly higher  $Q$  for Sn than for Pn; Sn greater than 5,000 near 10 Hz.

In Figures 12B and C and in Table III, we compare apparent source spectra for Pn and Sn of each individual earthquake recorded at Wake. The source spectra are obtained using each of the three  $Q$  estimates to correct the observed spectra. The results provide both an estimate of the source

TABLE III

APPARENT SOURCE SPECTRA VS. DISTANCE: 2-10 Hz

## OBSERVED SPECTRA

	DISTANCE		D/D $\Delta$
	2000-2400 KM	2900-3600 KM	
P <sub>N</sub>	-14 dB/OCT	-17 dB/OCT	-3 dB/OCT
S <sub>N</sub>	-13 dB/OCT	-14 dB/OCT	-1 dB/OCT

## SOURCE SPECTRA

Q METHOD	DISTANCE		
	2000 KM	3600 KM	
$(\bigcirc - \frac{\partial^2 \ln A}{\partial p \partial r})$	P <sub>N</sub>	+3 dB/OCT	+9 dB/OCT
	S <sub>N</sub>	+8 dB/OCT	+12 dB/OCT
	S <sub>N</sub> /P <sub>N</sub>	80 dB	+32 dB
$(\square - \frac{\partial \ln A'}{\partial r})$	P <sub>N</sub>	-9 dB/OCT	+4 dB/OCT
	S <sub>N</sub>	-10 dB/OCT	+5 dB/OCT
	S <sub>N</sub> /P <sub>N</sub>	2-3 dB	0 dB
$(\Delta - \text{OBS})$	P <sub>N</sub>	-1 dB/OCT	+6 dB/OCT
	S <sub>N</sub>	-7 dB/OCT	+5 dB/OCT
	S <sub>N</sub> /P <sub>N</sub>	18 dB	+8 dB

intensities between 2 and 10 Hz for Pn and Sn and a means of evaluating the reliability of the different methods of Q determination. The source spectra are all normalized to a distance of 100 km and  $m_b=5.0$ .

In Figure 12B, we compare normalized source spectral amplitudes at 7 Hz as a function of epicentral distance. The best Q estimate should show the least distance dependence. Vertical scales are in peak-to-peak pressure and in equivalent ground amplitude for a compressional wave in water. The highest Q values, from the square method, produce the least residual distance dependence, essentially none. The lower Q estimates appear to be undercorrected. The absolute amplitude levels also appear to favor the squares for the reference magnitude of 5.0 and distance of 100 km at 7 Hz: namely about -30 dB re 1  $\mu\text{m}/\sqrt{\text{Hz}}$  for both Pn and Sn. The low Q from the circle method produce unacceptably large amplitudes and strong distance dependence and therefore is inaccurate for some reason, currently unknown.

In Figure 12C, normalized amplitudes at 7 Hz are shown versus magnitude. In this case, the high Q squares appear to be slightly overcorrected while the OBS triangles are essentially independent of magnitude. The low Q circles, again, look wrong.

In Table III, we compare the slopes of the source spectra between 2 and 10 Hz and the ratio of Sn to Pn source levels of events at two distances. These spectra are for signal pressure, equivalent to ground velocity. Again, we expect no distance dependence if the Q values used in the inversion are accurate. These results are preliminary and subject to change.

Average values for observed spectral slopes in two separated distance ranges, 2000 to 2400 and 2900 to 3600 km, are shown at the top. Slight increases in negative slope with distance of -3 dB/oct for Pn and -1dB/oct for Sn are observed.

Of the source spectra shown below, the low Q from the circle method again produces unreasonable results showing increasing amplitude with frequency in the 2 to 10 Hz range for both Pn and Sn at 3600 km; a 32 dB increase with distance in the ratio of apparent source strength of Sn to that of Pn; and significant changes in the spectral slopes with distance.

The high Q's from the square method again seem to produce the most

reasonable results; showing no change with distance in the ratio of  $S_n$  to  $P_n$  source levels and an average spectral slope of  $-12$  dB/oct. However, the distance dependence of the slopes is about the same as for the  $Q$  from the OBS, triangle method. The  $Q$ 's from both the OBS and square methods seem somewhat in error. Bias resulting from differences in OBS location geology could be a source of error in the OBS method. Continuing research is expected to reduce the error in  $Q$ ; improve the estimates of the source spectra; and expand the frequency range determined.

### Catskill Seismic Array (CSA) and RSTN Analyses

Polarization and Array Analyses of CSA Data: A  $P$  wave from Novaya Zemlya recorded at CSA is shown in Figure 13. The data at CSA as originally recorded are flat to ground velocity between about .07 and 12 Hz. (All filters in this and the following figures are zero phase 3-pole Butterworth, 3 dB down at the corners.) The high coherence of the  $P$  arrival across the array is clear. However, in this case, the array element separation is much less than for WHA. (Compare with Figures 4 and 5 and see maps in Figure 1.)

To estimate the coherence of transient signals across the array as a function of frequency, we obtain cross-correlation between the array stations of octave-band samples from each motion component. In Figure 14A, we show apparent correlation between two, two second samples of random noise. The asterisks and number indicate the locations and values of the absolute maxima. Of course, meaningful correlations for this size sample should exceed these values. Note the increase with decreasing frequency; up to .87 in the .75 to 1.5 Hz band. The frequency bands and sample length used for the following Figure 15 are the same as these.

Figure 15 shows the correlations among each of the motion components, vertical, radial, and transverse (rotated from north-south and east-west) between the three CSA stations for the  $P$  wave of a local earthquake in Long Island Sound;  $\Delta = 1.4^\circ$ ,  $m_b = 3.5$ . Frequency increase left to right. Note that the vertical at station 2 was out of adjustment and correlations with it are distorted. With good correlation, the asterisks should line up near the center of the trace with the appropriate lags for propagation between the two

stations. This is generally the case for the three lower frequency bands. For the 6 to 12 Hz band, the correlations are greater than random but the lags are not appropriate. Note that the transverse component shows significant correlation. This is the result of a small difference between the calculated great circle path used for coordinate rotation and the direction of ground motion (or an equivalent error in instrument orientation).

In Figure 14B, we display the output of an automatic beam-forming program that uses the lags of maxima of running cross-correlations of a given component at the three array stations to determine the horizontal slowness and azimuth as a function of time. The three cross-correlations that are obtained over-constrain the solution and the sum of the three lags should be zero for a plane wave crossing the array. The value of this sum provides the error trace. The two high amplitude pulses produce near zero error centered near 1.2 and 4.3 seconds and reliable values for slowness and azimuth that are reasonable for incident P arrivals for this event.

Different analyses of the P wave from the Long Island Sound earthquake recorded at CSA are compared in Figure 16. The whole seismogram is compared with synthetics later in the report. The wave type, direction of approach, apparent angle of incidence, and phase slowness are obtained using three different procedures. Methods A and B use three-component data at a single station and Method C uses a single component of motion at three stations. The angle determinations in the instantaneous polarization method, A, are unstable when the particle motion passes through zero. This instability is avoided in the adaptive method, B, which uses the angles giving zero cross-covariance at zero lag, in a moving time window, between orthogonal horizontal components and between vertical and (adaptive) radial components as estimates of azimuth and angle of incidence, respectively. Beam forming, C, as in Figure 14, uses the lags of the maxima of the three cross-correlations among the three elements of CSA to obtain azimuth, slowness, and an error term. (Only two lags are needed for slowness and  $\theta$ ; the three lags should sum to zero.)

Figure 17 shows, for the Long Island Sound P and Lg waves, the result of summing the array elements with the proper delays, for a given azimuth, for successive values of horizontal slowness. The primary maxima for the P wave lie between slownesses of about 0.14 to 0.17 seconds per km, appropriate for

local P arrivals; those for S-Lg are near 0.25 (4 km/sec) before 5 sec and slow down to about 0.3 near 6 seconds.

Figure 18 is a record of all the CSA array elements from NTS explosion Harzer,  $\Delta=32.6^\circ$ ,  $m_b=5.6$ . In Figure 19, we examine the polarization of ground motions at station 0 from Harzer. This figure shows the unfiltered P wave, Lg, and sedimentary Rayleigh waves from Harzer. The largest half cycle of the P signal shows P type motion, on RZ and  $\int RZ$ , with reasonable angle of incidence,  $I$ , along the great circle path,  $\theta=0$ . For Lg, the azimuth is generally near  $90^\circ$  as expected from the dominant transverse motion. The product traces suggest an anomalous longitudinal arrival of predominantly P type motion near 90 seconds.

The sedimentary Rayleigh waves from Harzer decrease in period through the portion displayed from about 9 to 6 seconds. The angle of incidence and product traces indicate that the major axis of the particle motion ellipse is rotated toward the direction of an incident P wave. The azimuth trace suggests some coherent motion between the radial and transverse components.

Figures 20 and 21 are from a Rhode Island earthquake which, at  $m_b=2.7$ , is the smallest event chosen for study. Figure 20 illustrates the effect of octave band filtering on the character of the seismograms. Most of the energy exceeding noise is contained within the 1-8 Hz band. The N-S component is about  $40^\circ$  from being normal to the great circle path to the epicenter and should record mostly horizontally polarized shear waves and various Love wave modes which make up the transverse component of Lg in addition to the fundamental LQ mode. A small amount of scattered energy is evident in the 4-8 Hz band of the P arrival near 5 seconds. Note that the lower frequency energy arrives somewhat later on both the vertical and transverse components of Lg.

Figure 21 illustrates the change in character of the N-S and vertical components of motion across the array elements in two frequency bands, 1-2 and 2-4 Hz. Stations Tongore and 213 are about 2.6 km apart normal to the propagation. Tongore and Peak are about 1.8 km apart in the direction of propagation (see Figure 1). The vertical component of P and transverse component of S/Lg are quite coherent. Comparison with a synthetic seismogram will be described later in this report.



The spectrum from Lg of a New Brunswick, Canada earthquake of  $m_b=3.6$  is shown in Figure 22. It has a well defined 12 dB per octave corner near 1 Hz—somewhat lower than given by Street and Turcotte (1977). The Lg spectrum from an earthquake of  $m_b=4.5$  in the Northwest Territories, Canada is shown in Figure 23. The corner frequency is not quite so well defined in this case. A high-pass pre-filter of lower frequency would probably improve the resolution. However, there is good evidence that a corner of about 18 dB per octave lies near 0.65 Hz, in good agreement with Street and Turcotte. These and other Lg spectra are compared in Figures 8 and 10.

The Goodnow, New York and Related Earthquakes: The Goodnow, New York earthquake of 7 October 1983 and its aftershocks have provided a unique opportunity to determine, in detail, the associated ground motions as functions of distance and azimuth from earthquakes in an important seismogenic zone of the eastern United States. High quality broad-band digital records are available from the Regional Seismic Test Network (RSTN) ranging in distance from 0.6 to 29.8°. The Adirondack, New York station, RSNY, at 0.6°, recorded many aftershocks as well as the main shock. (The S arrivals for the main shock are clipped at RSNY.)

The map in Figure 24 locates the Goodnow and two other earthquakes that are being investigated in addition to the three closest RSTN stations and the Catskill Seismic Array (CSA). Two additional RSTN stations are located at Black Hills, Wyoming (RSSD,  $\Delta=21.4^\circ$  to Goodnow) and Yellowknife, NWT (RSNT,  $\Delta=29.8^\circ$  to Goodnow). The RSTN data are recorded in three frequency bands: SP; MP; and LP. However, since the data have high linear dynamic range modifying the response to other configurations is relatively straightforward (Harvey and Choy, 1982). As mentioned before, CSA data are recorded flat to velocity from about .07 to 10 Hz; Nyquist frequencies for the SP-RSTN and CSA data are 20 and 12.5 Hz, respectively.

The Goodnow earthquake of 10/7/83 and two aftershock recorded at RSNY, the closest station,  $\Delta=0.6^\circ$ , are shown in Figure 25. The P arrivals are well recorded for all three shocks and can be used for modeling the main shock using aftershocks. Much of S and Lg for the main shock is clipped. However, the S waves from the aftershocks can be used for modeling and scaling to other ranges and magnitudes.

P arrivals from the main shock and an aftershock recorded at RSNY are compared in Figure 26 and their spectra are compared in Figure 27. Although the signals are quite complex, secondary arrivals that might be surface reflected (depth) phases are apparent. Frequency and polarization filtering can improve such records before comparison with synthetic records. The overall signal to noise ratio is good for the aftershock as well as for the main shock. However, inspection of the spectra in Figure 27 shows that the main shock and aftershock can be compared directly above 2 Hz where the aftershock is above background.

The main earthquake recorded at RSON,  $\Delta=14.9^\circ$ , is shown in Figure 28. The P arrivals commence a few seconds after the beginning of the traces. P, S, Lg, LQ, and LR are all well recorded. Note the impulsive nature of LQ and that both a maximum and a minimum of the Rayleigh wave dispersion are clearly displayed on the MP and LP traces. The P arrivals are expanded in Figure 29. The signal to noise ratio is good and a secondary arrival could be sP. However, the signal on SPN, seen also on SPZ, complicates the record. Again, polarization filtering could simplify the record and aid in arrival interpretation.

The record of the mainshock from RSCP,  $\Delta=12.0^\circ$ , is shown in Figure 30. The back azimuth is nearly  $45^\circ$ . Simple rotation of the horizontal component to radial and transverse would aid the interpretation of the record. The P arrivals are expanded in Figures 31 and 32. As for RSON, they show a secondary arrival about 3 seconds after the onset that might be sP. Other secondary arrivals are apparent.

Figure 33, 34, and 35 are records from the Catskill Seismic Array (CSA) of earthquakes at Chaneville, Quebec and Cornwall, New York (located on Figure 24). The broad-band records have been frequency filtered with simple high-pass or band-pass filters to improve the record quality. The records are flat to velocity in the pass-band. In addition, the records in Figures 33 and 35 have been processed with a polarization filter program that rotates coordinates, plots motion in polar coordinates relative to the great circle path, and produces product and integral traces to sharpen secondary arrivals and aid in identification. Clear secondary P-type arrivals can be identified. However, angle traces do not appear to be very helpful.

### Modeling with "Whole Seismogram" Synthetics

Continental Models: Synthetic seismograms are an important part of the analysis procedure for determining the depth, mechanism, and size of an event as well as helping to verify velocity/attenuation/depth functions along the propagation path. Accurate depths for earthquakes are usually determined employing phases reflected from the surface near the source. At teleseismic distances, the depth of shallow focus earthquakes is difficult to determine to better than 10 kilometers; the initial arrivals overlap the surface reflected phases and limit the ability to pick phases arriving within a second or so of each other. More sophisticated techniques may lose resolution because of low short-period energy. At local and regional distances, however, there is often a substantial amount of high frequency energy in the signal and discrimination of these phases in the time domain is easier.

The "whole" seismogram synthesis program of Harvey, 1981, has been used (on CSS computers) for generation of full waveform synthetic seismograms. The four velocity/attenuation models in Table IV and Figure 36 have been used at RAI for continental source and propagation studies. They produce quite different synthetic seismograms and the Pulli model (Figure 36) appears to be the best fit to the specific arrivals for two eastern United States earthquakes, such as surface reflected "depth" phases, and in the general character of the "whole" seismogram. This latter point is strongly exhibited in the differences in seismograms and spectrums between 0 and 5 km depth for explosion sources (Figures 37-39).

--Effects of Focal Depth, Focal Mechanism, and Velocity Structure: Figures 37 and 38 demonstrate a remarkable change with increasing source depth between 0.1 and 3.0 km in the character and spectrum of S/Lg at  $\Delta=980$  km for an explosion in the CANSO model given in Table IV. Note that the spectral maxima change by more than an octave over this depth range.

Whole waveform synthetic seismograms computed for a suite of depths using a velocity model established by Pulli (Figures 36, 39, and 40A) also, show the sensitivity of the different phases to depth of focus. Except for the direct arrival, the primary phases arrive earlier with increasing focal depth and the surface reflected phases arrive later. For this model, assuming that the

TABLE IV  
CONTINENTAL MODELS

T (km)	$V_p$ (km/sec)	$V_s$ (km/sec)	$\rho$ (g/cm <sup>3</sup> )
SIMPLE			
30	6.5	3.5	2.5
80	8.1	4.7	3.0
CAP	20.0	15.0	10.0
VARIOUS VALUES FOR Q			
-----			
CANSO (Brune and Dorman, 1963)			
6.0	5.64	3.47	2.70
10.5	6.15	3.64	2.80
18.7	6.60	3.85	2.85
264.8	8.20	4.72	3.30
CAP	20.0	15.0	10.0
$Q_\alpha = 1100 + 150f$			
$Q_\beta = 5Q_\alpha/9$			

arrivals could be picked to an accuracy of 0.1 seconds and that there are not other errors, the depth could be determined to better than .5 km using a single station. Of course, the depth determination is model dependent (Figures 36 and 40C) and misidentification of phases can also lead to unreliable depths.

Once a good match to the arrival times has been obtained, then the task of matching the amplitudes is pursued. Relative amplitudes of the various phases are controlled by the fault orientation. Any fault orientation may be decomposed into a linear combination of three primary fault types; a vertical strike slip fault striking  $45^\circ$ , a vertical dip slip fault, and a dip slip fault dipping at  $45^\circ$  (Figure 40B). By combining the three basic fault types into different fault configurations, the best fit or fits of synthetic data to recorded data can be found (Pearce, 1977). The effects of orientation of faulting illustrated in Figure 40B are more subtle than those of depth of focus.

Unfortunately, for small events, the P waves at regional and teleseismic distances recorded with high quality digital instruments do not have adequate signal to noise ratios for detailed analysis of the compressional arrivals and more reliance must be placed on the analyses of the "whole" seismogram, since signal to noise is much greater for later phases, e.g. Pg, Sn, Lg, LR, and LQ. The work of Street and Turcotte (1977) and Herrmann and Goertz (1981) are good examples of fruitful attempts in this direction for earthquakes in the central and eastern United States. As demonstrated especially in Figures 37 and 38, synthesis of the later portions of a complex seismogram for use in the analyses can be accomplished fairly efficiently and capabilities are continually improving (e.g. Bache et al., 1981; Harvey, 1981; Herrmann and Goertz, 1981; Sutton and Harvey, 1981).

--Effects of  $Q(f)$ : Effects of  $Q(f)$  on full waveform seismograms and their spectra for an explosion source in the simple continental velocity structure of Table IV are summarized in Figures 41-47. The various models for  $Q$  in the crust are shown in Figure 41. Curve (3) from Singh and Herrmann (1982) for eastern United States was approximated by curve (2) in the calculations. Since the calculations are limited to frequencies of 2 Hz and below and distances are limited to 100 km, the more realistic  $Q$  values given by curves (1)

and (2) produce only a small amount attenuation. Results from the lower  $Q$  values given by curves (4) and (5) more clearly demonstrate the effects of frequency dependent attenuation. In all cases  $Q_c = 2Q_f$ ; for the higher  $Q$  values, cases (1) and (2), mantle  $Q$  values are two times those in the crust; for the lower  $Q$  values, cases (4) and (5), mantle  $Q$  values equal those in the crust.

Figure 42 shows the spectral attenuation of the complete vertical component seismic signal at a distance of 100 km for the four  $Q$  cases studied. Greater attenuation at higher frequencies for the cases of constant  $Q$  and appreciable attenuation, independent of frequency for the case  $Q=60f$  are clearly demonstrated. Radial horizontal and vertical waveforms for the four  $Q$  cases at  $\Delta=100$  are compared in Figure 43. There is little discernable difference between the higher  $Q$  waveforms, being similar to those for infinite  $Q$  as expected from Figure 42. However, the seismograms for the lower  $Q$  cases exhibit interesting differential attenuation, e.g., between the broad-band body wave arrivals and the low frequency Rayleigh wave pulse. The vertical component spectra for the four cases are compared in Figure 44. Note that at 1 Hz the spectra reflect the fact that the frequency dependent  $Q$  and constant  $Q$  are equal for both the high  $Q$  cases and the low  $Q$  cases.

Seismograms for the two low  $Q$  cases at  $\Delta=50$  km are compared in Figure 45 and the more prominent arrivals are identified. Changes in the seismograms and spectra between  $\Delta=50$  and 100 km can be seen in Figures 46 and 47, respectively. Greater attenuation at higher frequency for the constant  $Q=60$  case and attenuation independent of frequency for the case  $Q=60f$  is clearly demonstrated in the spectra. The latter case would be interpreted as infinite  $Q$  if determined by change in slope of the spectrum with distance (assuming constant  $Q$ ).

--Comparison with Data: In Figure 48, the local Long Island Sound and Rhode Island earthquakes mentioned earlier recorded at CSA are compared with synthetics from the Pulli model. This figure represents the best match we have obtained to date for these two earthquakes. While the match to the various compressional arrivals and general seismogram character seems fairly good. Preprocessing of the data using polarization and array techniques to minimize effects of lateral refraction and scattering, perhaps with some perturbation

of source and propagation models, could improve the fit markedly.

Oceanic Models: To date, little theoretical work has been completed on the generation and propagation of long-range high-frequency Pn and Sn. However, results to date indicate that these phases may become powerful tools for refining lithosphere structure and determining focal depths of shallow and normal focus events (Gettrust and Frazer, 1981 and Sutton and Harvey, 1981).

Considerably more observational and theoretical work has been done on continental Lg. Pomeroy and Chen (1980) provide an excellent summary of this work including that especially relevant to this research by Sutton et al., 1967; Isacks and Stephens, 1978; Knopoff et al., 1979; and Chinn et al., 1980. Bache et al. (1980 and 1981) provide an important investigation of the effects of velocity structure, source depth, focal mechanism, and Q on the character of synthetic Lg seismograms. Their results indicate the complexity of the interrelations among the various parameters involved in the production of the Lg signal. Pomeroy (1981) and Pomeroy et al. (1982) discuss the use of intermediate and long period waves at regional and near-teleseismic distances for discrimination and yield determination of nuclear explosions.

Modeling with synthetic seismograms for comparison with data provides a powerful tool for quantifying the predictability or reliability of various empirical discrimination techniques when used under circumstances different from those which produced the input data, e.g. Bache et al. (1980 and 1981). As appropriate, we have attempted to produce broad-band, complete ("whole") synthetic seismograms using realistic source and velocity-depth function for comparison with data and to test effects of changes in depth, velocity-Q structure, and source characteristics. The extremely low shear velocities in oceanic sediments and the existence of the water layer combine to produce a seismogram of extremely long duration. This produces computation difficulties.

Figures 49 and 50, from Sutton and Harvey (1981), illustrate the usefulness, and some of the limitations, of the Harvey procedure as implemented on the CIRES PDP 11/70 computer. The purpose of the research was to model the teleseismic, high-frequency Pn and Sn ( $P_0$  and  $S_0$ ) that is observed to propagate with high efficiency through the oceanic lithosphere. The character of these signals should be sensitive to lithosphere velocity structure and to

source depth.

Partly because of limitations in computer capability, we have not yet tried to model the high-frequency, long duration signals at WHA. To date, our synthetics have been limited to 3 Hz and below and to 1000 km or less. We are in the process of implementing and improving the programs for use on the computers at the Center for Seismic Studies.

The velocity-Q structures utilized are summarized in Table V. The high velocity cap at the bottom of the structure is required for the Harvey "locked-mode" procedure of synthetic calculation. Sharp, high phase velocity reflections from this layer can sometimes be bothersome.

--Effects of Low-Velocity Sediment and Water: A number of synthetics were generated for models without sediment or water and with infinite Q. These synthetics clearly demonstrate strong effects on record character of: focal depth, for normal and shallow focus events; the existence of a low velocity zone in the upper mantle for S and/or P; and the frequency content of the recorded signal. Synthetics for models with low velocity sediment alone (1 km thick, finite Q) and with low velocity sediment and water (0.5 km and 5 km thick, respectively, finite Q) show the importance of these layers to total record character. The source in all cases is a time step function, double couple  $45^\circ$  dip slip fault.

Figures 49A and B demonstrate the strong effect of source depth on wide-band (0 to 2 Hz) seismograms, especially between the surface and Moho, for an oceanic type lithosphere. At this range (600 km)  $S_n$  should start near one minute. Note that the relative amplitude of the P train compared to the S train increases with focal depth. The sharp signal near three minutes is a reflection from the high velocity cap layer and the small sharp arrival before 0 is a transient from the high phase velocity cut-off of the synthetics. The model for these figures has a LVZ for both P and S, infinite Q, and no sediment or water.

Figure 49C compares synthetics for different mantle structures: A-LVZ for both P and S; B-LVZ for S only; C-no LVZ. Removal of the LVZ for P and S tends to increase the higher velocity and higher frequency components of the P or S trains, respectively. The model for this figure has infinite Q and no sediment or water.



TABLE V

## Pn-Sn OCEAN STRUCTURE MODELS

	T (km)	V <sub>p</sub> (km/s)	V <sub>s</sub> (km/s)	P (g/cm <sup>3</sup> )	Q <sub>p</sub>	Q <sub>s</sub>
WATER	5	1.5	0	1	10,000	10,000
SEDIMENT	1/0.5	2	0.4	1.8	500/200	200/100
CRUST	0.8	5	2.9	2.5	5,000	5,000
	1	6	3.5	2.6	5,000	5,000
	2.7	6.7	3.9	2.8	5,000	5,000
	2.5	7.4	4.3	3.0	5,000	5,000
MANTLE	2	8.3	4.8	3.3	5,000	5,000
	1	8.5	4.9	3.4	5,000	5,000
	2	8.3/8.5	4.8/4.9	3.4	5,000	5,000
	21	7.8/8.5	4.5/4.9	3.4	5,000	5,000
	460	7.8/8.6	4.5/5.0	3.4	1,000	1,000
CAP		20	15	5	9,000	9,000

Effects of sediment and ocean on record character are illustrated in Figures 49D, 50L, and 50R. In these figures, source depth is 0.5 km above Moho and receiver is on top of the solid section. Figure 49D demonstrates the strong influence of 1 km of low velocity sediment (Trace B) and of 0.5 km of sediment with 5 km of water (Trace C). The model for this figure has a LVZ for S only and sediment  $Q=500$  and 200 for P and S, respectively. Traces B and C are both degraded by "wrap-around" of low velocity, low frequency energy. This effect is more serious below 1 Hz. Finer frequency sampling can cure this problem at the expense of more computation time. Frequency dependence of signal character is further illustrated in Figure 50L comparing three frequency bands (A=0 to 3 Hz; B=1 to 3 Hz; C=2 to 3 Hz) for the case with 0.5 km of sediment and 5 km of water. The model for this figure has a LVZ for S only and sediment  $Q=200$  and 100 for P and S, respectively. Distance=300 km. Traces B and C have some resemblance to observed Pn/Sn although the amplitude-velocity relationship is not quite right and the apparent frequency dispersion between B and C is not observed.

--Comparison with Data: In Figure 50R, we compare an actual OBS record (Trace C, Mariana Basin,  $\Delta=6.15^\circ$ ,  $h=33$  km,  $m_b=4.8$ , low gain vertical, 1 to 3 Hz band-pass filtered) with 1 to 3 Hz synthetics at 300 km (Trace A) and 600 km (Trace B). Parameters for the synthetics are the same as for Figure 50L. The regularly spaced pulses on the OBS trace are from minute marks incorporated in the original record.

Synthetics generated to date are near the short range and low frequency limits of observed Pn/Sn. To date, we have obtained the best qualitative match with a combination of LVZ for S only, low-velocity sediment, focus below Moho (perhaps), (and water?). We probably need thinner and lower Q sediments. A frequency dependent Q (as observed for Pn/Sn) will be required for an accurate model.

As indicated in the preceding paragraph, analysis of high-frequency teleseismic Pn and Sn recorded at WHA indicates a high Q for the lithosphere under the Western Pacific Basin with Q increasing strongly with frequency above 1 Hz; Sn indicates higher Q than Pn (McCreery and Sutton, 1981). This work is in progress and we expect to apply such work to estimates of source strength for Pn and Sn as a function of frequency.

There is continuing discussion of the relative merits of bottom hydrophones and bottom and sub-bottom seismographs. The Lopez Island experiment (Sutton et al., 1981a and b) was a fairly successful effort to evaluate the degree of distortion of seismic signals produced by coupling of OBS's of several different designs to soft ocean-floor sediments and to the near-bottom water. Another concern regarding OBS use is in the amount of noise generated by the flow of bottom current past the instrument package. Lopez results in this regard were inconclusive but Duennebier et al. (1981) demonstrate current generated noise on, at least one OBS design. Brocher et al. (1981) evaluated hydrophones and horizontal and vertical seismometers in a continental margin environment. RAI continues to be involved in research related to these problems with funding from ONR.

## References

- Aki, K., 1980a, Attenuation of Shear Waves in the Lithosphere for Frequencies from 0.05 to 25 Hz, *Phys. Earth Planet. Inter.*, 21, 50-60.
- Aki, K., 1980b, Scattering and Attenuation of Shear Waves in the Lithosphere, *J. Geophys. Res.*, 85, B11, 6496-6504.
- Aki, K., 1981, Source and Scattering Effects on the Spectra of Small Local Earthquakes, *Bull. Seis. Soc. Am.*, 71, 6, 1687-1700.
- Aki, K. and B. Chouet, 1975, Origin of Coda Waves: Source, Attenuation, and Scattering Effects, *J. Geophys. Res.*, 80, 3322-3342.
- Anderson, D.L. and R.S. Hart, 1978, Attenuation Models of the Earth, *Phys. Earth Planet. Inter.*, 16, 289-306.
- Bache, T.C., H.J. Swanger, and B. Shkoller, 1980, Synthesis of Lg in Eastern United States Crustal Models with Frequency Independent Q, Semi-Annual Technical Report to DARPA, Systems, Science, and Software, SSS-R-81-4668, 114 p., La Jolla, California.
- Bache, T.C., H.J. Swanger, B. Shkoller, and S.M. Day, 1981, Simulation of Short Period Lg in Final Report to DARPA, Systems, Science, and Software, SSS-R-81-5081, 145 p., La Jolla, California.
- Brocher, T.M., B.T. Iwataki, J.F. Gettrust, G.H. Sutton, and L.N. Frazer, 1981, Comparison of the S/N Ratios of Low-Frequency Hydrophones and Geophones as a Function of Ocean Depth, *Bull. Seis. Soc. Am.*, 71, 1, 1649-1659.
- Brune, J. and J. Dorman, 1963, Seismic Waves and Earth Structures in the Canadian Shield, *Bull. Seis. Soc. Am.*, 53, 167-209.
- Cheng, C.C. and B.J. Mitchell, 1981, Crustal Q Structure in the United States

from Multi-Mode Surface Waves, Bull. Seis. Soc. Am., 71, 1, 161-181.

Chinn, D.S., B.L. Isacks, and M. Barazangi, 1980, High-Frequency Seismic Wave Propagation in Western South America Along the Continental Margin, in the Nazca Plate, and across the Altiplano, Geophys. Jour. R. A. S., 60, 209-244.

Curtin, P.L., J.J. Pulli, and C.B. Godkin, 1983, A New Crustal Model for Central New England--Implications for Hypocentral Calculations and Fault Plane Solutions; Presented at the 55th Annual Meeting of the Seismological Society of America Eastern Section, September 1983 (Abstract).

Dainty, A.M., 1981, A Scattering Model to Explain Seismic Q Observations in the Lithosphere Between 1 and 30 Hz, Geophys. Res. Let., 8, 11, 1126-1128.

Dainty, A.M. and N.M. Toksoz, 1981, Seismic Coda on the Earth and the Moon: A Comparison, Phys. Earth Planet. Inter., 26, 250-260.

Duennebier, F.K., G. Blackinton, and G.H. Sutton, 1981, Current-Generated Noise Recorded on Ocean Bottom Seismometers, Marine Geophys. Res., 5, 109-115.

Gettrust, J.F. and L.N. Frazer, 1981, A Computer Model Study of the Propagation of the Long-Range Pn Phase, Geophys. Res. Let., 8, 749-752.

Harvey, D., 1981, Seismogram Synthetics Using Normal Mode Superposition: The Locked Mode Approximation Method, Geophys. J. Roy. Astron. Soc., 66, 37-69.

Harvey, D. and G.L. Choy, 1982, Broad Band Deconvolution of GDSN Data, Geophys. J. R. A. S., 69, 659-688.

- Herrmann, R.B. and M.J. Goertz, 1981, A Numerical Study of Peak Ground Motion Scaling, Bull. Seism. Soc. Am., 71, 1963-1980.
- Isacks, B.L. and C. Stephens, 1978, Conversion of Sn to Lg at a Continental Margin, Bull. Seis. Soc. Am., 65, 234-244.
- Knopoff, L., R.G. Mitchell, E.G. Kausel, and F. Schwab, 1979, A Search for the Oceanic Lg Phase, Geophys. Jour. R. A. S., 56, 211-218.
- McCreery, C.S. and G.H. Sutton, 1980, Wave Train Characteristics of Long-Range High-Frequency Pn, Sn Crossing an Ocean Bottom Hydrophone Array, Bull. Seis. Soc. Am., 70, 437-446.
- McCreery, C.S. and G.H. Sutton, 1981, Attenuation and Source Spectra of High Frequency Teleseismic Pn and Sn in the Northwestern Pacific, EOS, 62, 334, Abstract.
- McCreery, C.S., D.A. Walker, and G.H. Sutton, 1983, Spectra of Nuclear Explosions, Earthquakes, and Noise from Wake Island Bottom Hydrophones, Geophys. Res. Let., v. 10, no. 1, 59-62.
- Menke, W. and P. Richards, 1980, Crust-Mantle Whispering Gallery Phases: A Deterministic Model of Teleseismic Pn Wave Propagation, J. Geophys. Res., 85, 5416-5422.
- Mitchell, B.J., 1981, Regional Variation and Frequency Dependence of Q in the Crust of the United States, Bull. Seis. Soc. Am., 71, 5, 1531-1538.
- Pearce, R.G., 1977, Fault Plane Solutions Using Relative Amplitudes of P and pP, Geophys. J. Roy. Astr. Soc., 50, 381-394.
- Pomeroy, P.W. and T.C. Chen, 1980, Regional Seismic Wave Propagation, Final Technical Report to ARPA/AFOSR, Rondout Associates, Incorporated, Stone Ridge, New York, 87p.

- Pomeroy, P.W., 1981, The Use of Intermediate and Long Period Seismic Waves for Discrimination and Yield Determination, RAI Annual Technical Report No. 2 under Contract F4960-80-C-0021 with AFOSR, 106p.
- Pomeroy, P.W., W.J. Best, and T.V. McEvilly, 1982, Test Ban Treaty Verification with Regional Data--A Review, Bull. Seis. Soc. Am., 72, S89-S129.
- Pomeroy, P.W., G.H. Sutton, and J.A. Carter, 1983, The Use of Regional Seismic Waves for Discrimination and Yield Determination, RAI Final Report, Vol. II under Contract F49620-80-C-0021 with AFOSR, RAI-FTR-04-83-01, 115p.
- Singh, S. and R.B. Herrmann, 1982, Regionalization of Crustal Q in the Continental United States, J. Geophys. Res., 88, 527-538.
- Street, R.L. and F.T. Turcotte, 1977, A Study of Northeastern North American Spectral Moments, Magnitudes, and Intensities, Bull. Seism. Soc. Am., 67, 599-614.
- Sutton, G.H., W. Mitronovas, and P.W. Pomeroy, 1967, Short Period Seismic Energy Radiation Patterns from Underground Nuclear Explosions and Small-Magnitude Earthquakes, Bull. Seis. Soc. Am., 57, 249-267.
- Sutton, G.H., C.S. McCreery, F.K. Duennebier, and D.A. Walker, 1978, Spectral Analyses of High-Frequency Pn, Sn Phases Recorded on Ocean Bottom Seismographs, Geophys. Res. Let., 5, 745-747.
- Sutton, G.H., F.K. Duennebier, B. Iwataki, J.D. Tuthill, B.T.R. Lewis, and J. Ewing, 1981a, An Overview and General Results of the Lopez Island OBS Experiment, Marine Geophys. Res., 5, 3-34.
- Sutton, G.H., F.K. Duennebier, and B. Iwataki, 1981b, Coupling of Ocean Bottom Seismometers to Soft Bottom, Marine Geophys. Res., 5, 35-51.

- Sutton, G.H. and D.J. Harvey, 1981, Complete Synthetic Seismograms to 2 Hz and 1000 km for an Oceanic Lithosphere (Abstract), EOS, 62, 327.
- Talandier, J. and M. Bouchon, 1979, Propagation of High-Frequency Pn Waves at Great Distances in the Central and South Pacific and Its Implications for the Structure of the Lower Lithosphere, Jour. Geophys. Res., 84, 5613-5619.
- Walker, D.A., C.S. McCreery, G.H. Sutton, and F.K. Duennebie, 1978, Spectral Analyses of High-Frequency Pn and Sn Phases Observed at Great Distances in the Western Pacific, Science, 199, 1333-1335.
- Walker, D.A., G.H. Sutton, and C.S. McCreery, 1981, Spectral Analyses of High-Frequency Pn, Sn Phases from Very Shallow Focus Earthquakes, Technical Report to AFOSR, Hawaii Institute of Geophysics, 15p.
- Walker, D.A., C.S. McCreery, and G.H. Sutton, 1983, Spectral Characteristics of High-Frequency Pn, Sn Phases in the Western Pacific, J. Geophys. Res., 88, 4289-4298.
- Wu, R.S., 1982, Attenuation of Short Period Seismic Waves Due to Scattering, Geophys. Res. Let., 9, 1, 9-12.



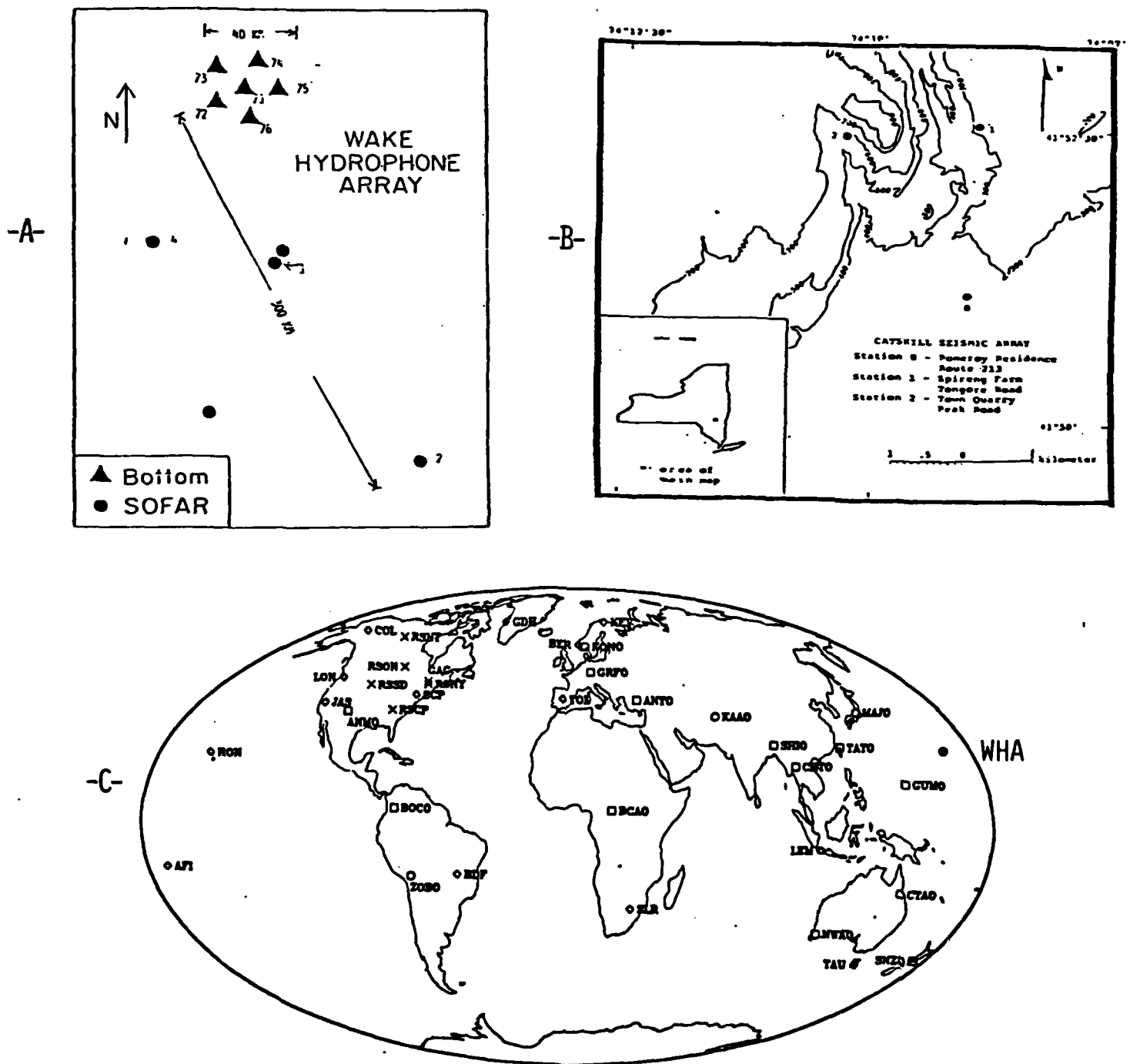


Figure 1. A, Wake Hydrophone Array (WHA); B, Catskill Seismic Array (CSA); C, Global Digital Seismic Network (GDSN):  $\square$  = SRO;  $\circ$  = ASRO;  $\diamond$  = DWSSN;  $\times$  = RSTN.

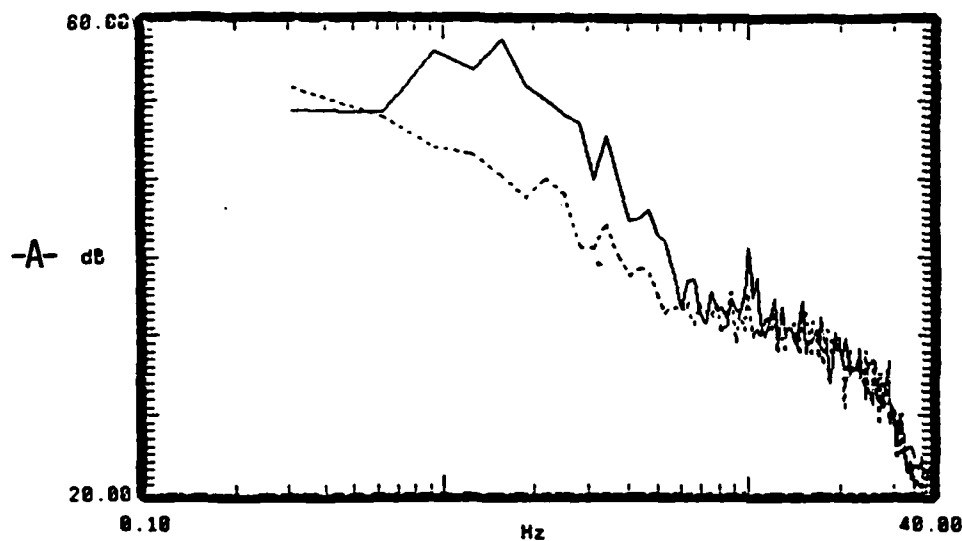
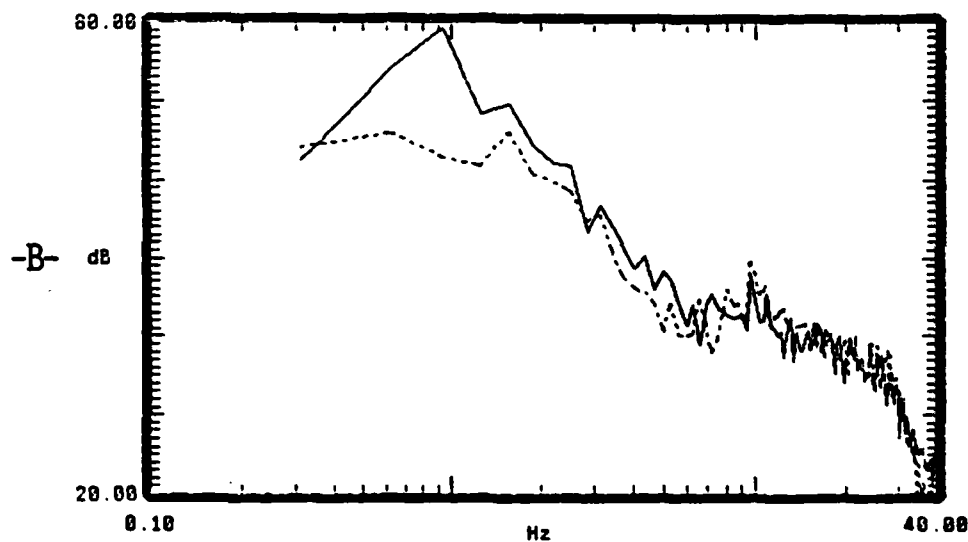
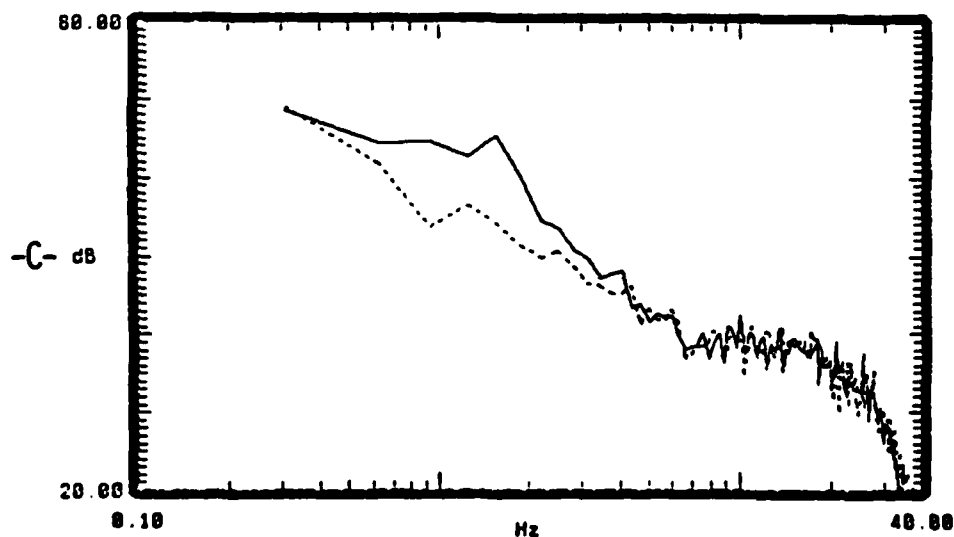


Figure 2. P wave spectra from WHA for 20 sec of data including P through PsP2 for three explosions listed in Table I; dashed spectra are noise before P: A-Eastern Kazakh (EK); B-Tuamotu (TU); C-NTS. Spectral points are independent averages of 8 estimates.

Fourier Spectrum (re units per Hz)



Fourier Spectrum (re units per Hz)



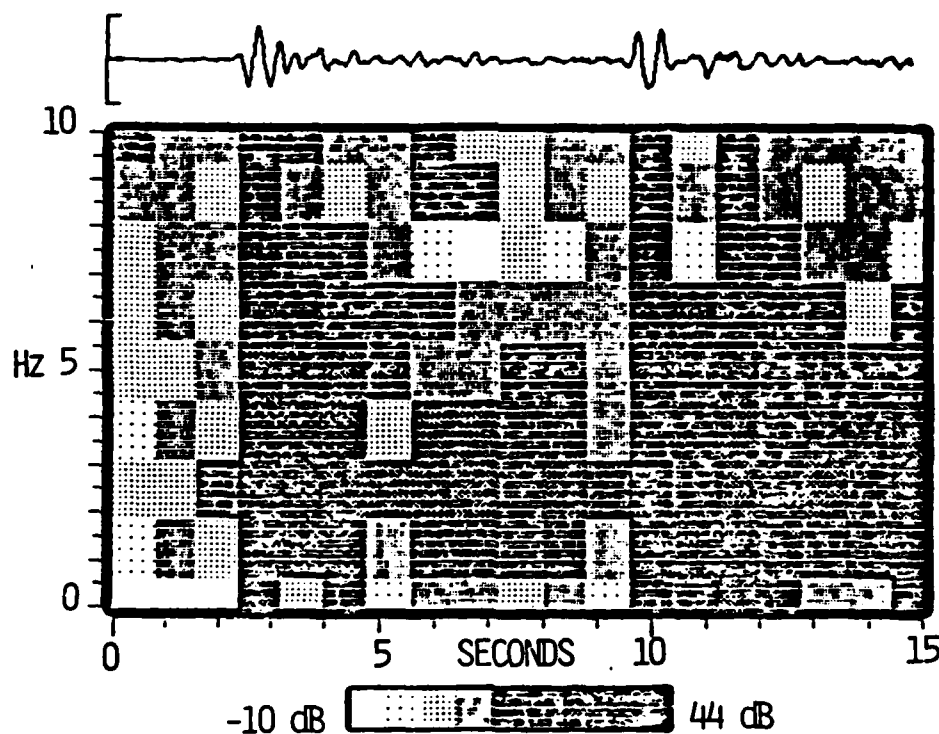
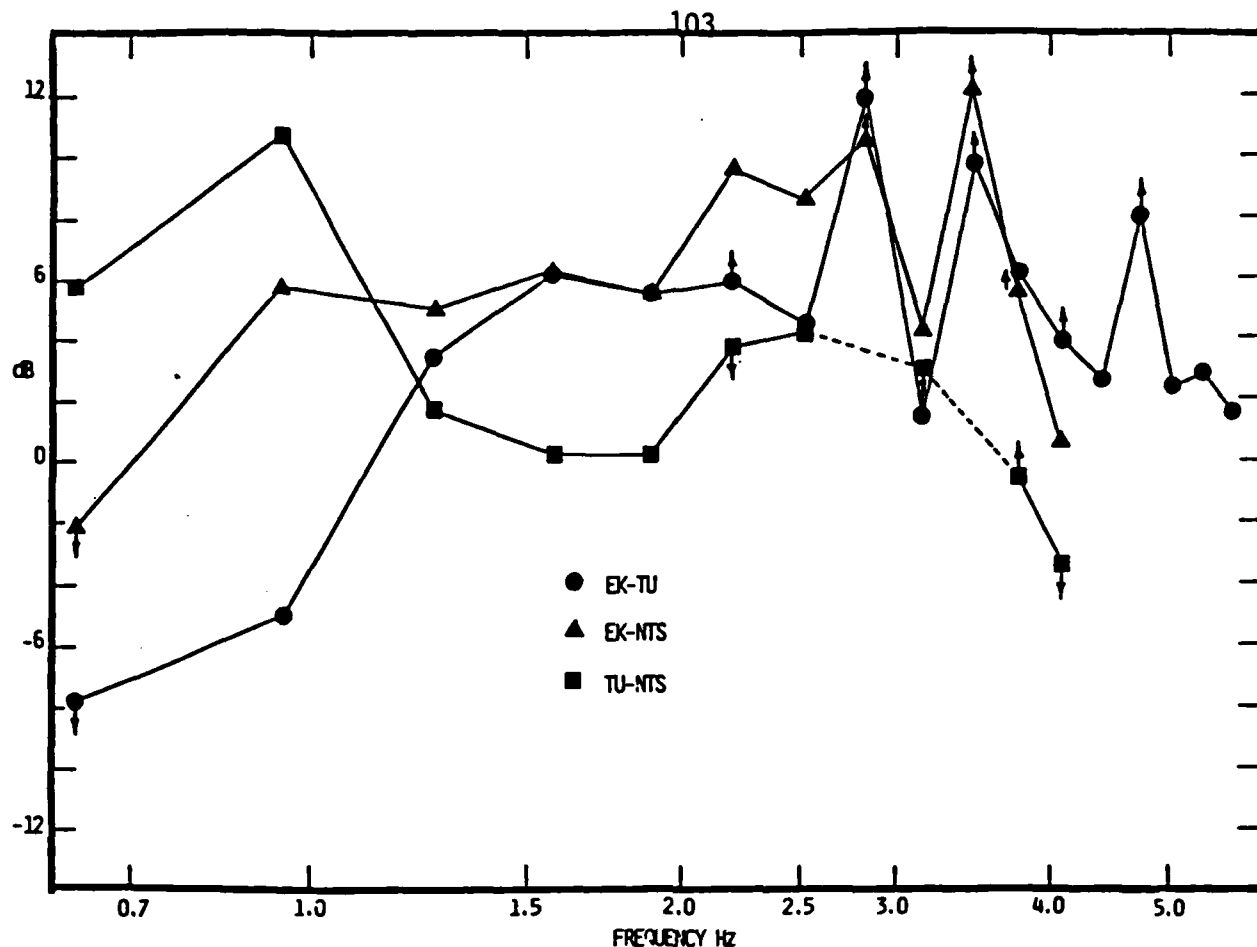


Figure 3. Upper: Spectral ratios (dB differences) of P arrivals among Eastern Kazakh (EK), Tuamotu (TU), & NTS explosions (listed in Table I) recorded at WHA. Spectra are for 20 sec of data including P through PsP2. Points are from averages of 8 spectral estimates. Arrows indicate minimum or maximum values where one of arrivals is less than 3 dB above noise. Lower: Spectrogram of P and PsP1 from the Eastern Kazakh event uncorrected for instrument response (designed to flatten background spectrum) 6 dB contour interval. Note that signal maxima are well above background at 10 Hz with peak recorded energy between 2 & 3 Hz. Arrivals and coda are above background in the interval shown.

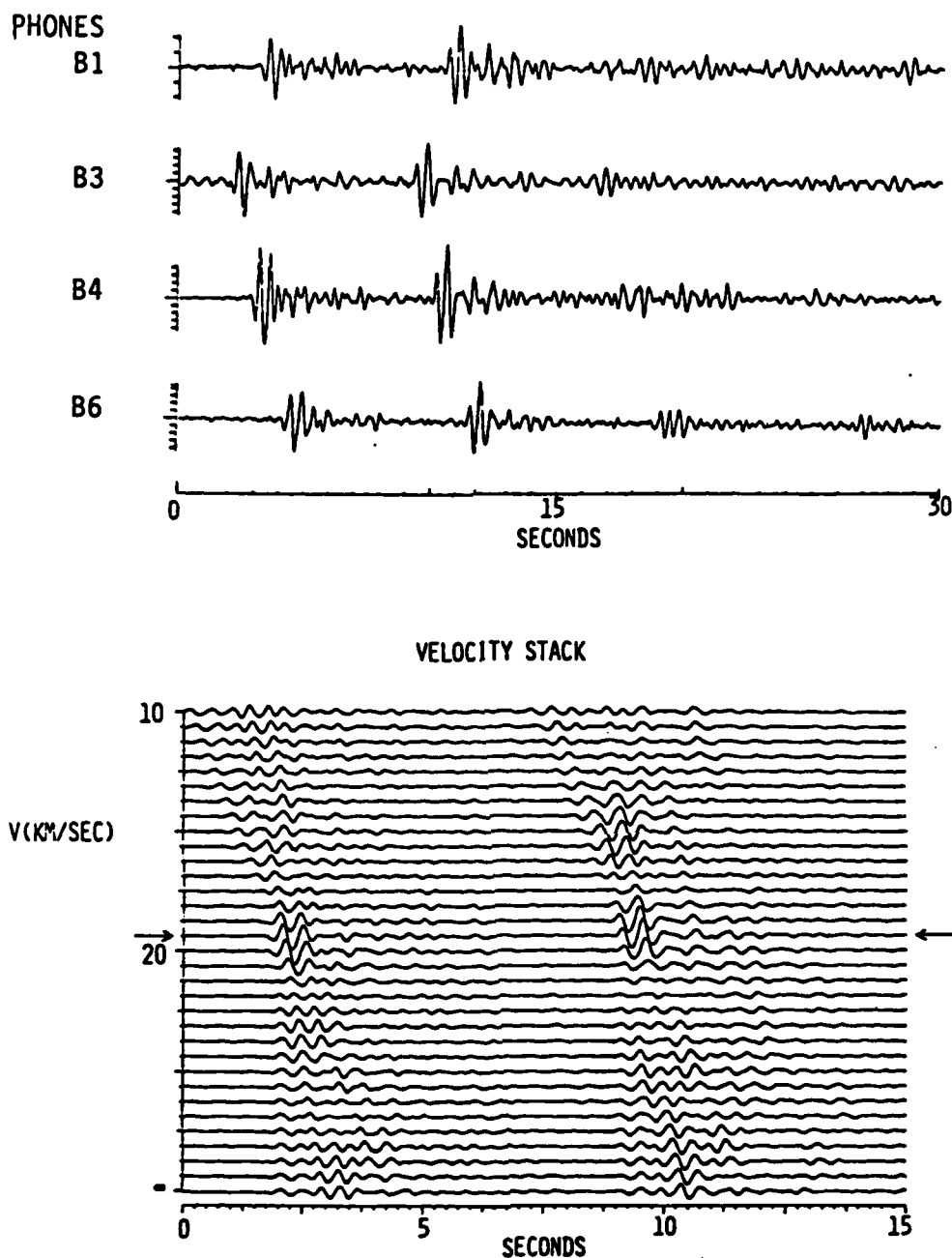


Figure 4. East Kazakh explosion,  $m_b=5.7$ , recorded at WHA,  $\Delta=73.0^\circ$ ,  $\theta=317.7^\circ$ . Seismograms and velocity stack from <sup>b</sup>Phones B1, B3, B4, and B6, filtered 1-5 Hz bandpass. Arrows indicate arrival phase velocity. Second and third arrivals are ocean surface reflection and its multiple. Note high coherence of P and surface reflection across 40 km array.

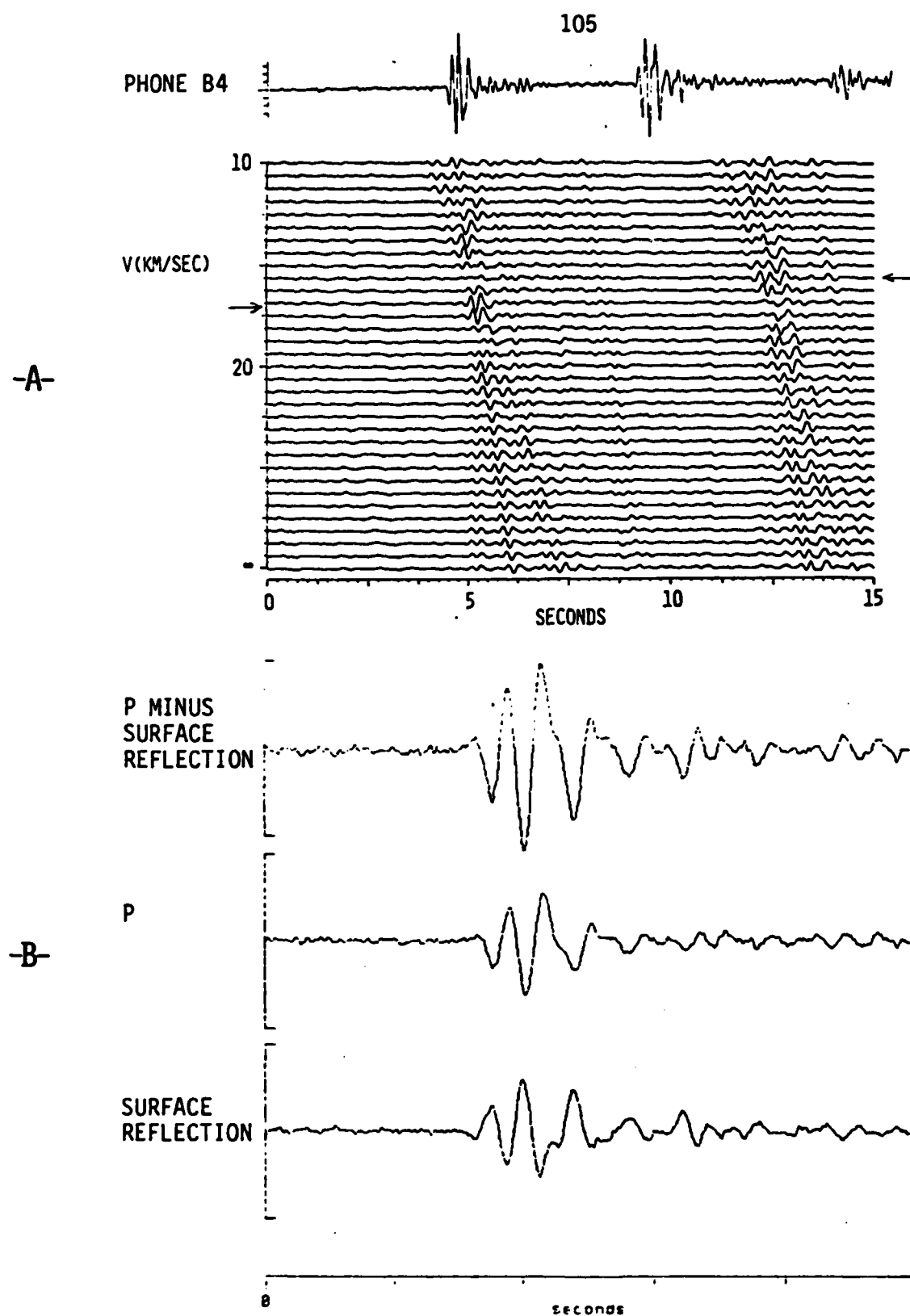


Figure 5. Mindanao, PI earthquake,  $m_b=5.1$ ,  $H=601$  km recorded at WHA,  $\Delta=43.8^\circ$ ,  $\theta=257.1^\circ$ . A, seismogram from phone B4 and velocity stack of phones B1, B3, B4, and B6. Filtered 1-6 Hz bandpass. Arrows indicate arrival phase velocities. Second and third arrivals are ocean surface reflection and its multiple. B, delayed difference of P and first surface reflection, unfiltered.

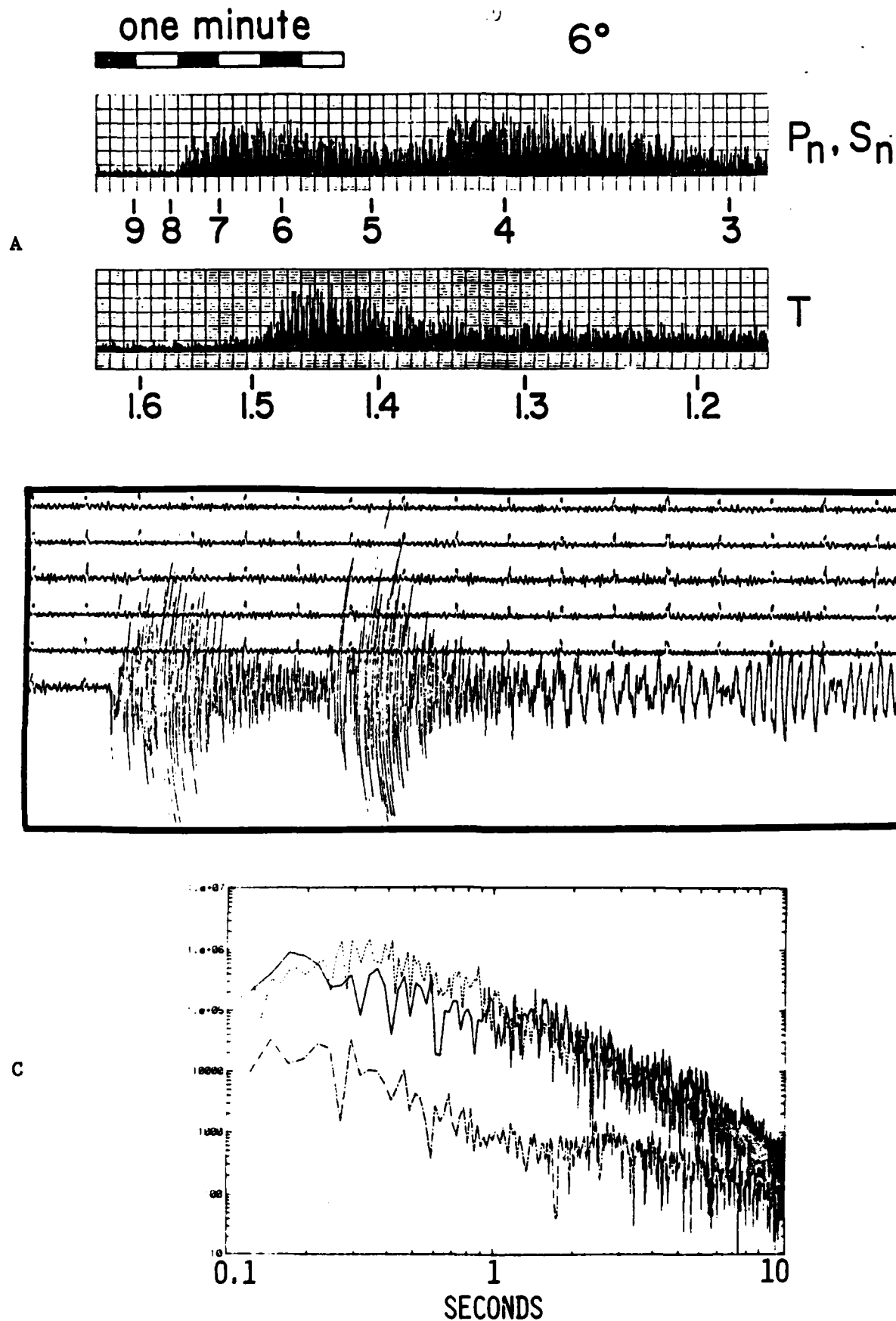


Figure 6. A, rectified high-frequency  $P_n$ ,  $S_n$ , and T phases recorded on OBS at  $6^\circ$ , numbers are great-circle velocities in km/sec; B, record from CSA of Puerto Rico earthquake, vertical component, station 2, one minute time marks; C, ground velocity spectra of  $P_n$  (solid),  $S_n$  (dotted), and background before P (dot-dash) for the Puerto Rico event.

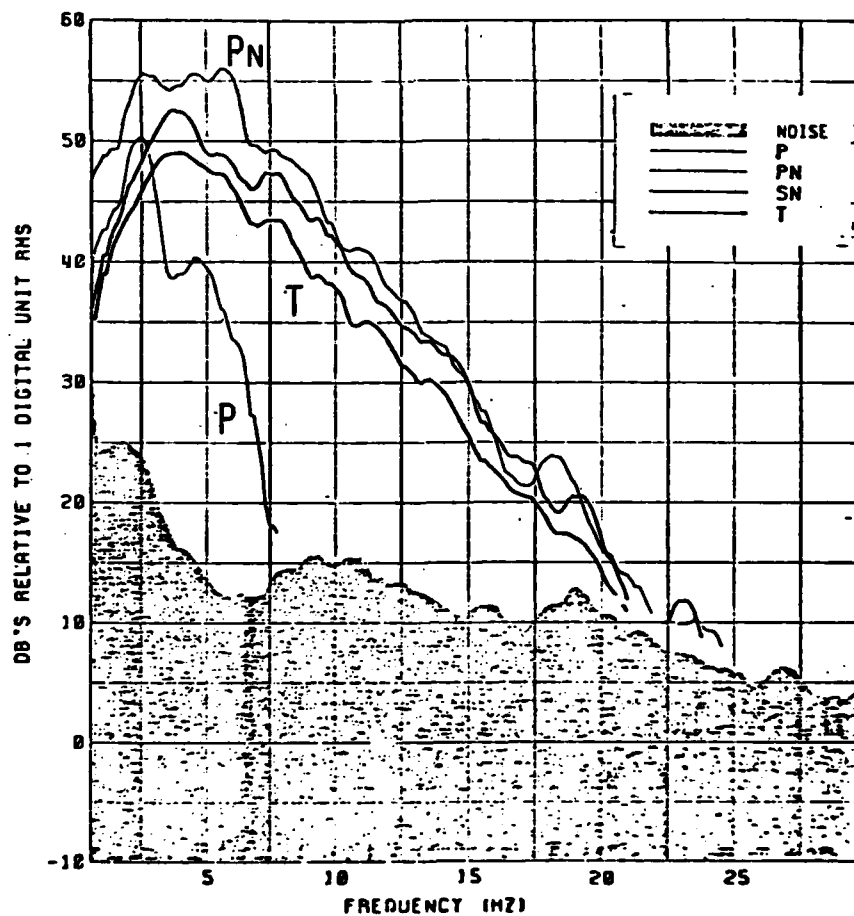
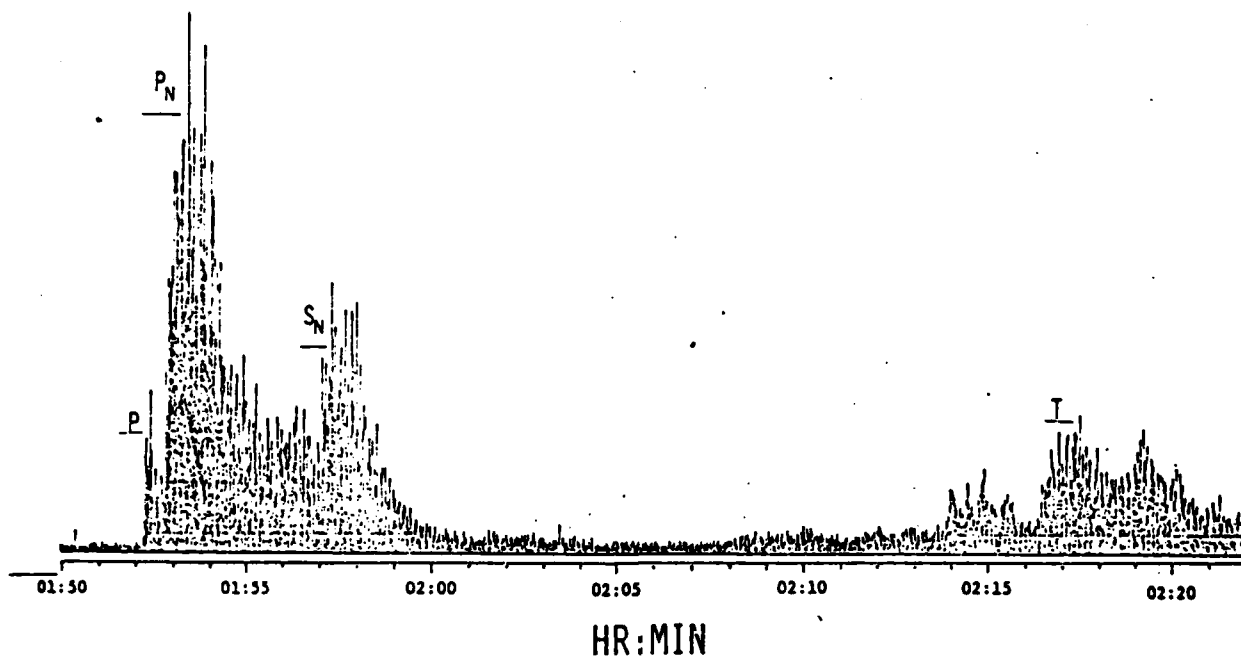
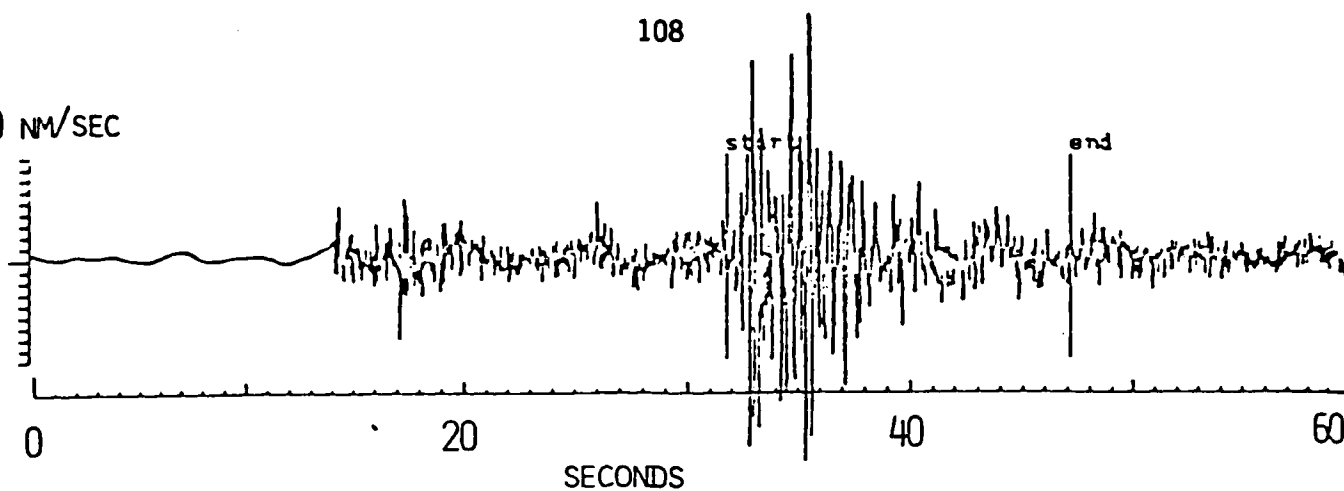


Figure 7. Earthquake south of Honshu recorded on WHA Bottom Phone 74,  $\Delta=25.2^\circ$ ,  $h=167$  km,  $m_b=6.6$ .

1000 NM/SEC



## LONG ISLAND SOUND

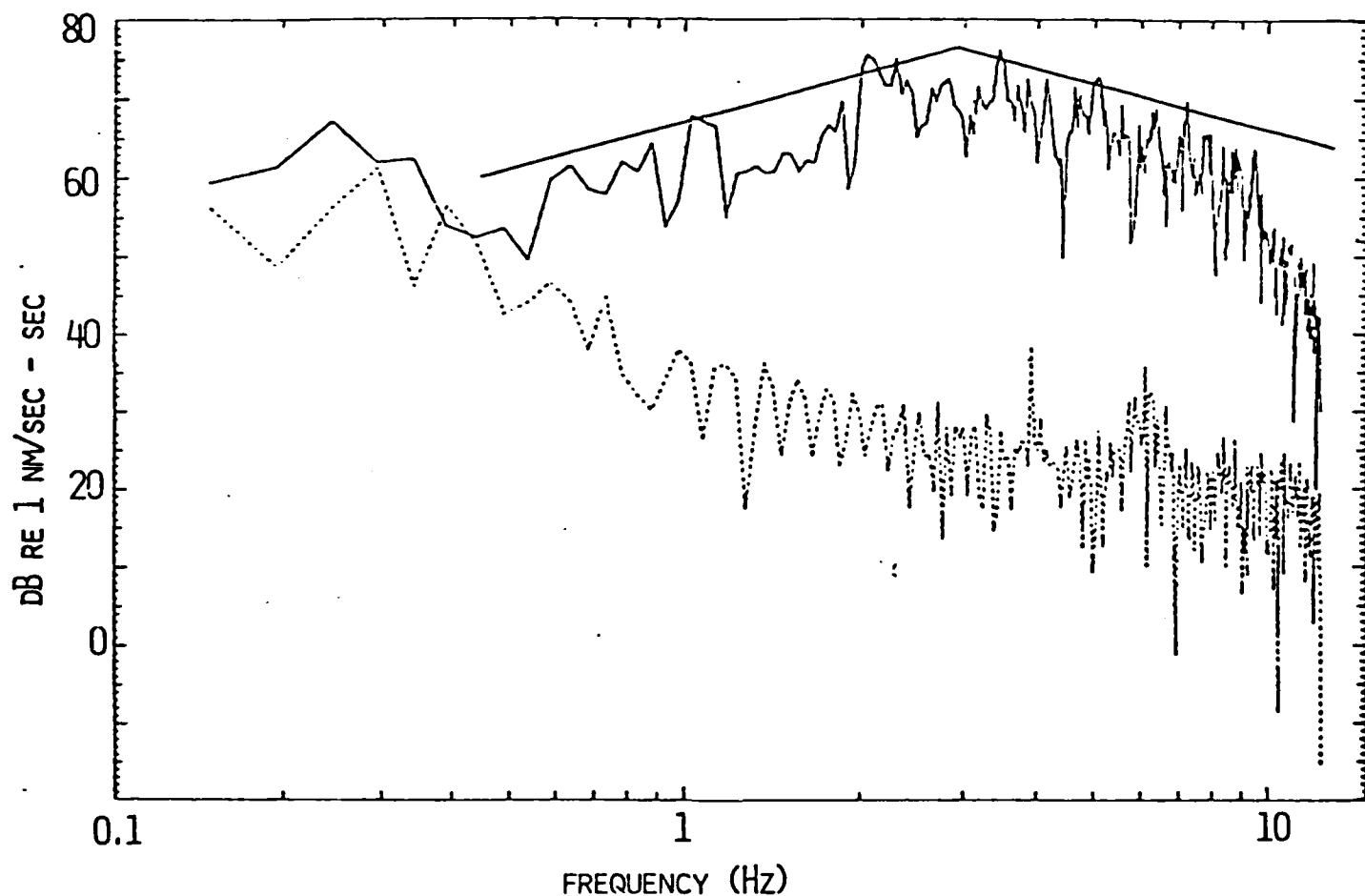
 $D = 1.4^\circ$  $M_B = 3.5$ 

Figure 8. Long Island Sound earthquake recorded at CSA ( $m_b = 3.5$ ,  $\Delta = 1.4^\circ$ ). Spectra are of noise before P, dashed, and S/Lg, between start and end marks on the record. Lines are  $\pm 6$  dB/octave.

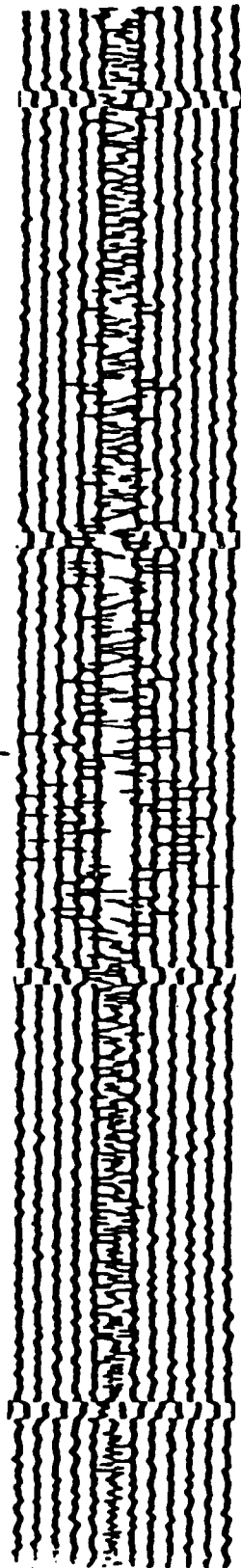


ALF  $\Delta = 13.59^\circ$ 

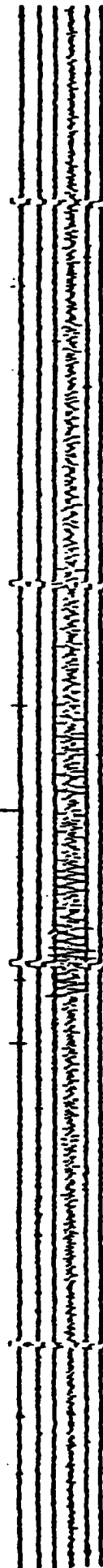
3.4 km/sec

ATL  $\Delta = 14.1^\circ$ 

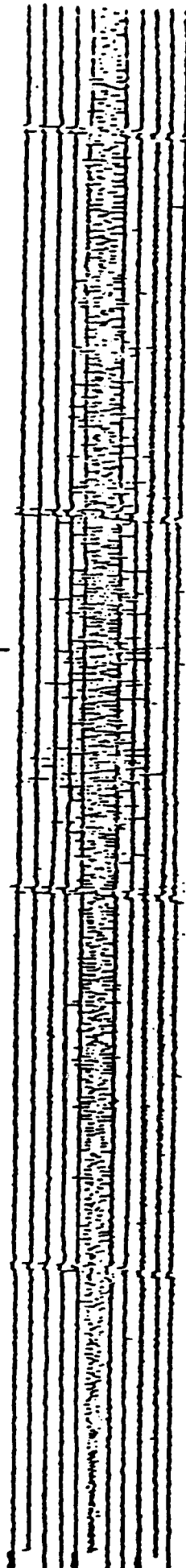
3.4 km/sec

HNY  $\Delta = 14.98^\circ$ 

3.4 km/sec

CTR  $\Delta = 15.43^\circ$ 

3.4 km/sec

OGD  $\Delta = 16.224$ 

3.4 km/sec

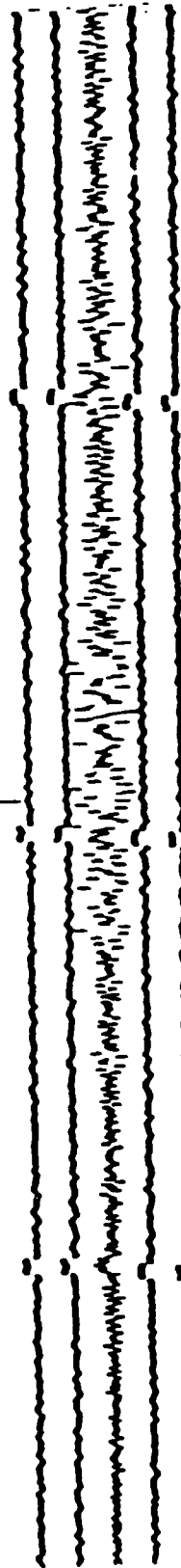


Figure 9. Short period recordings of eastern North America event at five different stations showing the predominance of energy centered at 3.5 km/sec (Lg).

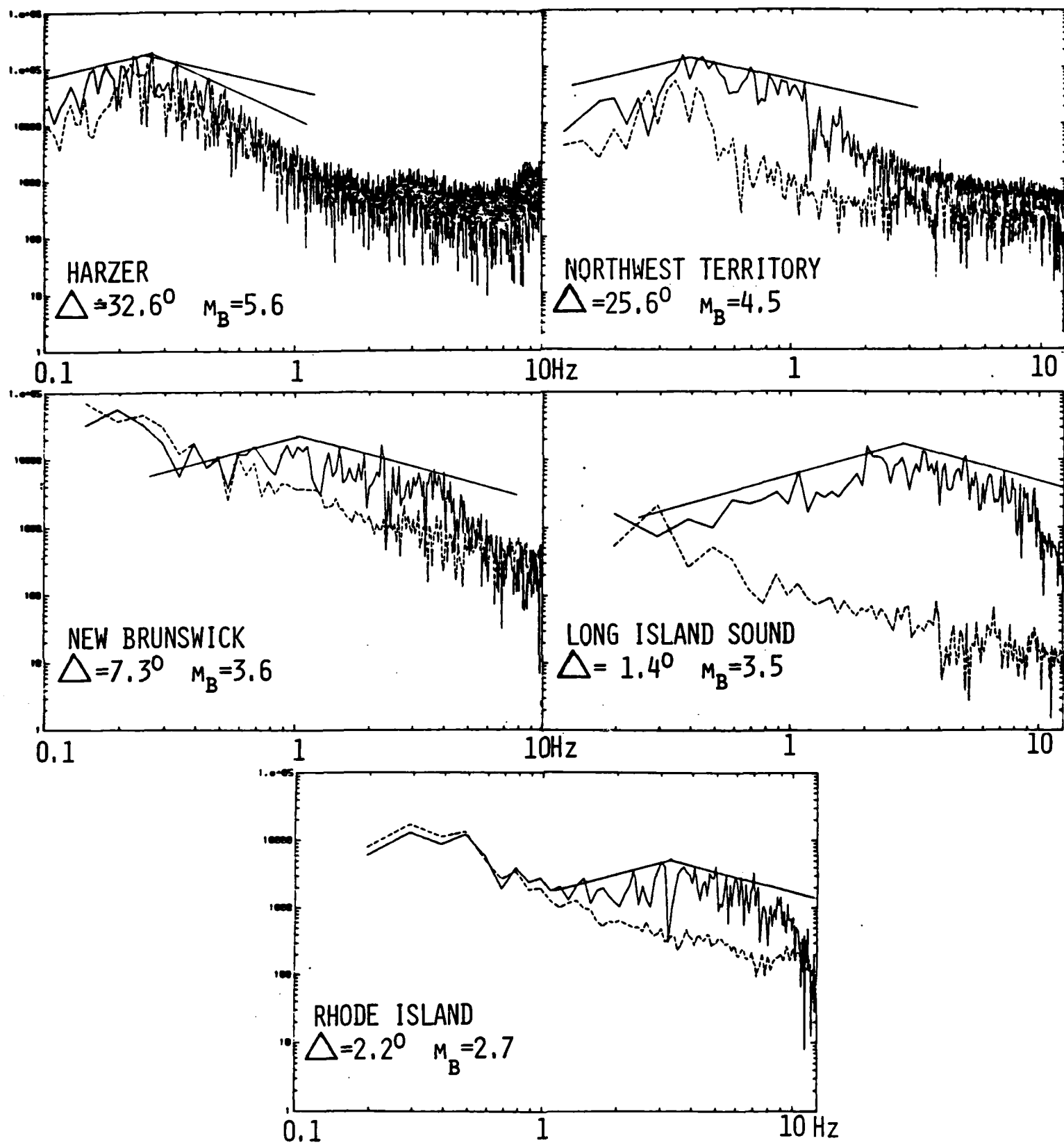


Figure 10. Vertical ground velocity spectra (relative amplitudes); straight lines are  $\pm 6$  dB/oct (equivalent to 0 and -12 dB/oct in displacement) and -12 dB/oct for Harzer recorded at CSA.

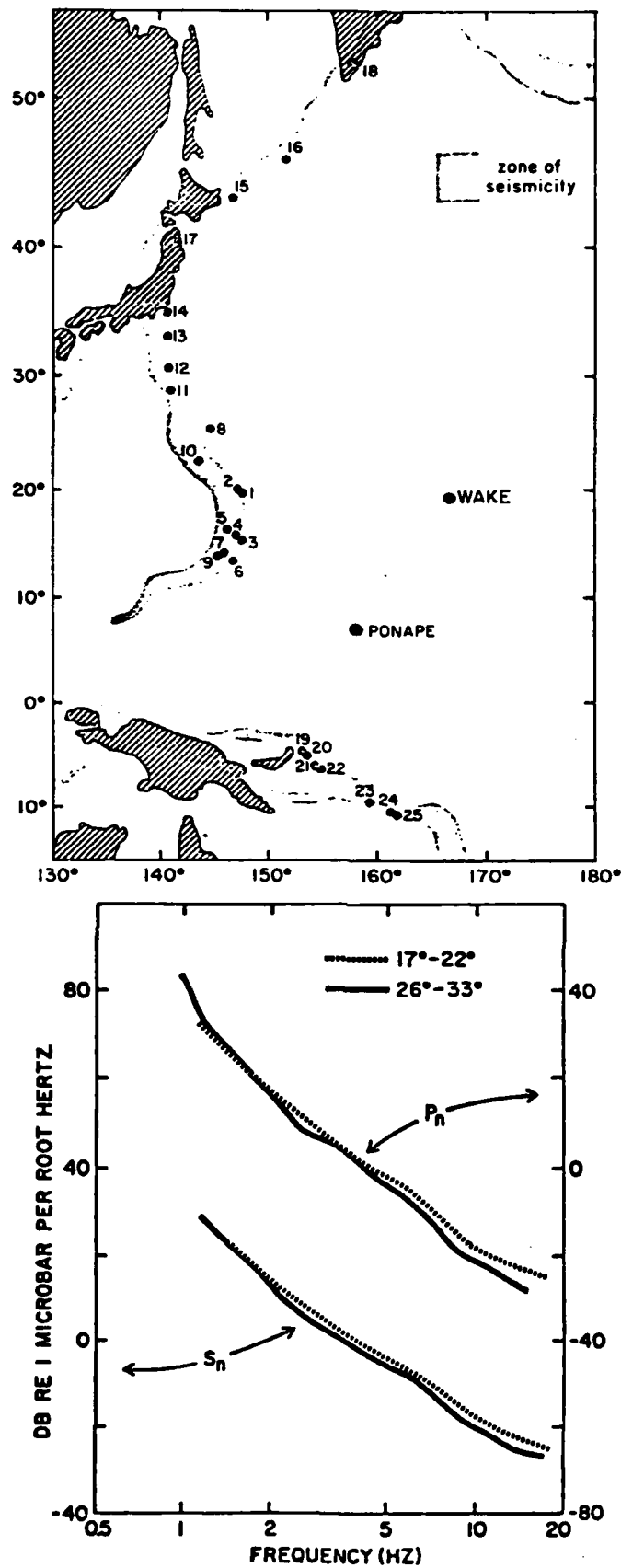


Figure 11. Upper, locations of earthquake used by Walker et al., 1983, in studies of P<sub>n</sub> and S<sub>n</sub>. All sources discussed here are north of Ponape. Lower, averaged spectra for P<sub>n</sub> and S<sub>n</sub> in two distance ranges.

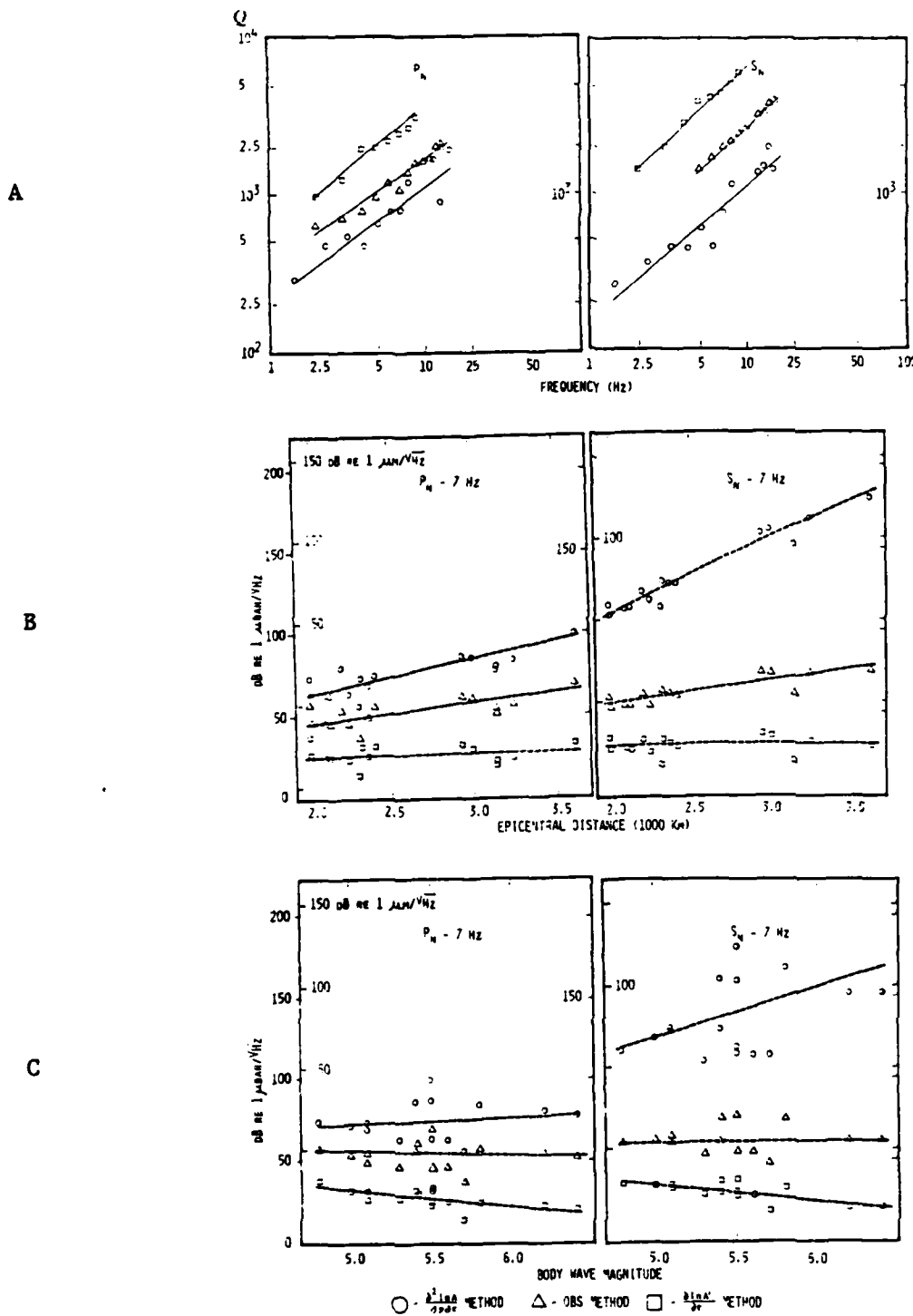


Figure 12. A,  $Q$  as a function of frequency from  $P_n$  and  $S_n$  by three methods; B and C, apparent source strength at 7 Hz,  $\Delta=100$  km and  $m_b=5.0$  versus observed distance and magnitude; a reliable estimate of  $Q$  should show no dependence on distance or magnitude.

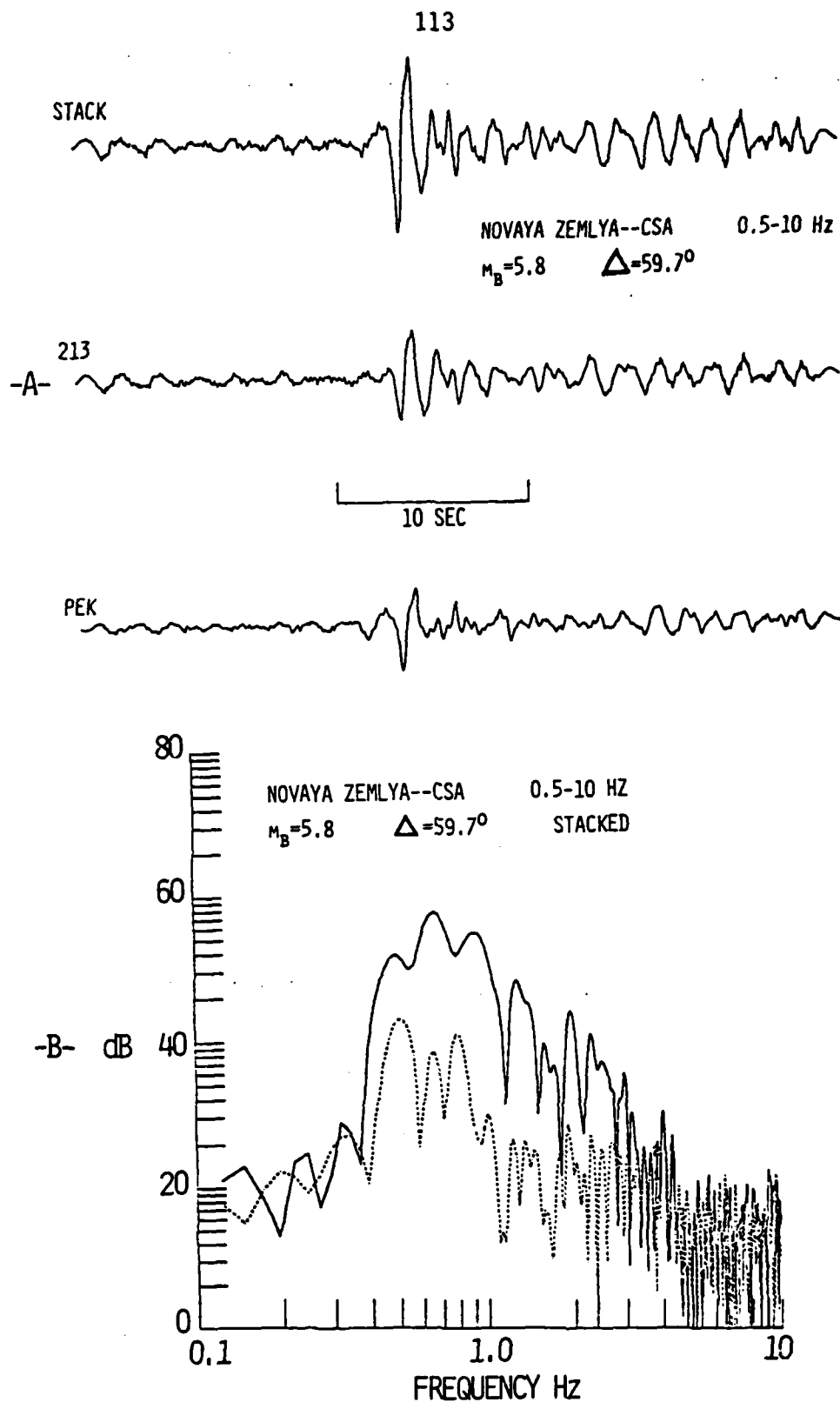
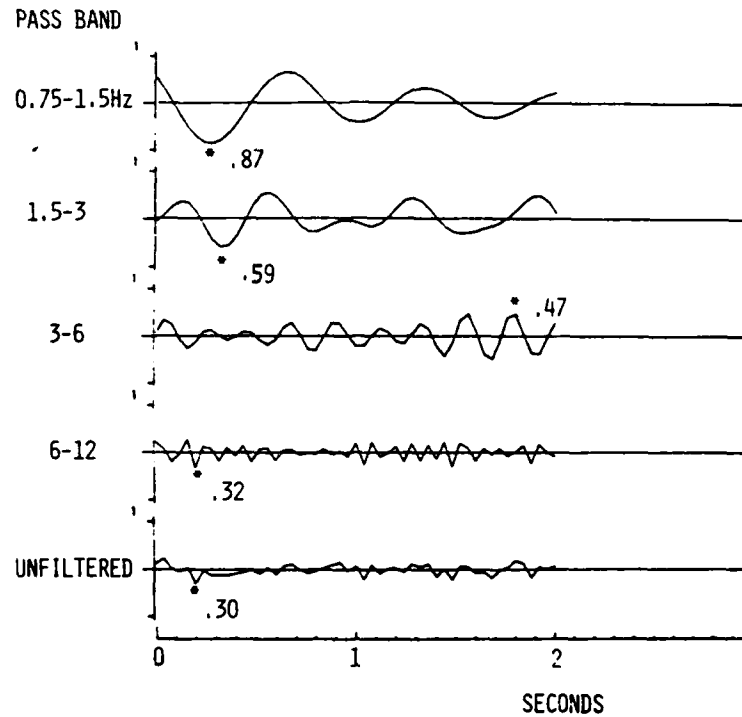


Figure 13. P wave from Novaya Zemlya recorded at CSA, filtered 0.5-10 Hz band-pass: A-Individual and stacked (delay sum) verticals; B-Relative particle velocity spectrum of stacked verticals, prefiltered 0.5-10 Hz; dashed spectrum is noise level before P.

A

## CROSS CORRELATION-RANDOM NOISE



B

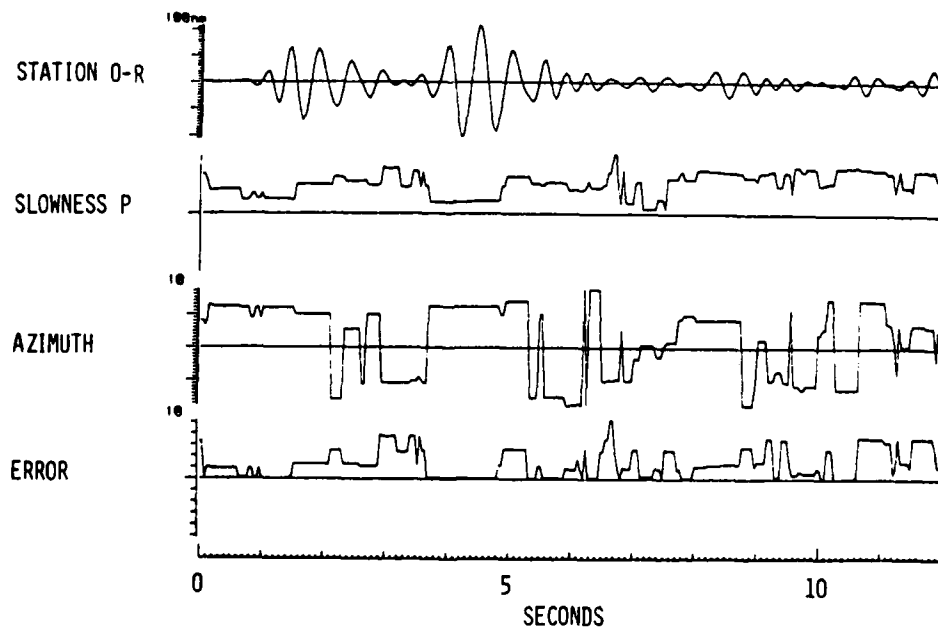
LONG ISLAND P-WAVE BEAM FORMING  
1.5-3 Hz BAND PASS

Figure 14. A, cross-correlation between two, two second samples of random noise, in octave bands and wide band (to 12.5 Hz); B, output of automatic beam-forming program from Long Island Sound P wave at CSA.

STATIONS

FREQUENCY (Hz)

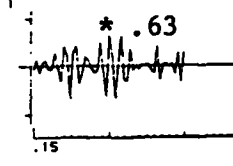
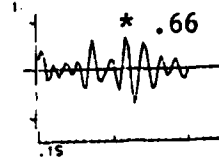
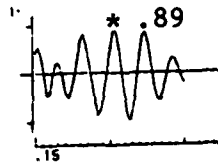
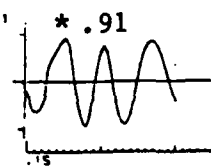
0.75-1.5

1.5-3

3-6

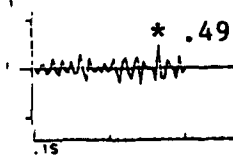
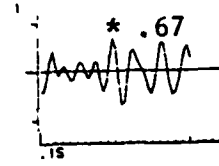
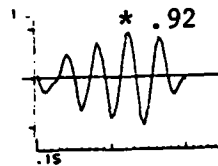
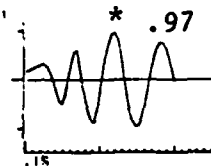
6-12

Z

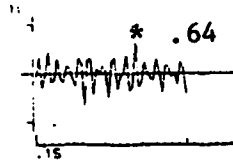
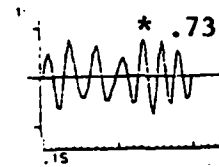
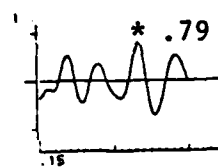
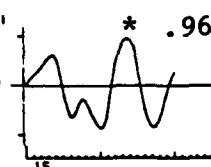


1-2

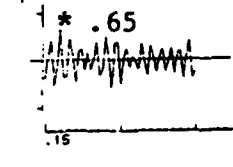
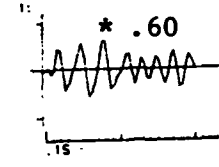
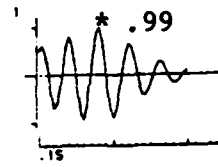
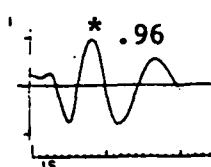
R



T

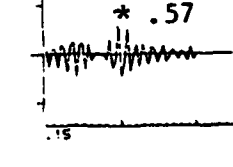
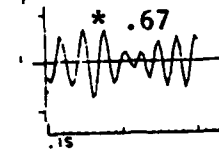
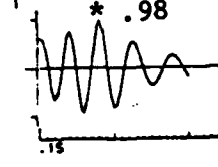


Z

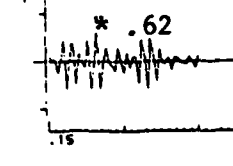
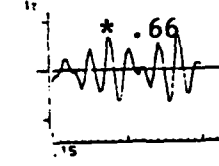
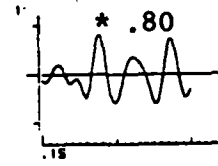
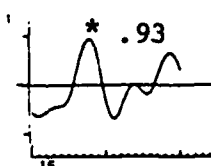


1-0

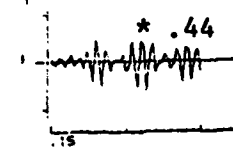
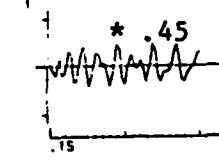
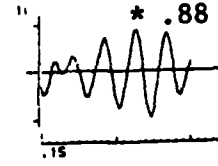
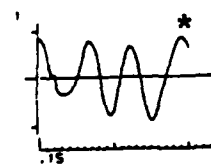
R



T

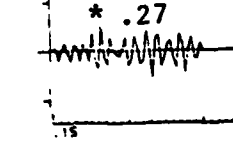
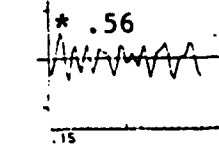
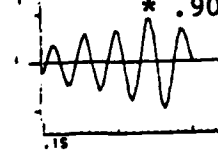
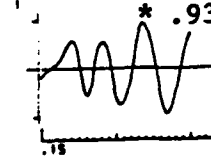


Z



0-2

R



T

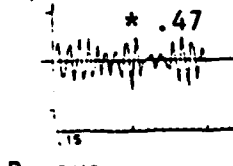
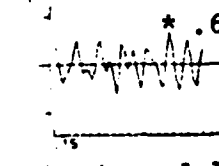
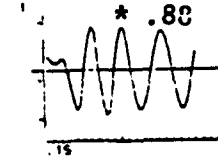
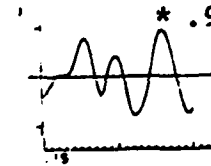


Figure 15. CSA cross-correlation in octave bands, Long Island P wave.

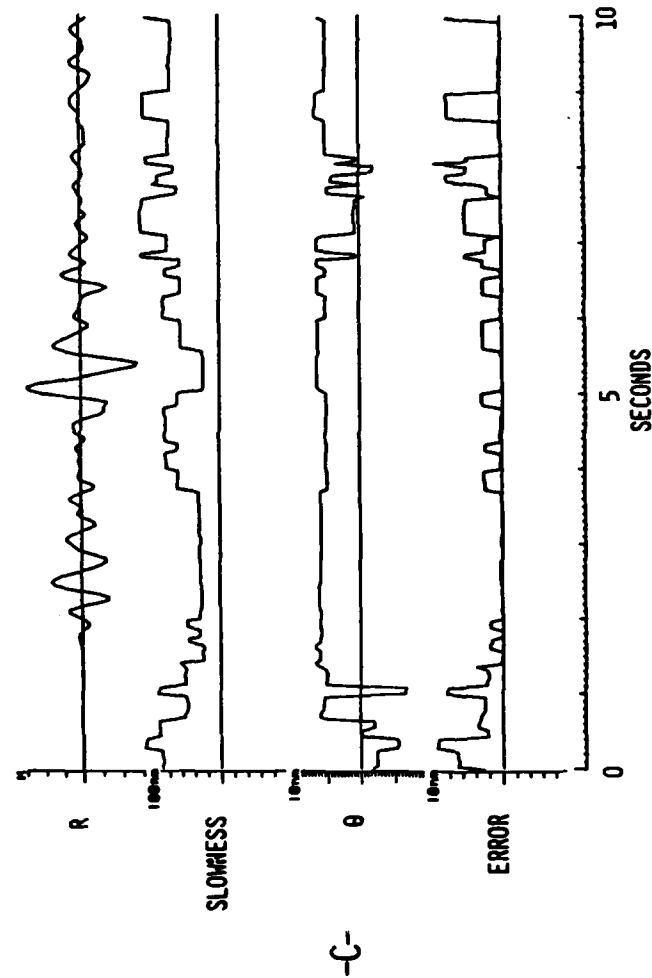
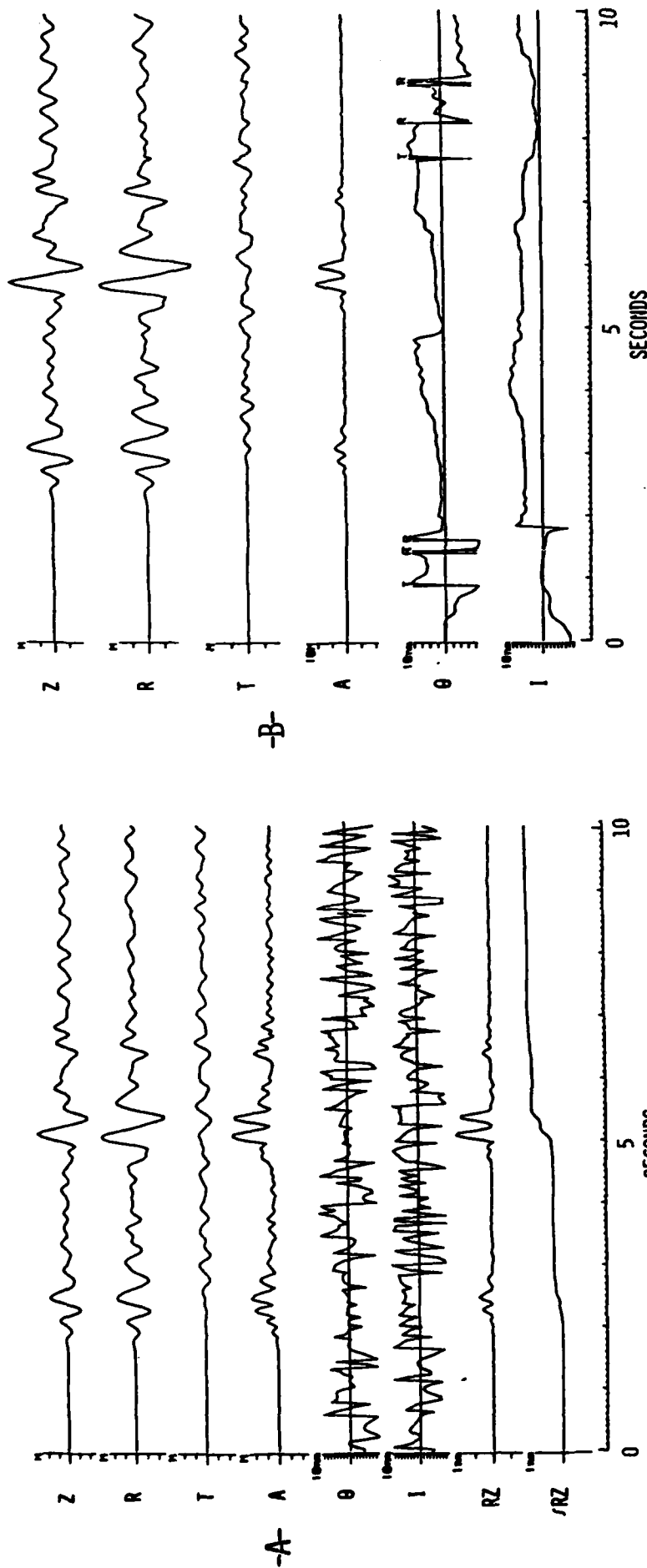


Figure 16. Long Island Sound P wave recorded at CSA. A, instantaneous polarization filtering; B, adaptive polarization filtering; C, tripartite beam-forming. Trace identifications: Z=vertical; R and T=horizontal radial and transverse to great circle path;  $A = (Z^2 + R^2 + T^2)^{1/2}$ ;  $\theta$ =particle azimuth; I=apparent angle of incidence between radial and vertical traces; RZ=product of R and Z traces;  $\int RZ$ =integral of the trace above.



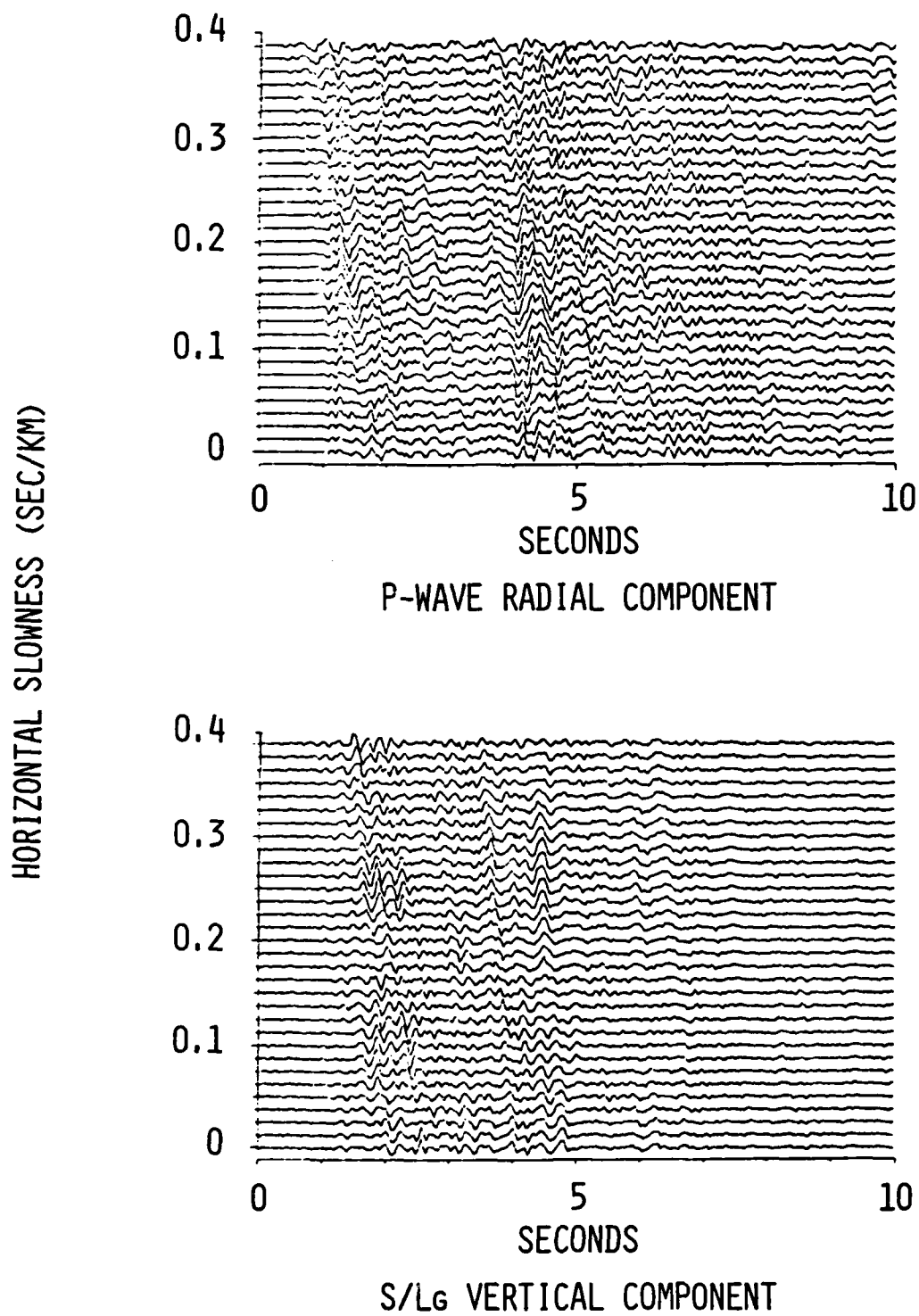


Figure 17. Slowness stack of Long Island Sound earthquake P wave, upper, and S/Lg, lower.

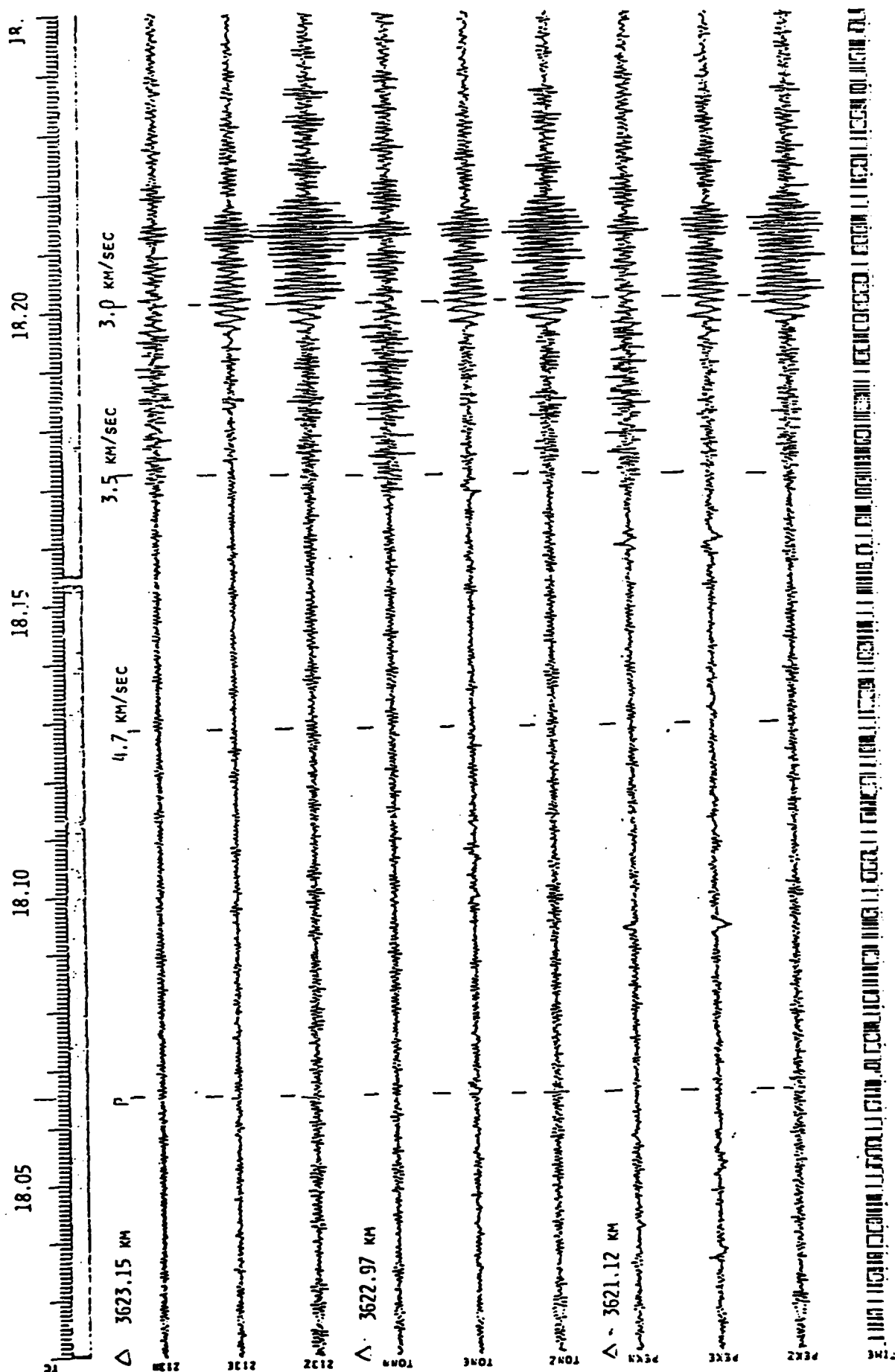
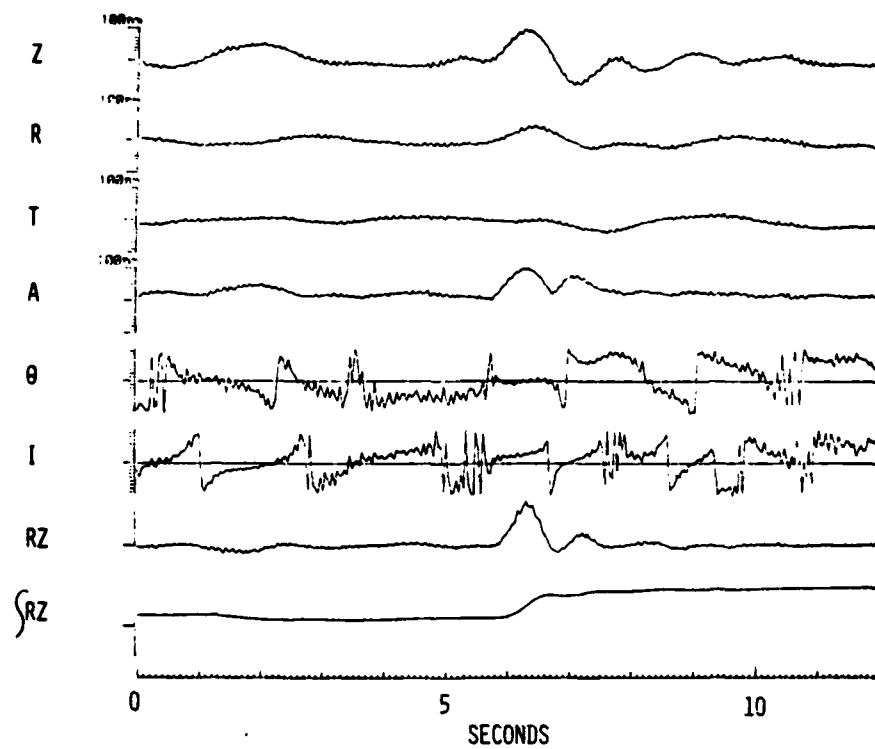
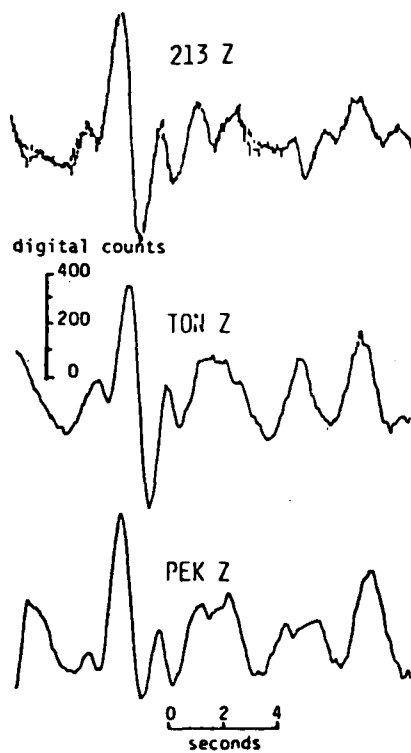
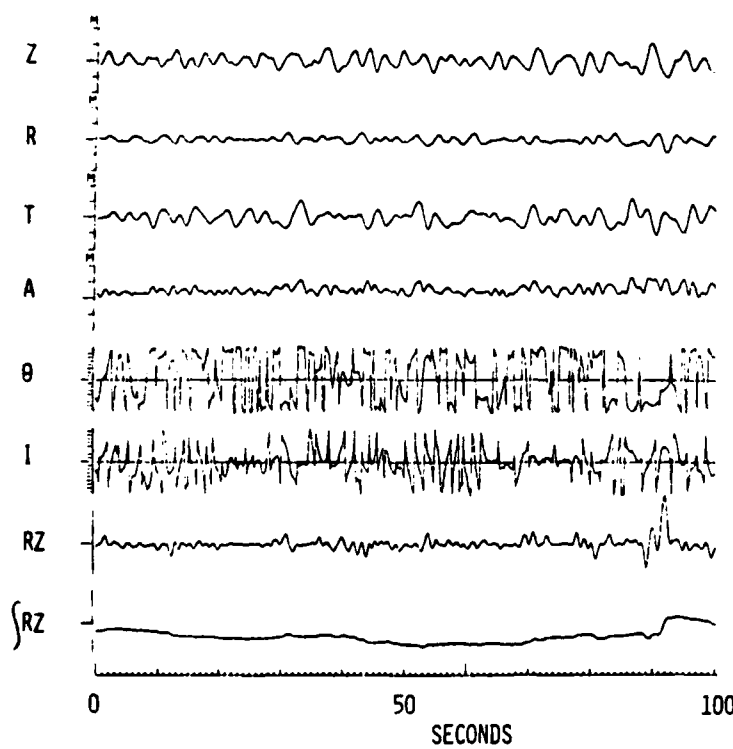


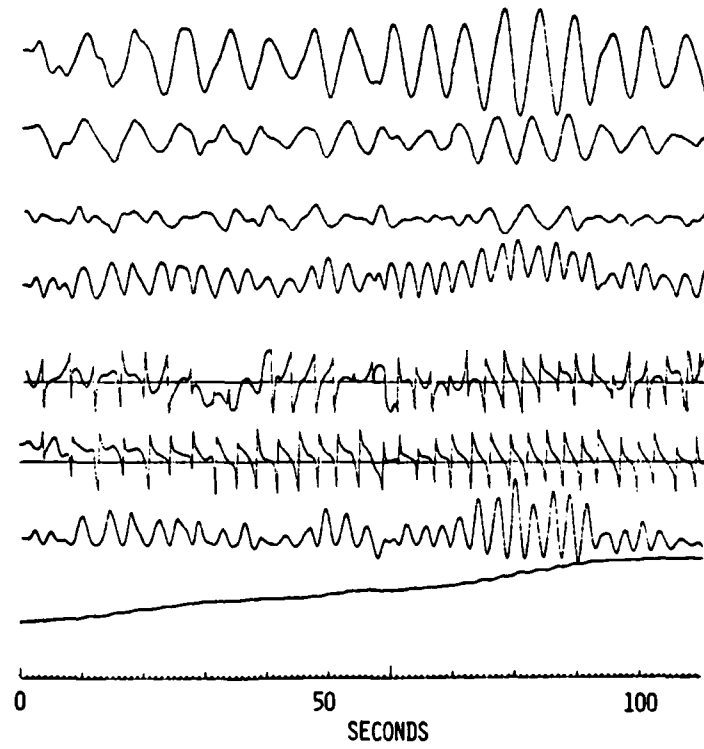
Figure 18. CSA wide-band records of NTS explosion HARZER,  $\Delta=32.6^\circ$ ,  $m_b=5.6$ .



HARZER P WAVE



HARZER Lg



HARZER LR

Figure 19. Unfiltered vertical component of P from Harzer at CSA stations, upper left, and outputs from polarization filtering program for P, Lg, and LR, as indicated. Scales for  $\Theta$  and I,  $10^0$ /division; amplitude scales, 100nm/sec. Trace identifications as in Figure 16.

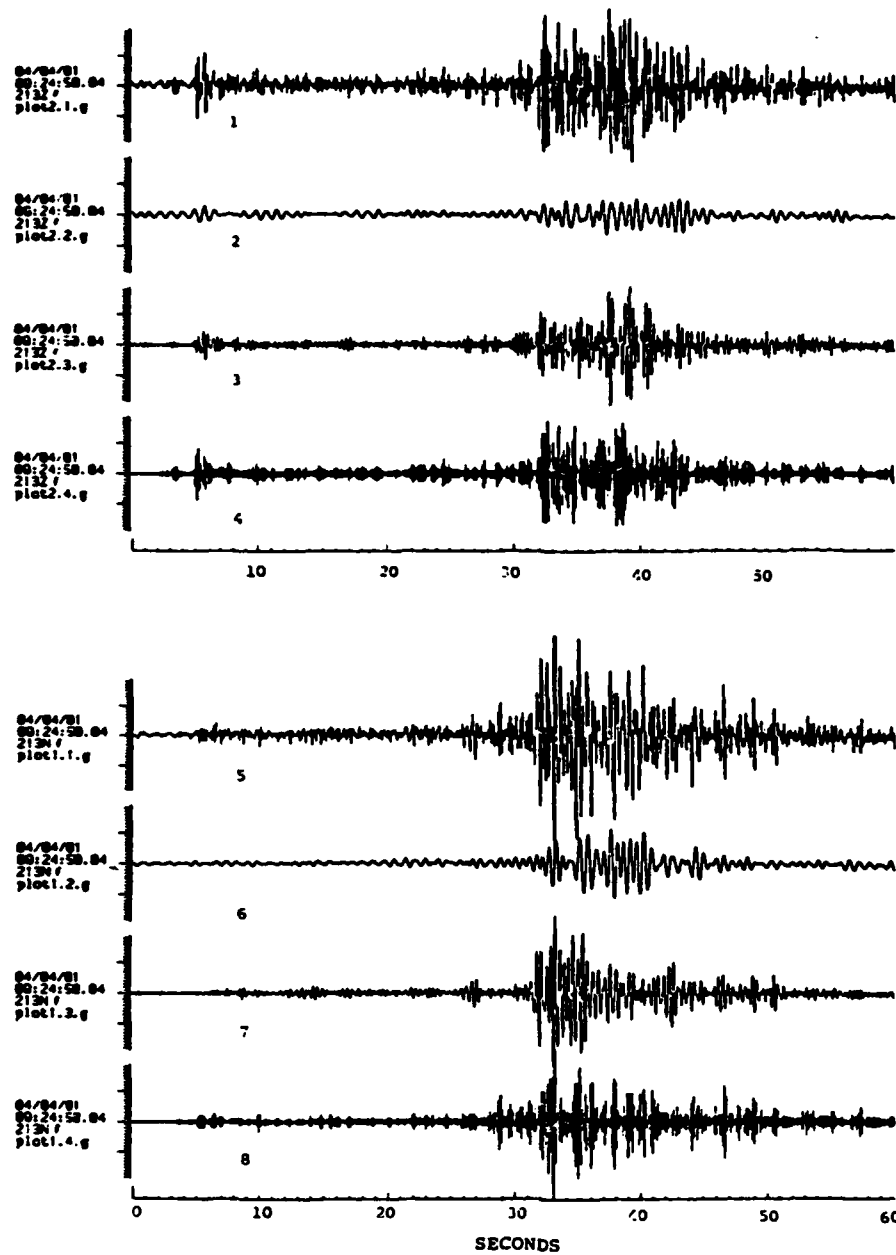


Figure 20. Catskill Seismic Array (CSA) seismograms from Rhode Island earthquake (4/4/81,  $m_s=2.7$ ,  $\Delta=2.2^\circ$ ) recorded at station 213: traces 1 through 4, vertical component band pass filtered 1-8, 1-2, 2-4, and 4-8 Hz, respectively; traces 5 through 8, N-S (transverse) component band pass filtered 1-8, 1-2, 2-4, and 4-8 Hz, respectively. All filters are zero phase 3-pole Butterworth.

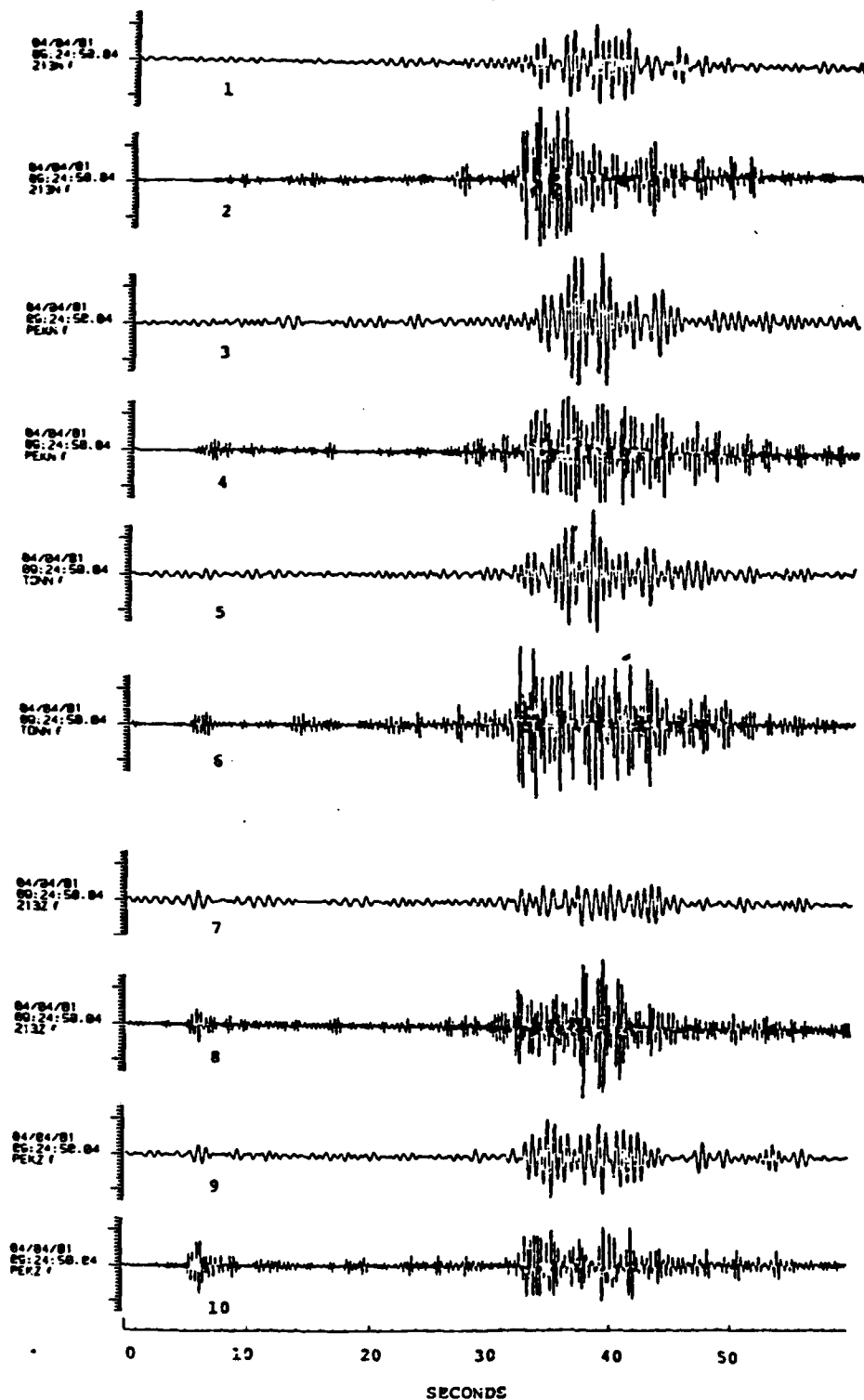


Figure 21. CSA seismograms from Rhode Island earthquake with alternating 1-2 and 2-4 Hz band pass filtering; traces are from array elements: N-S (transverse) component, 1-2 station 213, 3-4 station peak, 5-6 station tongue; vertical component, 7-8 station 213, 9-10 station peak.

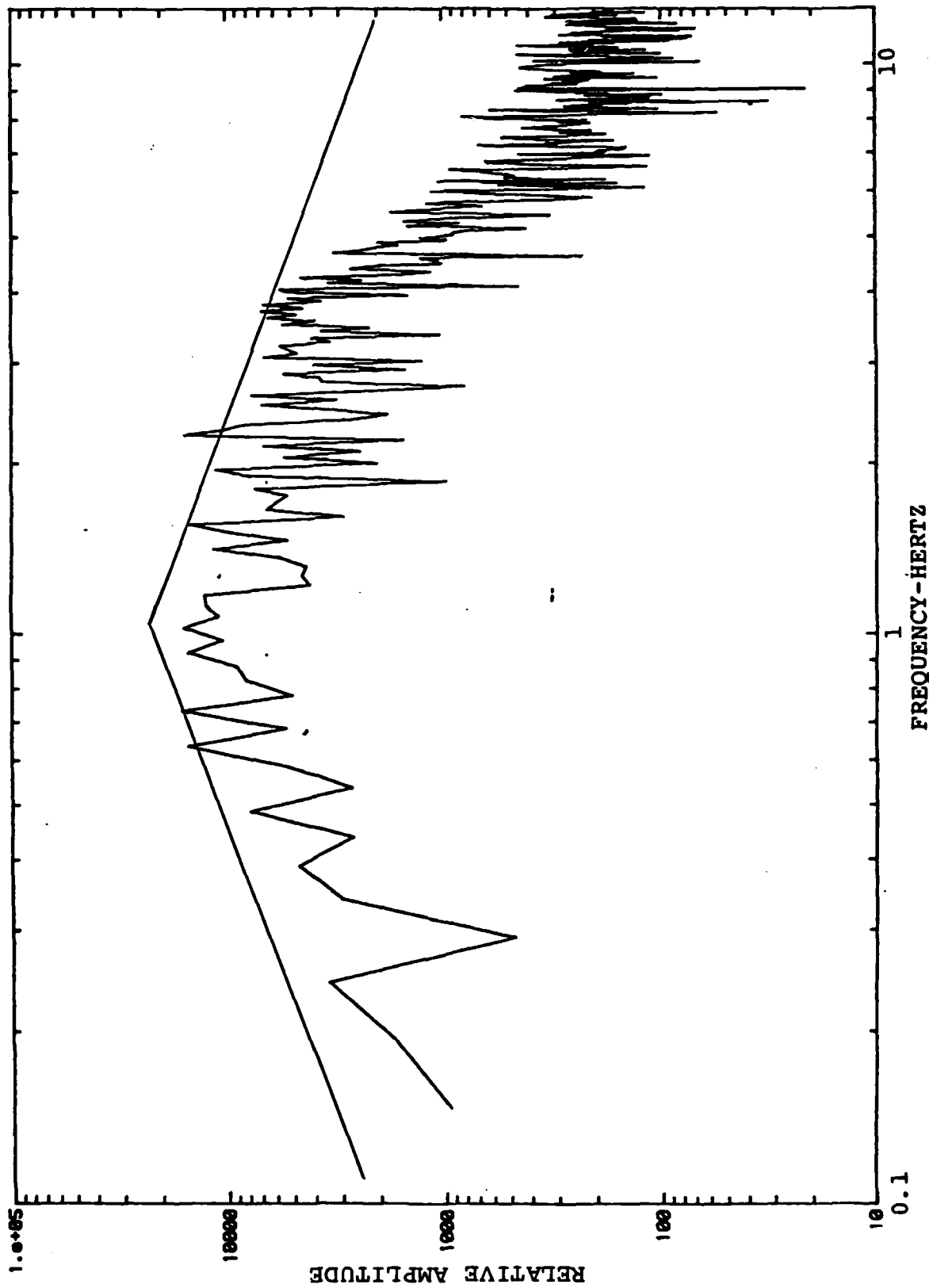


Figure 22. Vertical ground velocity spectrum from Lg of New Brunswick earthquake (4/13/81,  $m_b=3.6$ ,  $\Delta=7.3^\circ$ ) at station 213, pre-filtered 0.4 Hz high-pass; asymptotes are  $\pm 6$  dB per octave; portion of signal analyzed is indicated on seismogram.

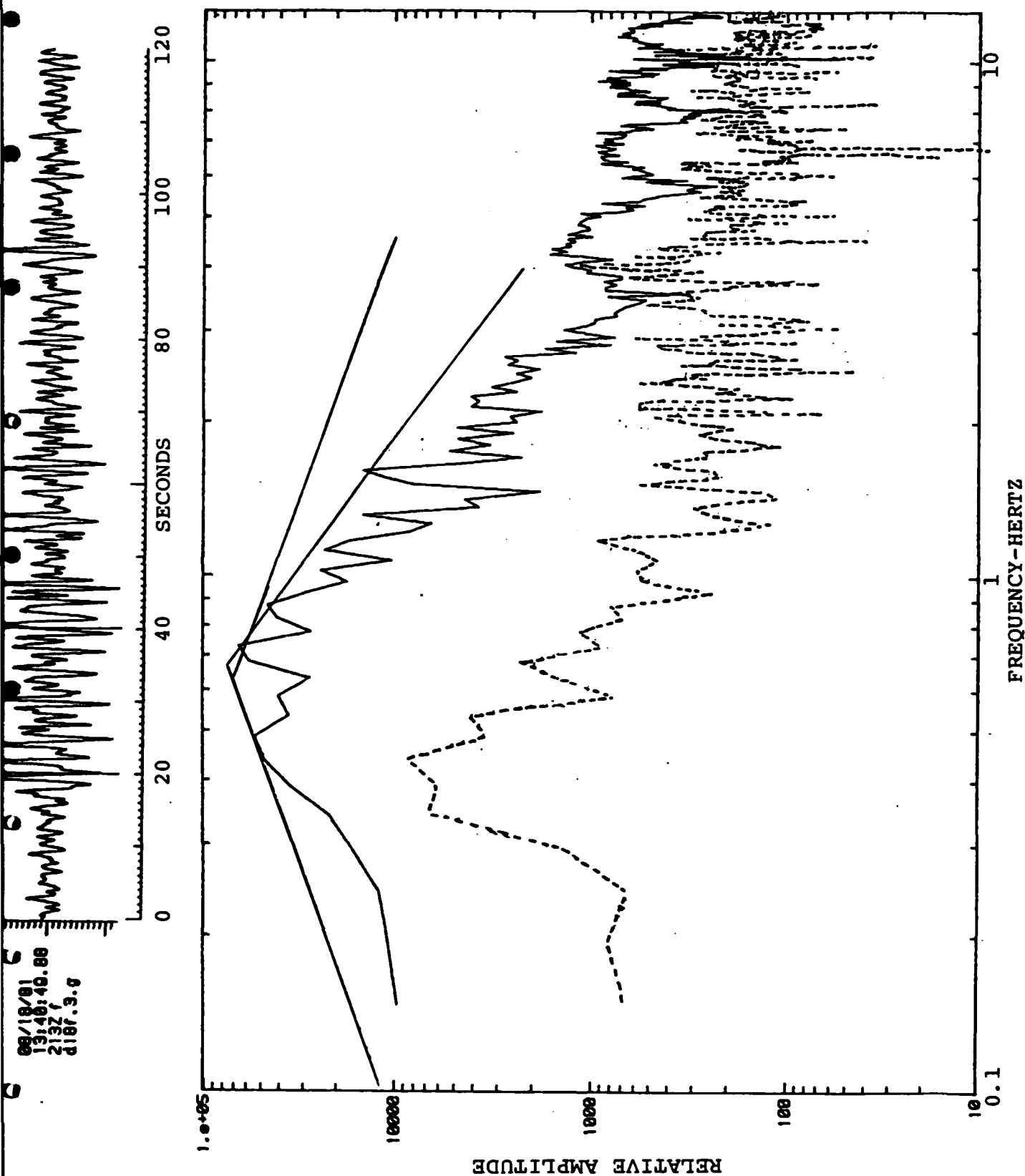


Figure 23. Vertical ground velocity spectrum from Lg of Northwest Territories earthquake (8/18/81,  $m_b=4.5$ ,  $\Delta=25.6^\circ$ ) at station 213, pre-filtered 0.4 Hz high-pass; dashed spectrum is noise before the P arrival; asymptotes are  $\pm 6$  dB and  $-12$  dB per octave; portion of signal analyzed is indicated on seismogram.

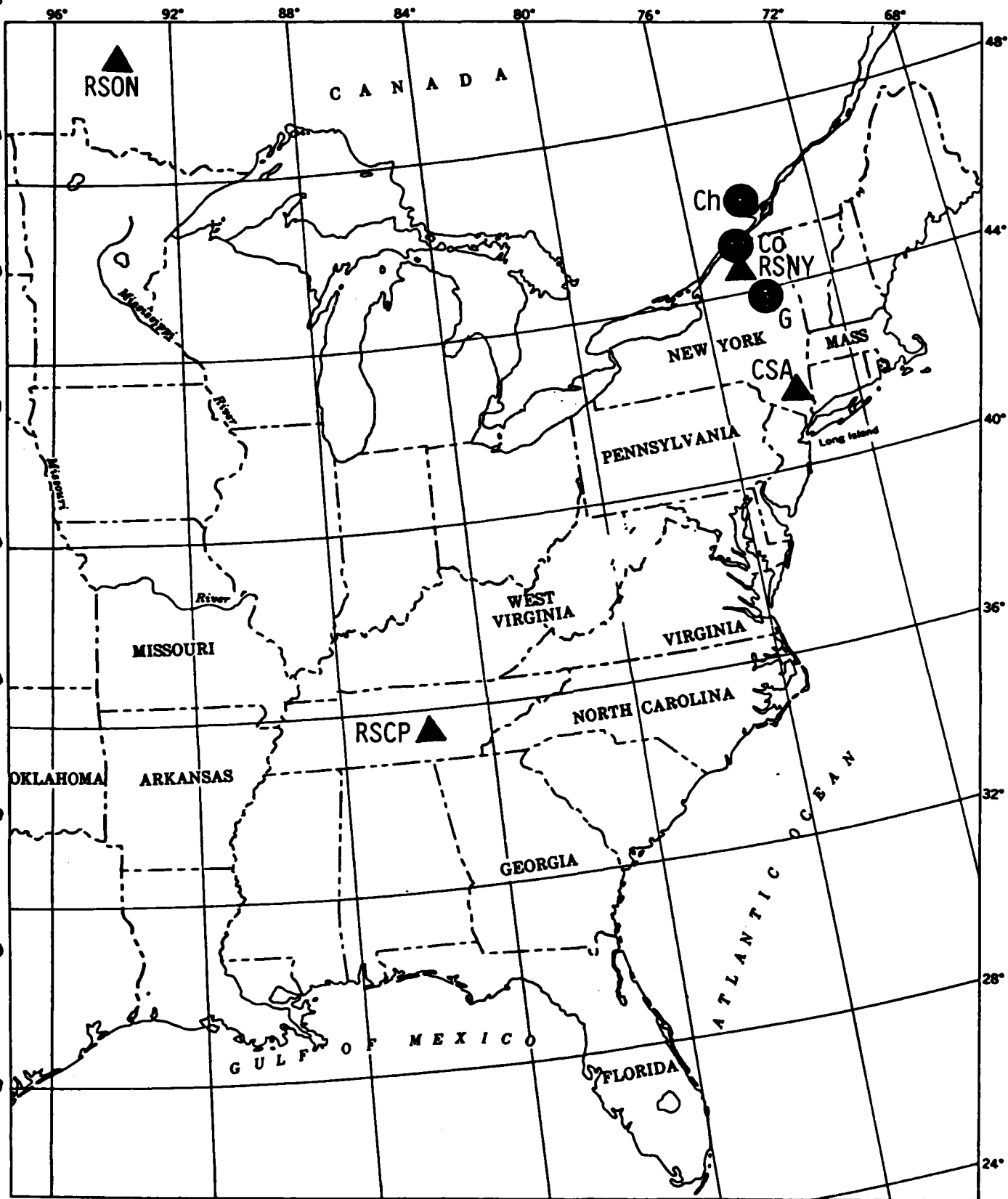


Figure 24. Locations of Goodnow, G, Chaneville, Ch, and Cornwall, Co, earthquakes; Regional Seismic Test Network, RSTN, seismic stations Adirondack, New York, RSNY, Cumberland Plateau, Tennessee, RSCP, and Red Lake, Ontario, RSON; and Catskill Seismic Array, CSA.



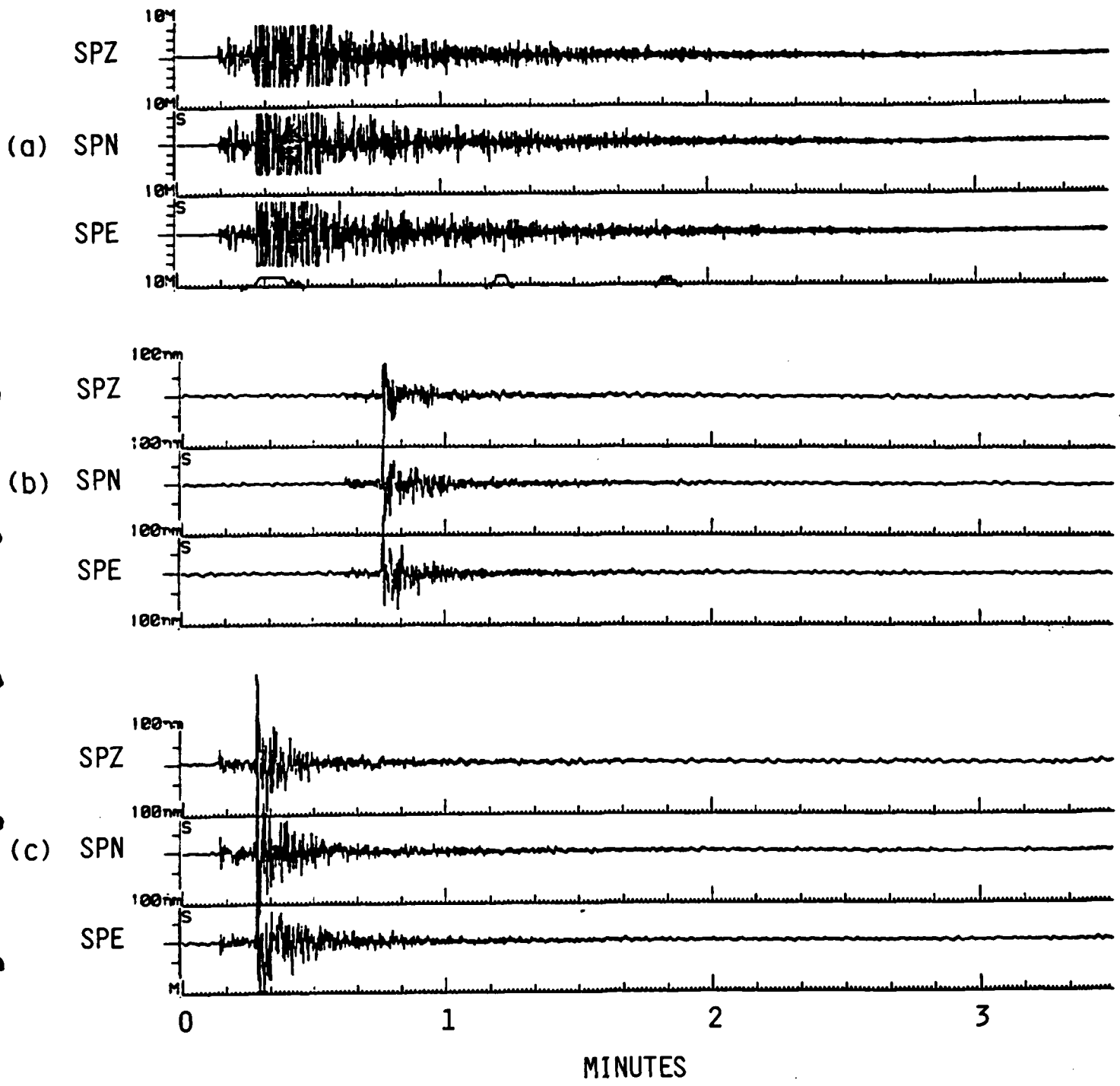


Figure 25. Goodnow earthquakes recorded at RSNY ( $\Delta=0.6^\circ$  (71 km),  $\Theta=162^\circ$ ): (a) 10/7/83,  $m_b Lg=5.2$ ; (b) 10/11/83,  $m_{bc}=2.9$ ; (c) 10/12/83,  $m_{bc}=3.1$ .

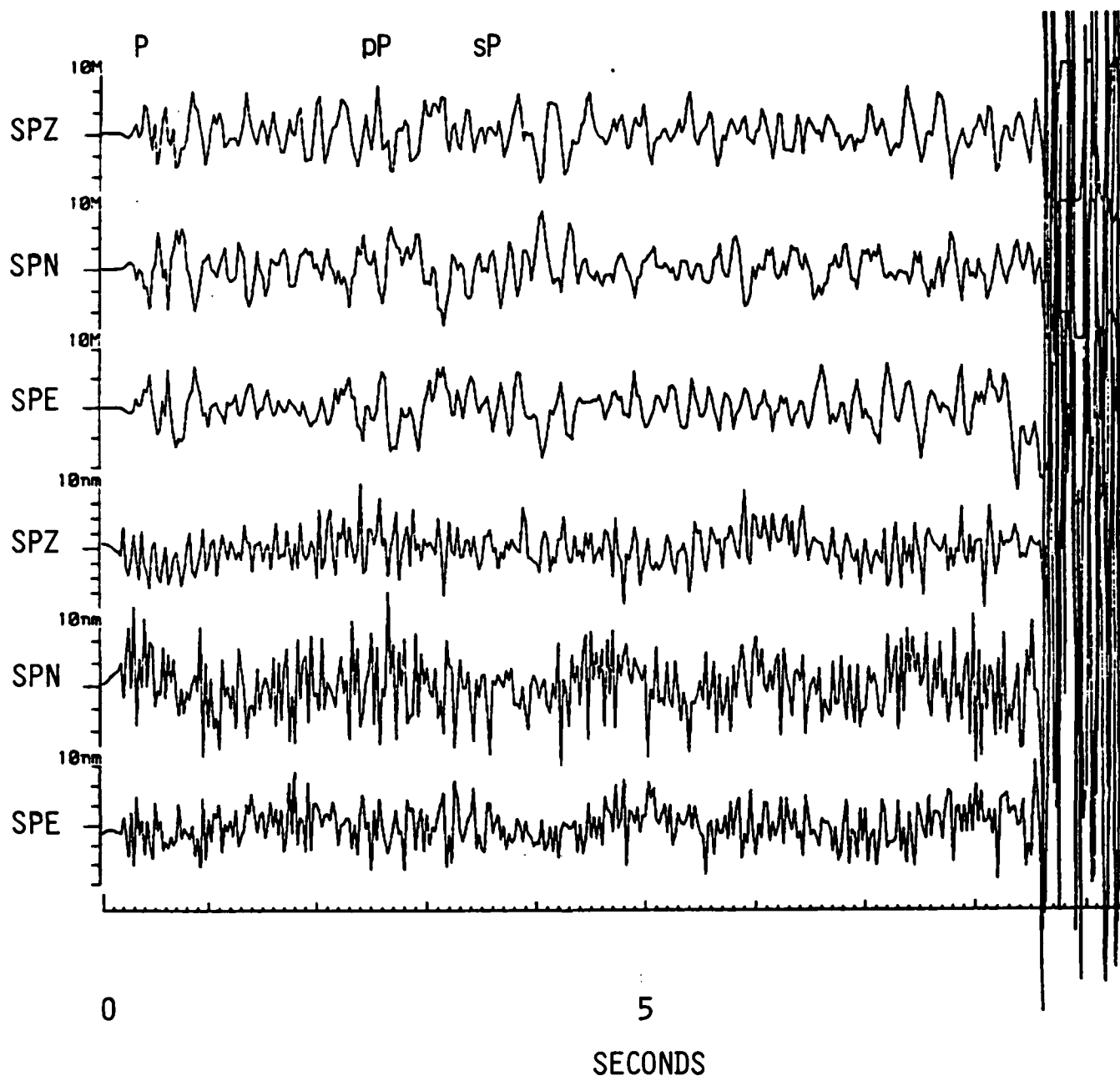


Figure 26. Goodnow earthquake P arrivals at RSNY: upper, 10/7/83; lower, 10/11/83. pP and sP are at approximate times for a 7 km focal depth.

## Fourier Spectrum (re units per Hz)

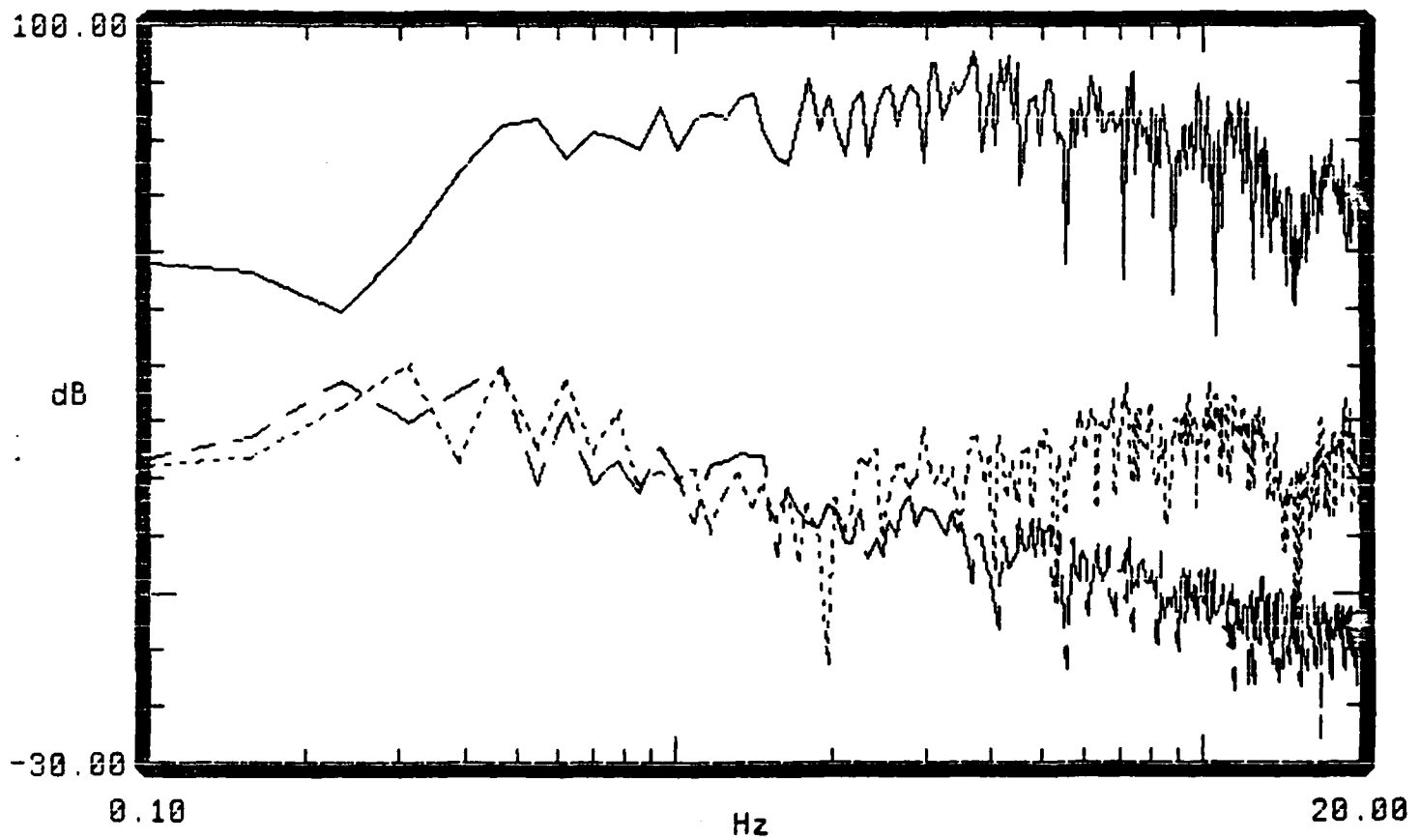


Figure 27. P wave spectra for Goodnow main shock, solid line; after shock, dotted line; and noise, dashed line.

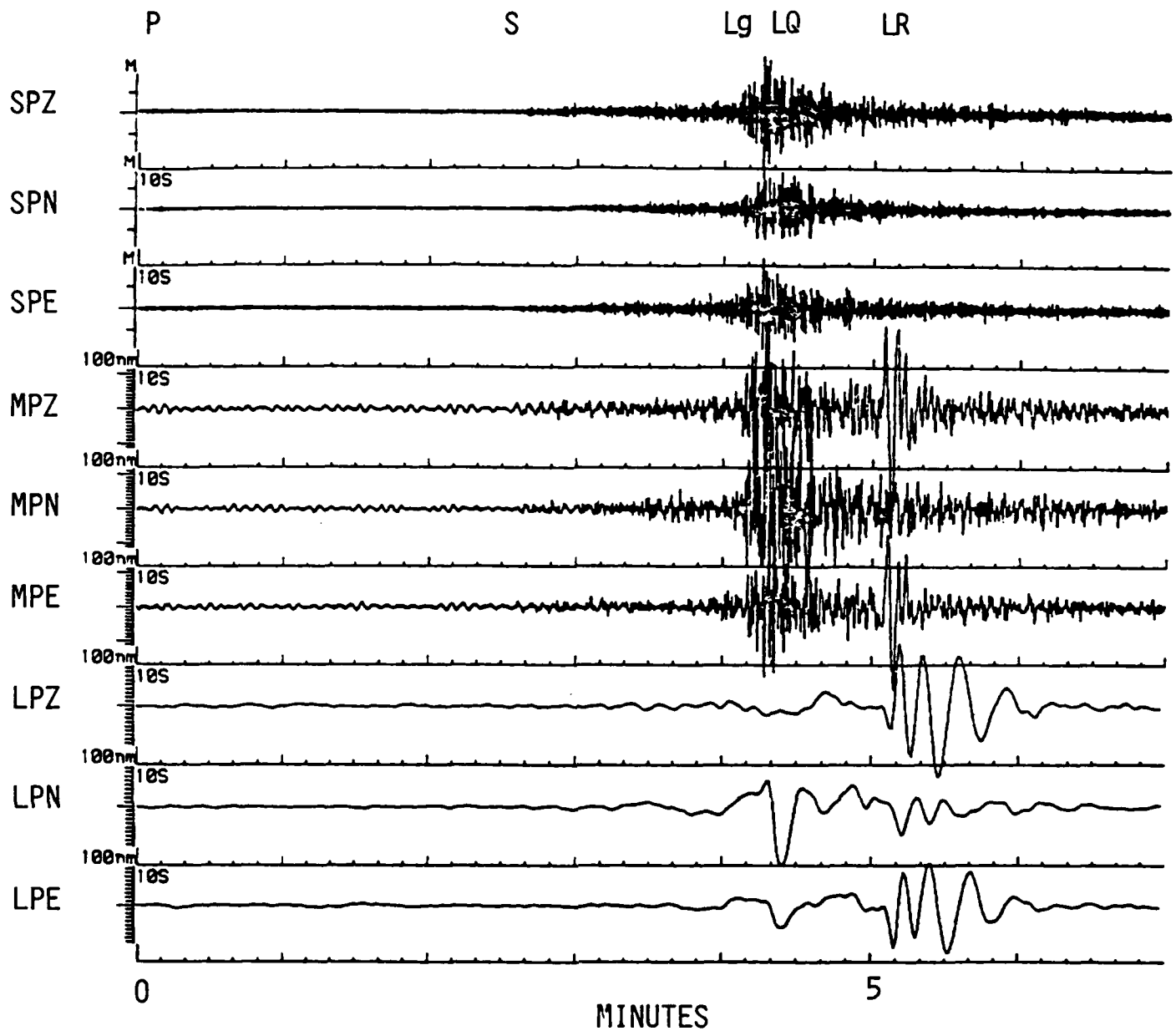


Figure 28. Goodnow earthquake, 10/7/83, recorded at RSON ( $\Delta=14.9^\circ$ ,  $\Theta=110^\circ$ ). Note LQ and RG on LP records and sedimentary Rayleigh waves on MP records.

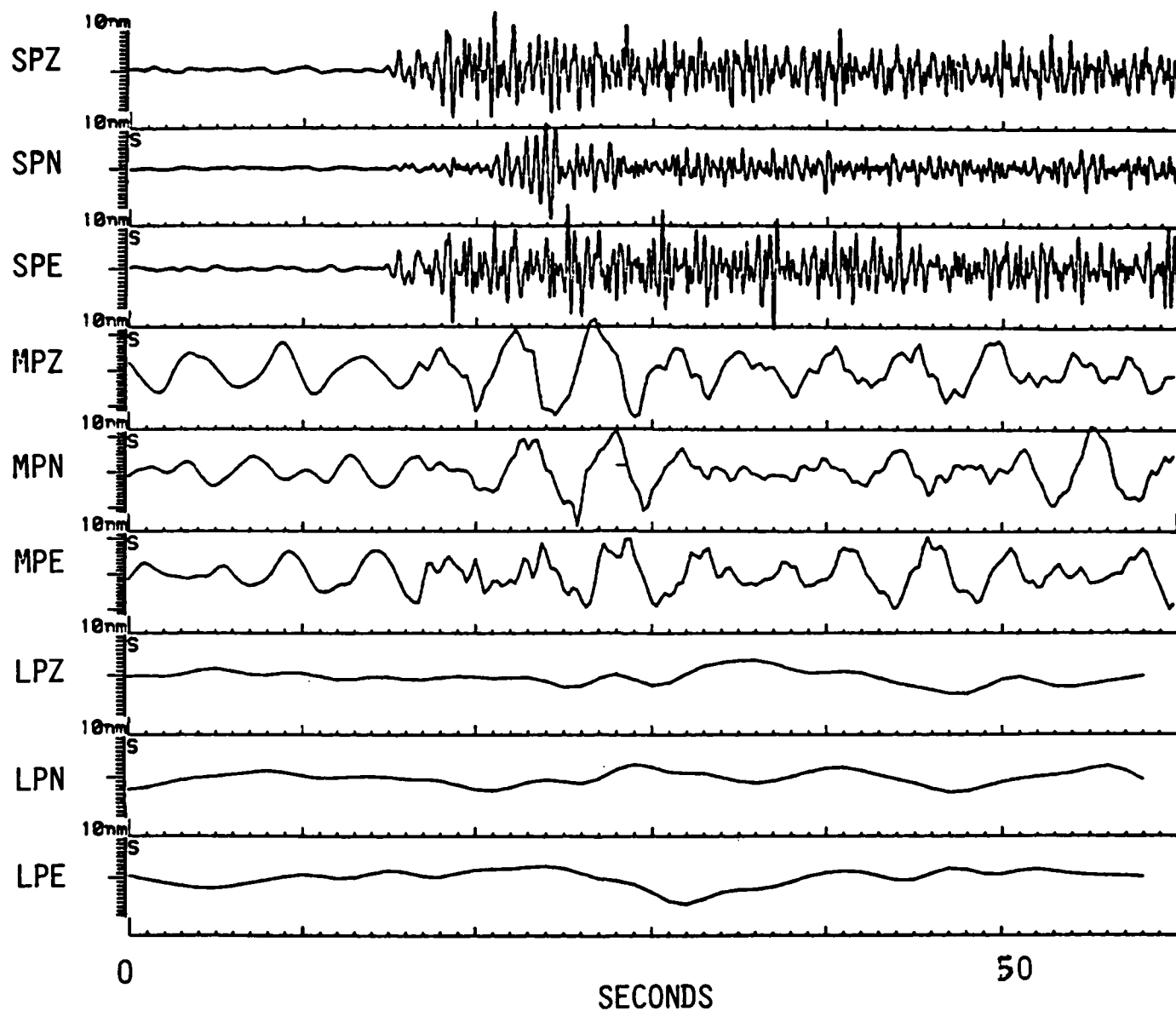


Figure 29. Goodnow earthquake P arrivals at RSON. Arrival about 3 sec after beginning is a candidate for sP.

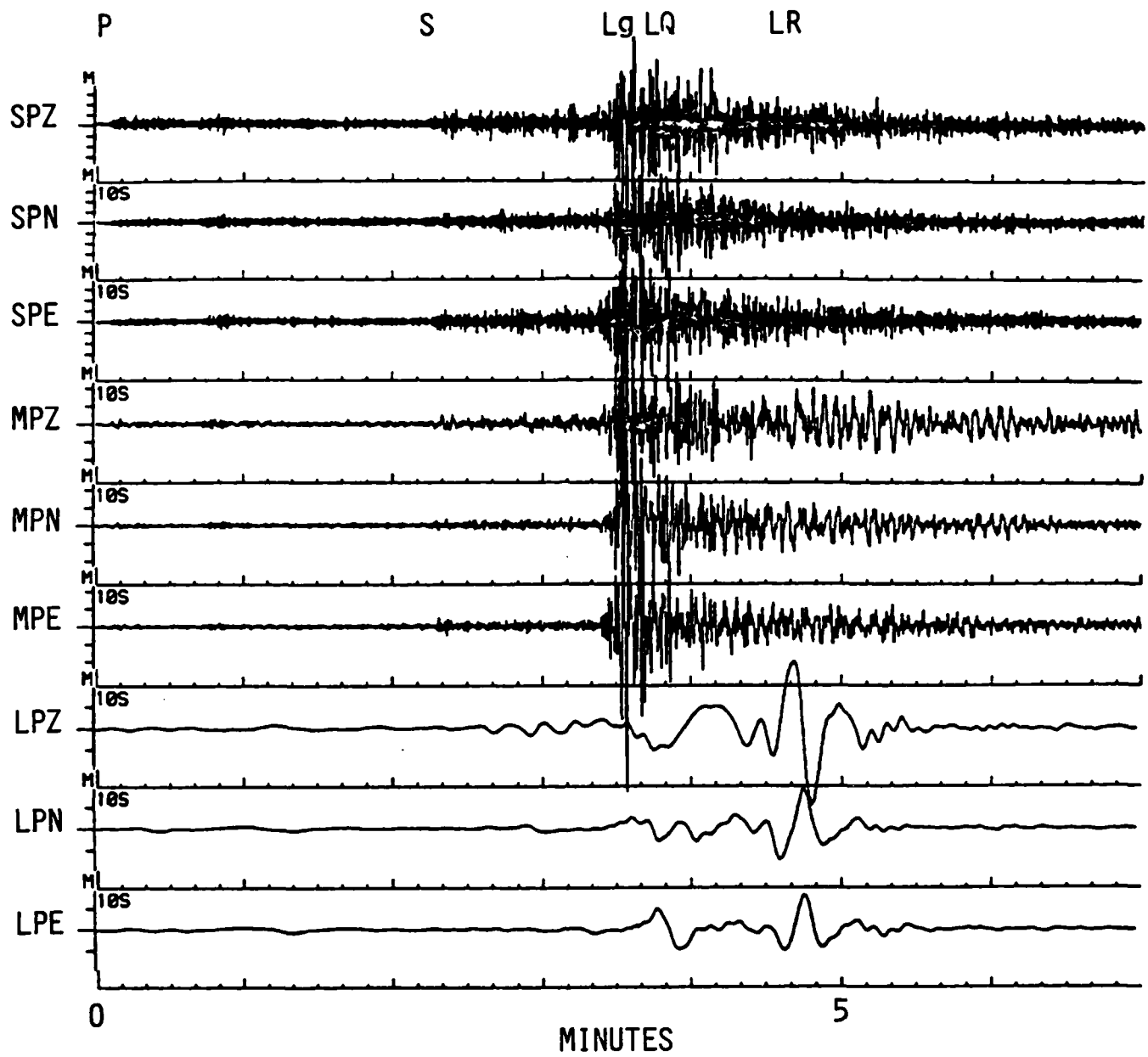


Figure 30. Goodnow earthquake, 10/7/83, recorded at RSCP ( $\Delta=12.0^\circ$ ,  $\Theta=43^\circ$ ).

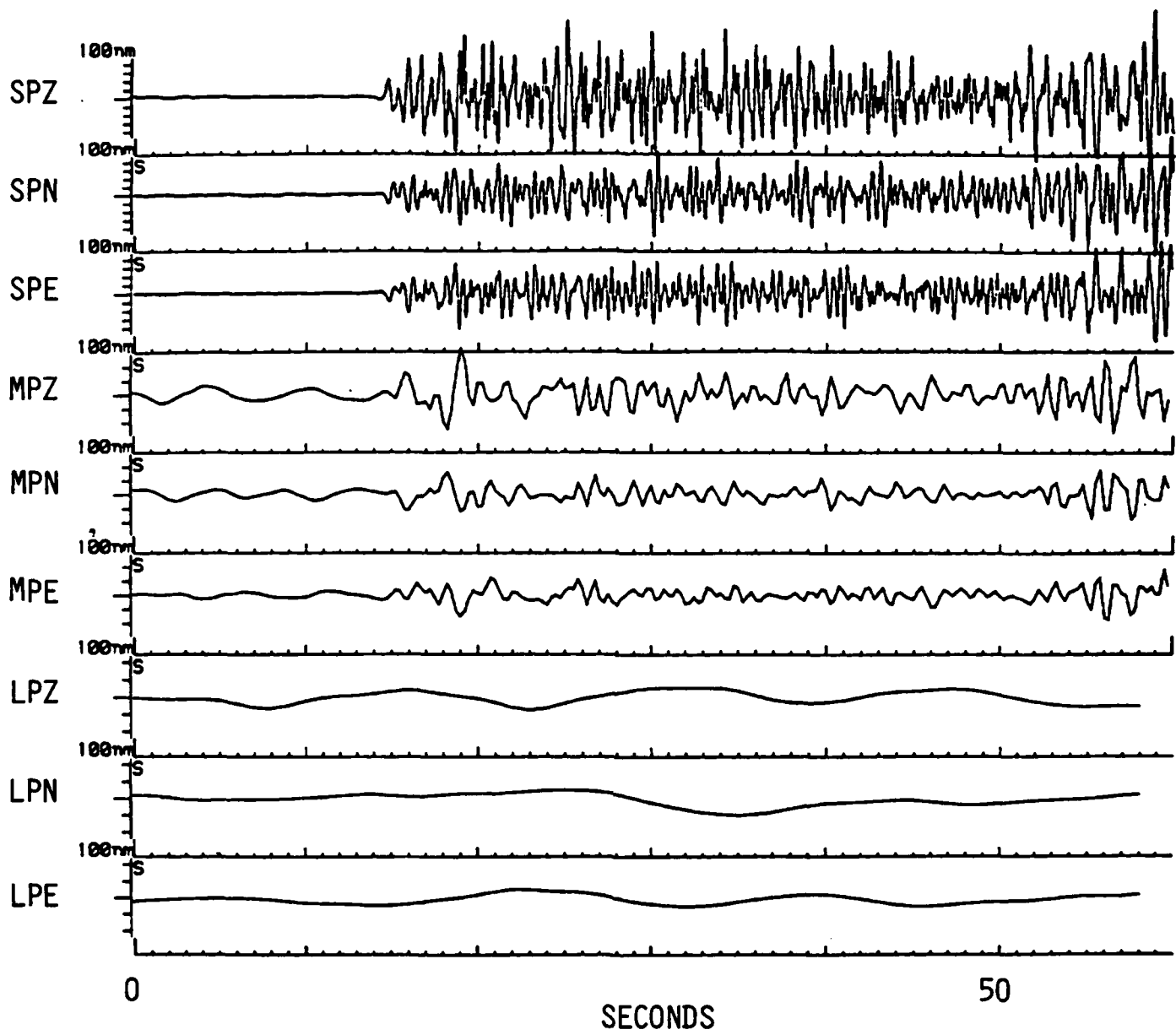


Figure 31. Goodnow earthquake P arrivals at RSCP. Arrival about 3 sec after beginning is a candidate for sP.

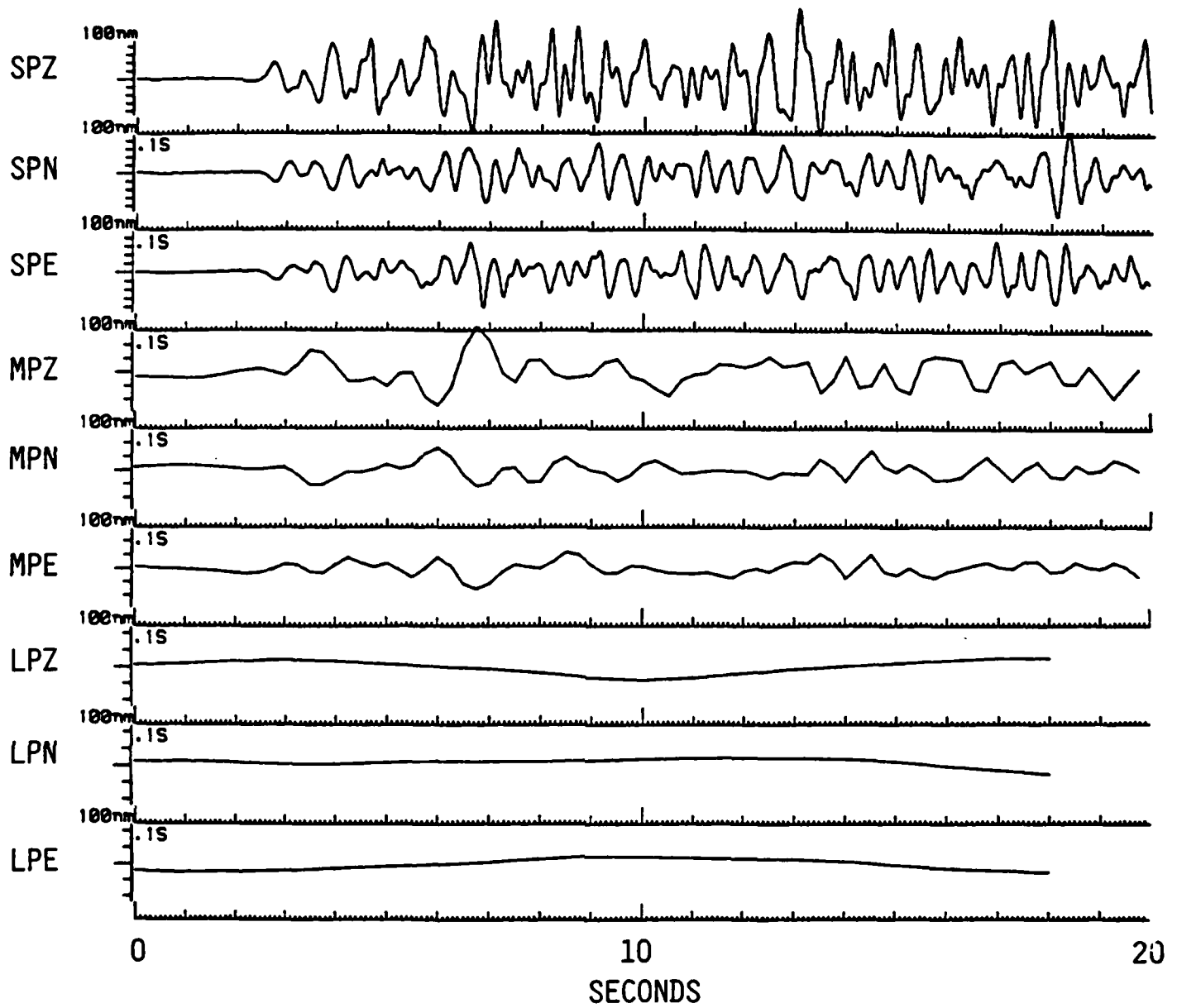


Figure 32. Expanded scale P arrivals at RSCP from the Goodnow earthquake. Note emergent higher frequency energy (~5 Hz).



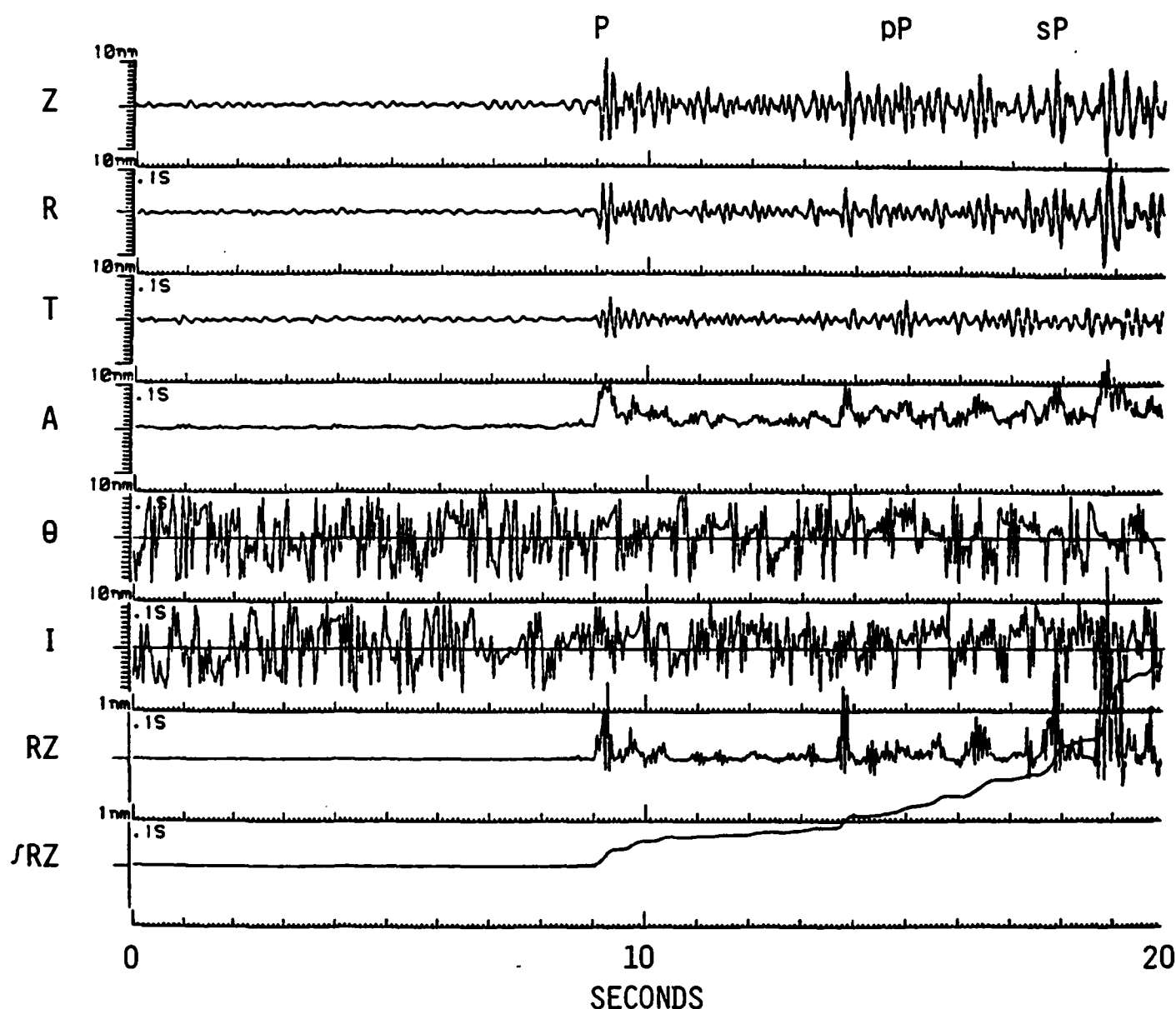


Figure 33. P arrivals from Chaneville earthquake, 9/18/81,  $m_b=3.6$ ,  $h=18$  km, recorded at CSA ( $\Delta=4.3^\circ$ ,  $\theta=352^\circ$ ). pP and sP are at approximate times for  $h=18$  km. Filtered 4-8 Hz bandpass. Trace identifications: Z=vertical; R and T=horizontal radial and transverse to great circle path;  $A=(Z^2+R^2+T^2)^{1/2}$ ;  $\theta$ =instantaneous particle azimuth; I=instantaneous apparent angle of incidence; RZ=product of R and Z traces;  $\int RZ$ =integral of the trace above.

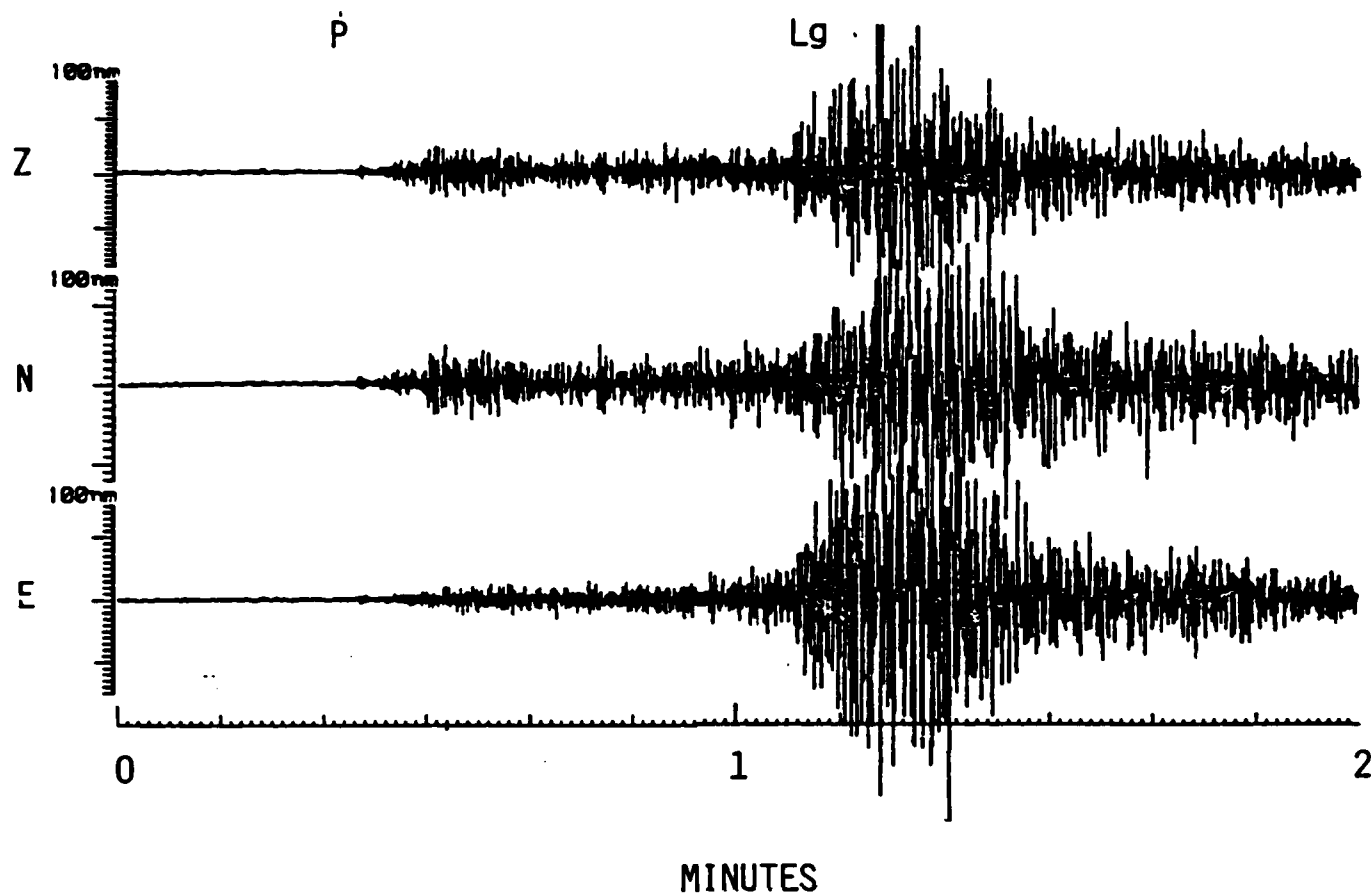


Figure 34. Cornwall earthquake, 7/4/81,  $m_b=3.5$ ,  $h=16$  km, recorded at CSA ( $\Delta=3.3^\circ$ ,  $\Theta=354^\circ$ ). Filtered 1 Hz highpass.

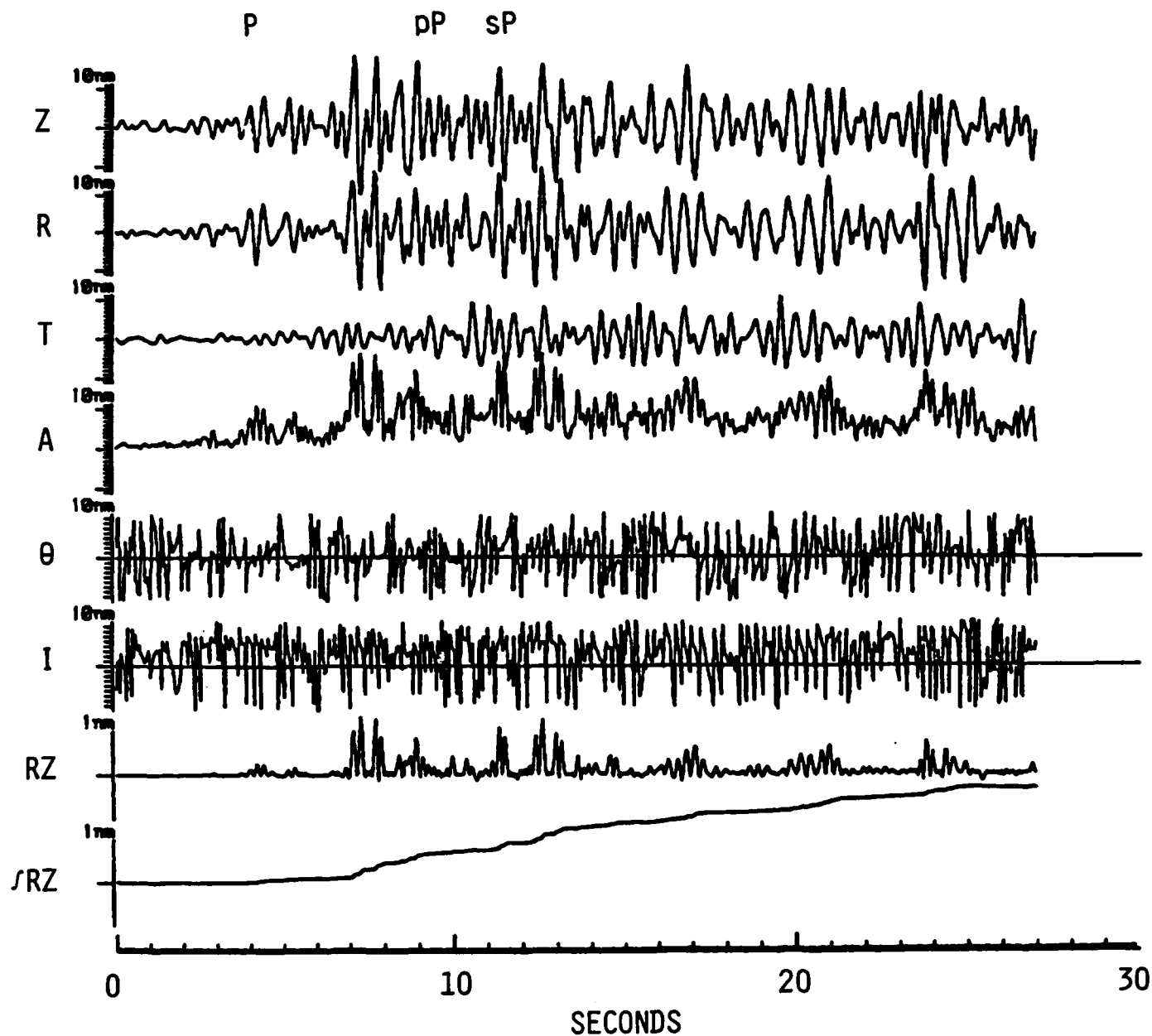


Figure 35. P arrivals from Cornwall earthquake at CSA. pP and sP are at approximate times for  $h=16$  km. Filtered 1.5-3 Hz bandpass. Trace identifications same as in Figure 33.

EASTERN U.S. CRUSTAL MODELS								
BACHE					PULLI			
DEPTH	Vp	Qp	Vs	Qs	DEPTH	Vp	Qp	Vs Qs
	6.1	250	3.3	125		6.0	1000	3.5 500
-10-					-10-			
	6.6	250	3.6	125		6.4	3000	3.9 1000
-20-					-20-			
	6.6	2000	3.6	1000				4.0 2500
-30-					-30-	7.0	5000	
-40-	8.1	2000	4.5	1000	-40-			4.7 2500
						8.2	5000	

Figure 36. Velocity/attenuation models used for generation of synthetic seismograms: Bache et al. (1980) and Curtin et al. (1983) (PULLI).

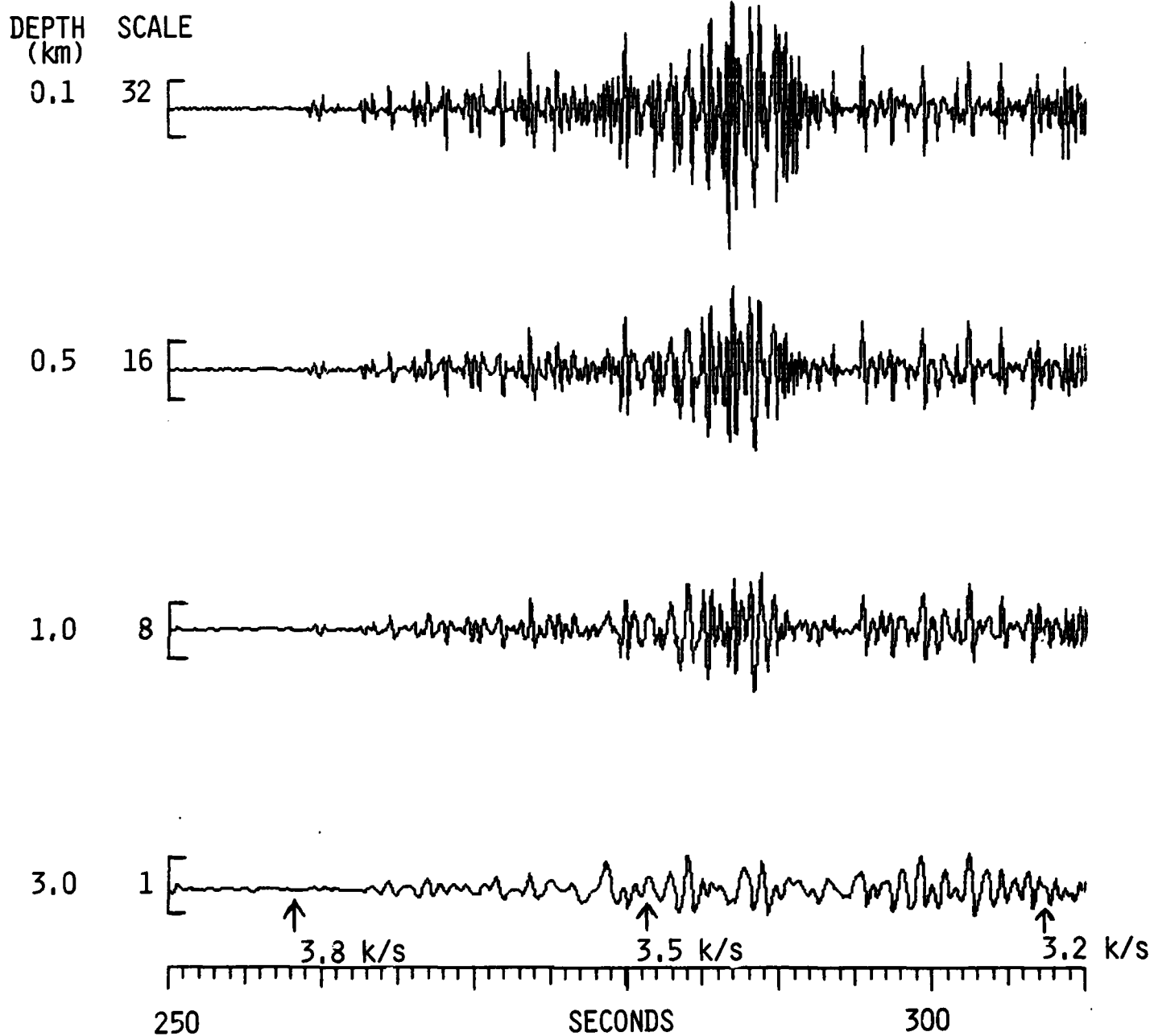


Figure 37. Vertical component S/Lg synthetics, 0-5 Hz, explosion in CANSD model listed in Table IV. Note different amplitude scales as indicated.  $\Delta=980$  km. Short period seismometer filter;  $T_0=0.5$  sec,  $h_0=0.7$  critical.

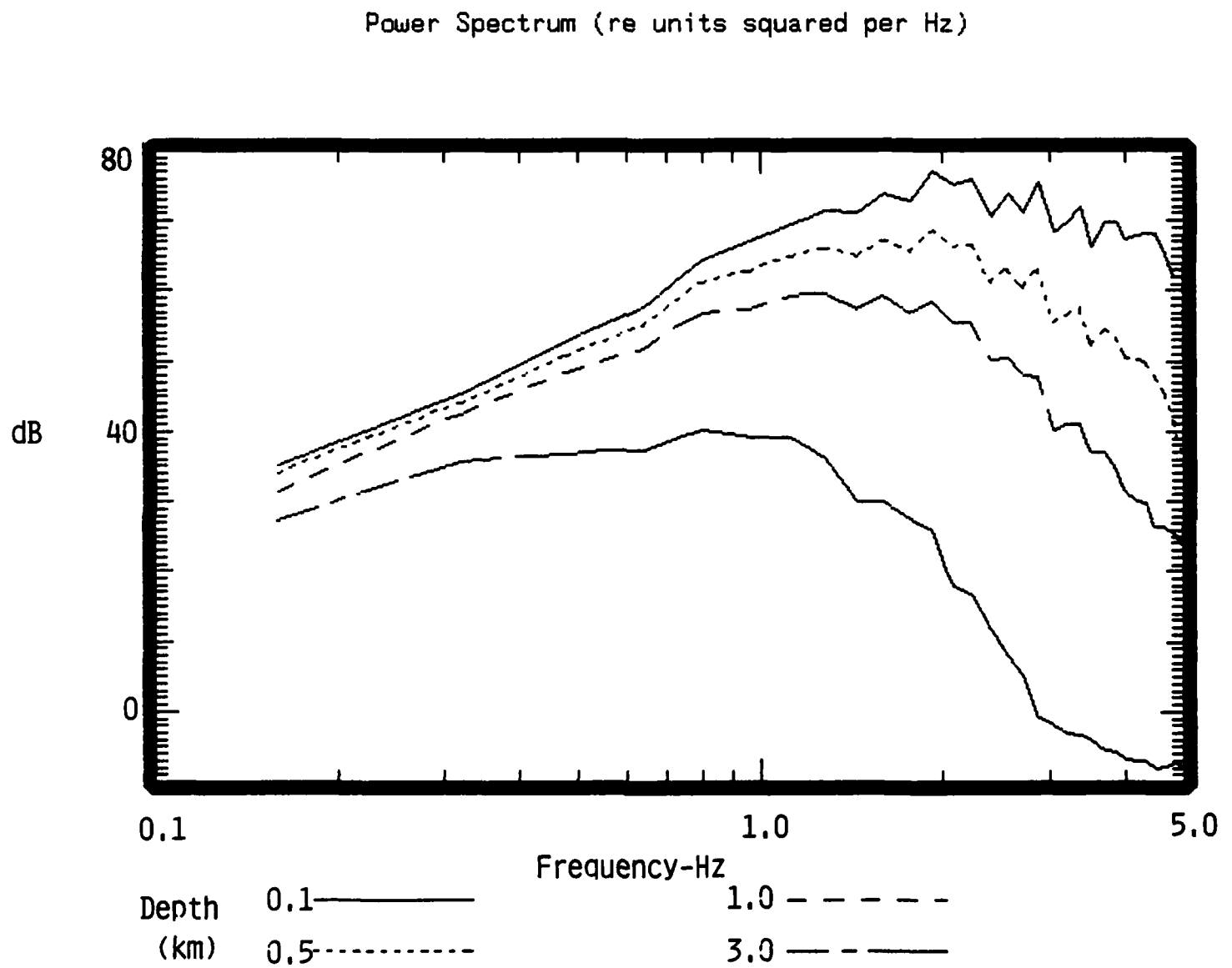


Figure 38. Spectra of S/Lg synthetics shown in Figure 37.

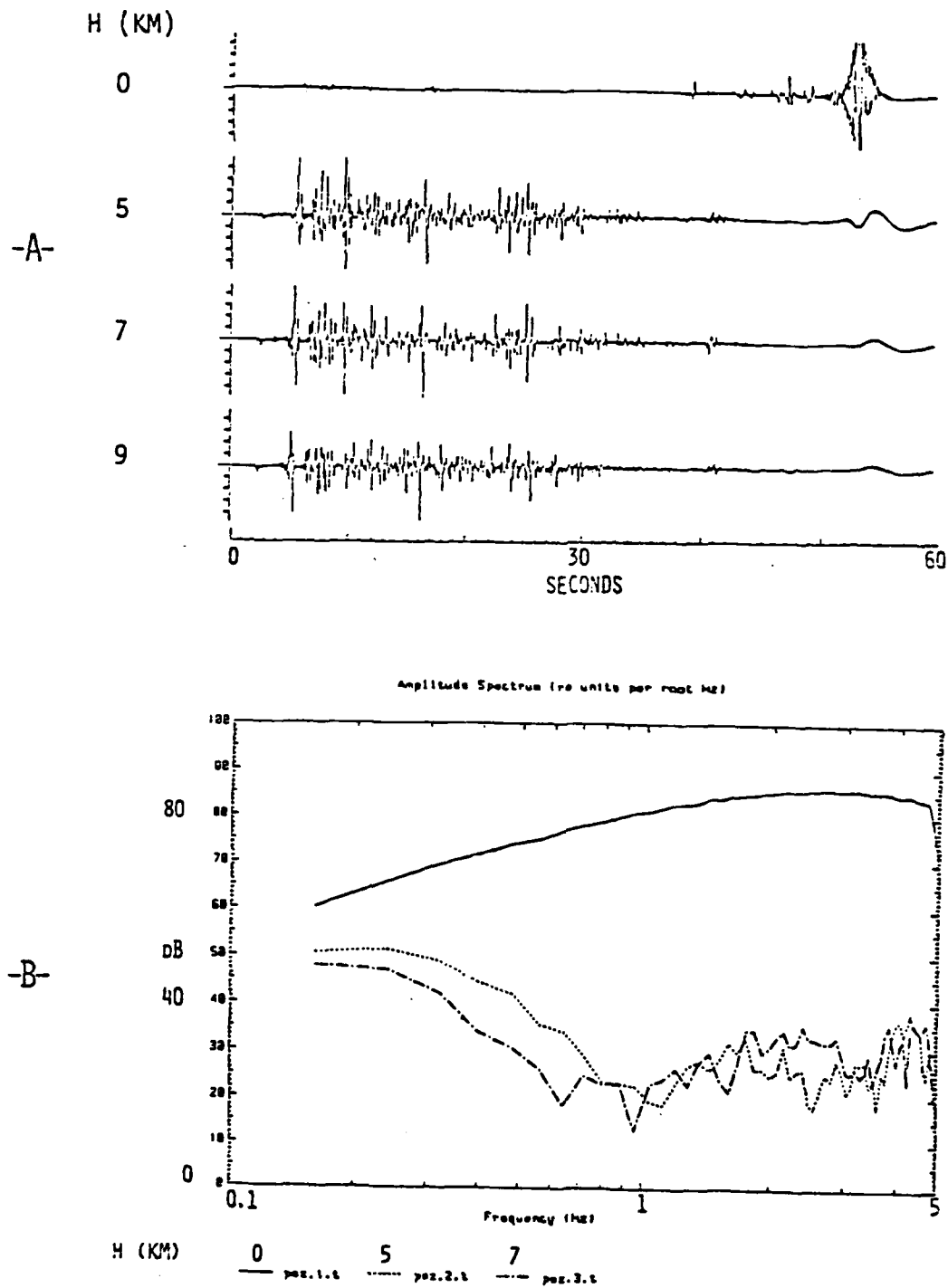


Figure 39. Synthetic seismograms and spectra for explosion source at different depths, Pulli model,  $\Delta=300$  km, 0-5 Hz bandpass. A, seismograms (note that late arrival for  $H=0$  is clipped); B, spectra of S/Lg.

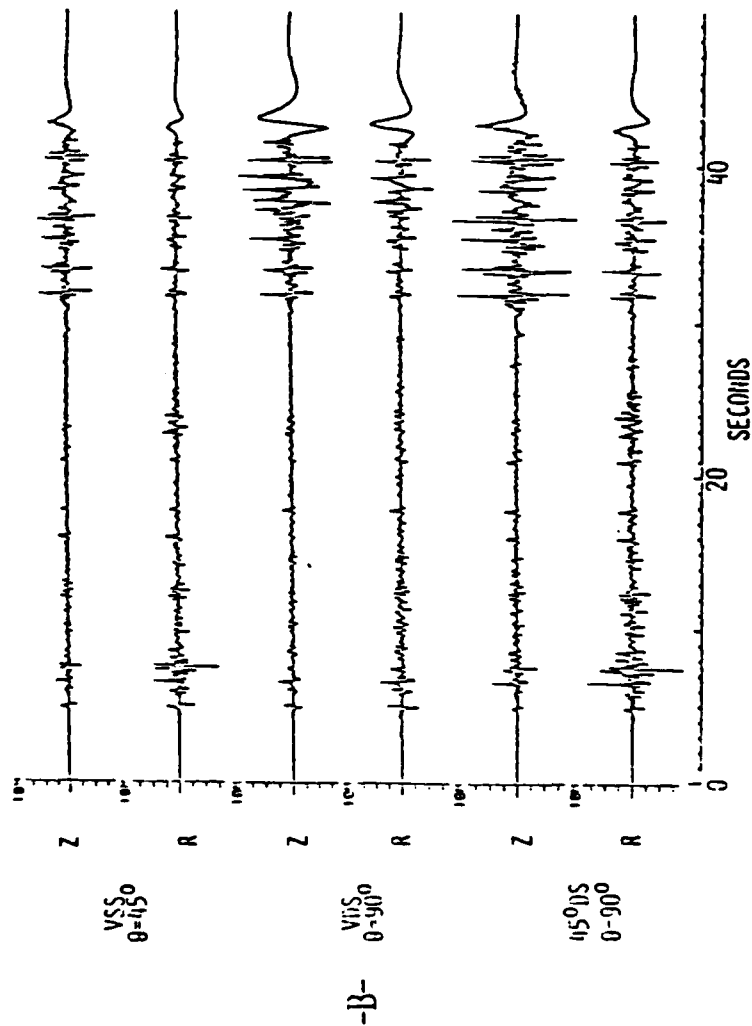
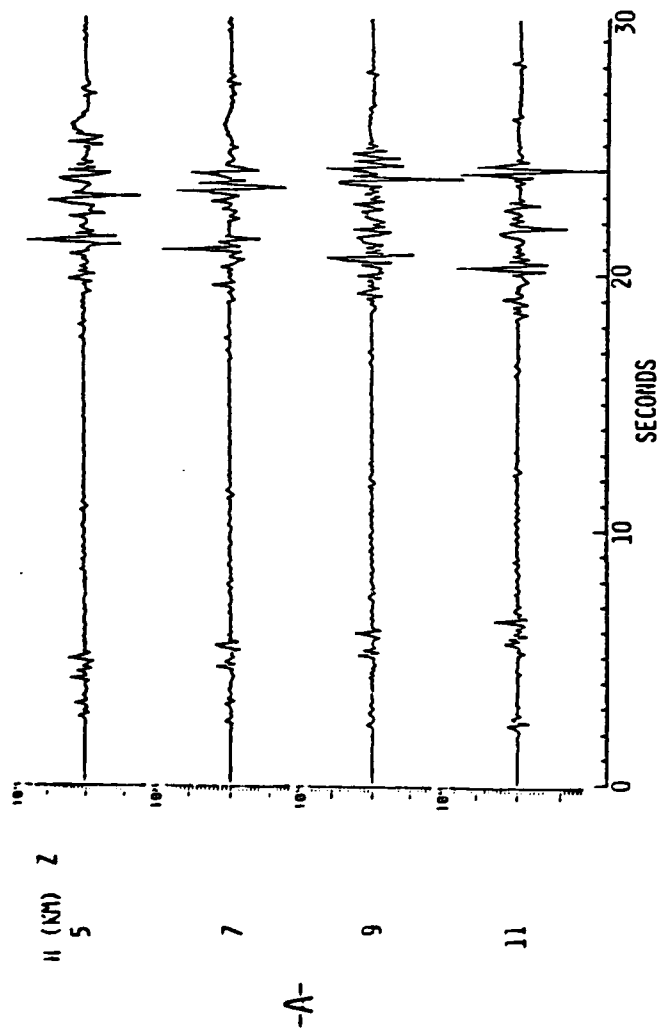
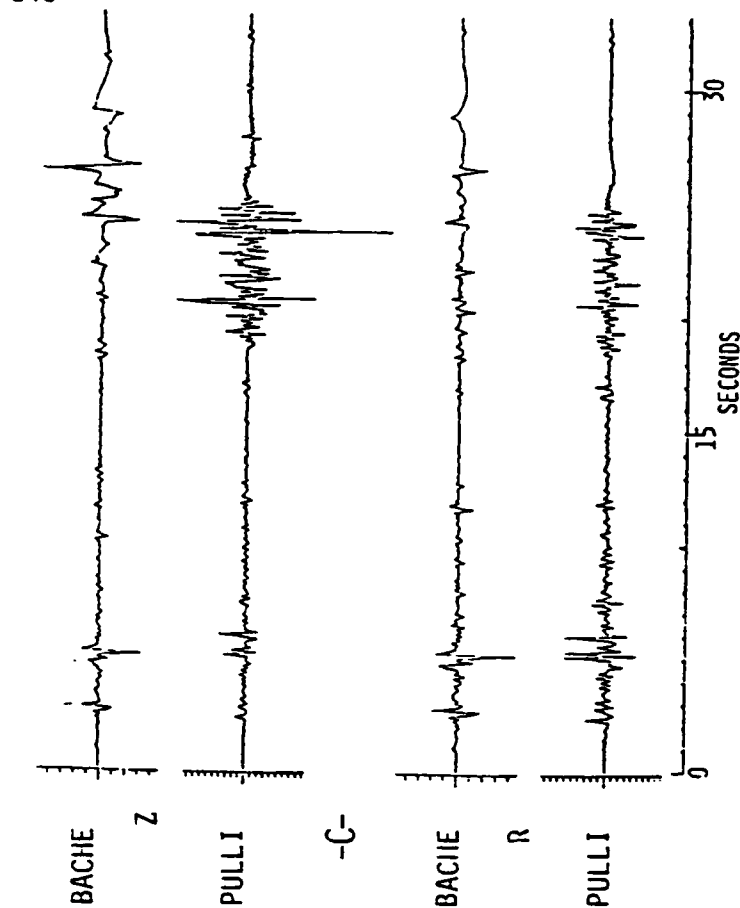


Figure 40. Synthetic seismograms for Eastern U.S.: A, effect of focal depth, Pulli model,  $\Delta=156$  km,  $45^\circ$  dip slip,  $\theta=75^\circ$ , 0-5 Hz bandpass; B, effect of orientation of faulting, Pulli model,  $\Delta=245$  km,  $H=5$  km, 0-5 Hz bandpass; C, effect of velocity structure,  $\Delta=156$  km,  $45^\circ$  dip slip,  $\theta=75^\circ$ ,  $H=7$  km for Bache model and  $H=9$  km for Pulli model.





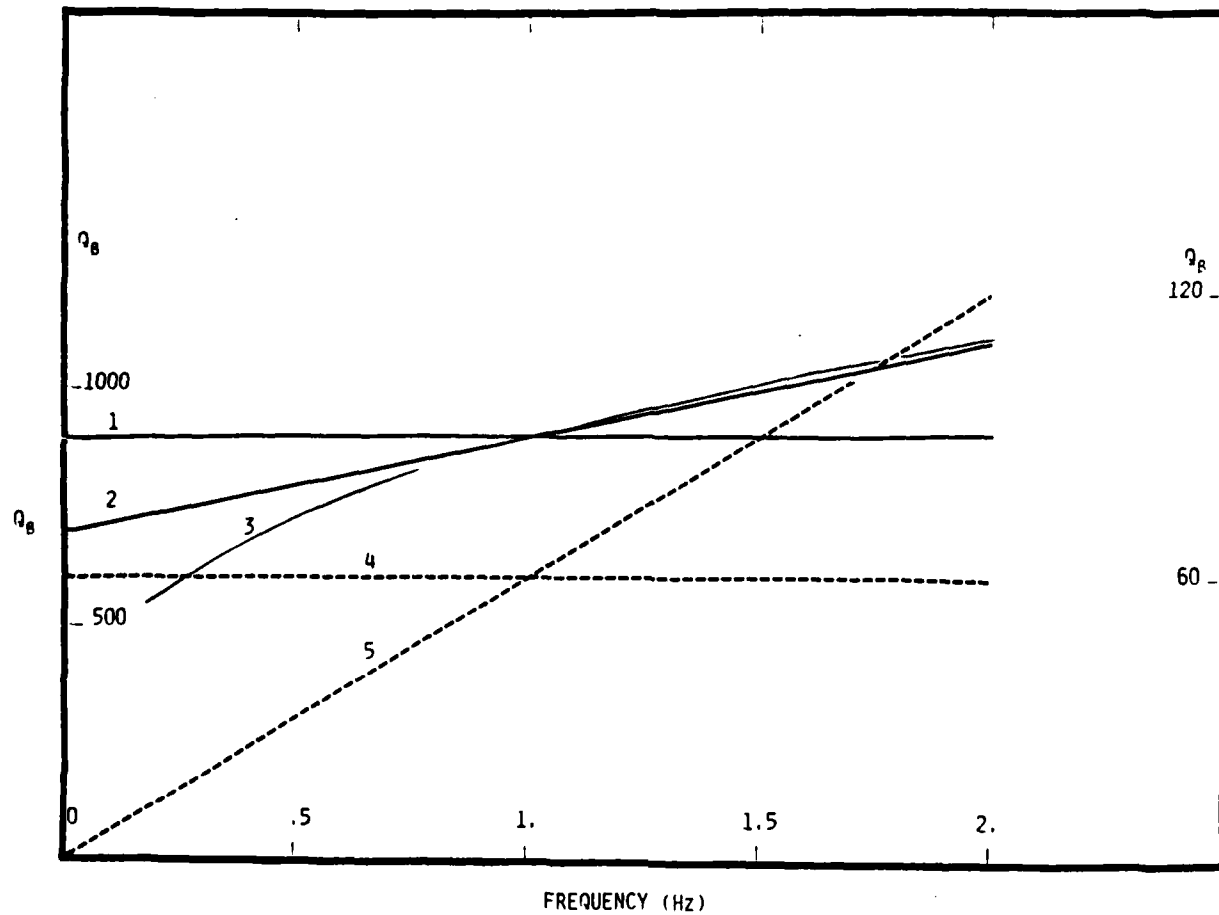


Figure 41. Crustal  $Q$  models used in Figures 42 through 47. Solid curves, left hand scale: 1)  $Q=900$ ; 2)  $Q=700+200f$ ; 3)  $Q=900f^{0.3}$ . Dashed curves, right hand scale: 4)  $Q=60$ ; 5)  $Q=60f$ .

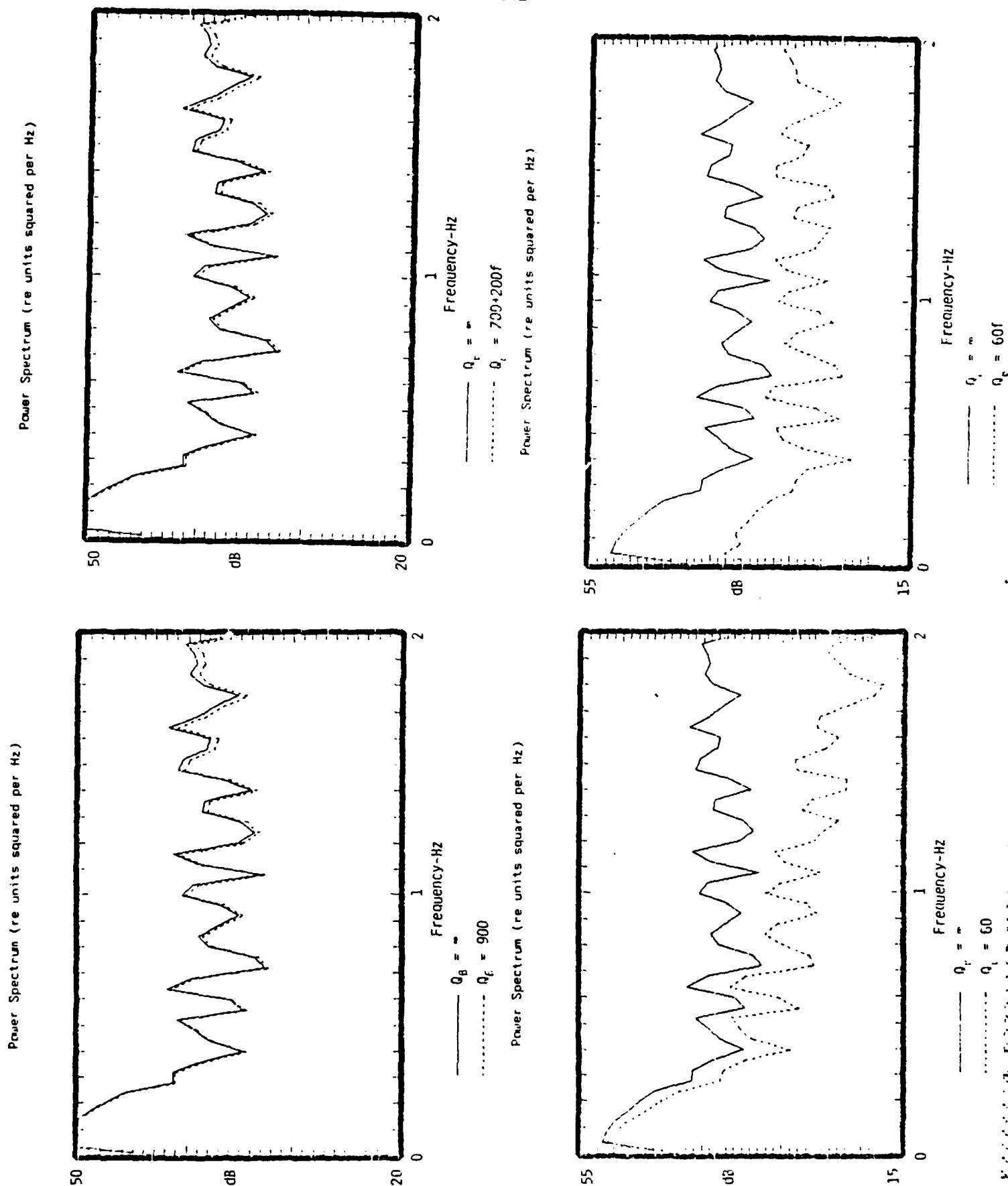


Figure 42. Vertical component full waveform spectral attenuation (four point averaged) for different Q models for explosion source in simple continental model listed in Table IV.  $Q_0=20$ ,  $\Delta=100$  km,  $h=5$  km. Note dB scales are different. Q listed is for crust. Mantle Q is 2X crustal Q for high Q cases and equal to crustal Q for low Q cases.

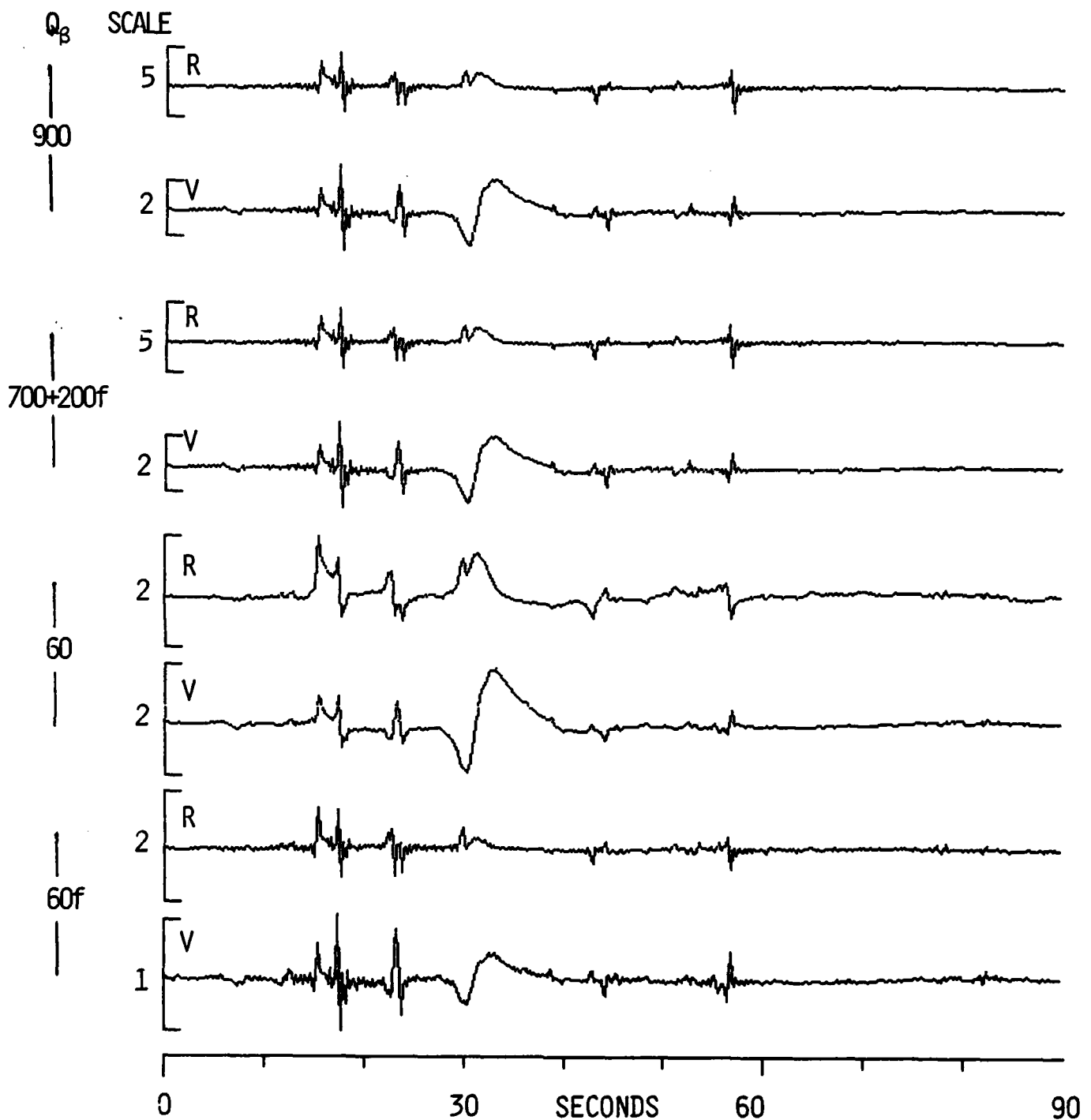


Figure 43. Radial horizontal (R) and vertical (V) full-waveform synthetic seismograms, 0-2 Hz, for explosion in simple continental model listed in Table IV illustrating effects of different Q models.  $Q_\alpha \approx 2Q_\beta$ ,  $\Delta=100$  km,  $h=5$  km. Note different amplitude scales as indicated. Q listed is for  $\beta$  crust. Mantle Q is 2X crustal Q for high Q cases and equal to crustal Q for low Q cases.

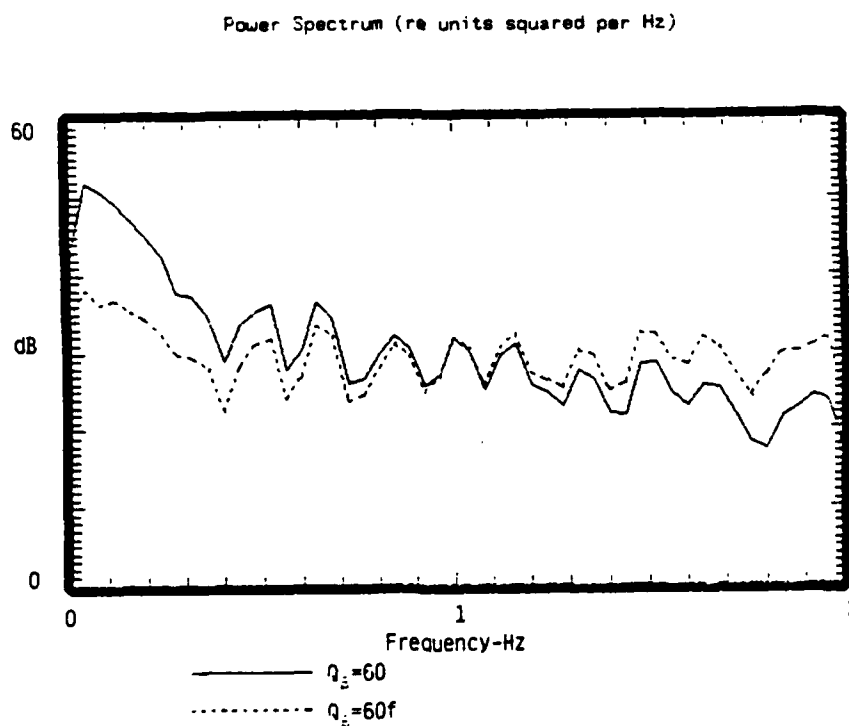
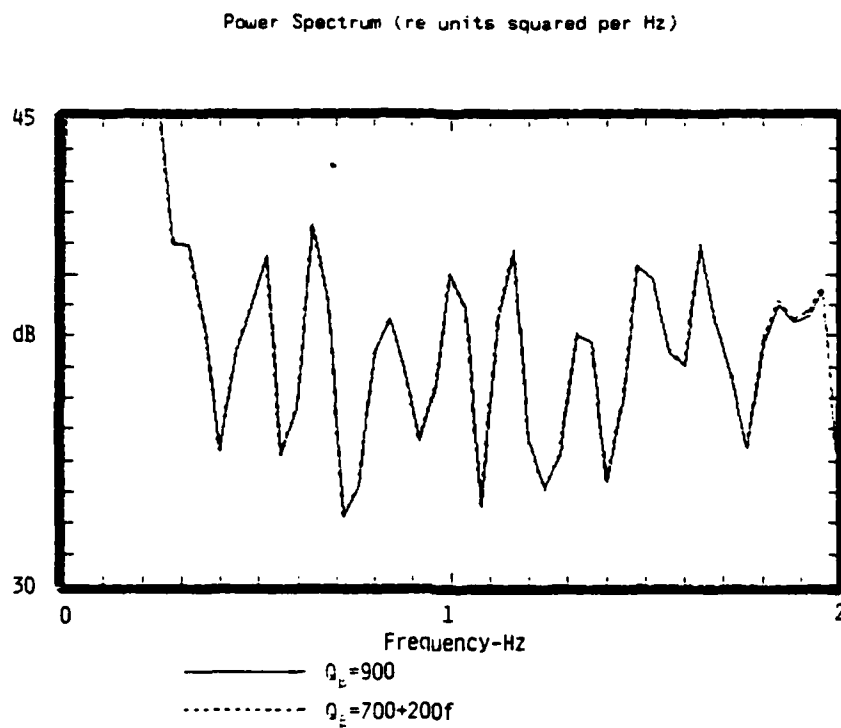


Figure 44. Four point averaged spectra of vertical component synthetics shown in Figure 43. Note dB scales are different.

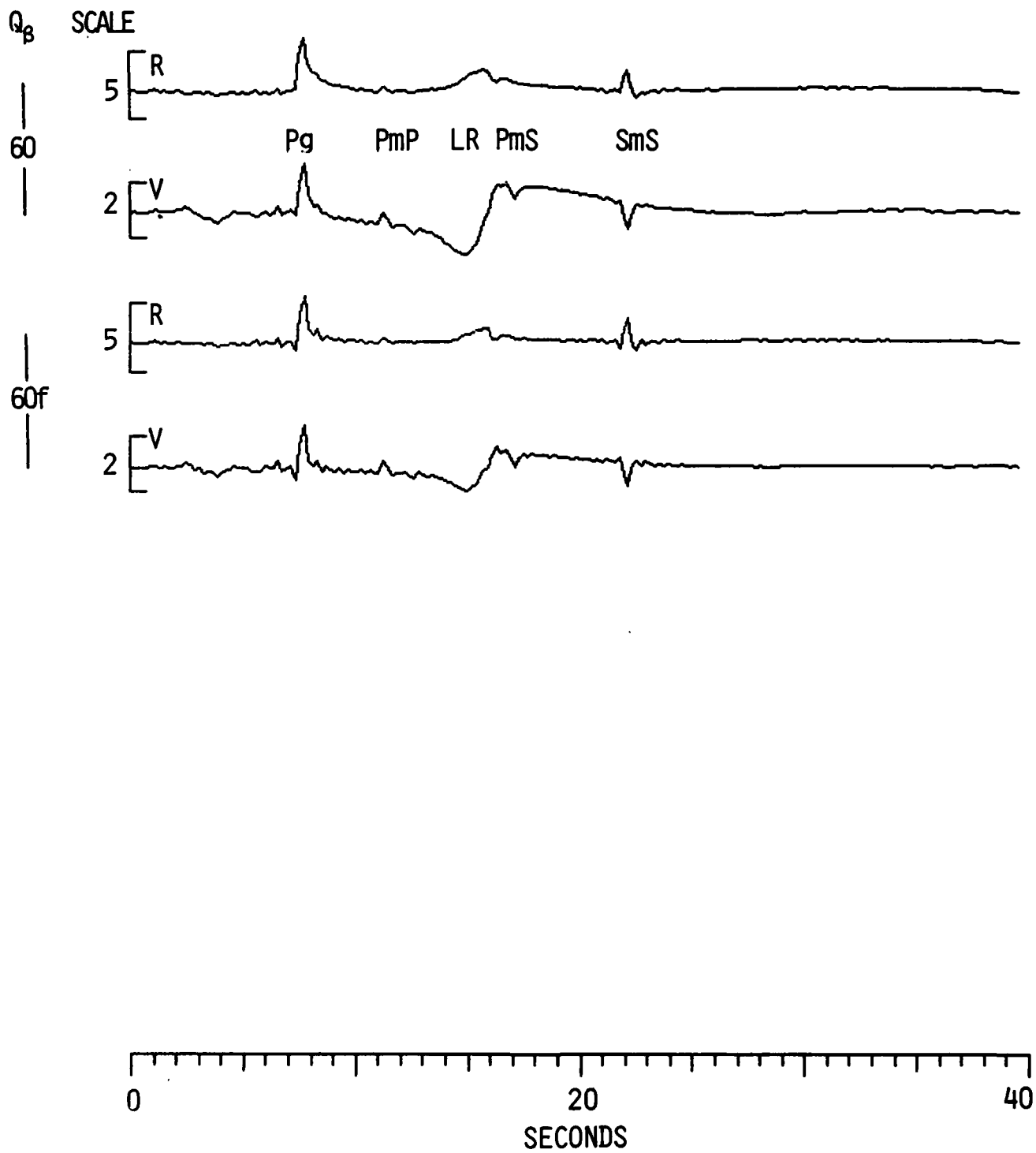


Figure 45. Full waveform synthetics. Parameters as in Figure 43 except  $\Delta=50$  km.

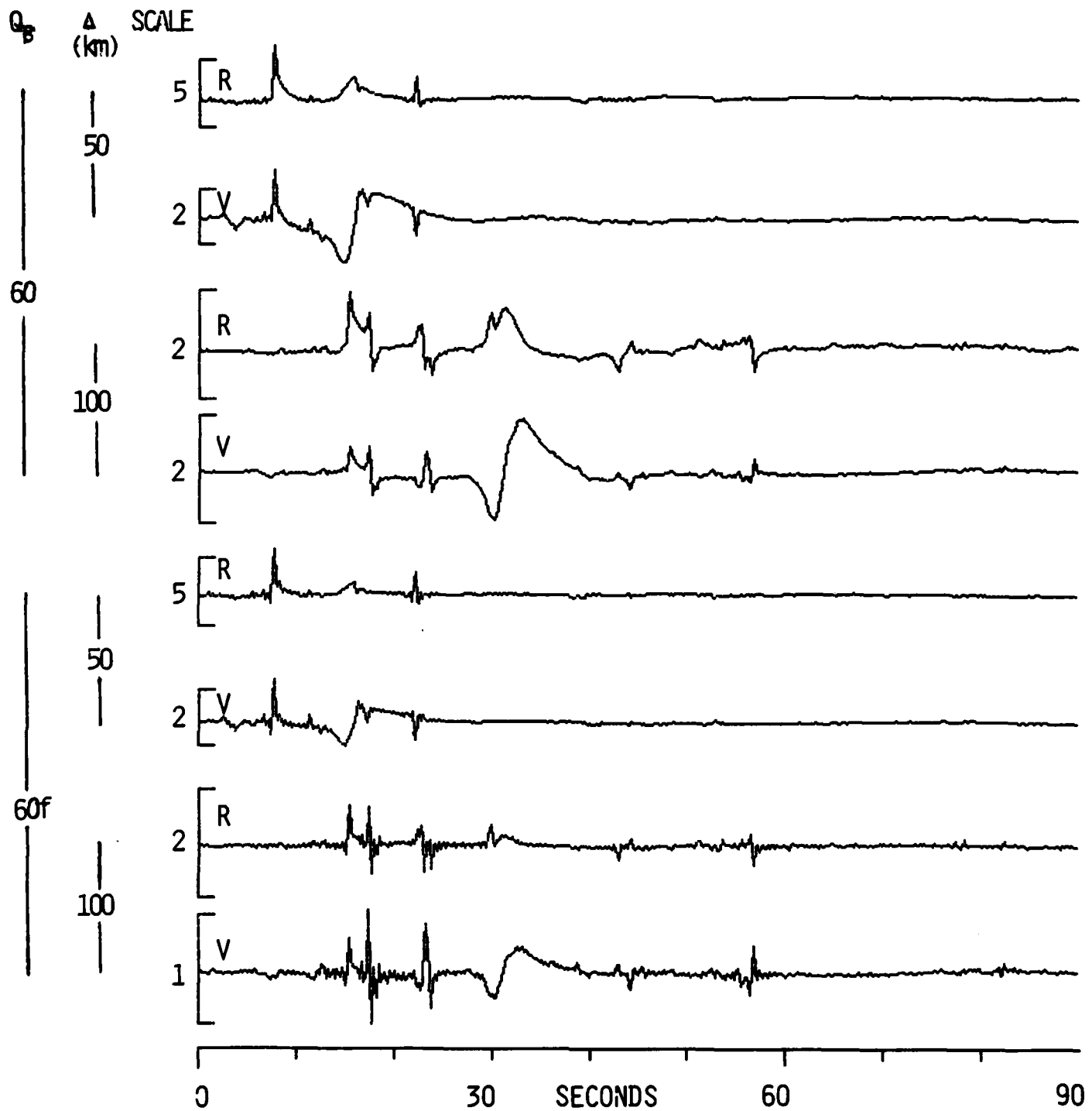


Figure 46. Full waveform synthetics. Parameters as in Figures 43 and 45.

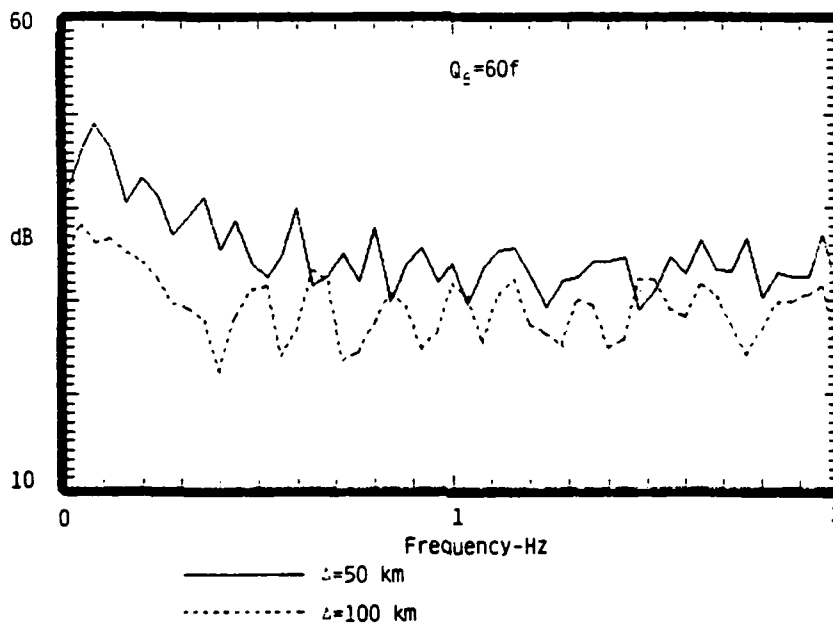
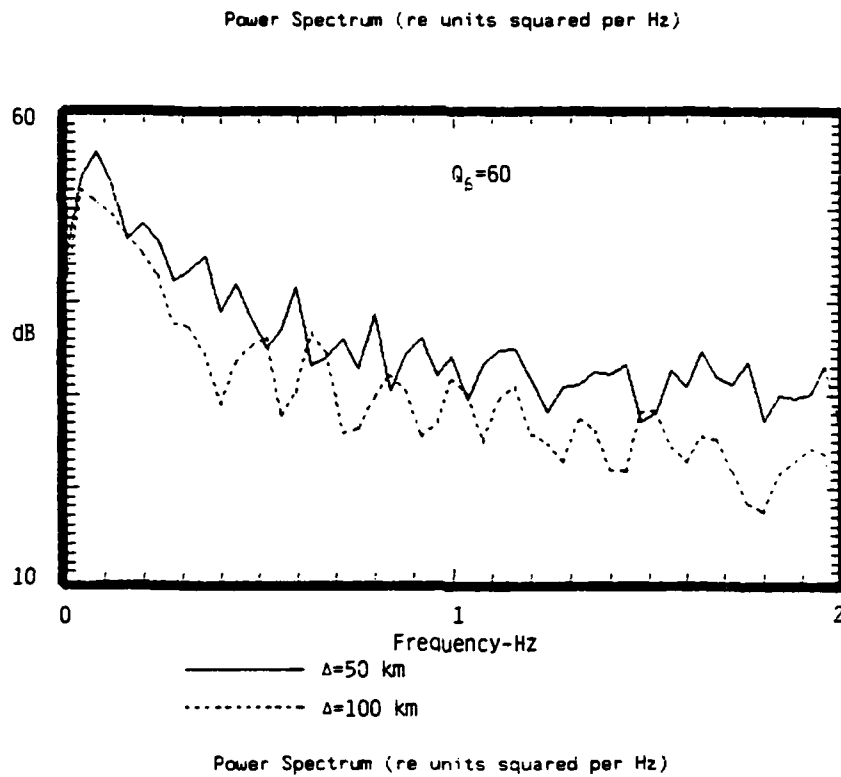


Figure 47. Four point averaged spectra of vertical component synthetics shown in Figure 46.

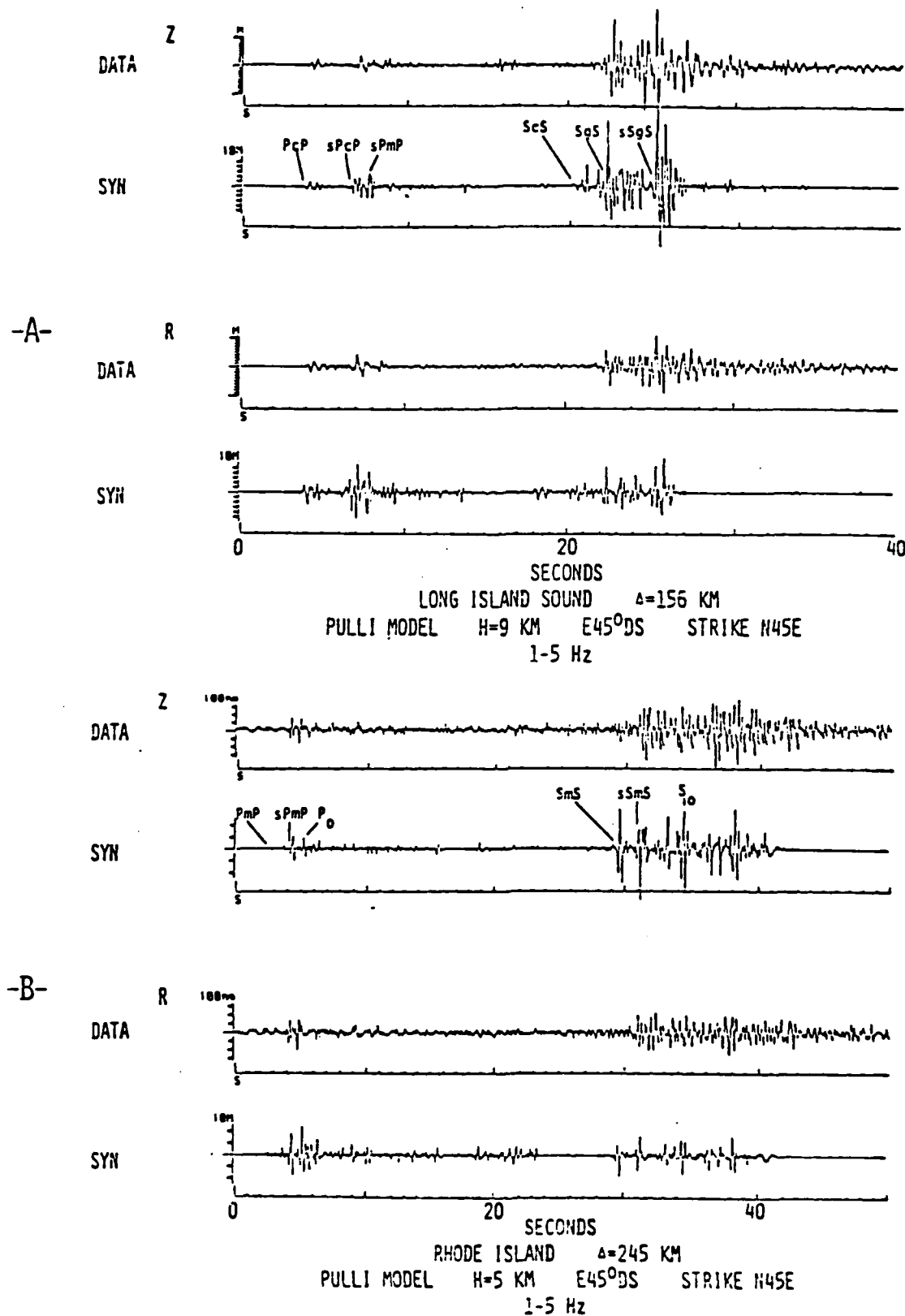


Figure 48. Comparison of data with synthetic ground motion: A, from the Long Island Sound earthquake; B, from a Rhode Island earthquake ( $m_b=2.7$ ). o, g, c, and m identify the direct arrival and the three successively deeper crustal reflections, respectively. Prefix s leaves the source upward as an S wave.



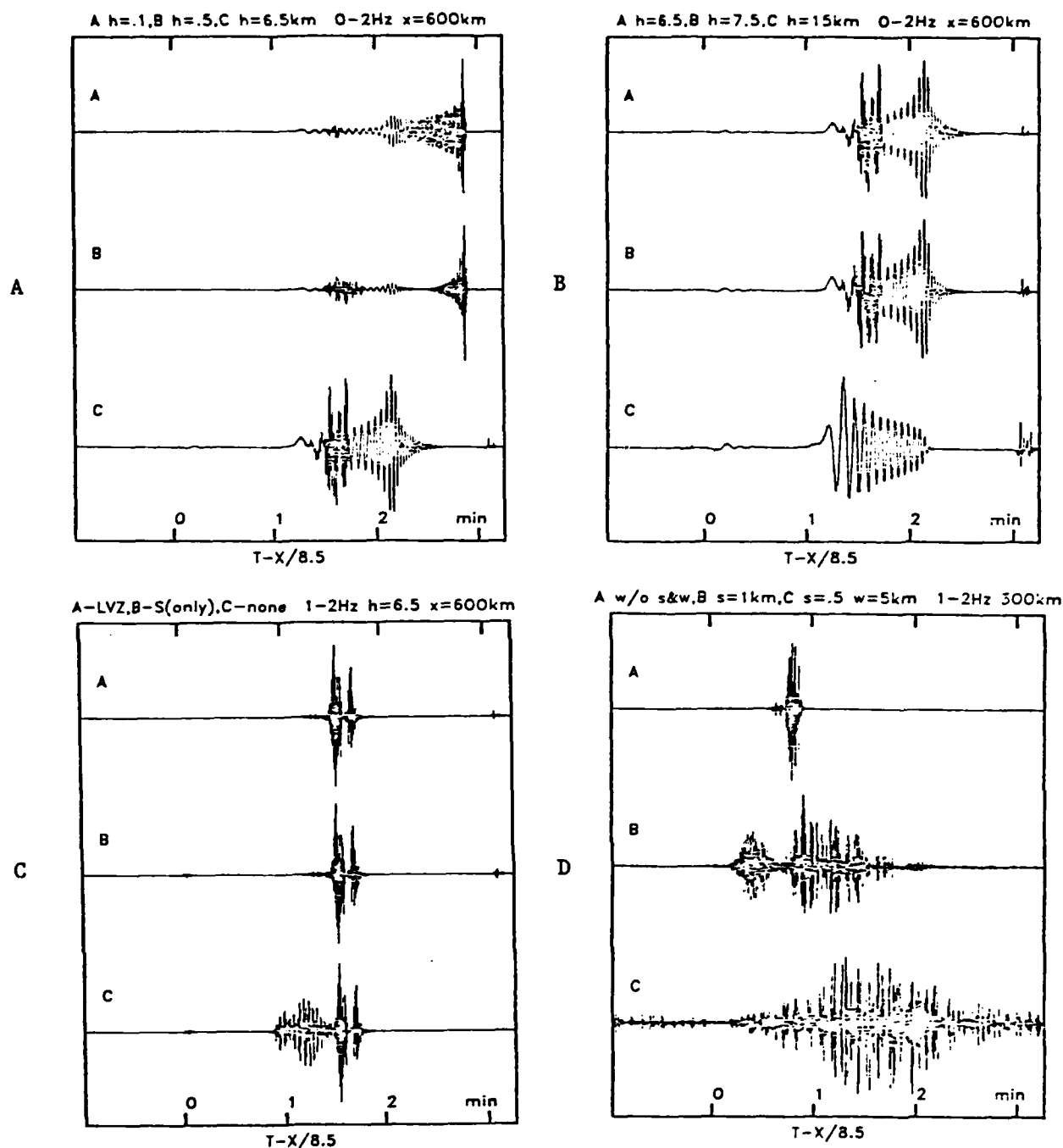


Figure 49. Synthetic seismograms. A and B, variations with source depth. C, variations with mantle velocity structure. D, variations with near surface velocity structure. See text for details.

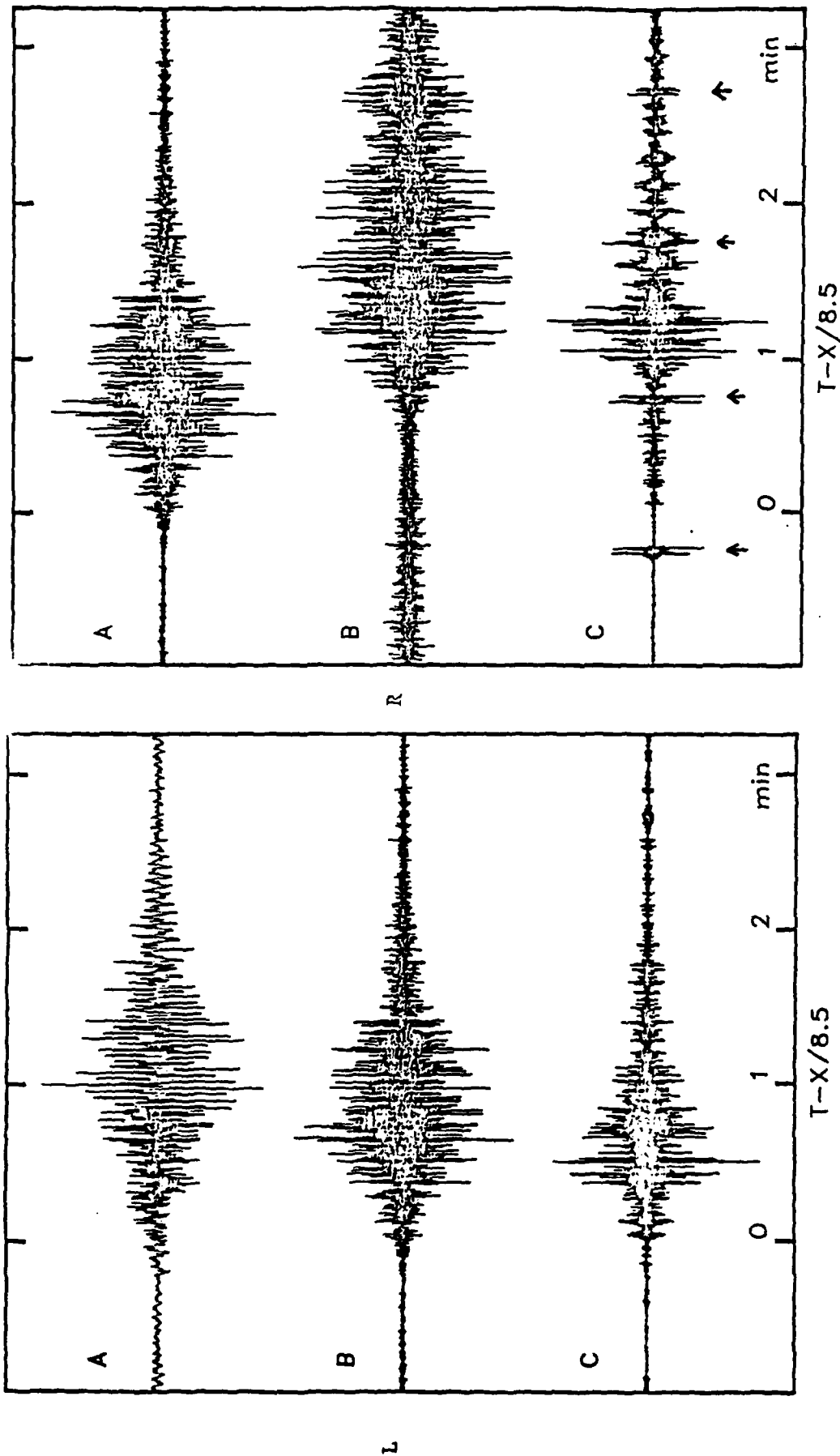


Figure 50. L, synthetic seismogram. Effects of frequency filtering on synthetic Pn-Sn wave trains. R, synthetic seismograms (A and B) compared with filtered OBS record (C). Equally spaced pulses in C are minute mark signals. See text for details.

TASK C

## Introduction

This report has been divided into three main sections. The first section gives a description of the broad band digital seismic station SRNY installed near the Rondout Associates, Incorporated (RAI) offices in Stone Ridge, New York. Included in the discussion are software descriptions to programs for data recording as well as playback. An important aspect of the data retrieval software is that the data is put into the Center for Seismic Studies (CSS) format version 2.6 and is easily transferred from RAI to CSS over the computer network.

The second section gives details of the data analysis methods used in studying broad band and array data. Although several methods have been studied, much of this section is devoted to the adaptive polarization method which has shown promise as a single station location tool.

The final section documents software that has been implemented on both the RAI SUN microcomputer, raisun, and the CSS SUN, css-sun. These programs have been designed for ease of use and make extensive use of the graphics capabilities of the SUN computer.

## Broad Band Seismic Station

In the northeastern section of the United States, there are now three broad band digital seismic stations in operation; the regional seismic test network station in the Adirondacks (RSNY) (Taylor and Qualheim, 1983), the SRO station in State College, Pennsylvania, and a station located in Stone Ridge, New York (SRNY) operated by Rondout Associates, Incorporated for the Nuclear Regulatory Commission. These three stations make a large aperture tripartite array of digital broad band seismometers. The Stone Ridge station will be described in detail below.

SRNY is located at the southeastern corner of the Catskill range at 41.849°N, 74.151°W. The sensors sit on a concrete pier that was poured on Paleozoic limestone bedrock two meters below the surface. A 6' by 9' concrete

box houses the sensors and digitizing electronics and is covered with a half meter of soil (Figure 1a). Power and signal cables extend underground from the vault site to the RAI offices approximately 400 meters distant where the recording electronics are housed.

Inside the vault (Figure 1b) are the three seismometers as well as amplifiers, anti-alias filters, digitizer, multiplexer, and line driver purchased from Refraction Technology. The sensors are Wielandt wide-band feedback seismometers which are flat to velocity from .2 to 20 seconds and have a 140 dB dynamic range. Output from the seismometers is amplified, digitized at approximately 60 samples per second per channel, multiplexed and transmitted by cable to the recording station (Figure 1c). A 16 bit digitizing scheme is used with 14 bit mantissa and a 2 bit exponent. Each gain step is 12 dB making the dynamic range of the digitized signal 120 dB.

At the recording station end, the digitized signals are sent to both a Columbia PC which controls the digital recording of the signals and a digital-to-analog converter where any one of the signals may be chosen to be input to a Helicorder (Figure 2). Paper records from the Helicorder offer a quick look at the seismic activity and are very useful in identifying problems with the seismometers. Time is provided to both the digital and analog recording devices by a Kinometrics satellite clock. The Columbia formats the data and time information for recording and then writes that data to one of two tape recorders (3M 1/4" cartridge drives with controllers, assembled by Secondary Computer Storage). The 1/4" magnetic tape cartridges each have a capacity of 67 megabytes which corresponds to 38 hours of data. Using two transports, a total of 76 hours of data can be recorded unattended. Control of the tape drives and recording by the Columbia is provided through two programs, scs and rai. Descriptions of these programs and the data format used to record on the 1/4" cartridges can be found in Appendix C.

As part of the station operation, each new tape cartridge must be certified and a table of bad blocks generated and stored in blocks 8 and 9. The bad block information allows the tape drive to skip those blocks when recording. The transport not being used to record data is used for this task but as the Columbia is not a multitasking machine, a second computer must be used for certification and playback. At RAI, a SUN Microsystems workstation is used

for these tasks as well as for data analysis and transfer to the Center for Seismic Studies. Descriptions of the certification and playback routines may be found in Appendix D.

## Analysis Techniques

### Polarization Analysis

Polarization analysis or polarization filtering has come to include a broad range of analysis techniques. Although the utility and methodology of these different techniques are extremely diverse, they share common characteristics; all of the methods require multiple components of motion, usually a vertical and two horizontals, and one or more of the components is rotated to a new direction. Of the many three component methods, most rely upon a knowledge of the horizontal radial direction. The horizontal components are rotated to the appropriate radial and transverse direction and then further processed to aid identification of and/or enhance the arrivals.

Sutton and Pomeroy (1963) applied polarization methods to analog data. After rotating the horizontal components to the radial and transverse directions, they produced traces of radial times vertical and the integral of radial times vertical to help distinguish between the motions of compressional, vertically polarized shear, and Rayleigh waves. Phinney and Smith (1963) developed a method for distinguishing between P and SV type motion in digital data. Using a small time window, the data were fit by a least squares line in the vertical radial plane. The angle obtained was indicative of the type of motion.

Polarization filters are used to enhance the arrivals traveling in a specified direction and thus phase identification is made easier through their use. Shimshoni and Smith (1964) multiplied a time averaged cross-product of the radial and vertical components by the vertical and radial traces to aid identification. They also computed the angle of incidence using a method similar to that of Phinney and Smith (1963). In addition to computing the least squares line through the data in the radial vertical plane, the eccentricity of the motion was also measured. Valid rectilinear motion was

recognized by the eccentricity having a value close to one and the angle of incidence was defined only where this was true. This method was extended to three dimensions by Flinn (1965) who computed the rectilinearity of particle motion over a given time window by measuring the ratio of the principal axes of the covariance matrix. Deviation from the specified azimuth and angle of incidence was measured from the largest principal axis of the covariance matrix. The rectilinearity and direction were then combined as a gain function used to modulate the amplitudes of the output traces. Other polarization methods have been developed for use on multichannel data (Samson and Olson, 1981).

Two types of polarization analysis have been studied. One is based on the earlier work of Sutton and Pomeroy (1963) and is a point by point instantaneous method; the other we call adaptive polarization analysis and has proved to be the more useful of the two in terms of earthquake location.

#### Instantaneous Polarization

Instantaneous polarization filtering was developed for use with analog records by Sutton and Pomeroy (1963) and has been adapted to be used on digital data. Assuming a back azimuth to the event from the station, the horizontals can be rotated into radial and transverse directions. The product trace RZ and its integral are plotted in addition to instantaneous values of absolute amplitude, azimuth, and angle of incidence. The collection of these traces is indicative of specific types of seismic motion. A description of how these parameters are obtained follows.

Denote the three orthogonal components of the station as N, E, and Z for the north-south horizontal, east-west horizontal, and vertical records, respectively. The great circle azimuth  $\theta'$  that the earthquake signals are theoretically following is usually known so the radial and transverse components of motion can be easily computed

$$R = N \cos \theta' + E \sin \theta'$$

$$T = E \cos \theta' - N \sin \theta'.$$

The radial and transverse components are valuable in discriminating between energy polarized in the radial direction (i.e. P, SV, and Rayleigh) and that polarized in the transverse direction (SH and Love waves). Picking arrival onsets may be difficult even when the horizontals have been properly rotated. To aid in making better time picks, the absolute amplitude of the signal is plotted.

$$A = (N^2 + E^2 + Z^2)^{1/2}$$

In general, the amplitude of an arrival will be larger on this trace than on any of the individual components. The instantaneous azimuth relative to the radial direction and apparent angle of incidence between the radial and vertical components are given by

$$\theta = \tan^{-1}(T/R)$$

$$\text{and } I = \tan^{-1}(R/Z)$$

respectively. In addition to indicating the apparent velocity of an arrival, the angle of incidence helps distinguish between P and SV type motion as, for a given azimuth, the two different types of motion will have opposite signs. The angle of incidence is also used to distinguish between rectilinear motion and elliptical motion. Rectilinear motion will give a constant angle of incidence whereas elliptical motion will rotate through all angles of incidence. The final two traces computed for the polarization analysis are the product of the radial and vertical components RZ and its integral  $\int RZ dt$ . RZ will be positive for P type motion, negative for S type motion and oscillatory for Rayleigh wave motion and its integral will increase, decrease, and oscillate, respectively. A synopsis of how most of these traces respond to different types of wave motion can be found in Table I.

The weaknesses of this type of polarization filtering are found primarily in the azimuth and angle of incidence determinations. Both are unstable at low signal-to-noise ratios (S/N). Thus, when both horizontal components are near zero, the azimuth is unreliable and similarly, when the vertical and radial components are near zero, the angle of incidence is unreliable. Figure

TABLE I

TRACE TYPE OF MOTION	R	T	$\theta$	I	RZ	$\int RZ dt$
P	OSCILLATES	0	$\theta'$	+ OR -	POSITIVE	INCREASES
SV	OSCILLATES	0	$\theta'$	- OR +	NEGATIVE	DECREASES
SH	0	OSCILLATES	$\theta' + 90$	0	0	0
RAYLEIGH	OSCILLATES	0	$\theta'$	ROTATES	OSCILLATES	OSCILLATES
LOVE	0	OSCILLATES	$\theta' + 90$	0	0	0



3 shows an instantaneous polarization filter applied to a synthetic P-wave arriving at a  $45^\circ$  angle of incidence. Because the motion is strictly compressional, as seen on the RZ and RZ traces, there are no arrivals on the transverse component. Both the azimuth and angle of incidence traces show erratic fluctuations before and after the arrival and relatively stable behavior during the signal. Where the radial and vertical traces pass through zero, however, the azimuth and angle of incidence become unstable.

The azimuth trace, because it is dependent on the two horizontal components, is also sensitive to the angle of incidence of a passing wave and whether or not there is any SH motion mixed in with the arrival. A P-wave arriving at near vertical incidence will have very little motion in the horizontal directions. The small S/N resulting will make the azimuth erratic. This would not be the case for a near vertically incident SV wave as the motion for this phase would be predominantly on the horizontals. However, if there is SH energy arriving at the same instant, then an unreliable azimuth would result.

Figure 4 demonstrates the results of applying the instantaneous polarization filter to a synthetic Rayleigh wave. As in the P-wave example, the  $\theta$  trace is unstable where R is near zero. The I trace, however, is stable because the R and Z traces are never both near zero. All of the other traces behave as expected.

#### Adaptive Polarization

Unlike the instantaneous polarization method, adaptive polarization does not require an a-priori knowledge of the azimuth to the source although that information is easily incorporated, eliminates a 180 degree ambiguity inherent in the calculations, and helps in the identification of phases. Because no assumptions are made as to the direction of motion, this method could be an important tool for studying situations where the source is not stationary. We have called this method "adaptive" because rather than rotating the horizontal components to their assumed radial and transverse directions, they are rotated to the direction of maximum signal and do not represent the motion in a single direction. Along with the adaptive horizontal components, the apparent azimuth and angle of incidence are plotted.

Initially we assume three component data from a digital seismic station and rectilinear motion at a constant azimuth and angle of incidence. Later in the discussion, we will consider simultaneous arrivals from different directions and non-rectilinear motion. We seek to determine the azimuth and angle of incidence over a small time window; one that is at least as long as one or two cycles of the predominant frequency. The azimuth is determined by examining the zero lag cross covariance between the two horizontal components as a function of azimuth angle. The angle at which this function is zero is the azimuth at which the predominant direction of motion within the window will be traveling. The horizontal components of motion as functions of the north (N) and east (E) horizontals and the azimuth ( $\theta$ ) are written:

$$\begin{aligned} H_1(t) &= N(t) \cos \theta + E(t) \sin \theta \\ H_2(t) &= E(t) \cos \theta - N(t) \sin \theta \end{aligned} \quad (1)$$

and, the cross-covariance between  $H_1$  and  $H_2$  at zero lag is:

$$ccv_0 = \frac{1}{n} \sum_{i=0}^n \bar{H}_1(t) \bar{H}_2(t)$$

where  $\bar{H}(t) = H(t) - \mu_H$  and  $\mu_H$  is the mean value of  $H(t)$  over the interval. In terms of  $\bar{N}$  and  $\bar{E}$ :

$$ccv_0(0) = a \cos 2\theta + b \sin 2\theta \quad (2)$$

where  $a = 1/n \sum \bar{N}(t) \bar{E}(t)$  and  $b = 1/n \sum (\bar{E}^2(t) - \bar{N}^2(t))/2$ . Setting (2) equal to zero and solving for  $\theta$ :

$$\theta = 1/2 \tan^{-1} (-a/b) \quad (3)$$

The azimuth  $\theta$  obtained from (3) will be between  $-45^\circ$  and  $45^\circ$  and could be either the radial or transverse direction or either of their supplements. To distinguish the component with the predominant motion, we examine the behavior of (2). The zero lag cross-covariance as a function of azimuth is a sinusoid

with a single cycle between azimuths  $-45^\circ$  and  $+45^\circ$ . The value of the function will be positive when the true direction of motion is within the quadrant bracketed by  $H_1$  and  $H_2$ . From this configuration, increasing  $\theta$  brings  $H_1$  closer to the predominant direction of motion and decreasing  $\theta$  brings  $H_2$  closer. Thus, if  $\theta$  is an azimuth where the  $ccv_o(\theta)$  is crossing from positive values to negative ones then  $H_1$  is the direction of predominant motion and if  $\theta$  is an azimuth where the  $ccv_o(\theta)$  is crossing from negative to positive values, then  $H_2$  is the direction of predominant motion. The proper direction is easily determined by examining (2) at  $\theta=0$  where  $ccv_o(\theta)=a$ . Because there is only one cycle between  $-45^\circ$  and  $+45^\circ$ , if  $a$  is positive, the azimuth obtained is the direction of largest motion. If  $a$  is negative, then the direction of largest motion is at  $\theta+90^\circ$ . This azimuth is used to rotate the horizontal components to the radial and transverse directions at the center of the window. The window is then advanced one sample and the process repeated.

The apparent angle of incidence is calculated in much the same manner as the azimuth. For this measurement, the adapted radial and vertical components are used as the orthogonal components from which the angle of incidence is determined.

An estimate of the relative accuracy of the azimuth and angle of incidence measurements is obtained through the maximum value of the zero lag cross-correlation function. At its maximum value, where the predominant direction of motion bisects  $H_1$  and  $H_2$ , the zero lag cross-correlation function ( $ccf_o(\theta+45^\circ)$ ) will be between 0 and 1, inclusive. A large value is indicative of strong rectilinear motion over the window and a small value indicates the lack thereof. Where there is little or no rectilinear motion, confidence in the results obtained is also small and we expect the error to be close to  $90^\circ$ . Conversely, a large value for  $ccf_o(\theta+45^\circ)$  indicates strong rectilinear motion and should have an error close to  $0^\circ$ . This subjective error evaluation can be written.

$$\text{error} = 90^\circ(1 - ccf_o(\theta+45^\circ))$$

Error determined in this manner is not an absolute quantity but rather a relative measure of the accuracy of the value.

Because the method presented here relies on the determination of the predominant direction of motion, the question arises; "What angle would be determined if two uncorrelated signals arrived at the station at the same time from different directions?". Let the two uncorrelated signals be  $x(t)$  and  $y(t)$  where the standard deviations of  $x$  and  $y$  are equal and define the north and east components of motion as

$$\begin{aligned} N(t) &= j x(t) + k y(t) \\ E(t) &= n x(t) + m y(t) \end{aligned} \quad (4)$$

$j$ ,  $k$ ,  $n$ , and  $m$  are scaling factors which can be set to simulate any combination of direction and amplitude for  $x$  and  $y$ . Substituting the values for  $N$  and  $E$  in (4) into equation (3)

$$\theta = 1/2 \tan^{-1} \left\{ \frac{-(jx + ky)(nx + my)}{(n^2x^2 + m^2y^2 + 2nmxy - j^2x^2 - k^2y^2 - 2jkxy)/2} \right\} \quad (5)$$

Because  $x$  and  $y$  are not correlated, the  $xy$  terms tend to zero as the length of the series gets large. Rewriting (5)

$$\theta = 1/2 \tan^{-1} \left\{ \frac{2(njx^2 + kmy^2)}{((j^2 - n^2)x^2 + (k^2 - m^2)y^2)} \right\} \quad (6)$$

Equation (6) may be used to predict  $\theta$  for two time series passing a station at different azimuths. The worst case occurs when the two wavetrains are traveling at azimuths  $45^\circ$  apart, for when one of the signals is showing no correlation at its azimuth, the other will be at a maximum. If the two signals are orthogonal, then the proper azimuth would be chosen.

The above analysis is valid only in the case that the two signals are not coherent. When the two signals are perfectly coherent then the azimuth determined will be that of the vector sum of the two signals. Partial coherency would result in some combination of the completely non-coherent result and the perfectly coherent result.

In Figure 5, we show synthetic vertical and horizontal components to be used as the input to the polarization program. The modulated arrivals on the horizontal components represent a constant amplitude signal that rotates smoothly in azimuth. A constant amplitude vertical component maintains an unchanging angle of incidence. The results of processing this data with the polarization program are shown in Figure 6. There are six output traces; the vertical, adapted radial, and adapted transverse components of motion, the product of the radial and vertical traces, and the azimuth and angle of incidence traces plotted with error bars. The radial trace exhibits a constant amplitude and the transverse component shows very little motion at all. Thus, the radial follows the predominant direction of motion. In the case of a short duration arrival, the  $rz$  trace would help to identify the first arrival and its direction but in this case, where the signal is continuous,  $rz$  has little use. The azimuth trace tracks the motion of the rotating arrival quite well and shows very little error. The same is true of the angle of incidence trace where there is no change throughout the duration of the analysis.

For the second example, two independent samples of random noise were combined on the N, E and Z components of motion to simulate one set of arrivals traveling at  $0^\circ$  azimuth,  $72^\circ$  angle of incidence with an amplitude of 1000 and another set of arrivals traveling  $N45^\circ E$ ,  $55^\circ$  angle of incidence and amplitude 547 (amplitudes are relative). In terms of the independent non-coherent time series  $x(t)$  and  $y(t)$ :

$$N(t) = 3.0 x(t) + y(t)$$

$$E(t) = y(t)$$

$$Z(t) = x(t) + y(t)$$

Using these number in equation (6), we obtain values of  $6^\circ$  for the azimuth and  $67^\circ$  for the angle of incidence (assuming an azimuth of  $6^\circ$  for the radial trace). The results of the polarization analysis are shown in Figure 7. The azimuth trace is centered about  $6^\circ$  over the length of the trace in excellent agreement with the theory. Error for the azimuth is large and is due to the fact that the two arrival sets are traveling at azimuths  $45^\circ$  apart; the worst possible case. For the angle of incidence, the measured value of  $67^\circ$  is also

in excellent agreement with theory and in this case the error is very small. The small error arises because the two arrival groups are traveling at similar angle of incidence in the vertical plane at  $60^\circ$  azimuth.

On 23 October 1984, a small earthquake occurred in the Adirondack mountains of New York. The event was located by the Lamont-Doherty short period network in upstate New York at  $43.603^\circ\text{N}$ ,  $73.951^\circ\text{W}$  with a depth of .31 kilometers and a coda length magnitude of 3.4. The event was also recorded by the RSTN station RSNY and by SRNY, both broad band, three component stations. Both sets of broad band data were used in an attempt to locate the event with the adaptive polarization method. The results for station RSNY are shown in Figure 8. Three locations were obtained using the two stations. The first two were determined using the S-P time to obtain a distance along the determined azimuth and the third was taken as the intersection of the two azimuths. As can be seen in Figure 9, all three of the broad band locations are within 30 kilometers of the location determined by the short period network.

#### Beam Forming

Beam forming determines the azimuth and apparent velocity of energy moving across an array of seismometers. Cross-correlations over a small window length between each pair of stations of a three component array are used to identify coherent signals moving across the array. The position of the maximum of the cross-correlation function determines the time it takes coherent energy to travel between stations. Repeating the procedure for all three pairs of stations gives the travel times between each pair of stations from which the horizontal slowness and azimuth can be determined. Moving the window along the trace gives the azimuth and apparent slowness as functions of time. A crude estimate of the error can also be obtained by summing the travel times between the stations. For a coherent plane wave traveling across the array, the travel time sum should be zero.

When using the beam forming method, the size of the array is an important consideration. While small arrays (a few kilometers across) require smaller lags between stations and are less apt to correlate two different arrival phases, they are less sensitive to small changes in azimuth and slowness. In contrast, large arrays are sensitive to small changes in the azimuth and

slowness but the large lags needed to do the cross-correlation increase the computation time and it is easy for a particular phase recorded at one station to have a high cross-correlation with a different phase recorded at another station.

For demonstration purposes, synthetic P waves with a  $45^\circ$  angle of incidence were generated assuming the geometry of the Catskill Seismic Array (Figure 10). Results of beam forming this data are shown in Figure 11. This method, like the adaptive polarization method, uses a small window of data to obtain its results and, therefore, is insensitive to zero crossings within the arrival. During the arrival, the error trace is very small and both the slowness and azimuth traces are stable. If each station in the array has three components, the component with the best S/N can be used to obtain the best results. Particular phases may have better S/N on different components in which case, the analysis can be done on all of the different components.

### Slowness Stacking

Slowness (velocity<sup>-1</sup>) stacking uses the knowledge of an earthquake's epicenter (thereby fixing the great circle azimuth) to determine an estimate of the apparent slowness. An apparent slowness ( $p$ ) is assumed and the traces from the same component of all stations are shifted relative to one another and summed (stacked). Repeating the procedure for a range of  $p$ 's yields a display of  $p$  versus time. The maximum values of this display should appear where the energy has been summed coherently, giving the apparent slowness at which the wave crossed the array. Figure 12 is a slowness stack of the same data used in the beam forming example. Although the maximum is spread out over a large range of slownesses, it is still easy to pick. The slowness stack of a synthetic Rayleigh wave traveling across the array at 5 km/sec is shown in Figure 13. There is clearly a maximum at 0.2 sec/km but there are also other large amplitude traces. These are the result of aliasing and demonstrate that care must be exercised when using this method.

### Synthetic Seismograms

Synthetic seismograms are an important part of the analysis procedure for determining the depth and orientation of an event as well as helping to verify

velocity depth functions along the propagation path. Accurate depths for earthquakes are usually determined employing phases reflected from the surface near the source. At teleseismic distances, the depth of shallow focus earthquakes is difficult to determine to better than 10 kilometers; the initial arrivals overlap the surface reflected phases and limit the ability to pick phases arriving within a second of each other. More sophisticated techniques lose resolution because of low short-period energy. At local distances, however, there is still a substantial amount of high frequency energy in the coda and discrimination of these phases is easier.

Synthetic seismograms computed for a suite of depths using the Pulli model (Figure 32) show the sensitivity of the different phases to depth of focus (Figure 33). Except for the direct arrival, the primary phases arrive earlier with increasing focal depth and the surface reflected phases arrive later. For this model, assuming that the arrivals could be picked to an accuracy of 0.1 seconds and that there are no other errors, the depth could be determined to better than .5 km using a single station. Of course, the depth determination is extremely model dependent and misidentification of phases can also lead to unreliable depths.

Once a good match to the arrival times has been obtained, then the task of matching the amplitudes is pursued. Relative amplitudes and polarities of the various phases are controlled by the fault orientation. Any fault orientation may be decomposed into a linear combination of three primary fault types: a vertical strike slip fault striking  $45^{\circ}$ ; a vertical dip slip fault; and a dip slip fault dipping at  $45^{\circ}$  (Figure 34). By combining the three basic fault types into different fault configurations, the best fit or fits of synthetic data to recorded data can be found (Pearce, 1977).

Unfortunately, for small events, the P waves at regional and teleseismic distances recorded with high quality digital instruments do not have adequate signal to noise ratios for detailed analysis of the compressional arrivals and more reliance must be placed on analyses of the whole seismogram, since signal to noise is much greater for later phases, e.g. Pg, Sn, Lg, LR, and LQ. The work of Street and Turcotte (1977) and Herrmann and Goertz (1981) are good examples of fruitful attempts in this direction for earthquakes in the central and eastern United States. Synthesis of the later portions of a complex



seismogram for use in the analyses can be accomplished fairly efficiently and capabilities are continually improving (e.g. Bache et al., 1980; Harvey, 1981; Herrmann and Goertz, 1981; Sutton and Harvey, 1981). The "whole" seismogram synthesis program of Harvey, 1981, was used (on CSS computers) for generation of the synthetics illustrated in this report.

## Applications

### Long Island Earthquake

The results of applying the array techniques described above on two east coast earthquakes follow. The first event, an  $m_b$  3.5 Long Island Sound earthquake on 21 October 1981, was listed in the weekly reports of the preliminary determination of epicenters (PDE) as having a depth of 6 km based on arrivals at nine stations. The second event occurred in Rhode Island on 4 April 1981 and was not listed in the PDE. Data from local arrays gave a magnitude of  $m_b$  2.7. The vertical component of the Long Island Sound event is shown in Figure 14 along with the noise and S/Lg signal spectra. The corner frequency as determined by the  $\pm 6$  dB lines drawn on the spectrum is 3 Hz. From 2 to 9 Hz the signal is about 40 dB above the noise and it remains well above the noise down to .6 Hz. Analysis of this event using array techniques was marred by poor data at one of the CSA stations so comparison of single station and array techniques would be unjustified. However, the results that were obtained will be presented below.

Figures 15 and 16 are the instantaneous and adaptive polarizations of the p waves in a passband between 1 and 3 Hz. The instantaneous azimuth and angle of incidence traces are quite noisy although some stability is evident in the azimuth trace during the two major arrivals. The first arrival appears to be traveling at an azimuth  $20^\circ$  south of the calculated great circle path and the second arrival, although inconsistent in azimuth, comes primarily from south of the great circle path also. The adaptive polarization method, shown in this figure in an old format, gives a clearer picture of the same arrivals. Both the first and second arrival groups show progressive shifts to the south through the wavetrain. This indicates the possibility of lateral refraction to the south. The apparent angle of incidence trace in the adaptive scheme is

much more stable than in the instantaneous case giving angles of 50 and 53 degrees for the first and second arrival groups, respectively. Assuming a Poisson's ratio of  $1/4$ , the true angles of incidence would be 47 and 51 degrees.

The beam forming and slowness stack of the same arrivals are shown in Figures 17 and 18. The azimuths obtained from beam forming the radial component of the p wave groups are similar to those observed using the polarization methods. The waves arrive generally from the south but the change in azimuth within the arrival groups is not indicated. The slowness trace gives apparent velocities of 6.33 to 7.19 km/sec for the first arrival group and if the true angle of incidence is assumed to be that given by the adaptive polarization analysis then velocities of 4.6 to 5.3 km/sec are obtained. The second arrival group gives an apparent velocity of 8.3 km/sec that does not coincide with the larger angle of incidence determined by adaptive polarization; a near-surface velocity of 6.5 km/sec is determined from the 51 degree incidence angle. The slowness stack results agree well with the beam forming analysis giving near-surface velocities of 4.9 to 5.3 km/sec for the first arrival group and 6.2 km/sec for the second. Near-surface velocities of 4.9 to 5.3 and 6.2 km/sec, respectively, are obtained when these apparent velocities are combined with the incidence angles obtained from the polarization analyses. Thus, the slowness stack analysis is somewhat more consistent than the beam forming with the polarization angles.

Analysis of the S/Lg part of the wavetrain are shown in Figures 19 through 22. Instantaneous polarization shows large fluctuations in azimuth and apparent angle of incidence. The rotating angle of incidence after second 6 is indicative of Rayleigh type motion. The RZ trace shows motion alternating between P and  $S_v$  which is also indicated by the angle of incidence and RZ traces of the adaptive polarization results (Figure 20). The azimuth trace of the adaptive results shows predominantly transverse motion with small inclusions of radial motion at 5.3 and 6.0 seconds. In contrast to the predominant southward deviations of the P-waves, the S/Lg group tends to arrive more to the north of the great circle path. This may be used as an argument against lateral refraction but with the plethora of wave types present in the S/Lg part of the wavetrain, adaptive azimuth and angle of incidence traces cannot be completely trusted. The array methods have similar

problems determining a consistent azimuth and slowness (Figures 21 and 22). However, at the beginning of the S/Lg group, both methods give apparent velocities of 4.4 km/sec as indicated by the arrows in the figures.

### Rhode Island Earthquake

An unfiltered record of the vertical component of the Rhode Island event is shown in Figure 23 along with the S/Lg signal and noise spectra. The corner frequency for this event is around 3.3 Hz. Results of polarization analysis are shown in Figures 24 and 25. As was the case in the previous example, the azimuth and angle of incidence traces are much more stable in the adaptive method than in the instantaneous method. They both give roughly the same results, however, especially for the second and third arrivals which have larger amplitudes than the first arrival. The apparent angle of incidence for the entire group of arrivals is between 45 and 55 degrees, similar to the Long Island Sound event. However, unlike the previous event, these P waves arrive farther from the north than the calculated great circle path predicts rather than farther from the south. This is not altogether surprising as the tectonic trend in the area is nearly perpendicular to the calculated great circle paths for these events. Lateral refraction in either direction offers a plausible explanation for the deviations. Beam forming the radial component of the three stations (Figure 26) gives a slightly different result although there is only one small spot where the error is zero (at second 4.4). The azimuth obtained here is 7 degrees south of the calculated great circle path. Beyond second 4.4, the azimuth does swing to the north, but the error trace, although small, is not zero and the slownesses are unreasonable. The slowness determined from both beam forming at second 4.4 and slowness stacking (Figure 27) are identical and give an apparent horizontal velocity of 7.3 km/sec. Assuming from the polarization results a  $49^\circ$  angle of incidence, the near-surface velocity is 5.5 km/sec which agrees well with the velocity obtained from the Long Island Sound event.

Analysis of the S/Lg portion of the Rhode Island event is presented in Figures 28 through 31. The motion in this part of the coda is predominantly transverse but because there is also radial energy arriving at the same time, the results of all methods are in doubt. What radial motion there is, is mostly  $S_y$  as indicated by the RZ and RZ traces of the instantaneous

polarization. The "cleanest" looking results are obtained from the adaptive polarization method. They indicate azimuths that vary drastically and apparent angles of incidence that stay close to zero (horizontally traveling S waves). The apparent velocity near the beginning of the arrival group from the slowness stack and beam forming is around 4.7 km/sec.

### Descriptions of Analysis Software

The software presented in this section has been implemented on both raisun, the SUN microcomputer at RAI, and on css-sun, the SUN at the Center for Seismic Studies. Some of the analysis programs presented in this report have yet to be installed on the SUNs and do not appear here. They are available but need to be converted to the new CSS format. CSS formats for .wfdisc files and for the .wfmk and .wfplot files are included at the end of this section. Examples of the outputs for many of the programs are shown in Figures 35 through 39

Although the methodology for these routines was developed at RAI, many of the subroutines used in their implementation were written for use in the Seismic Parameter Extraction Package (SPEX) (Wang et al., 1983). Access to these routines has been graciously provided by DARPA through the CSS and by the authors.

NAME            azdisp

SYNOPSIS        azdisp (waveform prefix from track (tr))

DESCRIPTION

Azdisp displays data output from the track program with the same format and options used in "display". The major difference between display and azdisp is that azdisp assumes that there are eight input .w files and plots tr.6.w as the error of tr.5.w and tr.8.w as the error of tr.7.w.

SEE ALSO        display, track

Figure 35.

NAME           display

SYNOPSIS       display (event)-(station)-(channel)

#### DESCRIPTION

The display program is an interactive tool with which the operator can display time series data stored in the digital seismic database format as defined by Berger et al. (1983). The user is given control over the placement of the data traces on the screen, their amplitudes, the amount of data to display, and the placement of markers. Most of the operations can be performed on either the entire group of waveforms or on individual traces. Display's main purposes are to allow the user to obtain hard copy of data in flexible format and to make available a method of marking data for further processing.

Display can be initiated in a number of ways depending on the data that one wishes to present. Generally, an event group will contain many different waveform files from several stations with up to nine components each. If display is called with just the event name, then the first nine waveforms listed in the wfdisc file will be displayed. The remaining traces can be accessed through the up/down option to be discussed later. The screen format is saved in the .wfplot file so subsequent calls to display will pick up where the previous session left off. Display may also be called with the event and station or the event and component to present either all components from a particular station for that event or a single component from all stations for that event. If only a single trace is desired, display may be called with event, station, and component.

Upon initialization, the program will display 60 seconds of the requested traces (or the configuration of the previous session) including any markers that may be inside the time interval, identification for each trace, a time line, a button descriptor line, and a horizontal menu. The traces are identified on their immediate left by station and channel, an amplitude measure for the trace, and in small characters the date and time of the beginning of the trace. The button descriptor line at the top of the screen is:

group operations: accept menu item    alternate menu    return

where the underlined items appear in reversed video. Below the button is printed the horizontal menu with the first item replot in reverse video. A menu option is selected by moving the mouse horizontally over the mouse pad until the desired operation appears in reverse video. Pressing the left hand mouse button accept menu item causes the desired action to be stored until the next replot. If the middle alternate menu button is pushed, then the individual operations menu appears. The individual operations work on single traces only in contrast to the group operations which perform their tasks on all of the traces. Pressing the right or return button exits the program and returns the user to the shell.

#### Group operations:

replot	redraws the entire screen. Several operations may be performed before redrawing.
time shift	moves the time window through which the data is displayed. The user is queried as to how many seconds to shift the window. A positive value will move the traces to the left and a negative one will move them to the right.
expand/squash	sets the amount of data to be displayed. The user must type in the number of seconds to be displayed.
amp scale	multiplies the scale factor of the traces by the given amount. The user is queried for the amount.
up/down	moves the entire screen of traces up or down a specified number of inches. If a positive number is specified, the traces will all move up; negative moves them down. Any trace which is moved out of the range of the screen window through this operation will not be displayed on the next <u>replot</u> . Conversely, any trace which moves into the screen window will be plotted.
markers	is an on/off switch for turning the markers on and off. The first call to markers turn them off, the next on and so forth.

- reset            resets the plot parameters to their original values as if display were being called for the first time.
- save raster     creates a file "raster" in the current directory and places a raster screen dump in it.

#### Individual Operations:

- replot           redraws the entire screen. Several operations may be performed before replotting.
- shift trace     works the same way that time shift does in the group options except that after typing in the number of seconds to shift, a vertical bar appears (see yank/put) so that a particular trace may be picked for shifting.
- yank/put        moves a waveform from one position to another on the screen. A vertical bar with a small crosshair appears on one of the traces and the mouse line changes to

choose option: accept    accept    no move

At the bottom of the page on the status line will be displayed the relative time from the beginning of the window to the position of the vertical bar, the absolute time at the vertical bar position, and the amplitude at the position of the small horizontal crosshair. By moving the mouse vertically on its pad, the vertical bar will shift from trace to trace as it enters the amplitude windows of the individual traces. Moving the mouse horizontally moves the bar along the trace. When either the left or middle button are pushed, the waveform on which the vertical bar is drawn is chosen as the one to be moved. A horizontal bar will then appear which can be moved vertically with the mouse. When the desired position is reached, pushing either the left or middle button will determine where that trace will be plotted on the next call to replot. If at any time, the right (no move) button is pushed, control will return the group menu options.



- scale works the same way that amp scale does in the group options except that after typing in the scale factor, the vertical bar appears so that a particular trace may be picked.
- erase removes a waveform from the screen. The trace to be erased is chosen using the vertical bar.
- unerase allows the user to decide which of the traces currently erased should be unerased. Each of the waveforms not displayed is printed on the mouse line in succession

station channel: accept reject no more.

If the accept button is pushed then that trace will be plotted on the next call to replot. Reject means that the trace will remain "erased" and no more returns control to the group menu.

- make marker allows the user to mark individual waveforms. The vertical bar appears and when the proper waveform and time has been chosen the program queries the user for the marker name. The marker is immediately displayed on the trace.
- save raster creates a file named "raster" in the current directory and places a raster screen dump in it.

A plot file is generated on the first call to display. The name of this file is (event).wfplot. It contains information on the placement and size of the traces, how much time to display, which traces to display and what time to start the display. Markers are placed in a marker file (event).wfmk. The marker file contains station, channel, epochal marker time, and marker name.

Figure 36.

NAME filter

SYNOPSIS filter (-n) (event) (station) (channel)

# DESCRIPTION

The corners of an "ideal" filter in the frequency domain are read in from the input parameter file "filterin" along with the filter length and window type. The ideal filter is transformed into the time domain, windowed, retransformed to the frequency domain, and plotted for inspection. If acceptable, the data between "start" and "end" markers in the .wfmk file (or by default the entire trace) is filtered in the time domain. The -n option omits the plotting of the filter response. If the file "filterin" does not exist, one is created in the current directory. The available windows include Bartlett, Hanning, Hamming, Blackman, and rectangular. An ideal filter is specified by giving the frequency and amplitude of the corners. For instance, to build a 100 pt 10 Hz high pass filter with a Hanning window, one might put the following lines in the the "filterin" file.

```
100      number of points in the filter
hn       window (re=rect; hn=Hanning; hm=Hamming; ba=Bartlett; bl=Blackman)
7.0 0.0  frequency amplitude
10.0 1.0 frequency amplitude
```

The zero and nyquist frequencies need not be specified. They are assumed to be the same amplitude as the lowest and highest frequencies given, respectively. Frequency must increase with successive lines in the input file.

FILES filterin

SEE ALSO display

Figure 37.

NAME            nspec

SYNOPSIS        nspec (transform file 1 (tf1)) (tf2) (tf3) (tf4)

# DESCRIPTION

Nspec is an interactive program for a SUN microcomputer that plots up to four spectra on the same graph. After invoking the program, an input parameter file "nspecin" is read (or created if one does not exist) and a button definition line appears at the top of the screen in reverse video. The user is given the option of plotting the spectra, editing the input parameters or quitting the program. Invoking the editing option produces a horizontal mouse menu whose choices are selected by moving the mouse across the mouse pad horizontally and pressing the accept menu item button on the mouse (left hand button). The menu choices are given below.

replot            plot the spectra.

frequency limits user is prompted to input the lower and upper frequency limits.

dB limits        user is prompted to enter the lower and upper dB limits.

average          smoother spectra are produced by averaging adjacent spectral estimates. The number prompted for should be a power of 2.

spectrum type    two types of spectrum are available, either Fourier spectrum for use with transients or a power spectrum for use with noise. The Fourier spectrum is defined as

$$\text{Fourier}(f) = 20 \log_{10} ( |X(f)| )$$

and the power spectrum is defined as

$$\text{power}(f) = 10 \log_{10} ( |X(f)|^2 / (N \Delta t) )$$

$$\text{where } X(f) = \Delta t \sum_{k=1}^N x(t) e^{-i2\pi kt/N}$$

log scale            the frequency scale may be plotted either linear (input 0) or logarithmic (input 1).

When the spectra have been plotted, the user is given the choice via the button descriptor line of saving the raster, editing the inputs or quitting the program. Pushing the left or save raster button creates a file named "raster" in the current directory and writes a versatec raster image of the screen to it. At the end of the program, the input parameter file "rspecin" is updated to reflect the changes made during the course of the program.

FILES            nspecin

SEE ALSO        transform

Figure 38.

NAME           specgram

SYNOPSIS       specgram (event) (station) (channel)

# DESCRIPTION

Specgram is an interactive program for a SUN microcomputer that plots power in dB as a grey scale with horizontal and vertical axis of time and frequency, respectively. The time series being analyzed is plotted just above the spectrogram. Input parameters are read from file "specgin" which is created if it does not exist. The user may choose to plot the spectrogram, edit the input parameters, or quit the program after invoking it by pressing the left, middle, or right button of the mouse. If the edit option is chosen a horizontal menu line appears whose choices are selected by moving the mouse horizontally over the mouse pad. The option is chosen by pushing the left mouse button when the desired option appears in reverse video. The options are described below.

replot           plot the spectrogram.

number of samples the number of points in a single transform is prompted for. This number must be a power of 2.

frequency limits user is prompted to give lower and upper frequency limits.

average          a smoother spectrum is produced by averaging adjacent spectral estimates. The number prompted for should be a power of 2. Resolution along the frequency axis will be decreased.

dB limits        user is prompted to give the lower dB limit and the dB step size. There are nine grey shades so the step size should be appropriate for the total dB range that is being plotted. (The two extremes of dB are given after plotting the spectrogram.)

title            a 30 character title may be entered that will appear across the top of the plot.

When the spectrogram has been plotted, the user is given the choice of saving

the raster, editing the inputs or quitting. If the left or save raster button is pushed, a file named "raster" is created and a versatec raster image of the screen written to it. The portion of the waveform file to be analyzed is marked with "start" and "end" markers in the .wfmk file. If no markers exist, then the first 10 seconds of data are used as the default.

FILES        specgin

SEE ALSO    display

Figure 39.

NAME            track

SYNOPSIS        track (event) (station) (vertical channel)  
(output prefix)

#### DESCRIPTION

Track is an adaptive polarization technique that has been tailored to track the largest component of motion in three component data. The direction of predominant motion is determined by finding the zero value of the zero lag cross correlation over a small window of orthogonal, three component data. The size of the cross correlation window is read in from an input parameter file "aziin" (one is created by the program if it does not already exist). The length of the input data to be analyzed is set by "start" and "end" markers in the event.wfmk file. If no markers are present, the entire trace is analyzed.

Output traces include the vertical, adapted radial, and adapted transverse components of motion; the product of the adapted radial and vertical traces; the azimuth and its error; and the angle of incidence and its error. The results should be displayed using "azdisp" on a SUN microcomputer.

FILES            aziin

SEE ALSO        azdisp

Figure 35.

NAME            transform

SYNOPSIS        transform (event) (station) (channel)

# DESCRIPTION

A real time series, or a specified portion of a real time series, is transformed into the frequency domain. The program checks for "start" and "end" markers in the .wfmk file. If they exist that portion of the data is transformed; if not, the lesser of the entire file or 10 seconds is transformed. Output is placed in the file event.#.t, where event and # correspond to the .w file from which the data was taken. The output file is  $2^{n+2}$  samples long where n is the power of 2 greater than the number of input samples. Frequency ranges from zero to nyquist with a real and imaginary sample at each frequency.

x(0) = zero frequency real part  
 x(1) = zero frequency imaginary part  
 :  
 :  
 :  
 x( $2^n$ ) = nyquist frequency real part  
 x( $2^n+1$ ) = nyquist frequency imaginary part

The transform is defined by

$$X(f) = \Delta t \sum_{K=1}^N x(t) e^{-i2\pi kt/N}$$

where t is time, f is frequency,  $\Delta t$  is the sample interval and N is the total number of samples being transformed.



File Formats:

## wfdisc

<u>NAME</u>	<u>FORMAT</u>	<u>CHARACTER POSITION</u>	<u>DESCRIPTION</u>
date	i8	1-8	julian date
time	f15.3	10-24	epoch time
sta	a6	26-31	station code
chan	a2	33-34	channel code
nsamp	i8	36-43	number of points
smprat	f11.7	45-55	sample rate (in samples/sec)
calib	f9.6	57-65	nominal calibration
calper	f7.4	67-73	calibration period
instyp	a6	78-80	instrument code
segtyp	a1	82-82	indexing method
dattyp	a2	84-85	numeric storage
clip	a1	87-87	clipping flag
chid	i8	89-96	instrument id
wfid	i8	98-105	waveform id
dir	a30	107-136	waveform directory
file	a20	138-157	waveform data file
foff	i10	159-168	byte offset
adate	i8	170-177	date last accessed
remark	a30	179-208	comment

## wfmk

<u>NAME</u>	<u>FORMAT</u>	<u>CHARACTER POSITION</u>	<u>DESCRIPTION</u>
sta	a6	1-6	station
chan	a2	8-9	channel
mktime	f15.3	11-25	epochal marker time
mark	a30	27-56	marker name

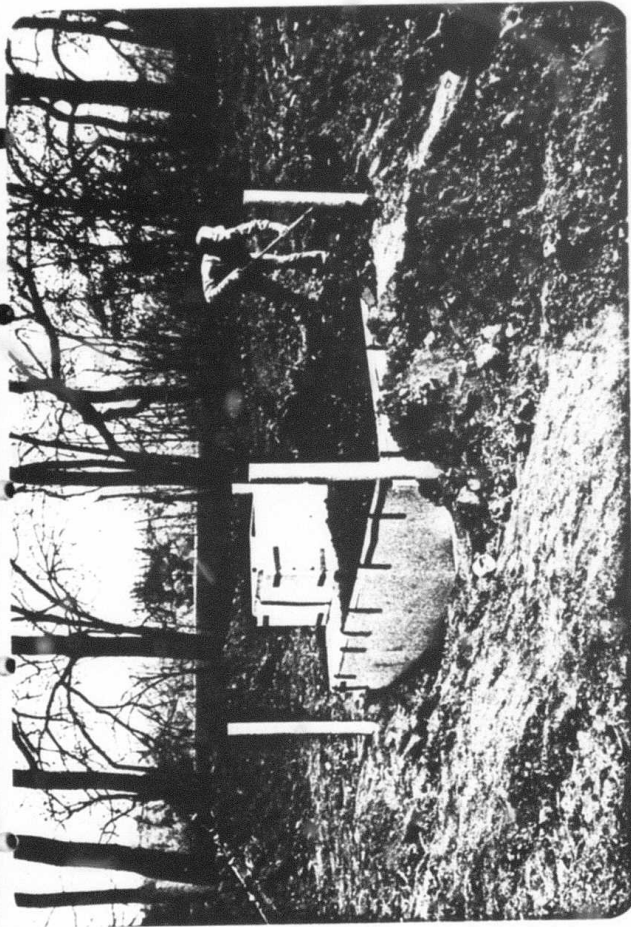
## wfplot

<u>NAME</u>	<u>FORMAT</u>	<u>CHARACTER POSITION</u>	<u>DESCRIPTION</u>
sta	a6	1-6	station
chan	a2	8-9	channel
y-pos	f8.5	11-18	vertical screen position
y-siz	f8.5	20-27	vertical window size
start-time	f15.3	29-43	display start time
end-time	f15.3	45-59	display end time
amp-scale	f8.4	61-68	amplitude scale
amp-units	a8	70-77	amplitude units
remark	a30	79-108	comment/remark

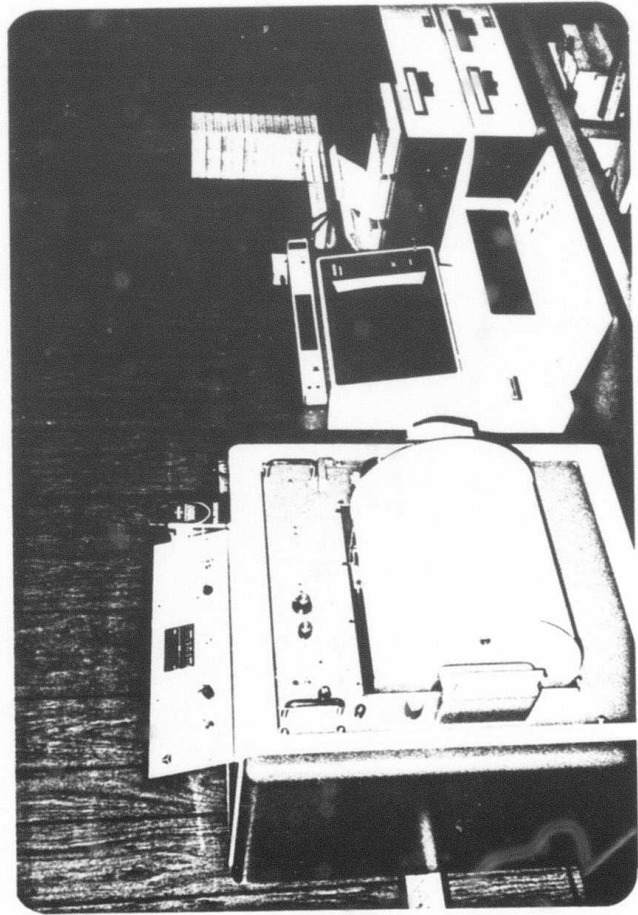
## References

- Bache, T.C., H.J. Swanger, and B. Shkoller, 1980, Synthesis of Lg in Eastern United States Crustal Models with Frequency Independence Q, Semi-Annual Technical Report to DARPA, Systems, Science, and Software, SSS-R-81-4668, 114 p., La Jolla, California.
- Berger, J., R.C. Goff, R.G. North, W.E. Farrell, M.A. Tiberio, B. Shkoller, 1983, Center for Seismic Studies: Prototype Design and Development, S-Cubed Report No. SSS-R-84-6354 submitted to AFOSR, S-Cubed, San Diego, California.
- Flinn, E.A., 1965, Signal Analysis Using Rectilinearity and Direction of Particle Motion, Proc. of IEEE, 53, 1874-1876.
- Harvey, D., 1981, Seismogram Synthetics Using Normal Mode Superposition: The Locked Mode Approximation Method, Geophy. J. Roy. Astron. Soc., 66, 37-69.
- Herrmann, R.B. and M.J. Goertz, 1981, A Numerical Study of Peak Ground Motion Scaling, Bull. Seism. Soc. Am., 71, 1963-1980.
- Pearce, R.G., 1977, Fault Plane Solutions Using Relative Amplitudes of P and pP, Geophys. J. R. Astr. Soc., 50, 381-394.
- Phinney, R.A. and S.W. Smith, 1963, Processing of Seismic Data from an Automatic Digital Recorder, BSSA, vol. 53, no. 3, 549-562.
- Samson, J.C. and J.V. Olson, 1981, Data-Adaptive Polarization Filters for Multichannel Geophysical Data, Geophysics, vol. 46, no. 10, 1423-1431.
- Shimshoni, M. and S.W. Smith, 1964, Seismic Signal Enhancement with Three-Component Detectors, Geophysics, vol. 29, no. 5, 664-671.

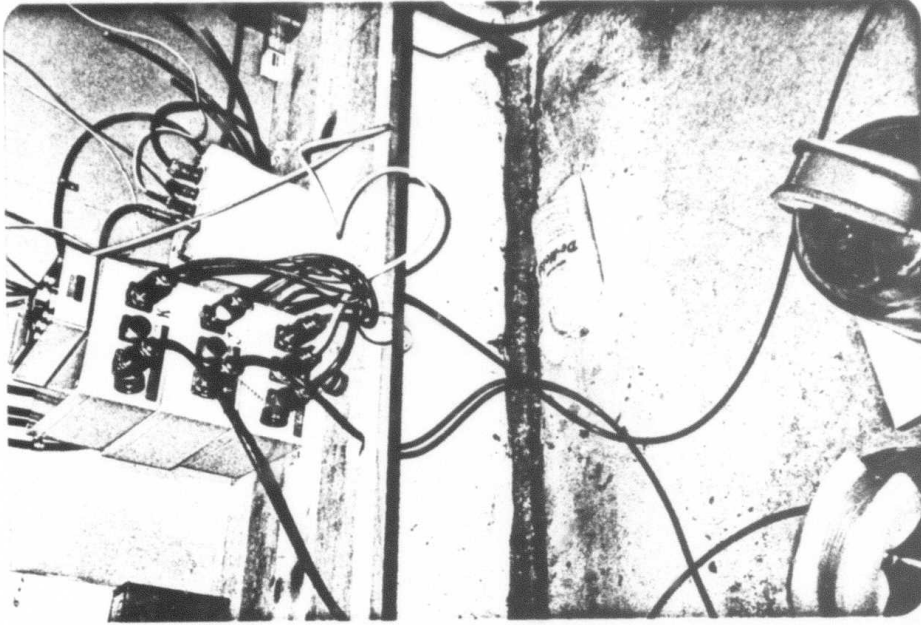
- Street, R.L. and F.T. Turcotte, 1977, A Study of Northeastern North American Spectral Moments, Magnitudes, and Intensities, Bull. Seism. Soc. Am., 67, 599-614.
- Sutton, G.H. and P.W. Pomeroy, 1963, Analog Analysis of Seismograms Recorded on Magnetic Tape, J. Geophys. Res., 68, 2791-2815.
- Sutton, G.H. and D.J. Harvey, 1981, Complete Synthetic Seismograms to 2 Hz and 1000 km for an Oceanic Lithosphere (Abstract), EOS, 62, 327.
- Taylor, S.R. and Bern J. Qualheim, 1983, Regional Seismic Test Network Site Descriptions, Lawrence Livermore Laboratory Report No. 19769 submitted to DOE, Lawrence Livermore Laboratory, Livermore, California.
- Wang, J., R.M. Rother, V.L. Hutchison, J.H. Alexander, J.B. Minster, 1983, Seismic Parameter Extraction Package (SPEX), S-CUBed Report No. SSS-R-84-6423 submitted to AFOSR, S-Cubed, San Diego, California.



A.



C.



B.

Figure 1. A- SRNY seismic vault exterior. B- Seismic vault interior. C- Recording station.

## SEISMIC VAULT

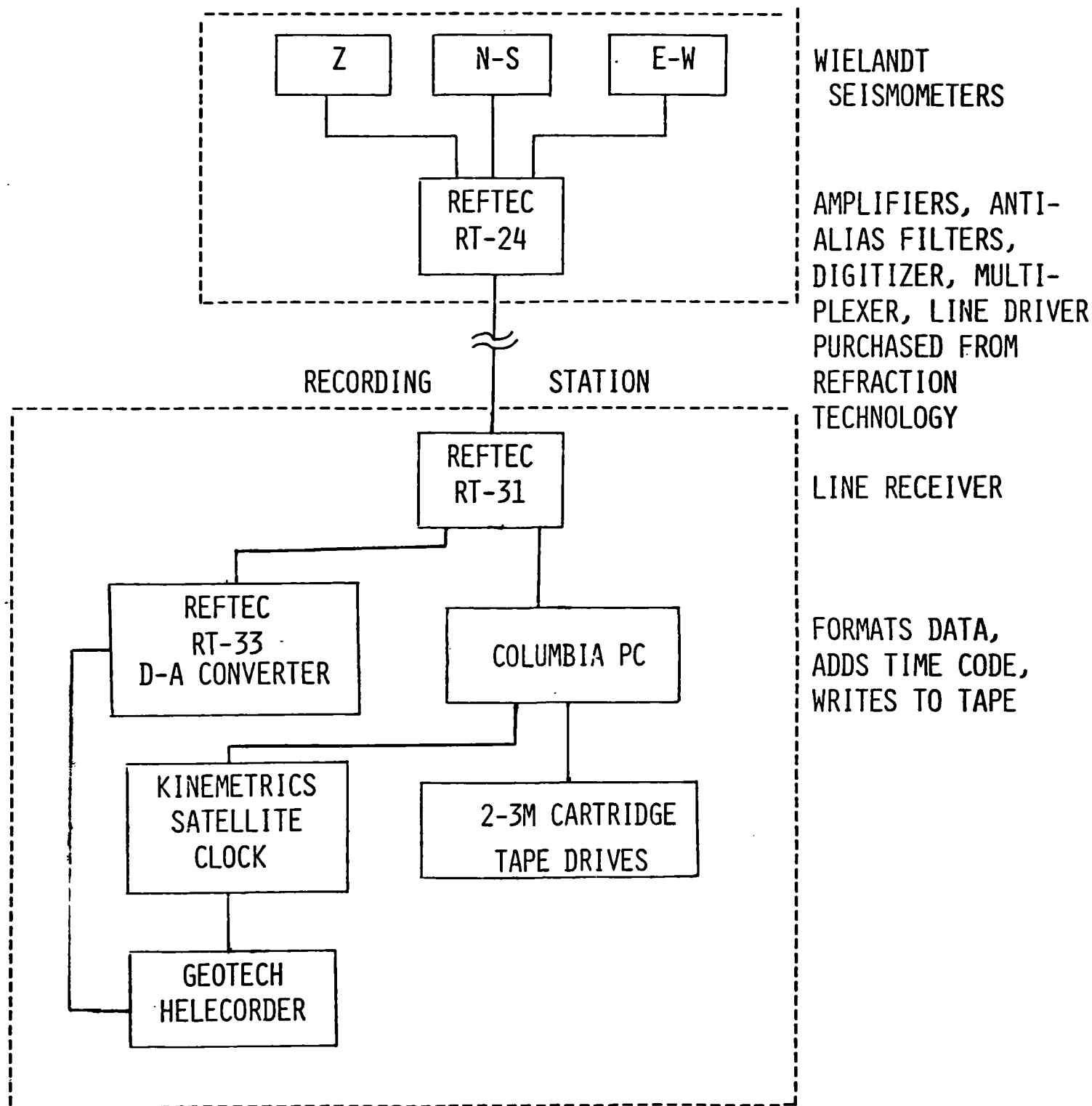


Figure 2. Digital seismic recording system.

# INSTANTANEOUS POLARIZATION ANALYSIS SYNTHETIC P-WAVE $I=45^\circ$

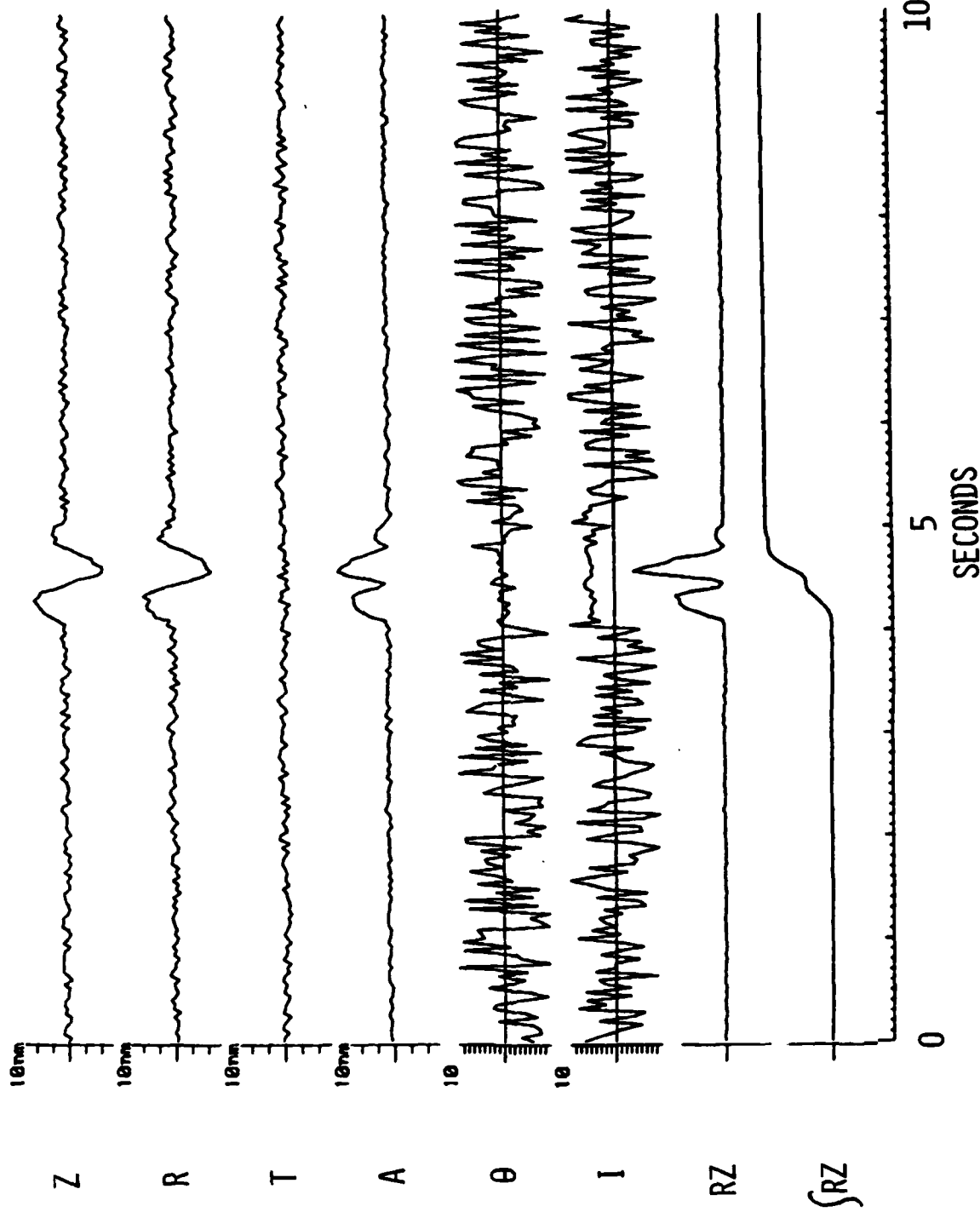


Figure 3. Output of instantaneous polarization filtering program. Traces, from top to bottom, are vertical; radial horizontal, i.e. in the great circle direction; transverse horizontal; total amplitude; azimuth deviation from the radial direction; apparent angle of incidence between the radial and vertical components; product of radial and vertical; and integral of RZ. Scales for  $\theta$  and  $I$ , 10/division.

# INSTANTANEOUS POLARIZATION ANALYSIS SYNTHETIC RAYLEIGH WAVE

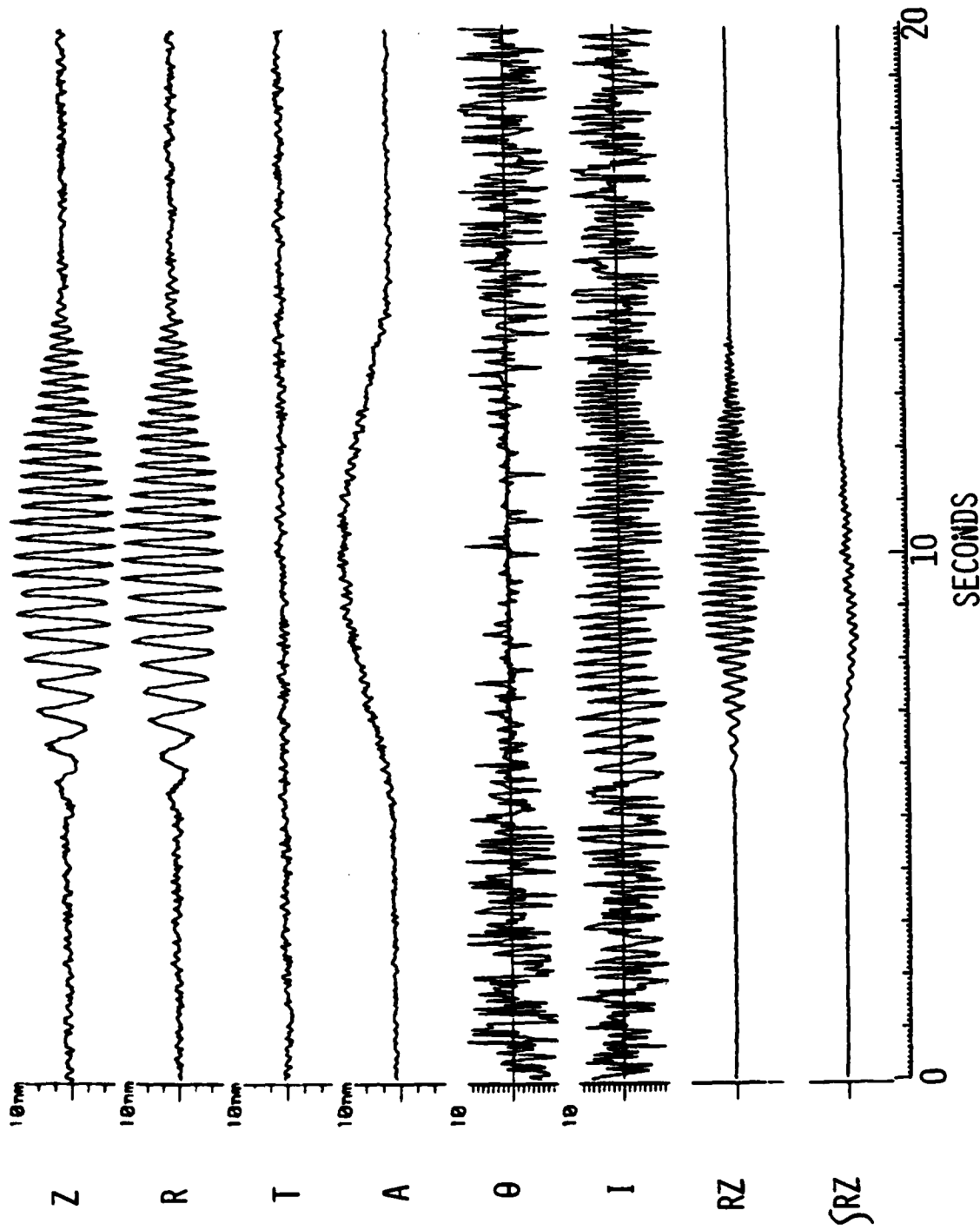


Figure 4. Format is same as Figure 2.



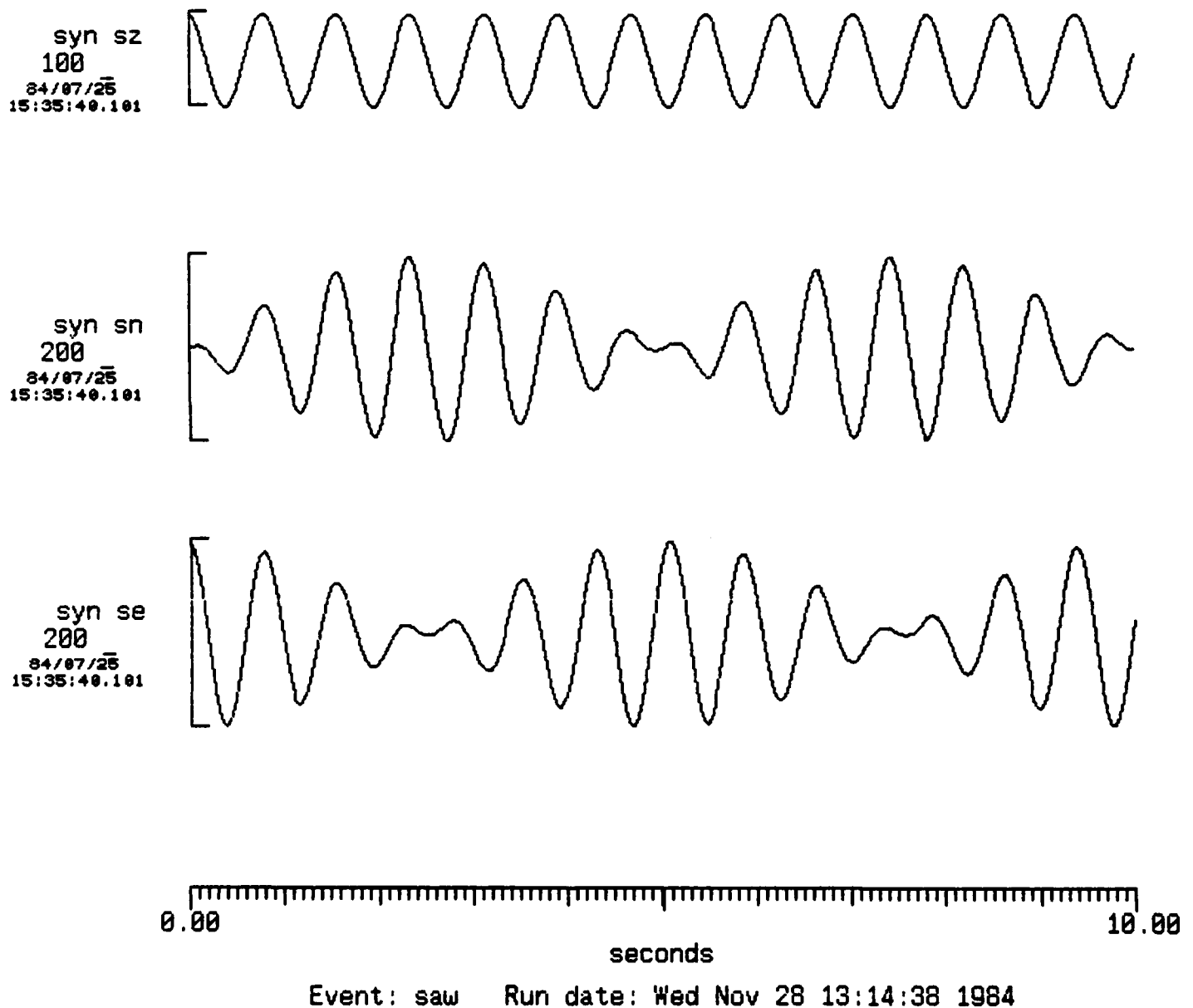
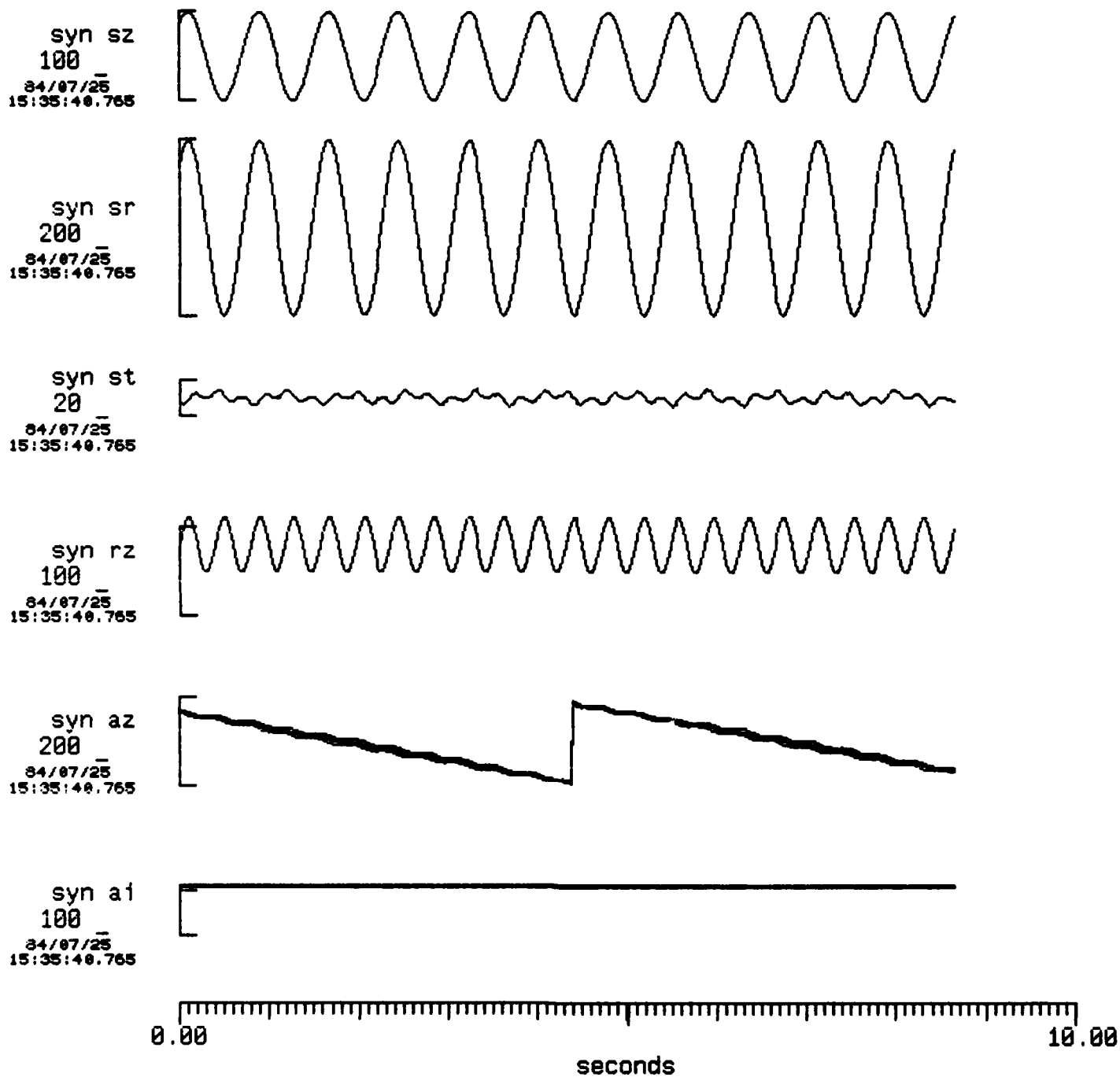


Figure 5. Vertical (sz), north-south horizontal (sn), and east-west horizontal (se) components of a signal rotating in azimuth but with constant angle of incidence.



Event: trsaw Run date: Wed Nov 28 13:20:21 1984

Figure 6. Output of the track program for a signal rotating in azimuth but with a constant angle of incidence. sz=vertical; sr=adapted radial; st=adapted transverse; rz=radial times vertical; az=azimuth with error bars; ai=angle of incidence with error bars.

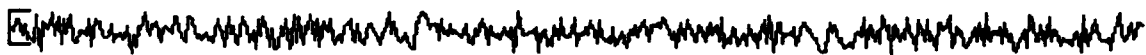
syn sz  
5000  
84/07/25  
15:35:40.765



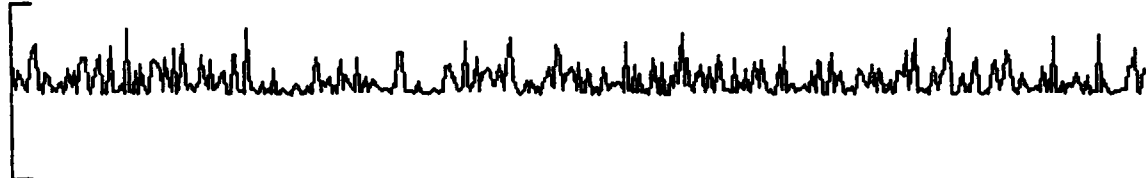
syn sr  
10000  
84/07/25  
15:35:40.765



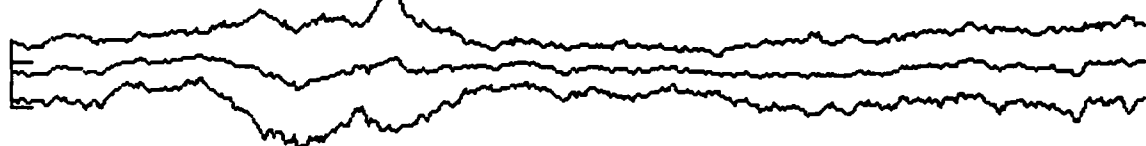
syn st  
2000  
84/07/25  
15:35:40.765



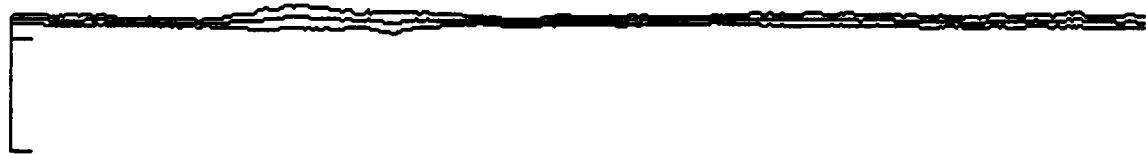
syn rz  
10000  
84/07/25  
15:35:40.765



syn az  
20  
84/07/25  
15:35:40.765



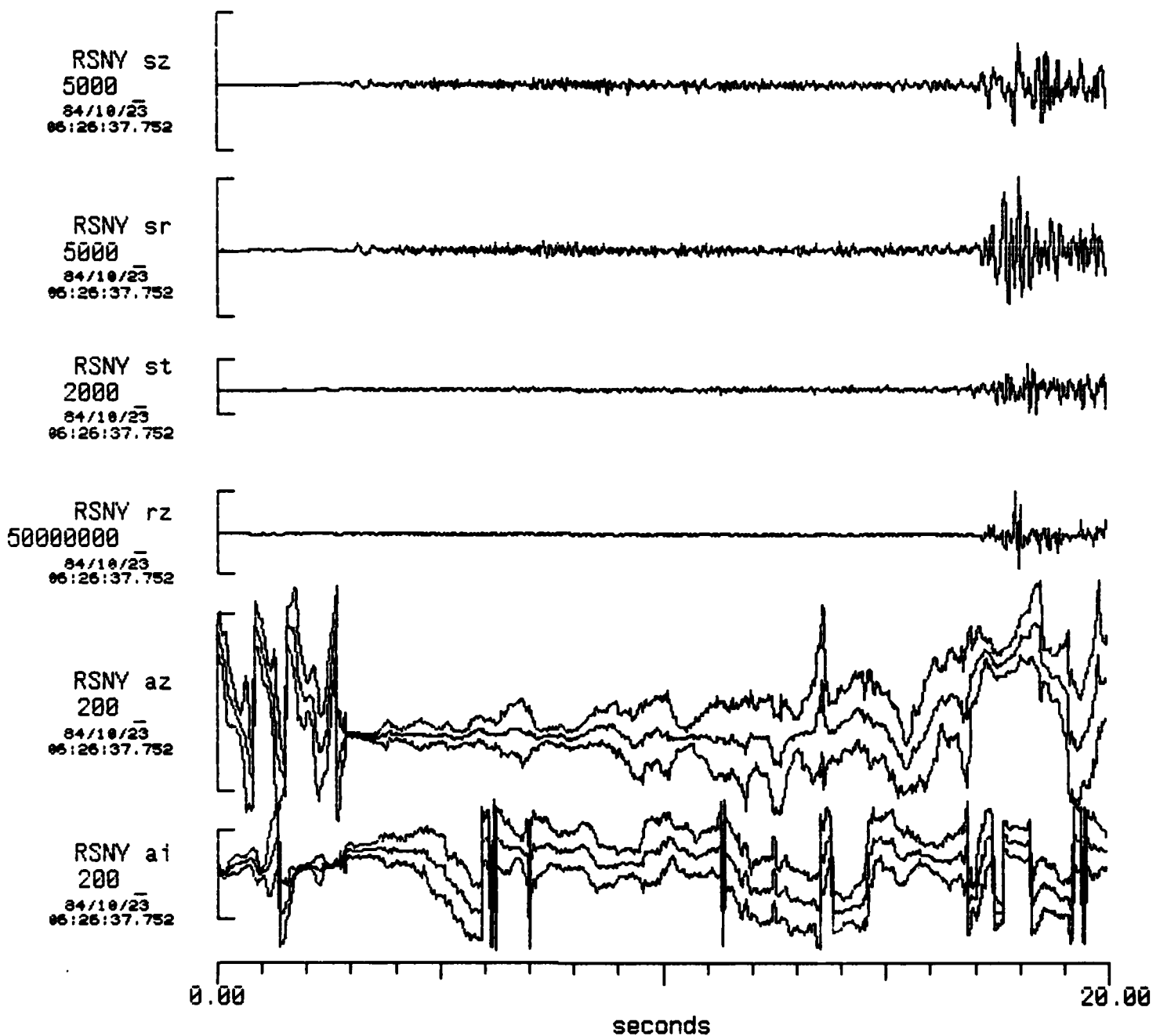
syn ai  
100  
84/07/25  
15:35:40.765



0.00 8.00  
seconds

Event: trsaw Run date: Wed Nov 28 13:48:54 1984

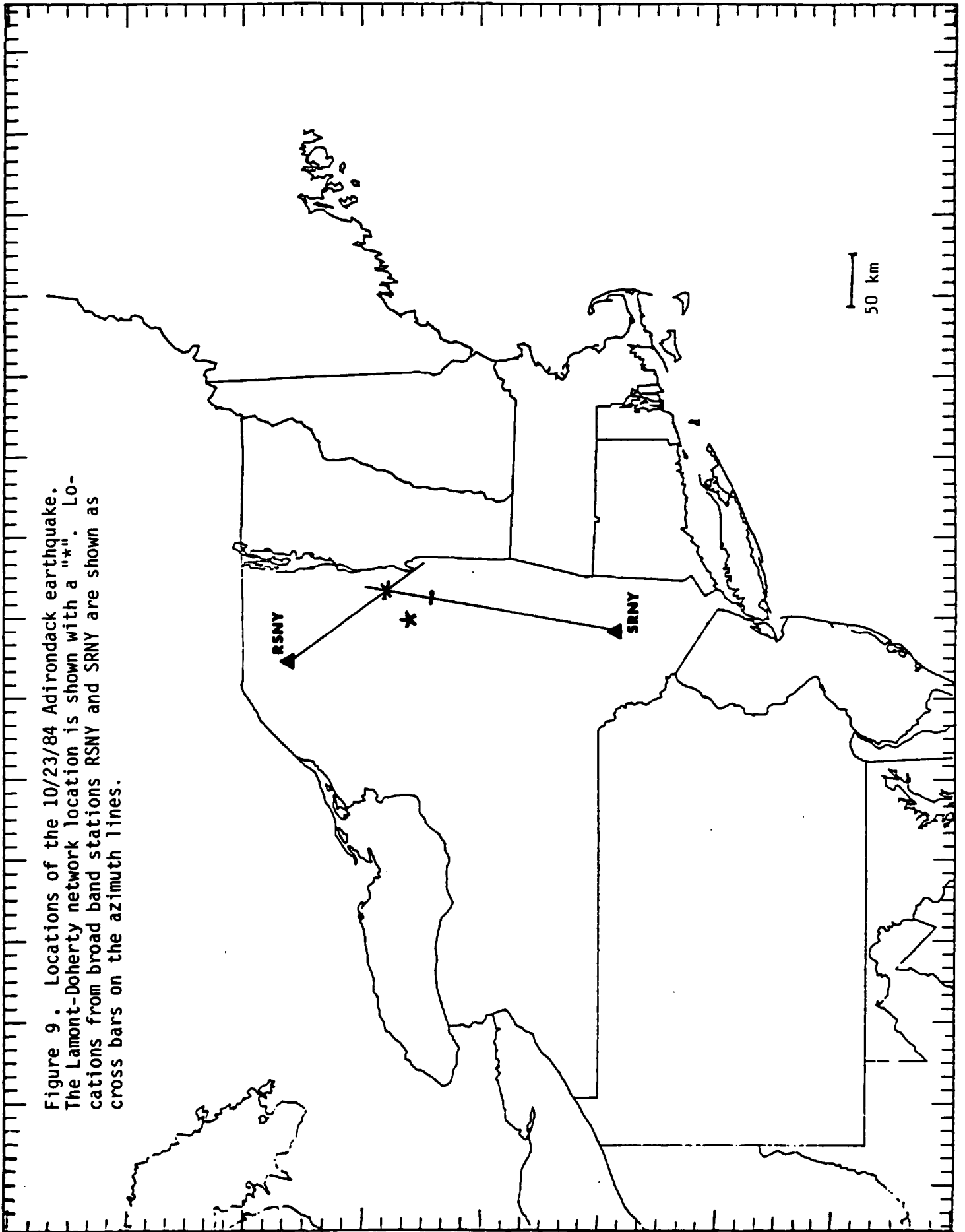
Figure 7. Results of trying to track two different sets of random noise traveling in different directions. One set is traveling to the northeast; the other is traveling due north and is more than twice the amplitude of the first.



Event: trNY Run date: Wed Nov 28 12:51:14 1984

Figure 8. Adaptive polarization analysis of the 10/23/84 Adirondack earthquake recorded at RSNY. sz=vertical; sr=adapted radial component; st=adapted transverse component; rz=product of radial and vertical traces; az=azimuth with error bars; ai=angle of incidence with error bars. Note the stability in the azimuth trace throughout most of the p coda.

Figure 9 . Locations of the 10/23/84 Adirondack earthquake. The Lamont-Doherty network location is shown with a "\*". Locations from broad band stations RSNY and SRNY are shown as cross bars on the azimuth lines.



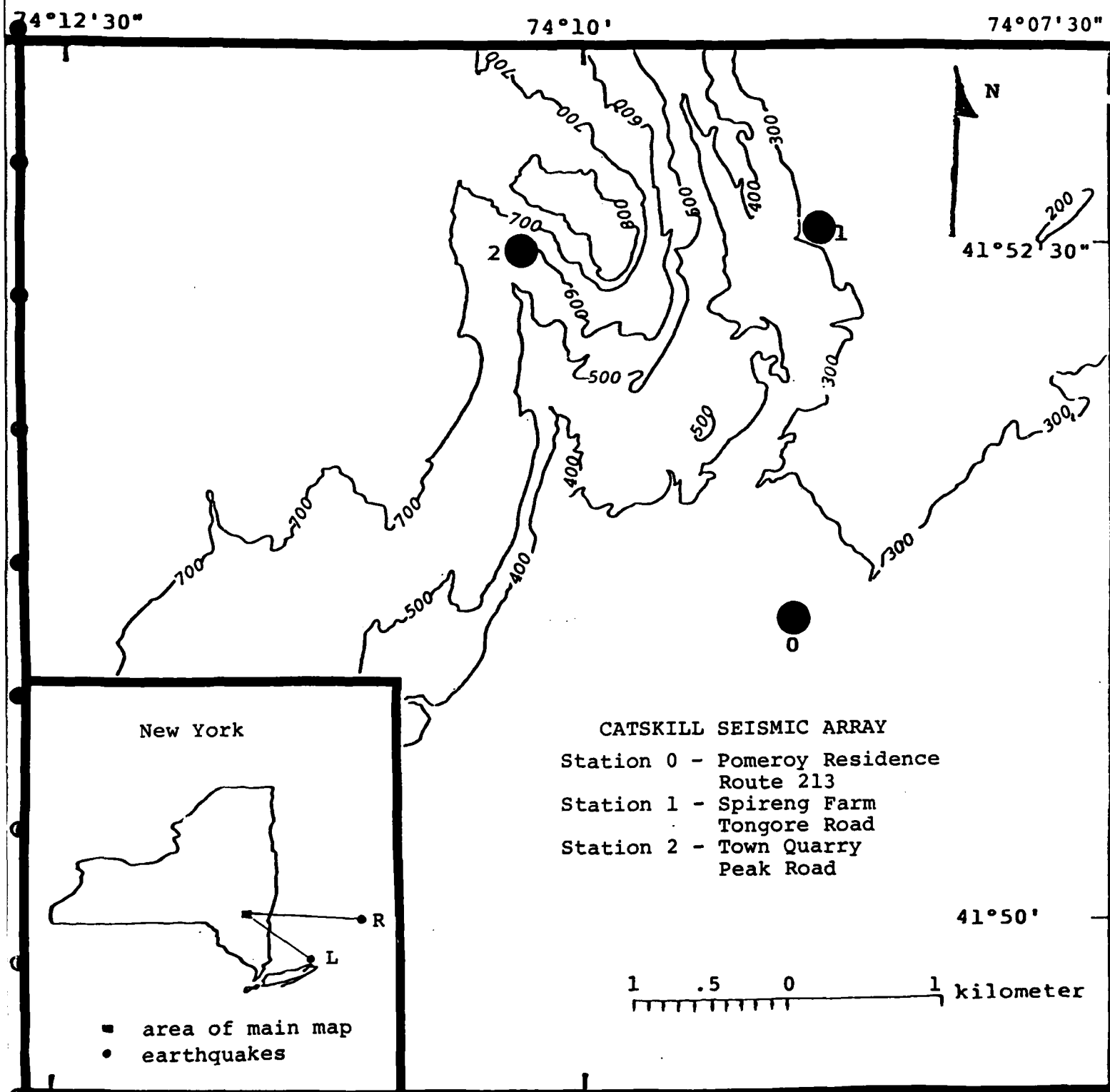


Figure 10. Location map of Catskill Seismic Array. Earthquakes L and R are Long Island Sound and Rhode Island earthquakes, respectively, used in examples of data processing procedures.

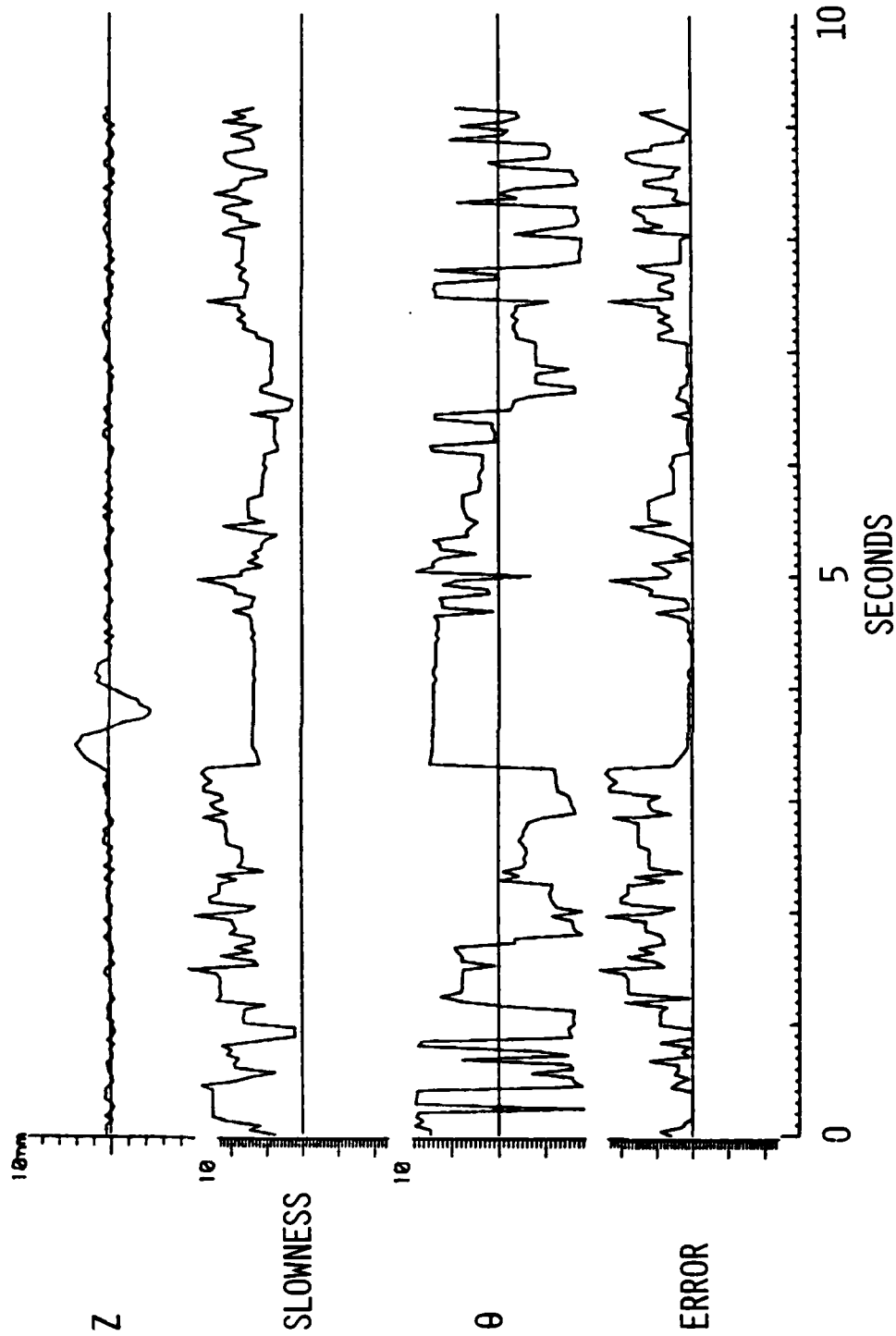


Figure 11. Output of beam forming program. Scale for slowness is .01 sec/km per division;  $\theta$ ,  $10^\circ$ /division; error, samples/division.

## SLOWNESS STACK

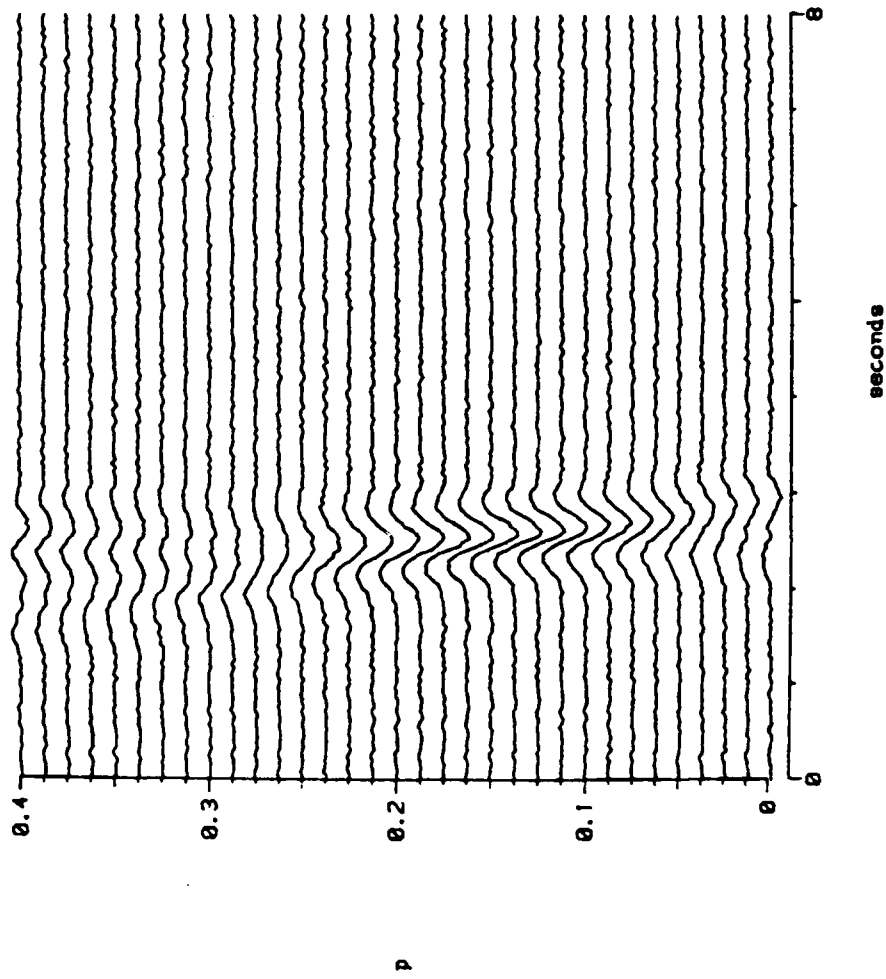
SYNTHETIC P-WAVE  $I=45^\circ$ ,  $P=.14$ 

Figure 12. Slowness stack of a synthetic p-wave. Units of  $p$  (slowness) are sec/km.



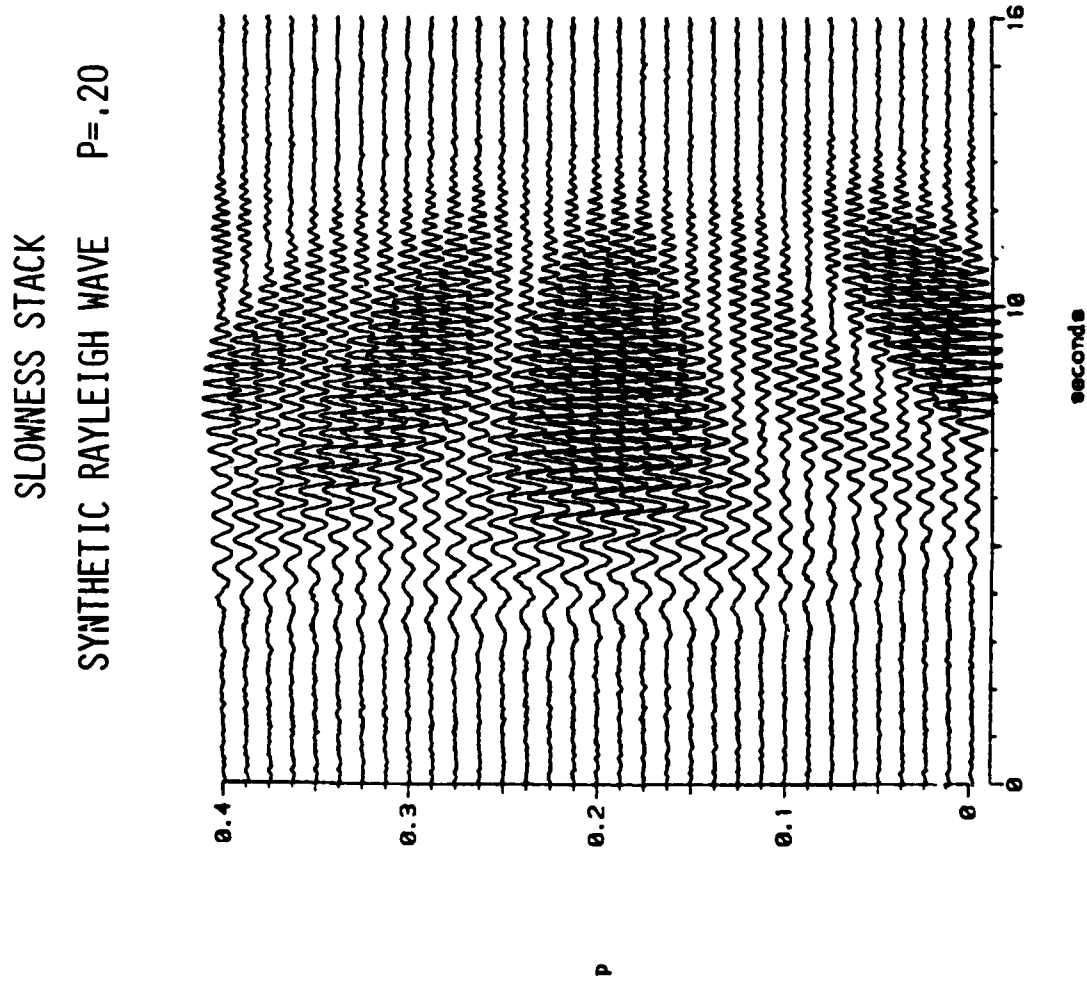
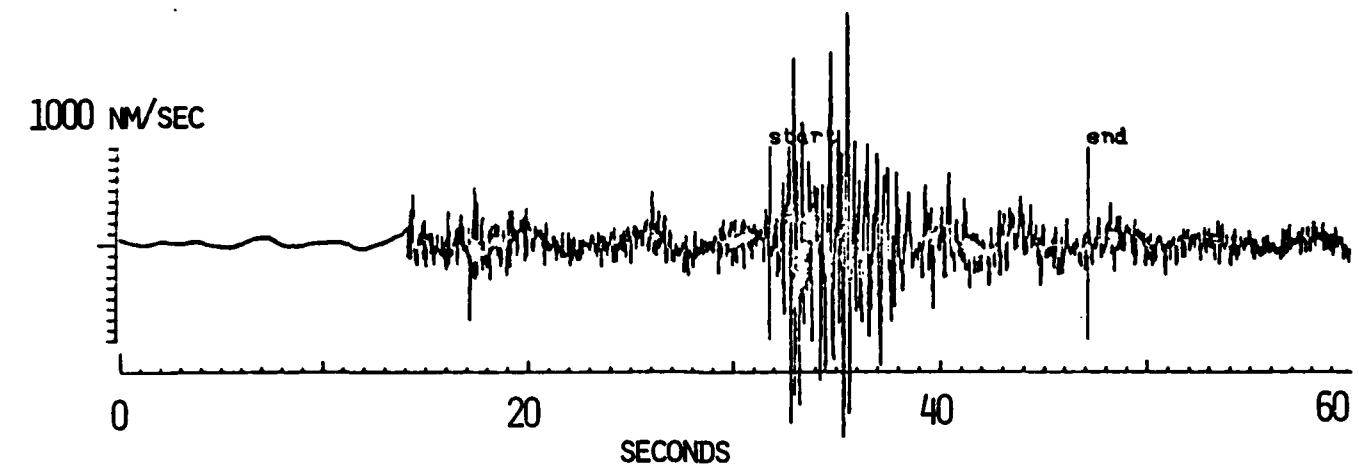


Figure 13. Format same as Figure 8.



## LONG ISLAND SOUND

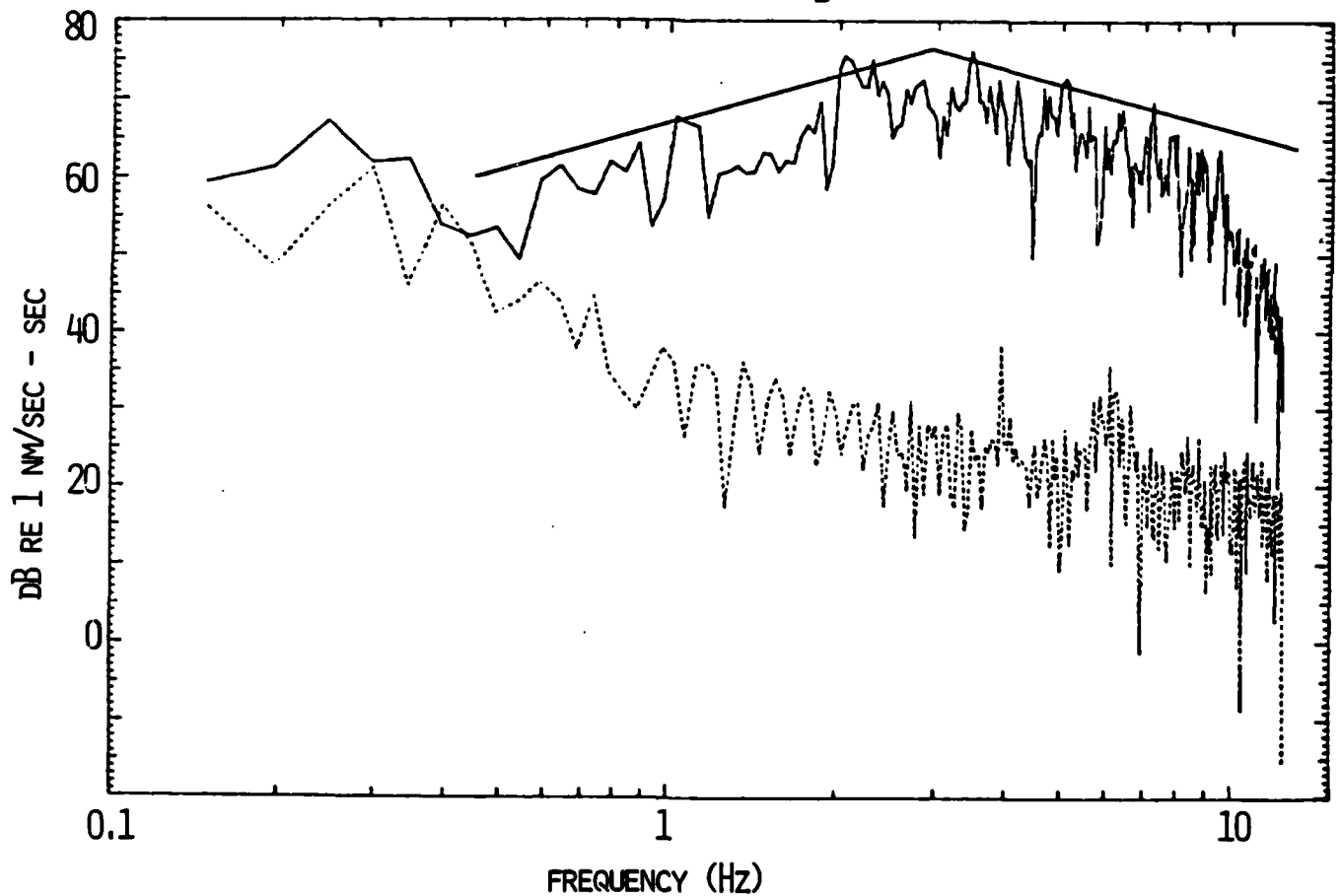
 $D = 1.4^{\circ}$  $M_B = 3.5$ 

Figure 14. S/Lg and noise spectra of the vertical component of ground velocity recorded at CSA for the Long Island Sound event. Straight lines are  $\pm 6$  dB.

LONG ISLAND P-WAVE  
INSTANTANEOUS POLARIZATION

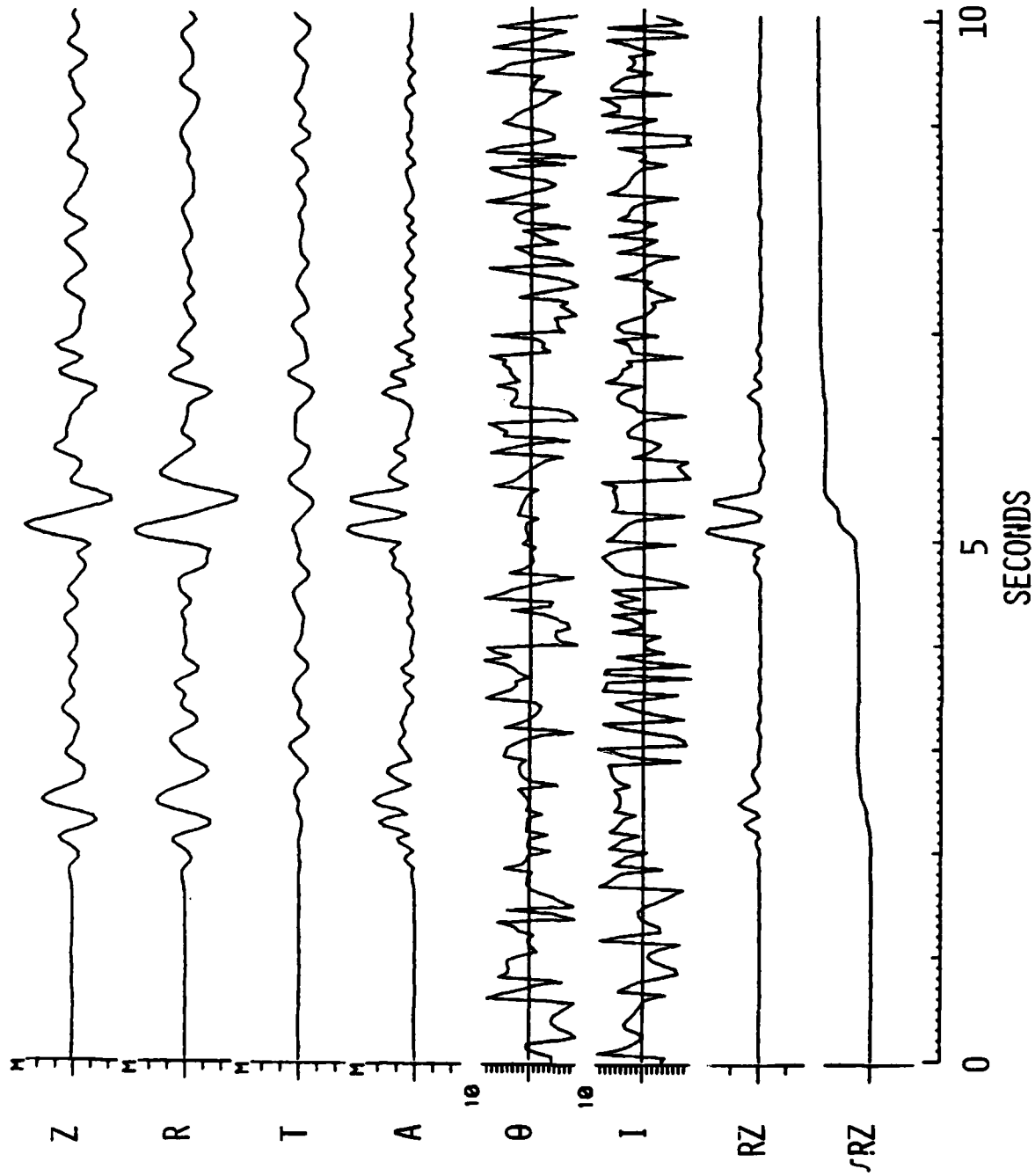


Figure 15. Instantaneous polarization of band pass filtered data (1 to 3 Hz). Format same as Figure 2.

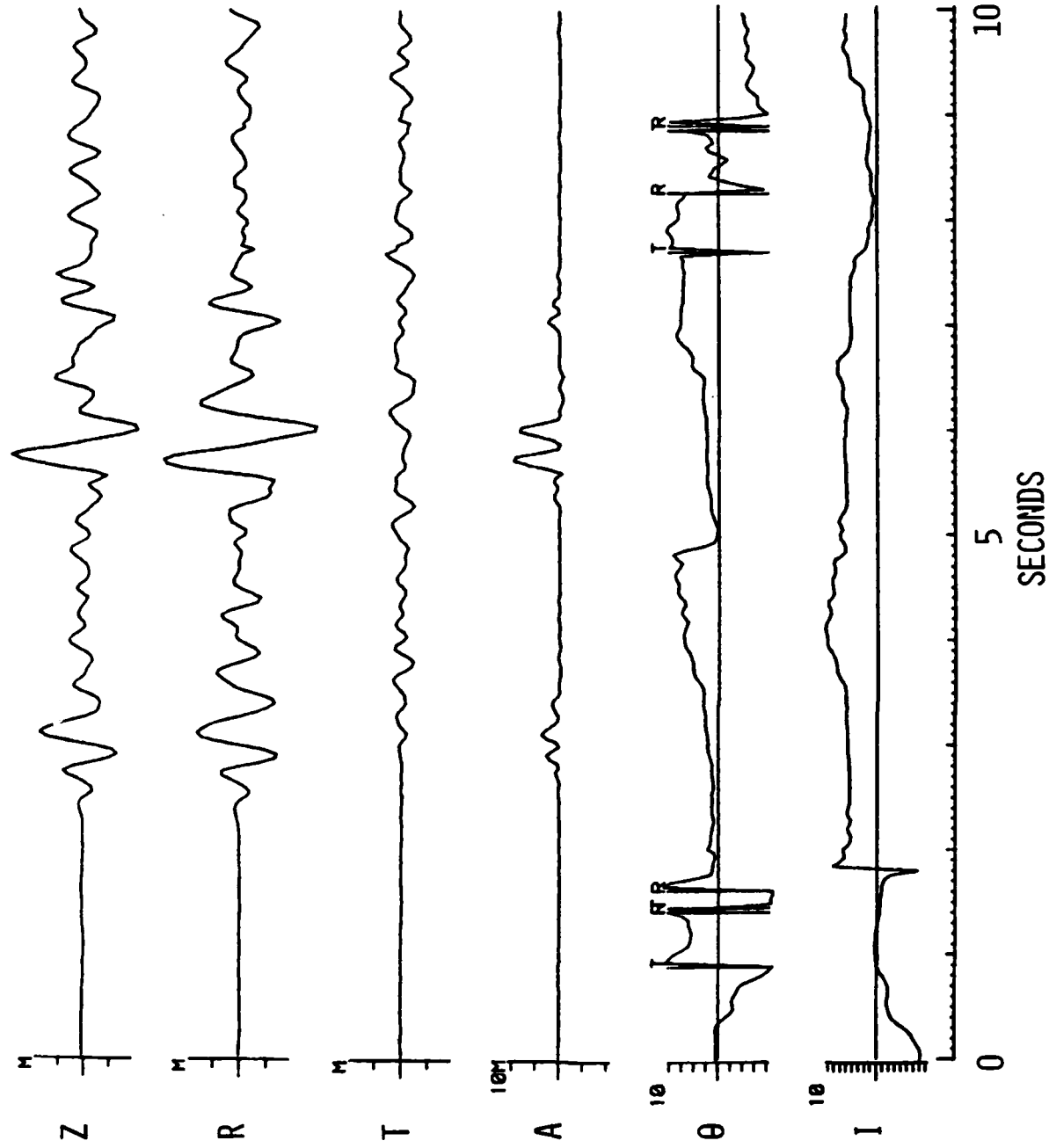


Figure 16. Adaptive polarization of band pass filtered data (1 to 3 Hz). Format same as Figure 4.

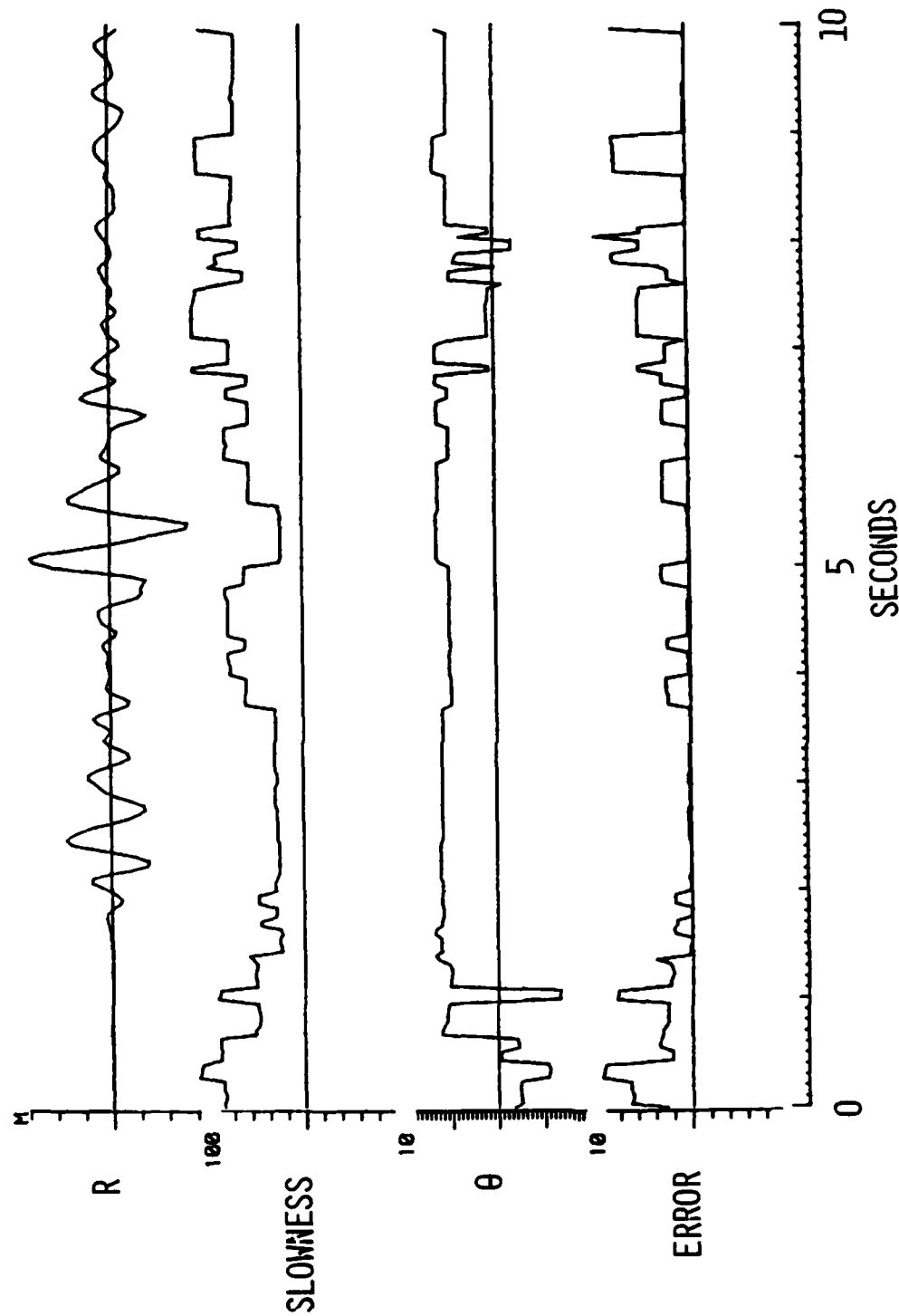


Figure 17. Beam forming of CSA band pass filtered data (1 to 3 Hz). Format same as Figure 7.

LONG ISLAND P-WAVE  
SLOWNESS STACK

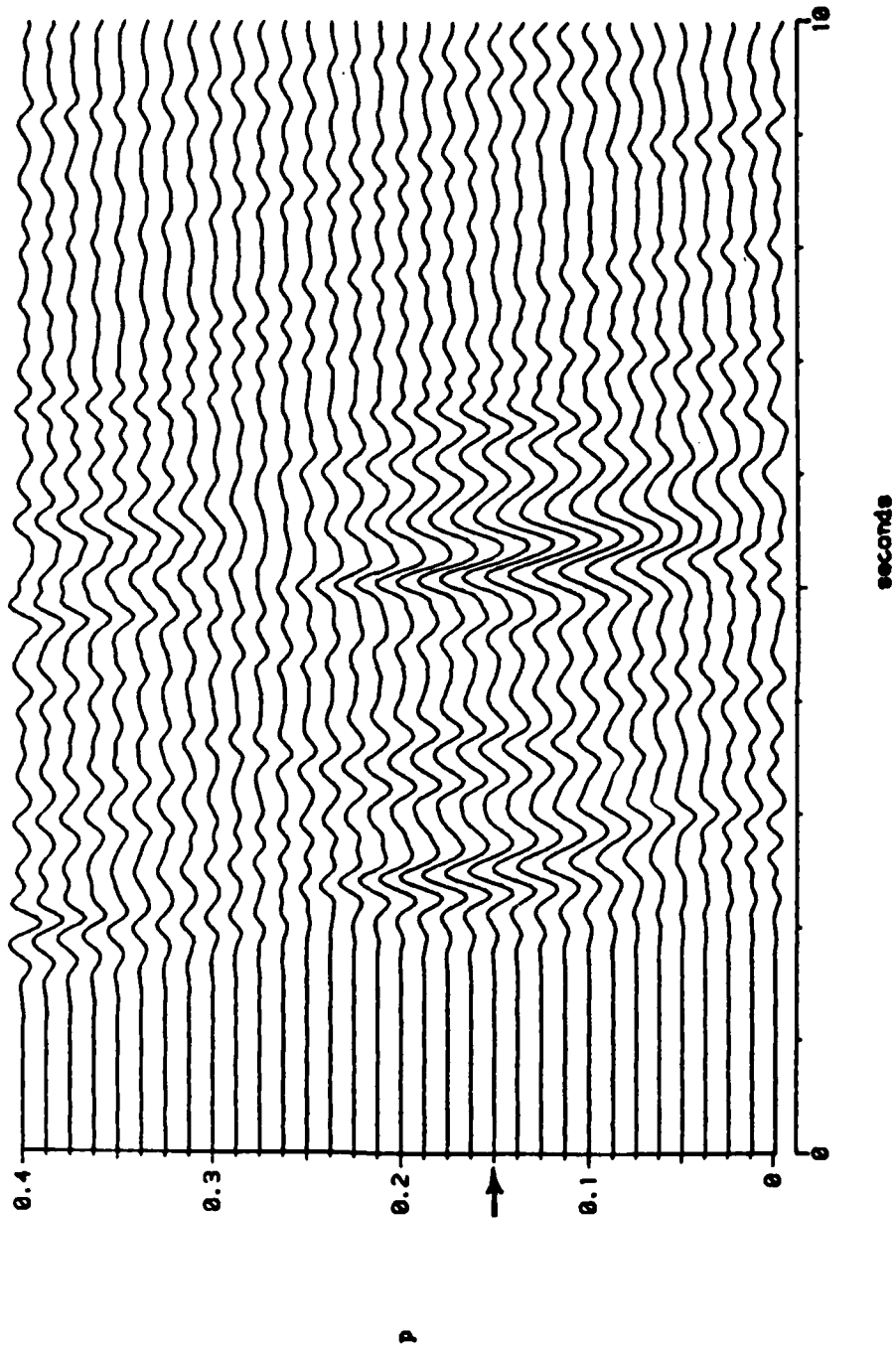


Figure 18. Slowness stack of CSA band pass filtered data (1 to 3 Hz). Format same as Figure 8. Arrow indicates the approximate slowness of the P-wave arrivals.

LONG ISLAND S/Lg  
INSTANTANEOUS POLARIZATION

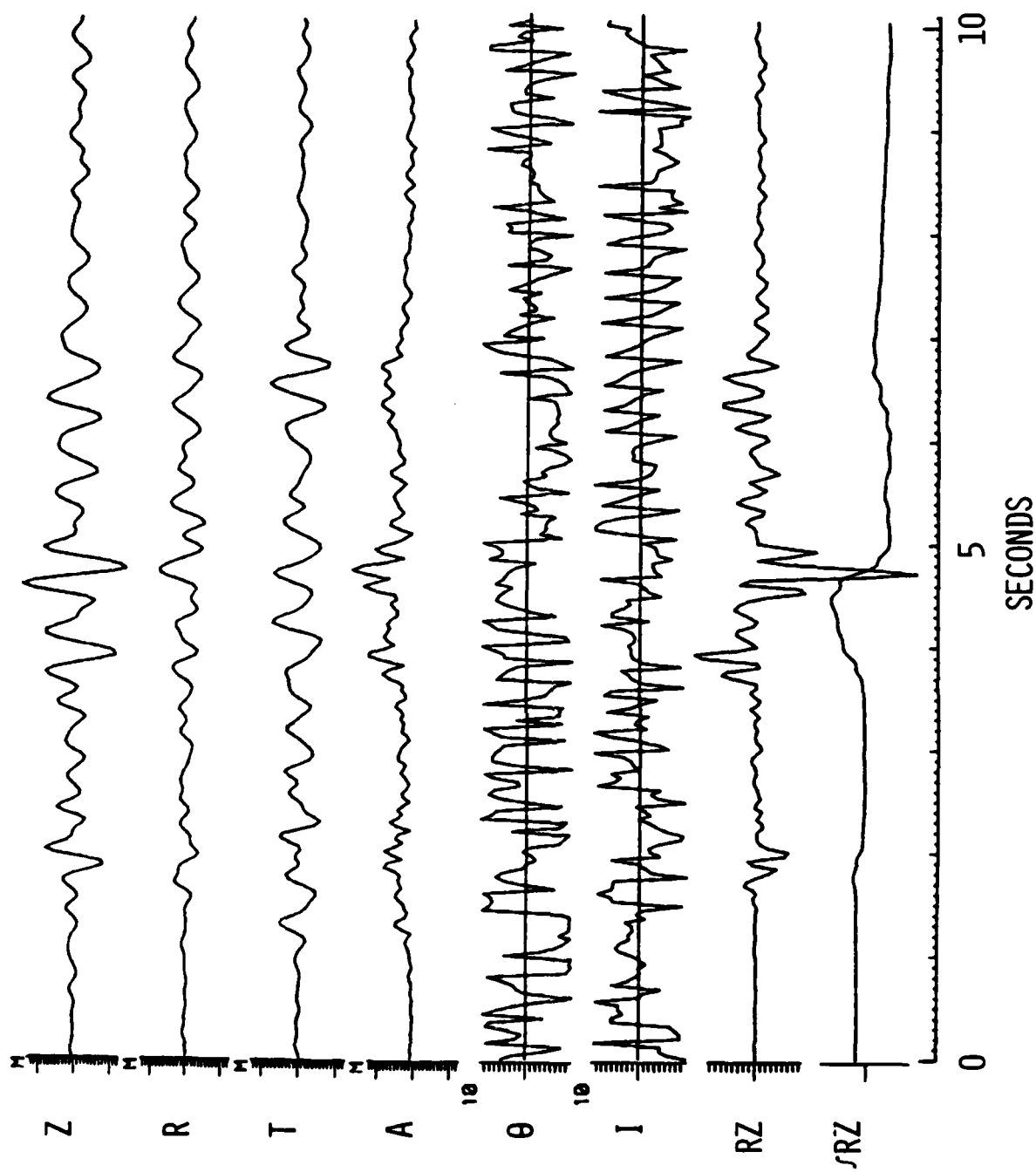


Figure 19. Pass band 1 to 3 Hz. Format same as Figure 2.

LONG ISLAND S/Lg  
ADAPTIVE POLARIZATION

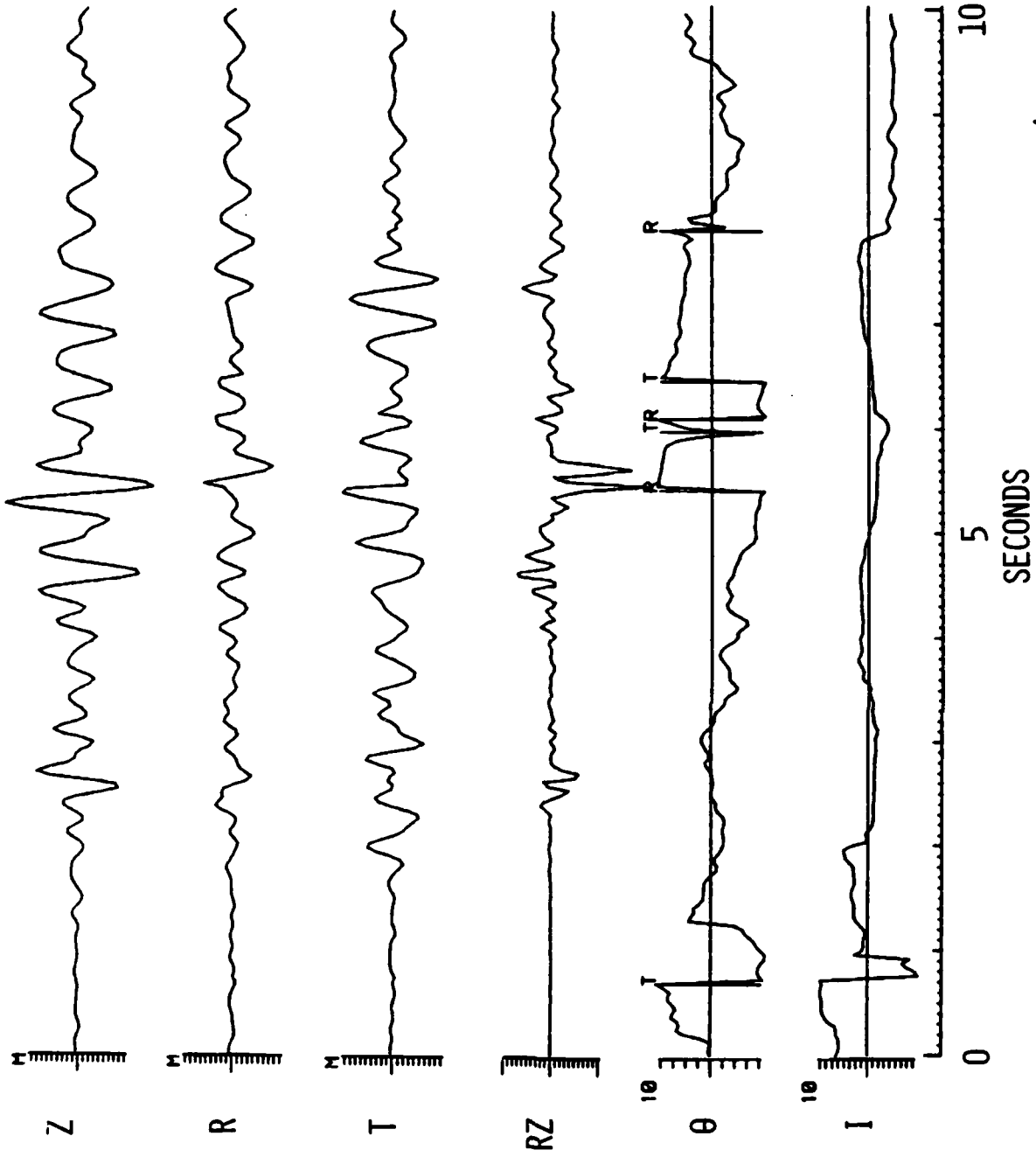


Figure 20. Pass band 1 to 3 Hz. Format same as Figure 4.



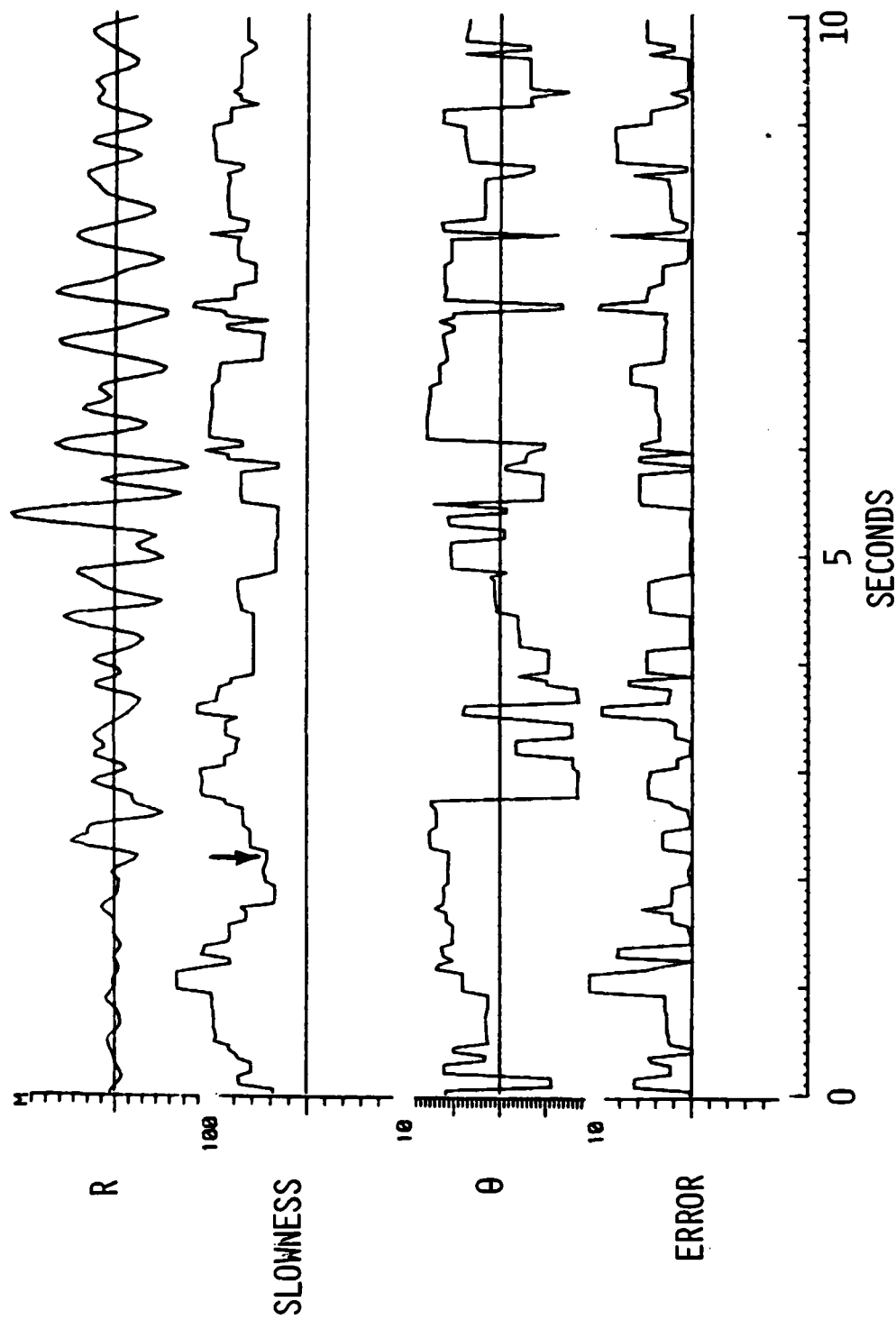


Figure 21. Pass band 1 to 3 Hz. Format same as Figure 7. Arrow indicates the slowness of the first arrival in this group.

LONG ISLAND S/Lg  
SLOWNESS STACK

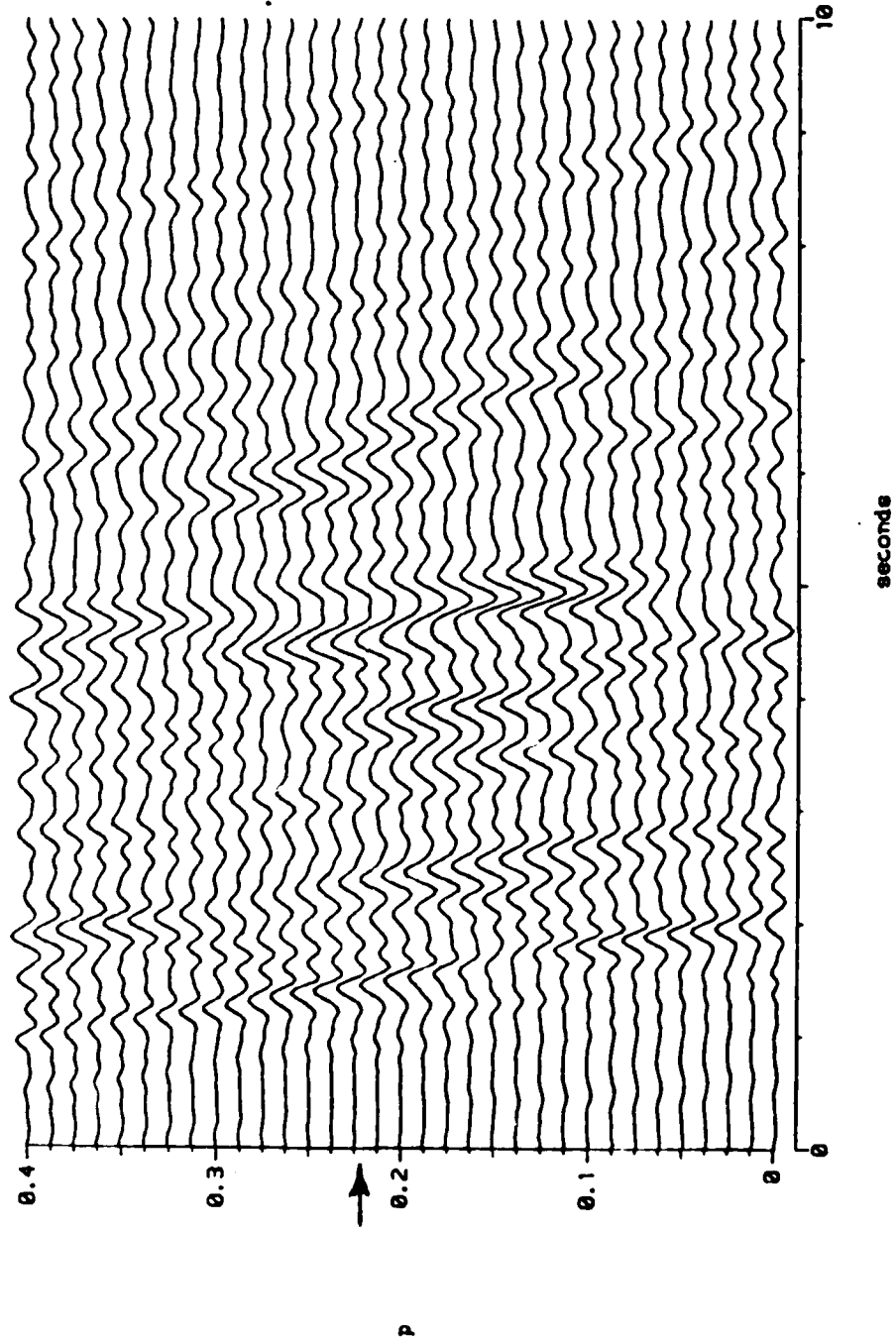


Figure 22. Pass band 1 to 3 Hz. Format same as Figure 8. Arrow indicates the approximate slowness of the first arrival in this group.

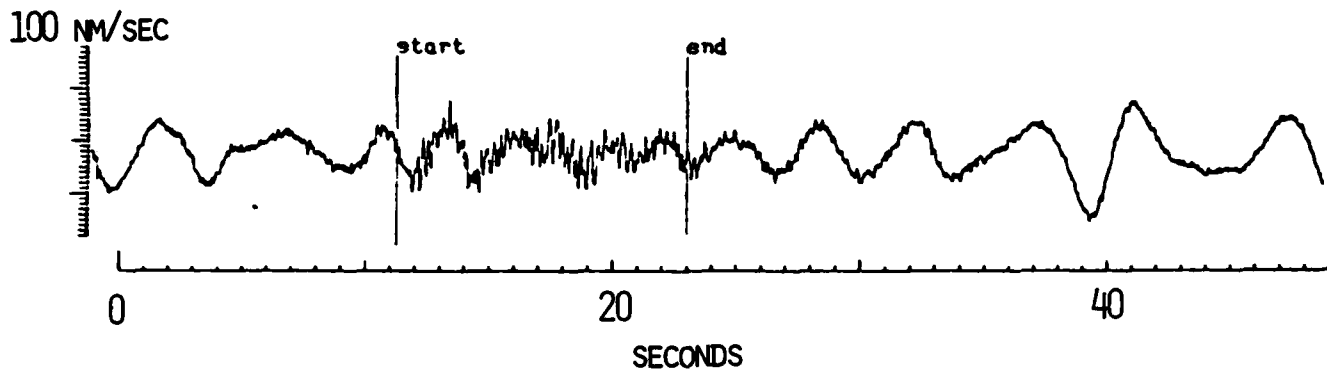
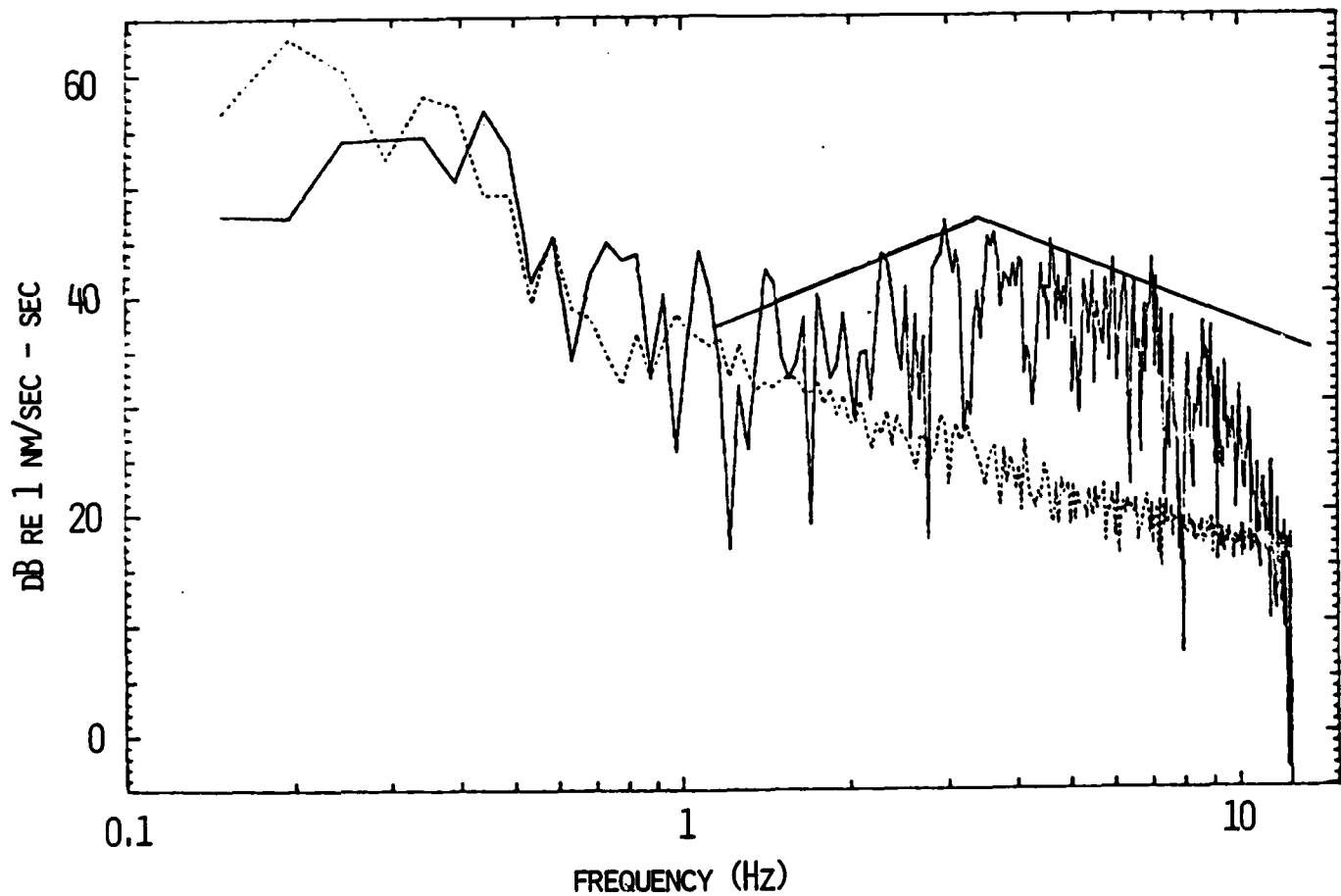
 $D = 2.2^{\circ}$  $M_B = 2.7$ 

Figure 23. S/Lg signal and noise spectra of the vertical component of ground velocity recorded at the CSA for the Rhode Island earthquake. Straight lines are drawn at  $\pm 6$  dB.

# RHODE ISLAND P INSTANTANEOUS POLARIZATION

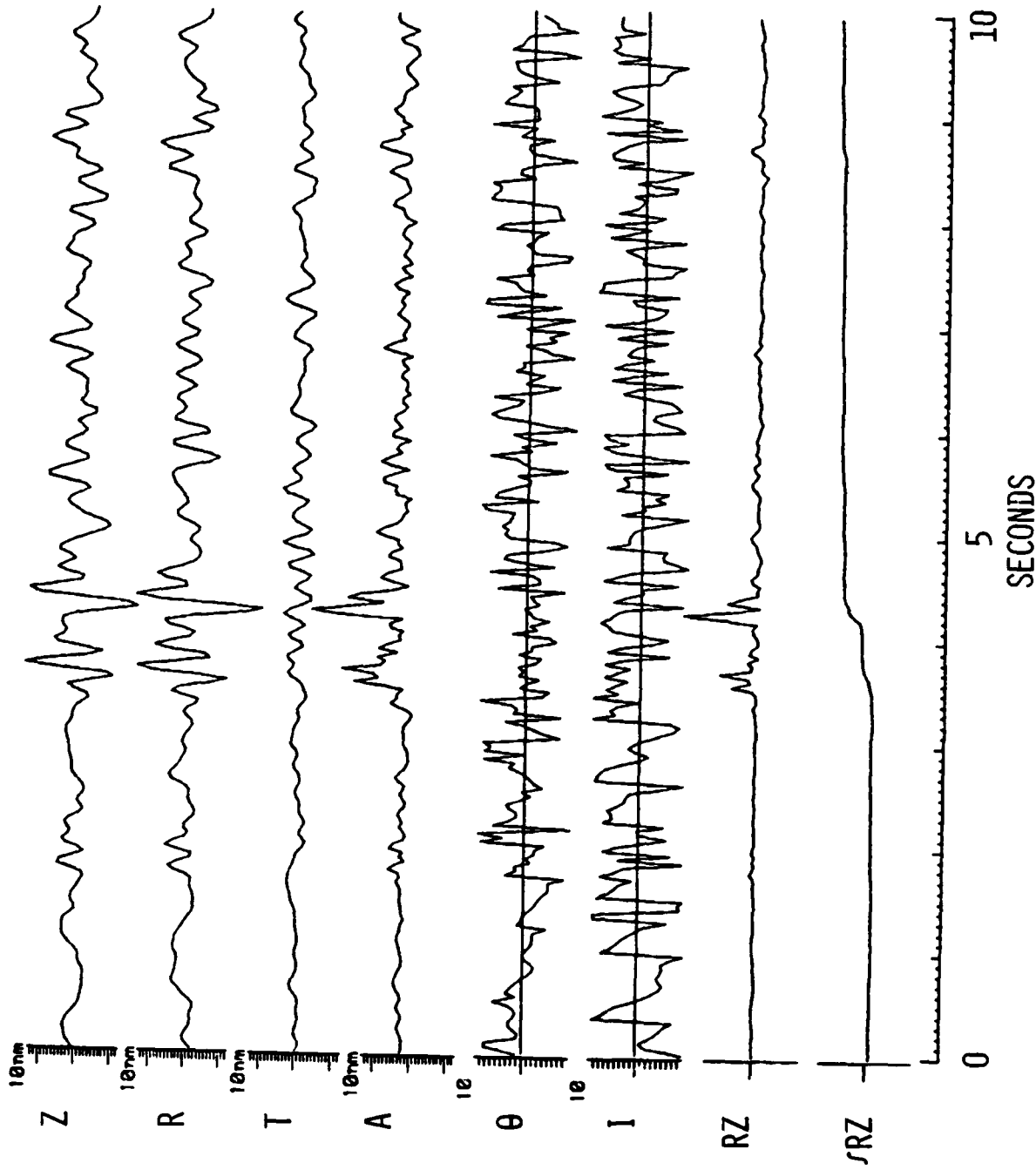


Figure 24. Pass band 3 to 6 Hz. Format same as Figure 2.

## RHODE ISLAND P-WAVE ADAPTIVE POLARIZATION

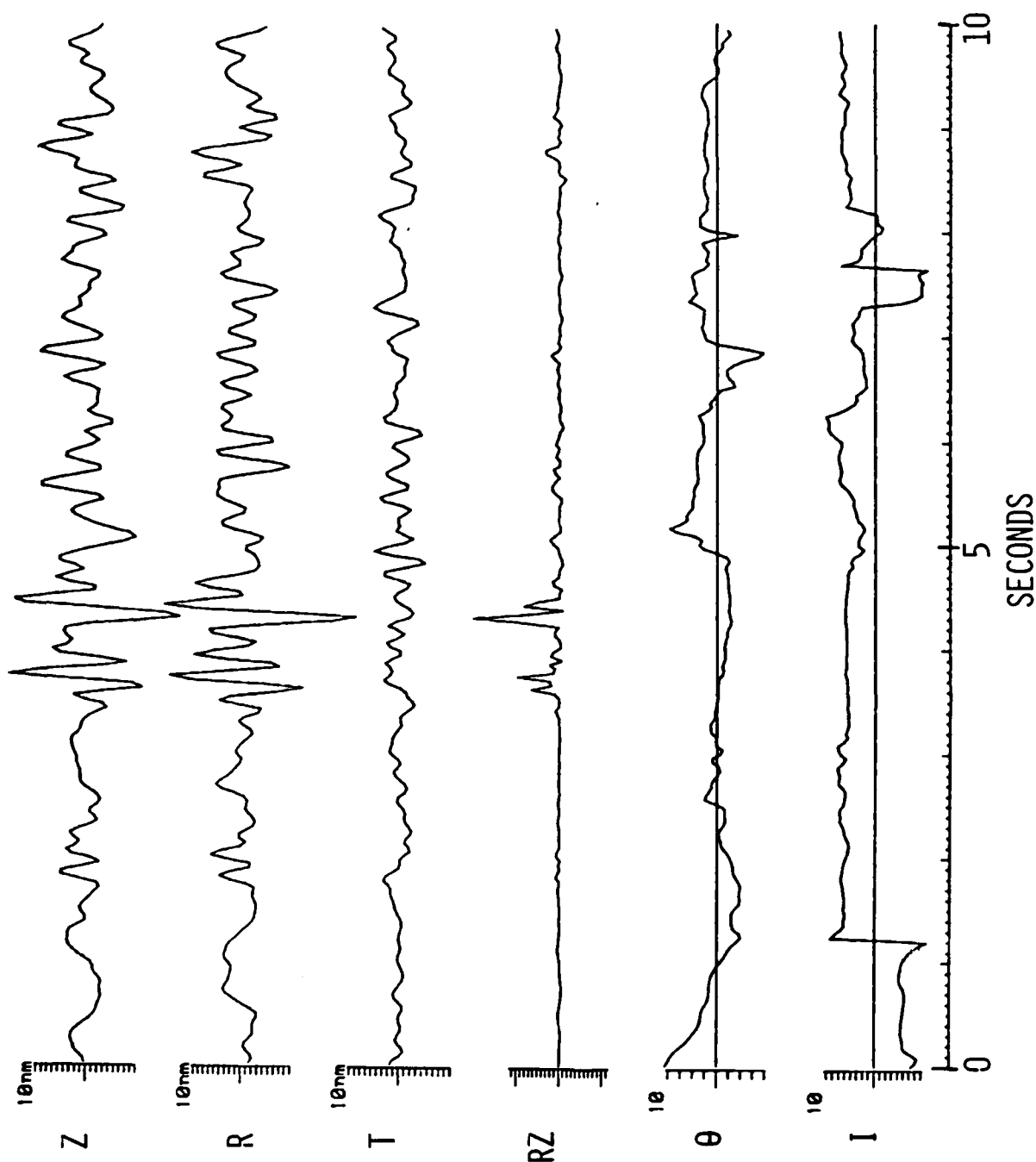


Figure 25. Pass band 3 to 6 Hz. Format same as Figure 4.

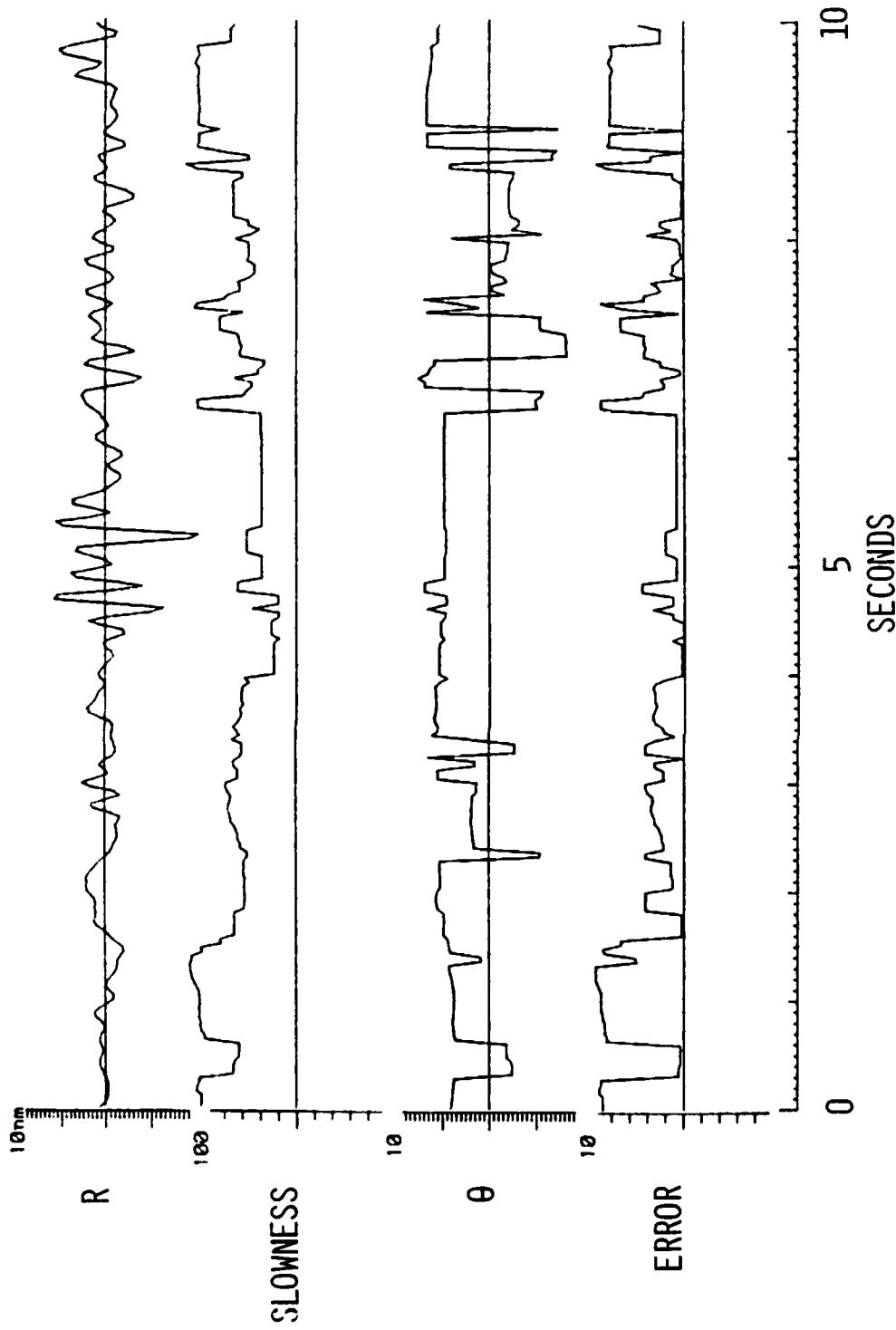


Figure 26. Pass band 3 to 6 Hz. Format same as Figure 7.

RHODE ISLAND P  
SLOWNESS STACK

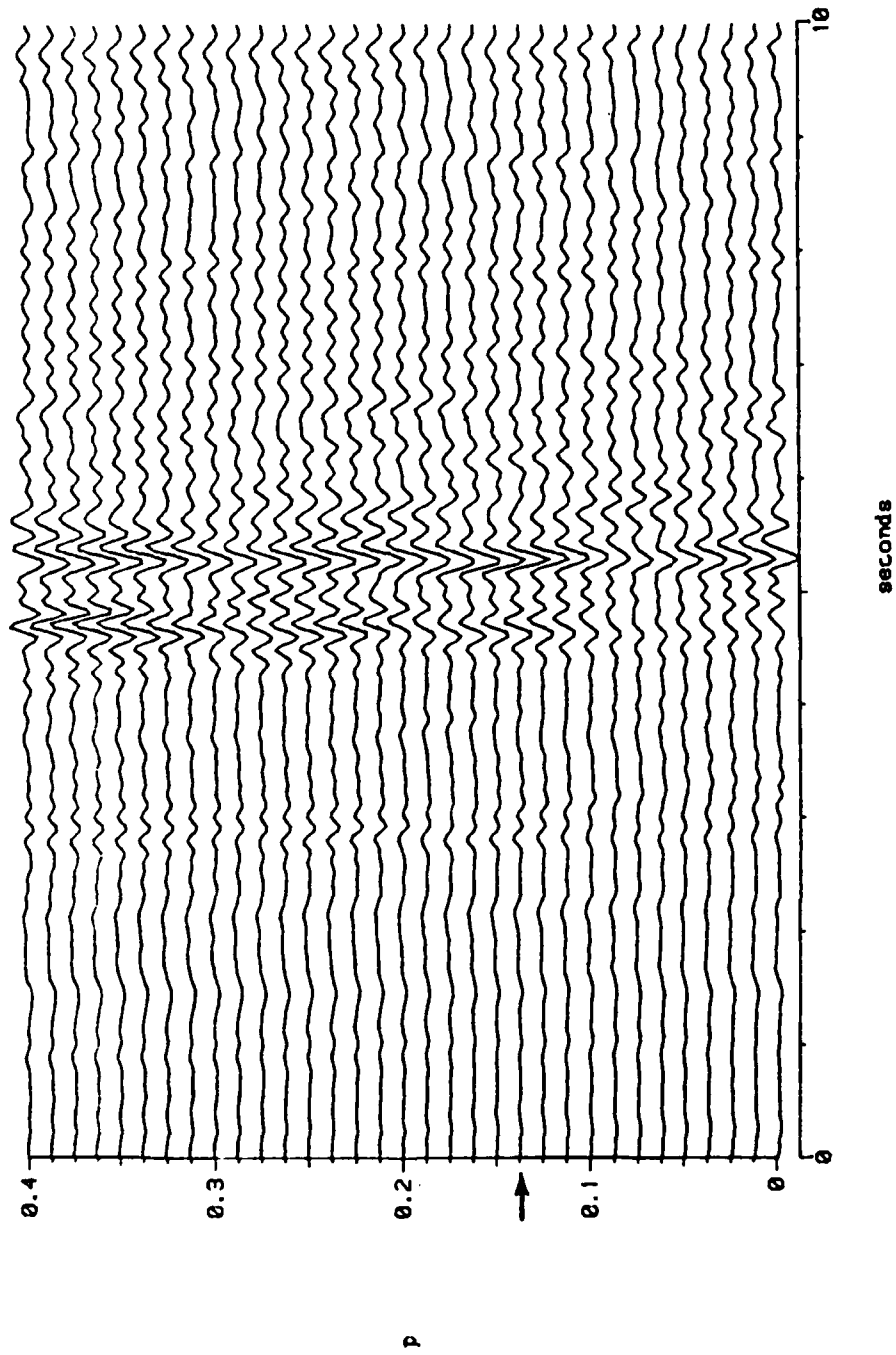


Figure 27. Pass band 3 to 6 Hz. Format same as Figure 8. Arrow indicates the approximate slowness of the P-wave arrivals.

RHODE ISLAND S/Lg  
INSTANTANEOUS POLARIZATION

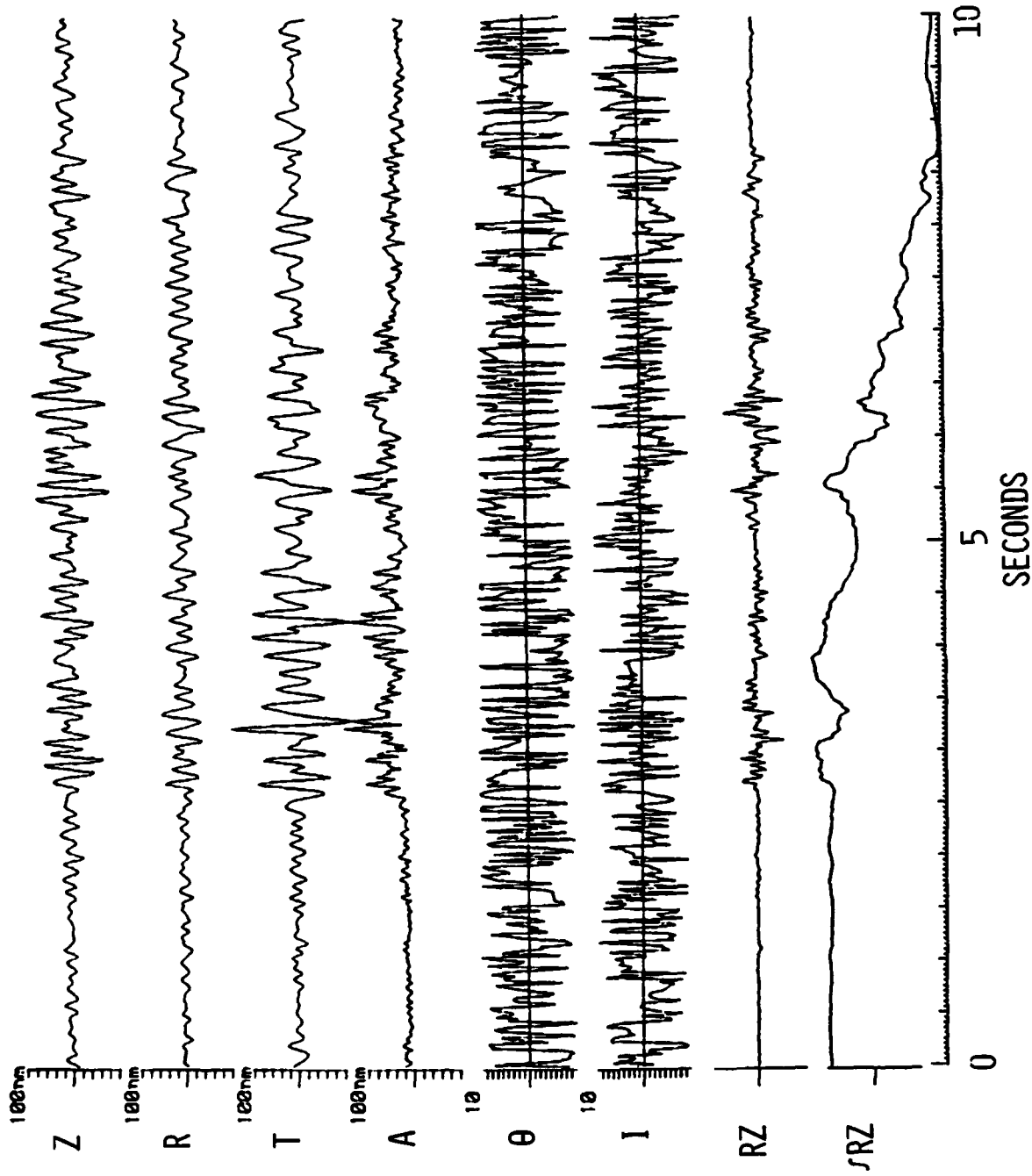


Figure 28 Pass band 3 to 6 Hz. Format same as Figure 2.



## RHODE ISLAND S/LG ADAPTIVE POLARIZATION

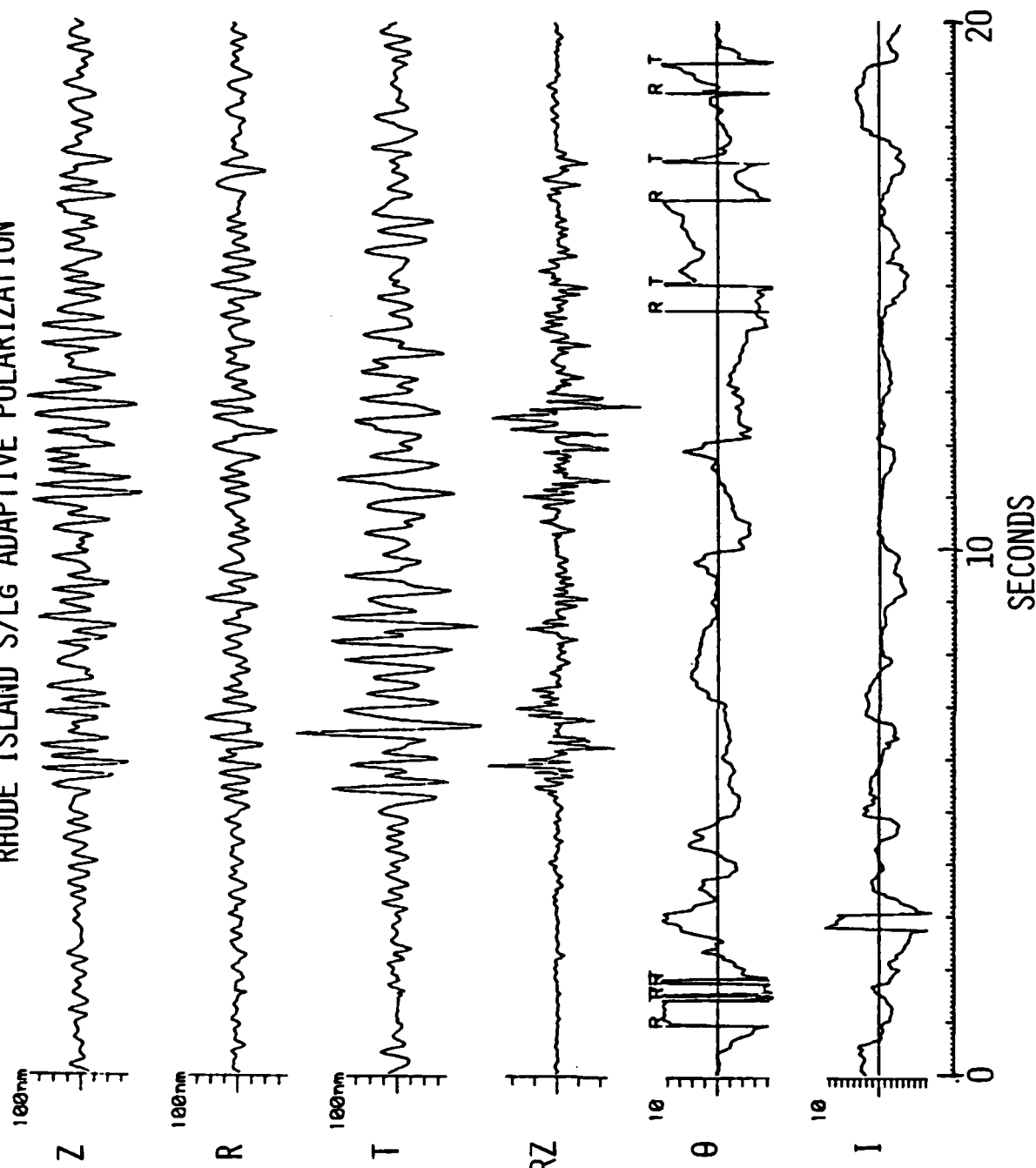


Figure 29. Pass band 3 to 6 Hz. Format same as Figure 4.

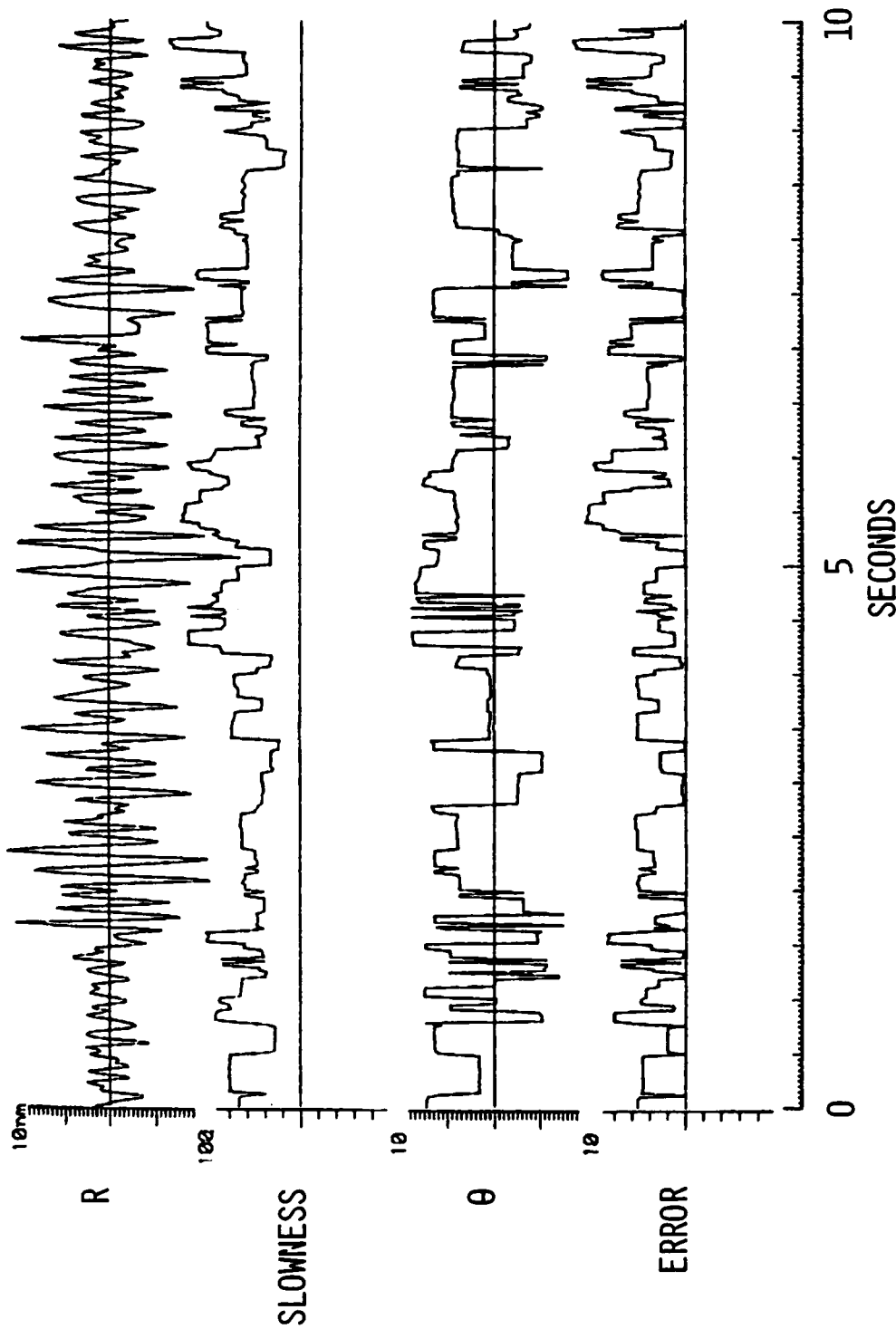


Figure 30. Pass band 3 to 6 Hz. Format same as Figure 7.

RHODE ISLAND S/L9  
SLOWNESS STACK

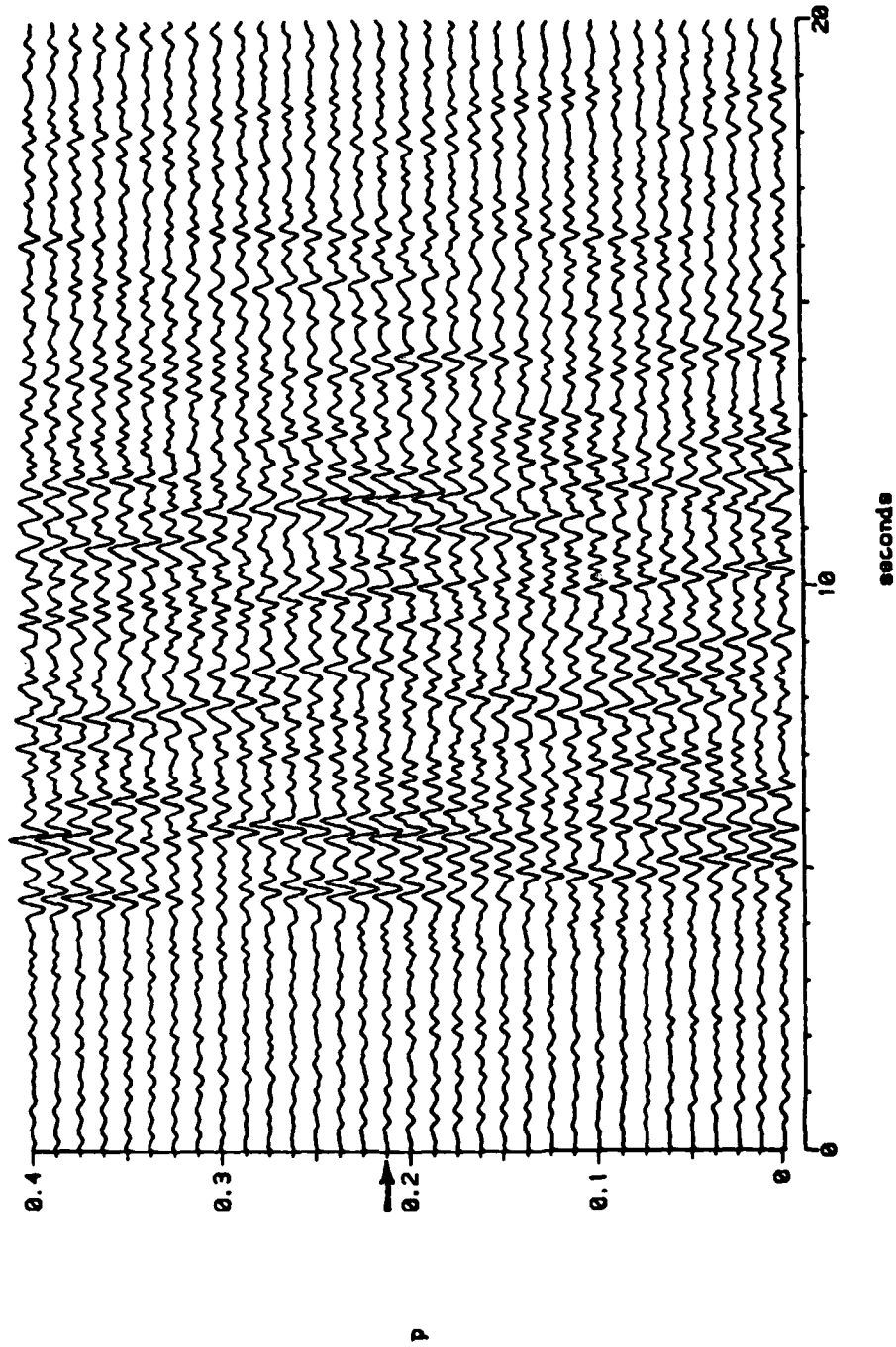


Figure 31. Pass band 3 to 6 Hz. Format same as Figure 8. Arrow indicates the approximate slowness of the first arrivals in this group.

## EASTERN U.S. CRUSTAL MODELS

BACHE					PULLI				
DEPTH	Vp	Qp	Vs	Qs	DEPTH	Vp	Qp	Vs	Qs
-10-	6.1	250	3.3	125	-10-	6.0	1000	3.5	500
-20-	6.6	250	3.6	125	-20-	6.4	3000	3.9	1000
-30-	6.6	2000	3.6	1000	-30-	7.0	5000	4.0	2500
-40-	8.1	2000	4.5	1000	-40-	8.2	5000	4.7	2500

Figure 32. East Coast velocity models.

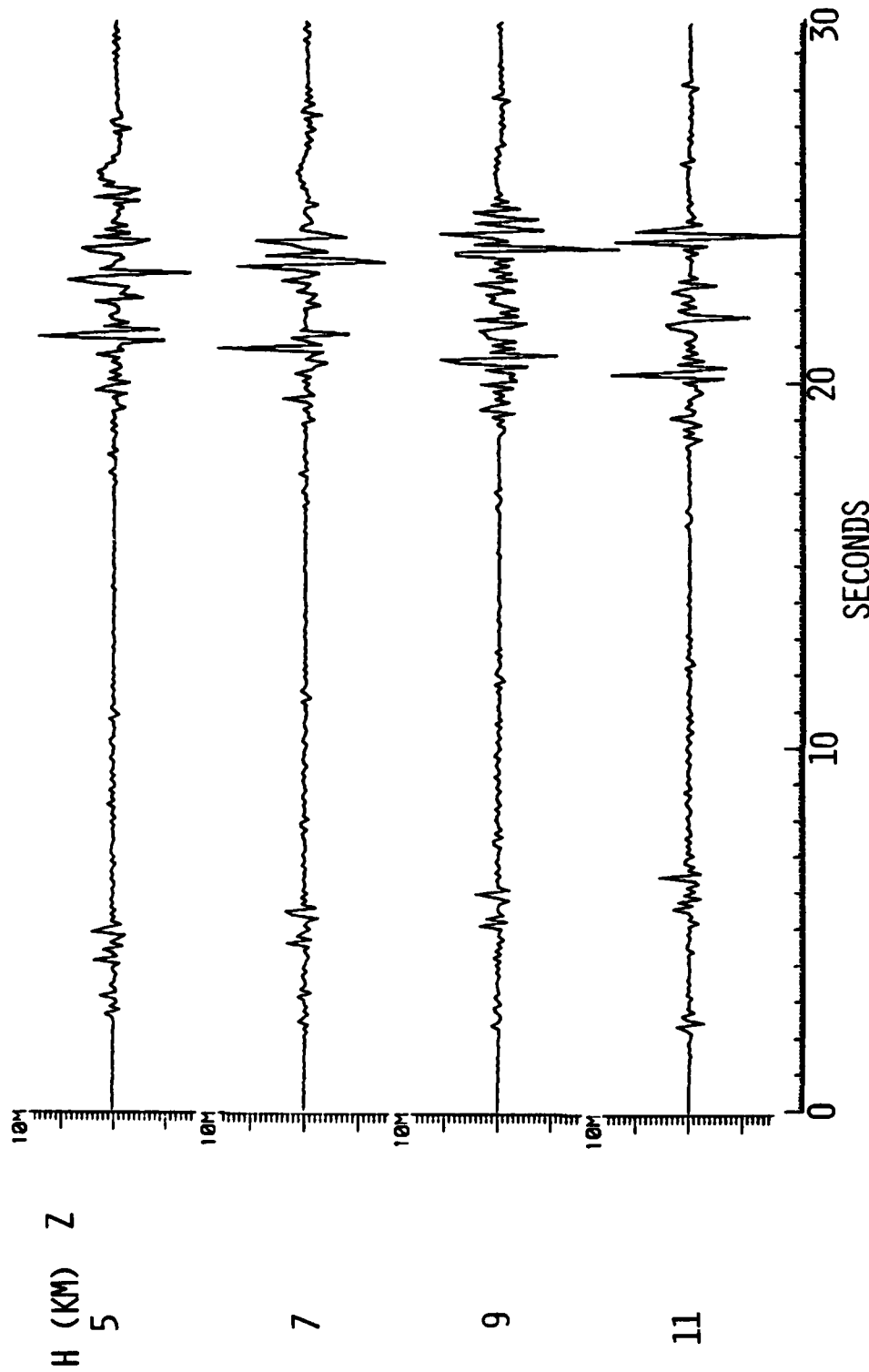


Figure 33. Effect of changing focal depth on synthetic seismograms generated using the Pulli model.

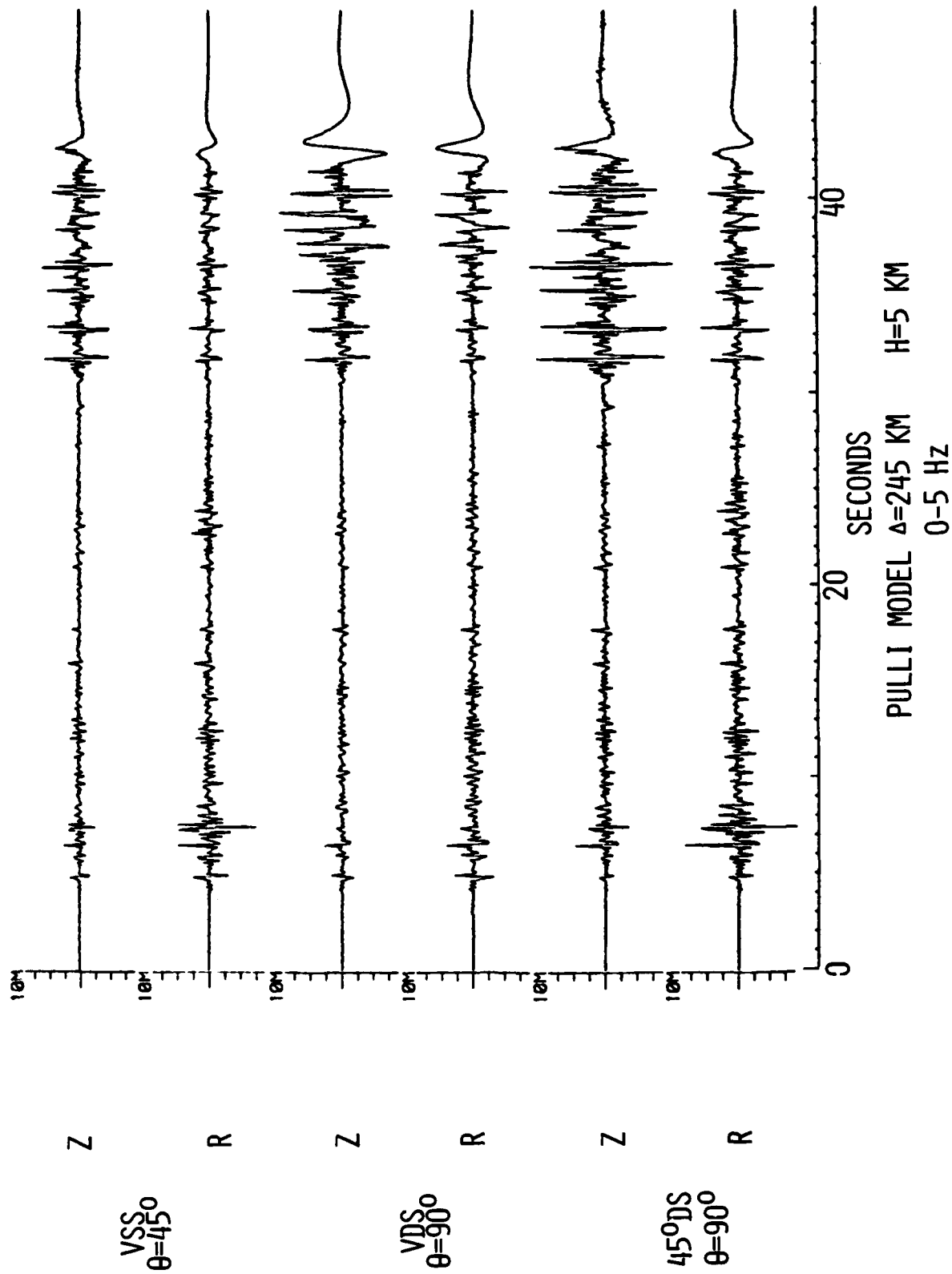
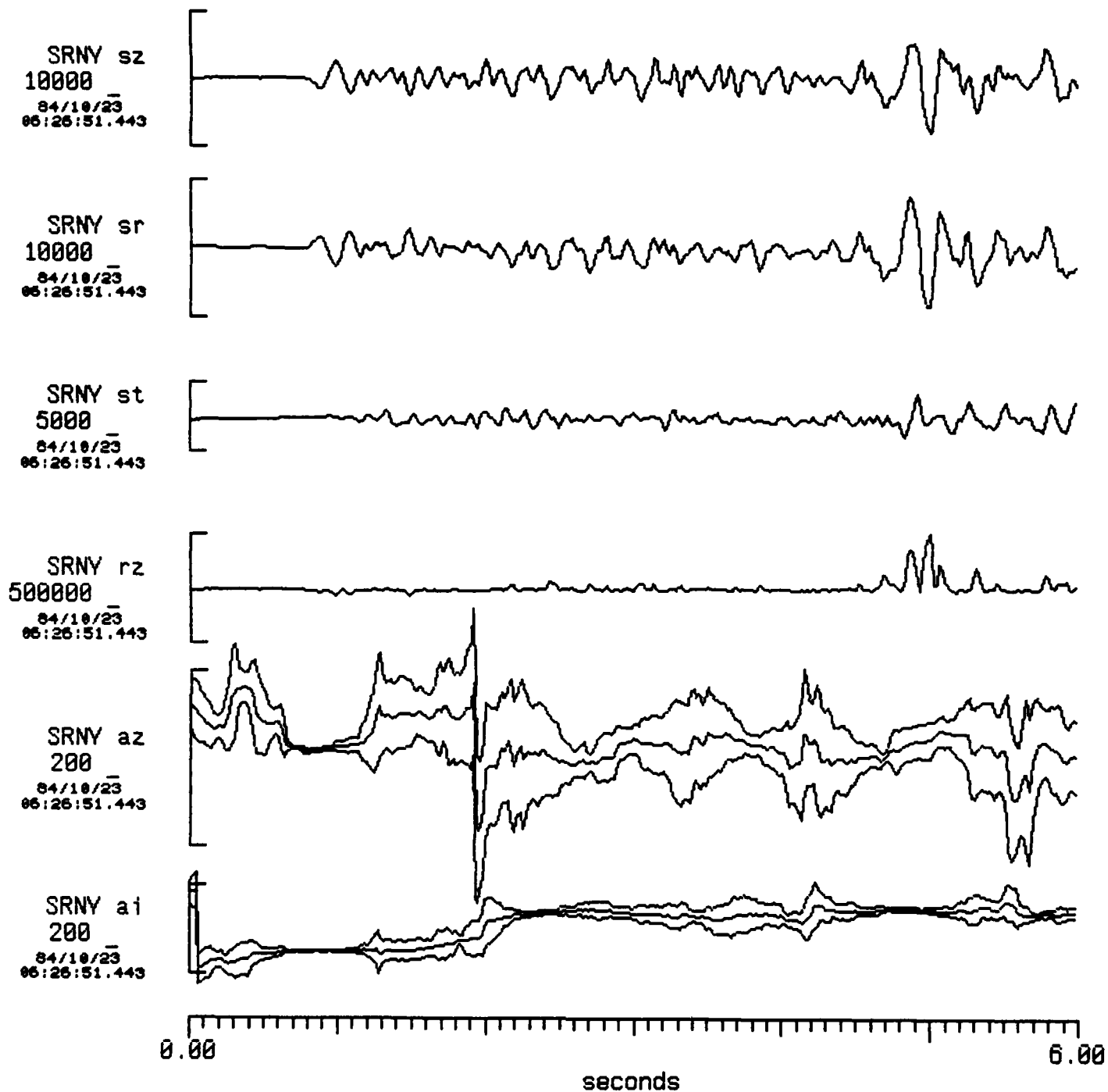


Figure 34. Effect of fault orientation on synthetic seismograms.



Event: trny Run date: Tue Nov 27 09:53:52 1984

Figure 35. Sample output from the track program for the p-wave portion of the 10/23/84 Adirondack earthquake recorded at SRY. sz=vertical component of motion; sr=adapted radial component of motion; st=adapted transverse component of motion; rz=product of radial and vertical traces; az=azimuth with error bars; ai=angle of incidence with error bars. The units of az and ai are degrees.

SRNY bz  
50000  
84/10/23  
06:26:38.943

p

s

SRNY bn  
20000  
84/10/23  
06:26:38.943

SRNY be  
20000  
84/10/23  
06:26:38.943

0.00 60.00  
seconds

Event: SRNY Run date: Tue Nov 27 08:58:32 1984

Figure 36. Sample output of the display program for the SRNY recording of the 10/23/84 Adirondack earthquake--bz=broad band vertical; bn=broad band north-south; be=broad band east-west.



Run date: Tue Nov 27 10:00:32 1984

## Frequency Response of Filter

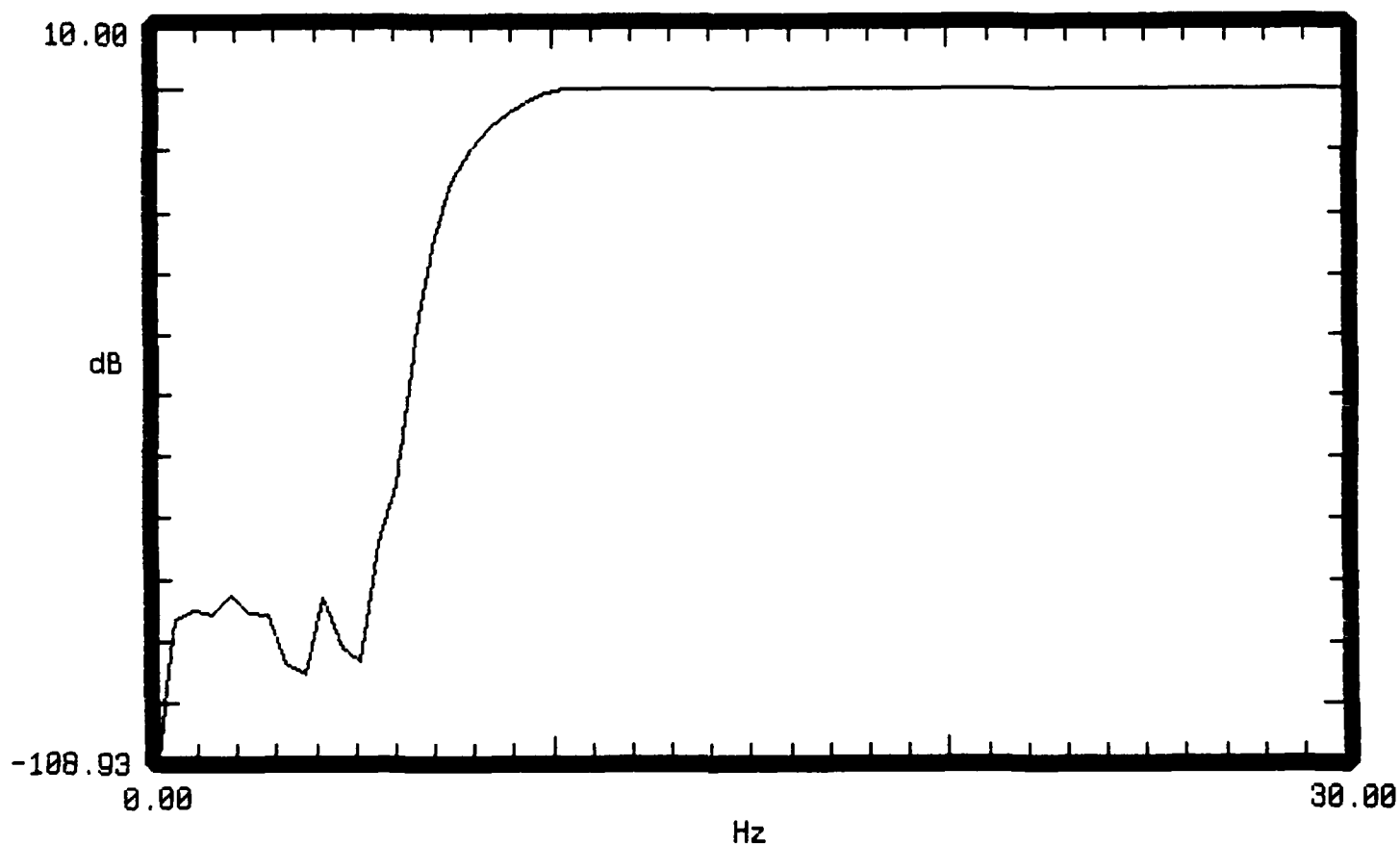


Figure 37. Sample frequency response function from program "filter" for a 100 point 10 Hz high pass filter with a Hanning window.

Run date: Tue Nov 27 09:50:50 1984

Fourier Spectrum (re units per Hz)

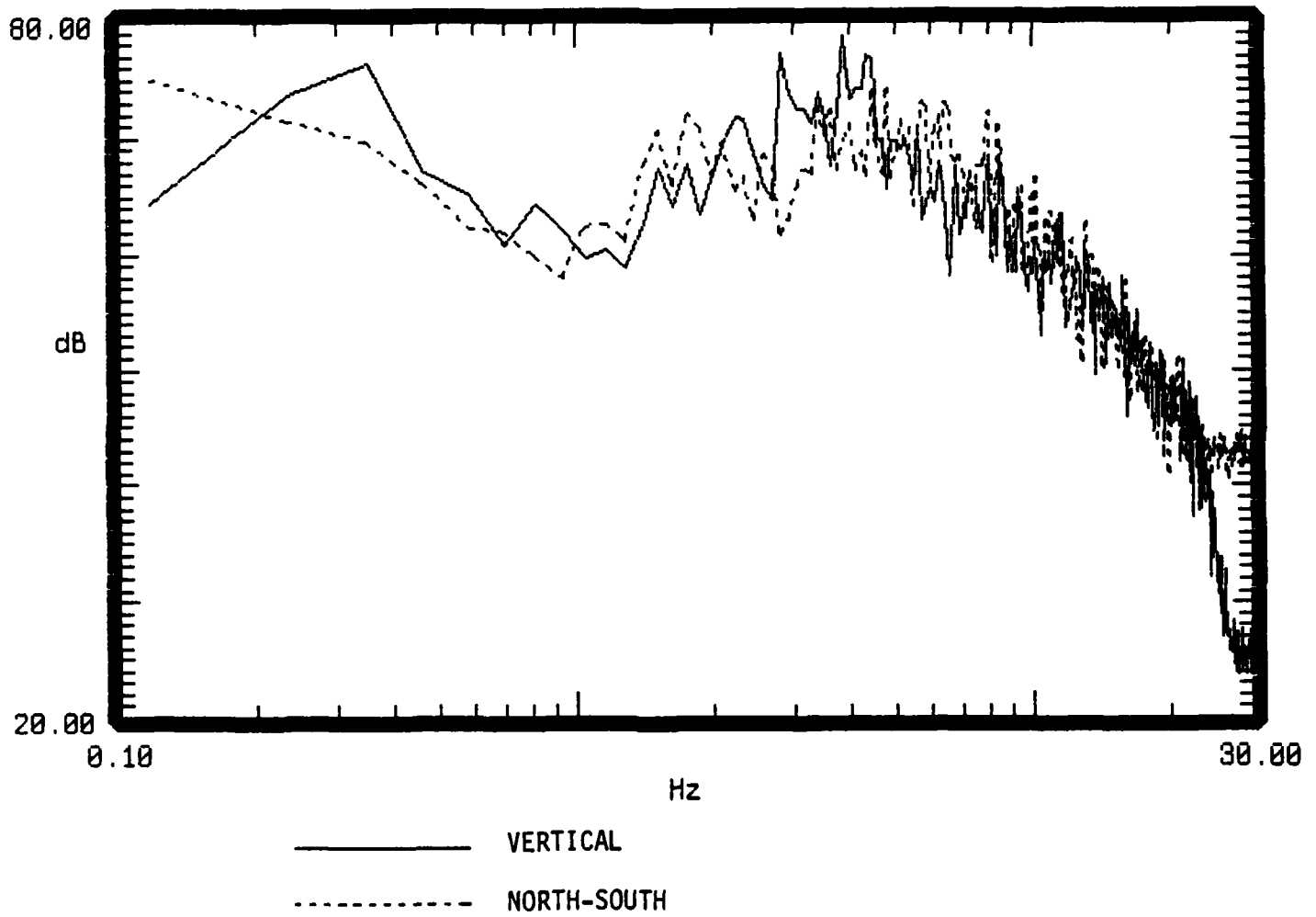


Figure 38. Sample output of nspec program showing the vertical and north-south horizontal spectra for the 10/23/84 Adirondack earthquake.

Adirondack Earthquake Tue Nov 27 11:19:22 1984

84/10/23 06:26:38.943 SRNY SRNY bz

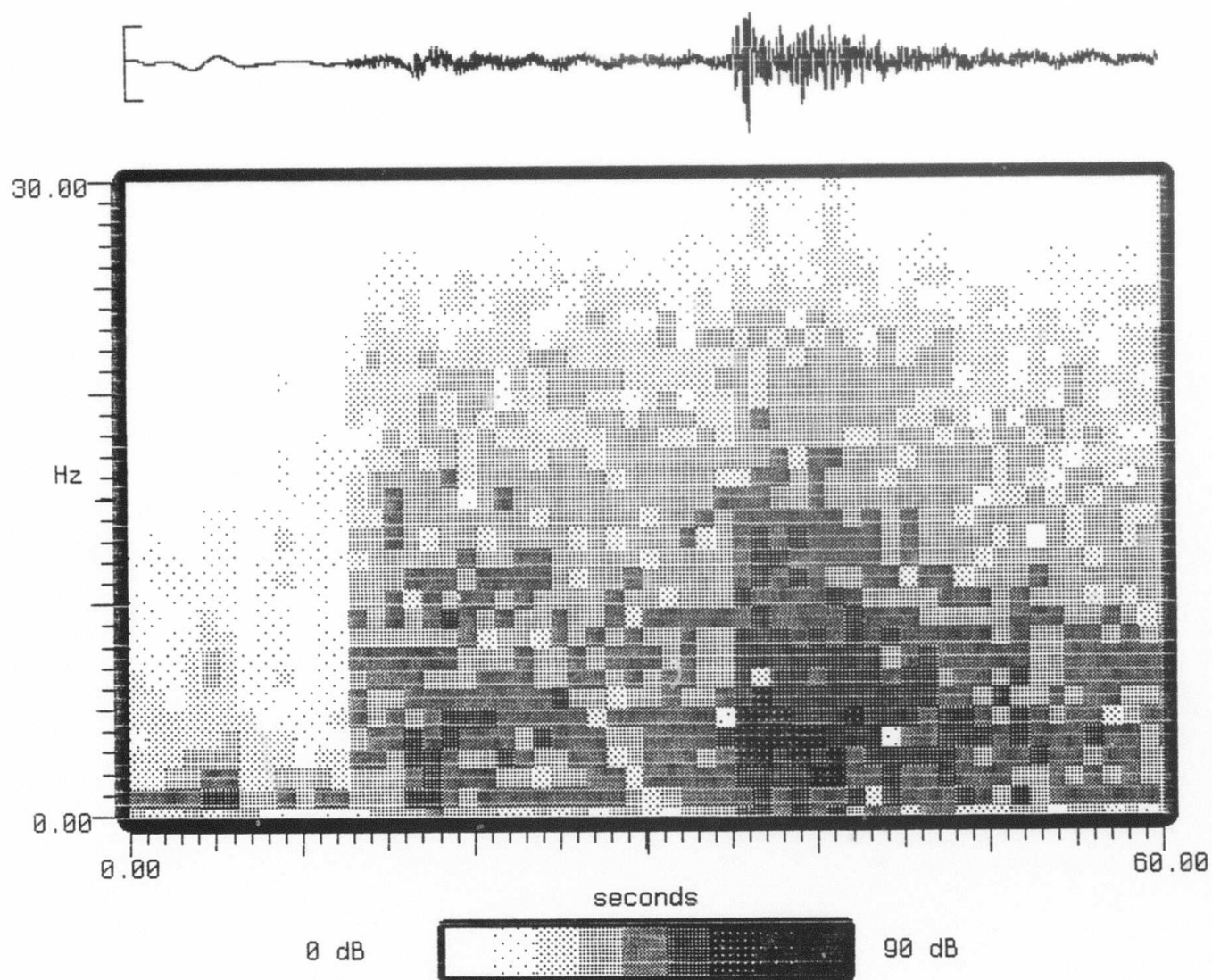


Figure 39. Sample output of the specgram program for the 10/23/84 Adirondack event recorded at SRNY.

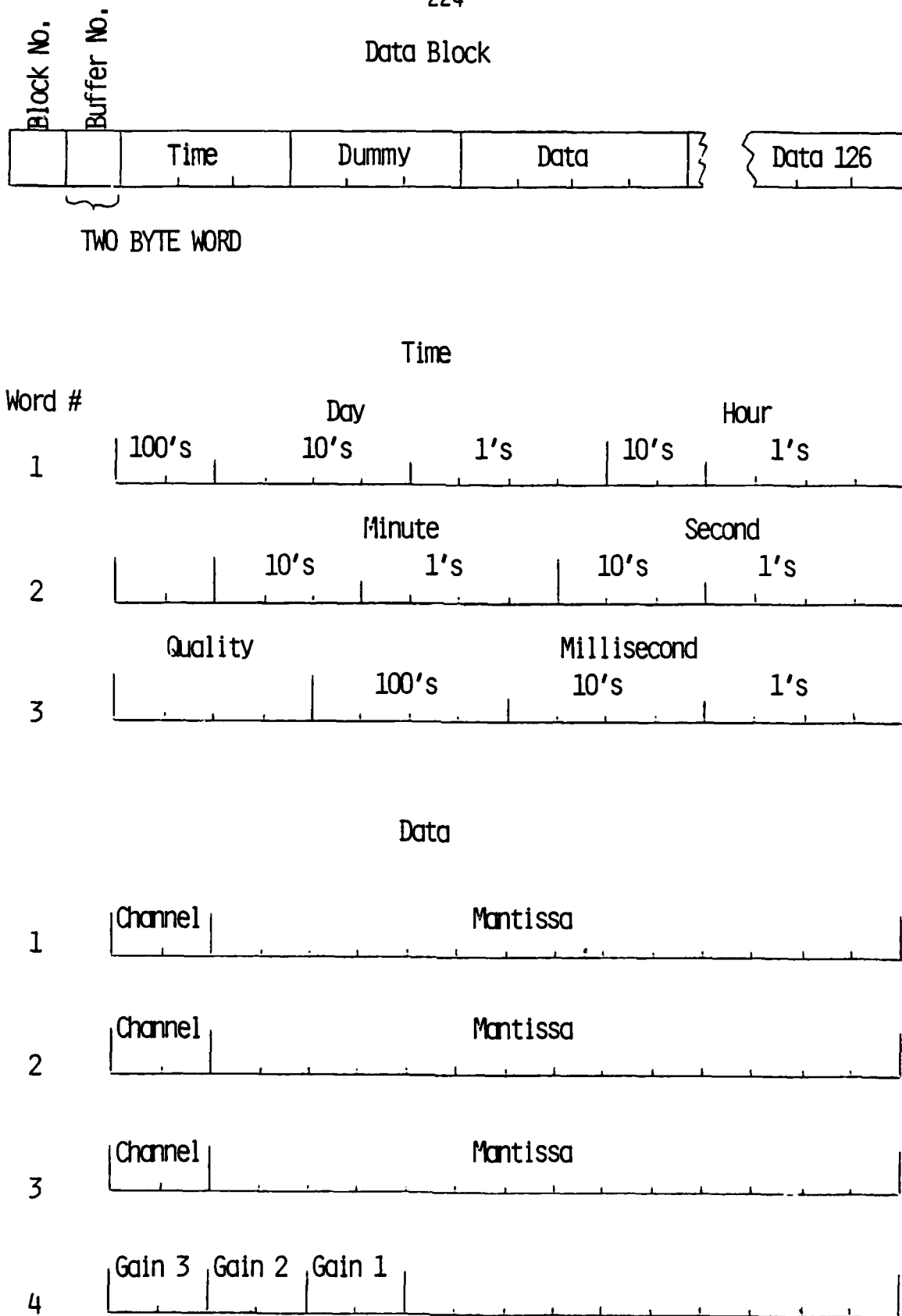


Figure 40. Data block format for 1/4" magnetic cartridge tapes.

## APPENDIX A

## SPECTRA OF NUCLEAR EXPLOSIONS, EARTHQUAKES, AND NOISE FROM WAKE ISLAND BOTTOM HYDROPHONES

Charles S. McCreery and Daniel A. Walker

Hawaii Institute of Geophysics, University of Hawaii, Honolulu, HI 96822

George H. Sutton

Rondout Associates, Inc., Stone Ridge, NY 12484

**Abstract.** Spectral characteristics of P phases from 4 shallow focus earthquakes and 8 underground explosions, and of 52 samples of ocean bottom background noise, are examined by using tape recordings of ocean bottom hydrophones near Wake Island from July 1979 through March 1981. Significant differences are found between spectra of large shallow focus earthquakes and explosions ( $5.7 < m_b < 6.3$ ) observed at  $61^\circ$  to  $77^\circ$  epicentral distance. For similar magnitudes, explosions were found to have less energy at frequencies below 1.5 Hz and more energy at frequencies above 2.0 Hz. Earthquakes were found to have a spectral slope of  $-28$  dB/octave (relative to pressure) over the band 1 to 6 Hz. Explosions were found to have the same spectral slope over the band 2.2 to 6 Hz, but a different slope of  $-12$  dB/octave over the band 1.1 to 2.2 Hz. High frequencies ( $>6$  Hz) observed in the teleseismic P phases indicate high Q values for the deep mantle. Ambient noise levels on the ocean bottom near Wake are comparable to levels at the quietest continental sites for frequencies between 3 and 15 Hz. Also high levels of coherence (at least as high as 0.85) have been observed for P phases recorded on sensors with 40-km separation.

## Introduction

In an earlier report (Walker, 1980), slow-speed paper recordings of hydrophones located near Wake Island were used in a study of P phases from underground nuclear explosions and earthquakes at comparable distances. That study was prompted by: (1) the work of Evernden (1977) and Evernden and Kohler (1979), which showed that P phases recorded in the  $60^\circ$  to  $90^\circ$  distance range from underground explosions were surprisingly rich in high-frequency energy (at least as high as 9 Hz); (2) the extreme sensitivity of the Wake hydrophones to high-frequency signals (Walker et al., 1978); and (3) the location of most known underground test sites in the  $60^\circ$  to  $90^\circ$  distance range from the Wake hydrophones. The major conclusion of Walker (1980) was that observable P phases were found for all Russian underground explosions with estimated yields in excess of 270 kilotons, whereas no such phases were found for earthquakes of comparable or greater magnitude at similar distances. Principal limitations of the investigation were that: (1) the slow-speed paper recordings were not suitable for detailed spectral analyses of either the recorded signals

or the noise; and (2) the filtering was not optimized for the recording of distant earthquakes and explosions.

This report discusses the spectra of P phases from underground explosions and earthquakes as well as the spectra of ambient noise derived from recent tape recordings of the Wake Island ocean bottom hydrophone array. The array consists of six hydrophones on relatively flat ocean bottom near Wake at about 5.5-km depth. The hydrophones are located at the vertices and center of a pentagon roughly 40 km across and are cabled directly to Wake Island. Only three of the hydrophones could be recorded simultaneously on the recording system used. This system was a four-channel (three data, one time code) slow-speed cassette recorder, with automatic gain-ranging amplifiers following low-noise preamps connected to the differential outputs (via cabling) of the moving coil hydrophones on the ocean bottom. These recorded signals were used to compute absolute spectra of the seismic phases and background noise by the following steps: (1) digitization at 80 samples per sec after anti-alias filtering; (2) normalization of the automatic gain levels; (3) computation of contiguous 512-point FFT's (6.4 sec per FFT) and their corresponding power spectra; (4) averaging of those spectra over the time window of interest; (5) normalization of the spectral bandwidth from 0.156 Hz to 1.0 Hz; and (6) removal of the hydrophone/recording system/anti-alias response. The recording system and anti-alias response were determined in situ. The hydrophone response was taken from the Columbia University OBS Calibration Manual (Thanos, 1966), which describes the estimated response between 0.05 and 100 Hz of an equivalent hydrophone. More specific information on the Wake hydrophone/cable responses at these frequencies is not available because of the age of the array (about 20 years), its formerly classified status, and the original bandwidth of interest ( $>10$  Hz) to those who installed the array.

## Spectra of Underground Explosions and Natural Earthquakes

The earthquakes and explosions investigated in this study are listed in Table 1. These events were chosen because they all occurred within  $60^\circ$  to  $90^\circ$  epicentral distance, were shallow focus, had large signal/noise ratios, and did not exceed the dynamic range of the recording system. Figure 1 shows the pressure spectra of some of these events, as well as composite pressure spectra for the earthquake and explosion groups. For purposes of comparison, pressure and vertical

Copyright 1983 by the American Geophysical Union.

Paper number 2L1384.  
0094-8276/83/ 002L-1384\$3.00

## A2

Table 1. Description of Events Used in Figure 1

No.	Date	Location	Distance (degrees)	Depth (km)	Magnitude (mb)	Type	Number of Hydrophones
1	07/24/79	S. of Java	65.7	31	6.3	Earthquake	3
2	08/04/79	E. Kazakh	73.2	0	6.1	Explosion	3
3	08/18/79	E. Kazakh	73.2	0	6.1	Explosion	3
4	09/24/79	Novaya Zemlya	76.7	0	5.7	Explosion	1
5	09/29/79	N. Sumatera	72.9	27	6.2	Earthquake	1
6	10/18/79	Novaya Zemlya	76.8	0	5.8	Explosion	1
7	10/28/79	E. Kazakh	73.2	0	6.0	Explosion	1
8	12/23/79	E. Kazakh	73.3	0	6.1	Explosion	1
9	07/29/80	Nepal	76.4	18	6.1	Earthquake	2
10	09/14/80	E. Kazakh	73.2	0	6.2	Explosion	2
11	10/12/80	E. Kazakh	73.2	0	5.9	Explosion	2
12	11/19/80	Sikkim	70.4	17	6.0	Earthquake	2

displacement may be related using the expression:  $P = \omega \rho v A$ , where  $P$  is pressure,  $\omega$  is angular frequency,  $\rho$  is seawater density,  $v$  is the speed of sound in seawater, and  $A$  is vertical

displacement. This relationship holds for compressional energy arriving vertically from below the hydrophone. The following differences in the spectral signatures between explosions and shallow focus earthquakes are evident: (1) lack of energy in explosion  $P$  relative to earthquake  $P$  at frequencies below 1.5 Hz, (2) changes in spectral slope (corner frequency?) for explosions from -12 to -28 dB/octave (equivalent to -18 and -34 dB/octave in ground displacement) at about 2.2 Hz, and (3) greater energy in explosion  $P$  relative to earthquake  $P$  at frequencies above 2.0 Hz, despite smaller magnitude of the average explosion (6.03) than that of the average earthquake (6.16). Differences between the explosion and earthquake  $P$  phases observed at these frequencies is not surprising. The high frequencies observed and the actual shape of these curves have implications regarding  $Q$  along the travel path. Although these implications will not be discussed here, it is pointed out that the observation of frequencies in excess of 6 Hz (and up to 9 Hz) at distances greater than 60° implies a high  $Q$  at least along the deep mantle part of the  $P$  travel path.

Although this study found a common high-frequency slope (-28 dB/octave) for both earthquakes and explosions, at least one other investigator (Evernden, 1977) has found earthquakes to fall off at least  $f^{-1}$  faster than explosions. This discrepancy might be explained by the small number of earthquakes used in the present study and the requirement in choosing those events of large signal/noise. Earthquakes having more high-frequency energy would have greater signal/noise because of much lower noise levels at high frequencies.

NTS events were not included in this study because they were rarely recorded with signal/noise greater than 2. Although signal levels near 1 Hz for NTS events are roughly equivalent to those observed for similar magnitude earthquakes and Soviet explosions, the signal fall-off above 1 Hz appears to be generally much greater for NTS. Therefore, little signal energy from NTS events is observed in the band above 2 Hz where lower ambient noise levels significantly enhanced the signal/noise of those events that were used. This rapid fall-off may be due to a recognized low  $Q$  effect in the source region (see for example Der et al., 1982).

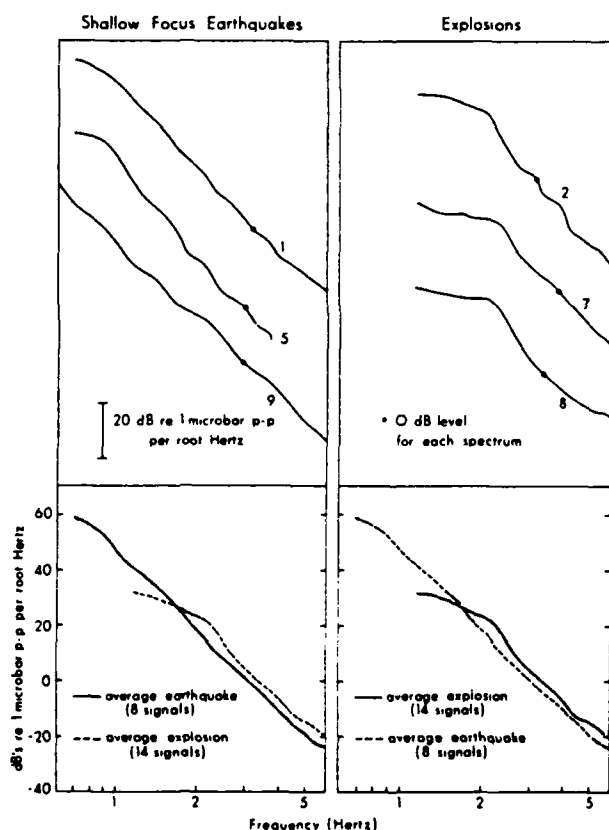


Figure 1. Sample spectra of  $P$  from some shallow focus earthquakes and nuclear explosions are shown in the upper portion of this figure. Numbers refer to the events as described in Table 1. The composite spectrum of each group, an average with  $\pm 1$  standard deviation, is shown in the lower portion of the figure. Before standard deviations were computed, individual spectrums were normalized by subtracting the difference between their mean dB value over the range 1.5-3.0 Hz and the mean dB value for all spectra over the same frequency range.

## Ocean Bottom Ambient Noise

The average background noise at the ocean bottom near Wake is shown in Figure 2 (labeled A). This average, along with its standard deviation, was determined from 52 samples of noise taken over 18 months of recording. Also plotted are an assortment of published noise curves for both ocean bottom and continental sites. When compared with noise levels from continental sites, the Wake ambient noise level could be described as: (1) high for frequencies between 0.2 Hz and 1.5 Hz; (2) average for frequencies between 1.5 Hz and 3.0 Hz; and (3) low for frequencies between 3.0 Hz and 15.0 Hz.

The observed low noise levels at higher frequencies affirm the ability of the Wake hydrophones to detect seismic signals at those frequencies. In addition, high-frequency phases recorded on the deep ocean bottom, which traverse only a few kilometers of homogeneous crust, may be less distorted than similar phases recorded on continents, which often traverse more than 40 km of crust. Consequently, coherence across the

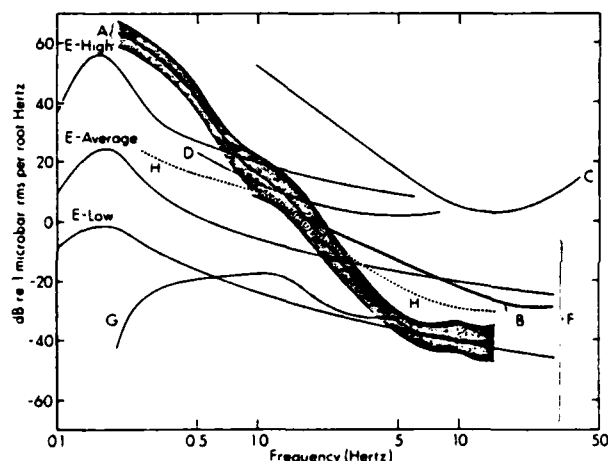


Figure 2. The average spectrum  $\pm 1$  standard deviation of 52 samples of background noise over 18 months from the Wake bottom hydrophones is labeled A. Also shown are some published noise curves for both ocean-bottom (B, C, D, and H) and continental (E, F, and G) environments, which have been converted from an assortment of units to the scale shown. B is a hypothetical "sample spectrum of deep-sea noise" (Urick, 1975; p. 188). C is a vertical seismometer measurement made in the Mariana Basin (Asada and Shimamura, 1976). D is a vertical seismometer measurement made at 46-km depth between Hawaii and California (Bradner and Dodds, 1964). H is a noise curve for a hydrophone bottomed off Eleuthera Island at 1200-m depth (Nichols, 1981). E represents low, average, and high noise levels estimated from curves compiled by Brune and Oliver (1959). F is an area bounded by the limits of noise curves measured on vertical seismometers for 16 locations within the United States and Germany (Frantti et al., 1962). G is the noise curve for the Oyer subarray of the Norwegian seismic array measured during a period "when most of the North Atlantic Ocean was very quiet" (Bungum et al., 1971).

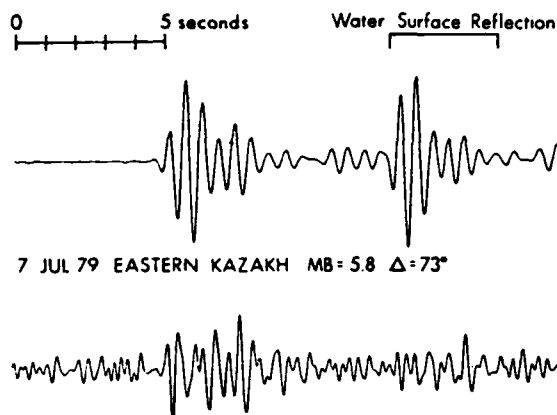


Figure 3. Sample time series of P, filtered to maximize signal/noise, from two nuclear explosions recorded on the Wake bottom hydrophones. The upper trace is from a single hydrophone and shows the direct arrival and its first water surface reflection. The lower trace is a composite of signals from two hydrophones with 40-km separation, obtained as follows: the filtered (1.5–5.0 Hz) time series from each hydrophone was inverted, shifted in time by the water surface reflection time, weighted to maximize the increase in signal/noise, and added to itself; the two resulting time series were then added with the appropriate propagation delay, and weighted to maximize the increase in signal/noise. Signal/noise was increased by 90% of the theoretical maximum with this method, indicating a high level of coherence between the signals added.

array appears to be high for teleseismic P. These factors (low noise levels and a thin, homogeneous crust) have enabled the Wake array to acquire some impressive recordings of underground nuclear explosions. Shown in Figure 3 is an Eastern Kazakh explosion at 73° with a body wave magnitude of 5.9. Its signal/noise ratio is approximately 50/1. Also shown in Figure 3 is a Western Siberian explosion at 77° with a body wave magnitude of 4.6. This arrival is the weighted sum of signals from two of the hydrophones, as explained in the figure caption. Coherence between the two hydrophone signals in the band 1.5 to 5 Hz was measured at 0.85 for this arrival.

## Summary

Significant differences are found between the spectra of P phases from explosions and from shallow focus earthquakes at 61° to 77° epicentral distance. Explosion spectra exhibit a change in spectral slope at about 2.2 Hz from -12 to -28 dB/octave relative to pressure. Earthquake spectra have a nearly constant slope of -28 dB/octave over the range of 1 to 6 Hz. High frequencies (>6 Hz) observed in these phases indicate a high Q in the deep mantle.

The ambient noise spectrum on the ocean bottom near Wake falls off at about -24 dB/octave over the range of 0.3 to 6 Hz. Between 3 and 15 Hz

the background noise levels are comparable to those at the quietest continental sites. Teleseismic P has been observed with a high level of coherence across a sensor separation of 40 km. The low level of ambient noise on the ocean floor at high frequencies and the high levels of coherence observed indicate that the ocean bottom may be an excellent observational regime for teleseismic P as well as other seismic phases rich in high frequencies.

**Acknowledgments.** This research was supported by the Advanced Research Projects Agency of the Department of Defense and was monitored by the Air Force Office of Scientific Research under Contract Nos. F 49620-79-C-0007 and F 49620-81-C-0065. Supplementary funds were provided by the U.S. Arms Control and Disarmament Agency. Installation of the recording system was partially funded by the Office of Naval Research (Code 425GG). The authors express special thanks to the Air Force and Kentron International for assistance in installing and maintaining the recording station at Wake, and to Al David for diligently changing tapes and making repairs. The authors thank Neil Frazer for critically reviewing this report and Rita Pujalet for editorial assistance. Hawaii Institute of Geophysics Contribution No. 1316.

#### References

- Asada, T., and H. Shimamura, Observation of earthquakes and explosions at the bottom of the western Pacific: Structure of oceanic lithosphere revealed by Longshot experiment, The Geophysics of the Pacific Ocean Basin and Its Margins, edited by G. H. Sutton, M. H. Manghnani, and R. Moberly, Am. Geophys. Union Monograph 19, p. 135-153, 1976.
- Bradner, H., and J. Dodds, Comparative seismic noise on the ocean bottom and land, J. Geophys. Res., **69**, 4339-4348, 1964.
- Brune, J., and J. Oliver, The seismic noise of the earth's surface, Bull. Seismol. Soc. Amer., **49**, 349-353, 1959.
- Bungum, H., E. Rygg, and L. Bruland, Short-period seismic noise structure at Norwegian seismic array, Bull. Seismol. Soc. Amer., **61**, 357-373, 1971.
- Der, Z. A., T. W. McElfresh, and A. O'Donnell, An investigation of the regional variations and frequency dependence of anelastic attenuation in the mantle under the United States in the 0.5-4 Hz band, Geophys. J. R. astr. Soc., **69**, 67-99, 1982.
- Evernden, J., Spectral characteristics of the P codas of Eurasian earthquakes and explosions, Bull. Seismol. Soc. Amer., **67**, 1153-1171, 1977.
- Evernden, J. and W. Kohler, Further study of spectral characteristics of P codas of earthquakes and explosions, Bull. Seismol. Soc. Amer., **69**, 483-511, 1979.
- Frantti, G., D. Willis, and J. Wilson, The spectrum of seismic noise, Bull. Seismol. Soc. Amer., **52**, 113-121, 1962.
- Nichols, R. H., Infrasonic ambient ocean noise measurements: Eleuthera, J. Acoustic. Soc. Am., **69**, 974-981, 1981.
- Thanos, S. N., OBS Calibration Manual, Lamont Geological Observatory, 1966.
- Urick, R., Principles of Underwater Sound, McGraw-Hill, 1975.
- Walker, D., Hydrophone recordings of underground nuclear explosions, Geophys. Res. Lett., **7**, 465-467, 1980.
- Walker, D., C. McCreery, G. Sutton, and F. Duennebie, Spectral analyses of high-frequency Pn and Sn phases observed at great distances in the western Pacific, Science, **199**, 1333-1335, 1978.

(Received August 6, 1982;  
accepted August 31, 1982.)



## APPENDIX B

SPECTRAL CHARACTERISTICS OF HIGH-FREQUENCY  $P_N$ ,  $S_N$  PHASES

## IN THE WESTERN PACIFIC

Daniel A. Walker and Charles S. McCreery

Hawaii Institute of Geophysics, Honolulu, Hawaii 96822

George H. Sutton

Rondout Associates, Stone Ridge, New York 12484

**Abstract.**  $P_N$  and  $S_N$  phases from 25 selected earthquakes recorded since July of 1979 on ocean bottom hydrophones near Wake Island are used to complement and extend prior investigations of high-frequency  $P_N$ ,  $S_N$  spectra in the Western Pacific. At a distance of about  $18^\circ$  ( $\approx 2000$  km), frequencies for  $P_N$  and  $S_N$  are as high as 30 and 35 Hz, respectively; at a distance of about  $30^\circ$  ( $\approx 3300$  km), as high as 15 and 20 Hz, respectively.  $P_N$  phases lose their high-frequency energy more rapidly than  $S_N$  phases do, yet  $P_N$  wavetrains are much longer than  $S_N$  wavetrains.  $P_N$  wavetrains of longer duration, more energy, and higher frequencies are found for travel paths primarily in the Northwestern Pacific Basin than for travel paths across the transition zone from the shallow Ontong-Java Plateau to the deep Northwestern Pacific Basin.  $S_N$  phases are extremely weak or absent for travel paths crossing this transition zone from the shallower Ontong-Java Plateau to the deeper Northwestern Pacific Basin, whereas  $S_N$  phases are well recorded for travel paths crossing the transition zone in the opposite direction. Although normal, mantle-refracted P phases are well recorded beyond about  $21^\circ$  ( $\approx 2300$  km), available data indicate that detectable normal, mantle-refracted P phases may not exist at distances from about  $17^\circ$  to  $21^\circ$ .

## Introduction

Recent investigations of high-frequency  $P_N$ ,  $S_N$  in the Pacific [Walker, 1977; Walker et al., 1978; Sutton et al., 1978; Talandier and Bouchon, 1979; and McCreery, 1981] suggest that the real character of these phases is revealed at frequencies much higher than those traditionally associated with normal, mantle-refracted body waves at teleseismic distances (i.e.,  $\approx 1$  Hz). For example, in one investigation [Walker et al., 1978], frequencies as high as 12 and 15 Hz were found for the  $P_N$  and  $S_N$  phases, respectively, of an earthquake recorded at a distance of  $28.3^\circ$  (3147 km).

In this report we offer a more comprehensive analysis of the spectral characteristics of  $P_N$ ,  $S_N$  using additional data recorded since July of 1979 on ocean bottom hydrophones near Wake Island. Only undistorted arrivals with signal/noise ratios of at least 3/1 were used in this investigation. Epicentral distances, origin

times, depths, and magnitudes are given in Table 1; and locations of epicenters are shown in Figure 1.

## Northwestern Pacific Basin Travel Paths

Spectrograms for some of the  $P_N$ ,  $S_N$  phases having travel paths primarily under the deep Northwestern Pacific Basin (i.e., events 1 through 18) are shown in Figure 2. All reveal high frequencies, with values in excess of 20 Hz for both  $P_N$  and  $S_N$  at a distance of  $18.0^\circ$  (2000 km; event 2) and values of up to 15 and 20 Hz for  $P_N$  and  $S_N$ , respectively, at a distance of  $29.4^\circ$  (3270 km; event 17). (More detailed spectral analyses of the phases for event 2 at  $18.0^\circ$  indicate values as high as 30 and 35 Hz for  $P_N$  and  $S_N$ , respectively.)

Spectrograms for events 17 and 18 show the normal, mantle-refracted P phases as well as high-frequency  $P_N$  and  $S_N$  phases. Other events for which normal, mantle-refracted P phases have been clearly recorded are 11, 12, 13, 15, and 16. The fact that all of these events are at distances in excess of  $21^\circ$  is not coincidental, for it is only at these distances (the precise crossover depending, in part, on focal depth) that P phases begin to arrive ahead of the high-frequency  $P_N$  phase (Figure 3). With increasingly shorter distances, high-frequency  $P_N$  arrives increasingly ahead of the expected P.

Although it might seem reasonable to assume that P does arrive at distances less than about  $21^\circ$ , but is masked by  $P_N$ , such an assumption should be tested. One test is to compare spectrograms where all of the P's energy, or large portions of it, might be suspected of being present within the  $P_N$  coda (i.e., events 1 through 10) to the spectrograms where only  $P_N$  is known to exist (i.e., events 13 through 18; 11 and 12 could not be used due to  $P_N$  clipping). Composite spectrograms have been made for the two groups of  $P_N$  arrivals (i.e.,  $P_N$  with P suspected, at distances from about  $17^\circ$  to  $22^\circ$ ; and  $P_N$  with P known to be absent, at distances from about  $26^\circ$  to  $33^\circ$ ), as well as for all P phases, at distances from about  $22^\circ$  to  $33^\circ$ , either clearly arriving well ahead of  $P_N$  (events 11, 12, 13, 15, 16, 17, and 18) or suspected of arriving close to, but ahead of,  $P_N$  (events 9 and 10). These composites and the individual absolute spectrograms from which they were derived are shown in Figure 4.

Individual and composite P spectrograms are obviously, and not unexpectedly, very different in character from individual and composite  $P_N$

Copyright 1983 by the American Geophysical Union.

Paper number 3B0272.

0148-0227/83/003B-0272\$05.00

TABLE 1. Epicentral Distances, Origin Times, Depths, and Magnitudes of Events 1-25 in Figure 1

Event Number	Distance, deg.	Date	Time	Depth, km	Magnitude, mb
1	17.8	July 8, 1980	1704:15.1	54	4.8
2	18.0	July 11, 1980	0942:00.2	33	5.3
3	18.7	June 9, 1980	1923:33.3	33	5.6
4	19.0	Dec. 8, 1979	1258:55.2	51	5.5
5	19.8	Dec. 16, 1979	1050:48.0	96	5.0
6	20.1	March 26, 1980	0722:37.0	45	5.5
7	20.7	Nov. 1, 1980	0440:37.7	109	5.6
8	20.9	Dec. 17, 1979	0728:48.2	33	5.1
9	21.2	Jan. 15, 1980	0523:25.7	120	5.1
10	21.7	Nov. 29, 1979	1708:21.3	109	5.4
11	24.9	Dec. 11, 1979	1726:22.1	161	5.9
12	25.4	Dec. 19, 1980	2332:41.6	79	6.2
13	26.5	Oct. 20, 1980	0329:21.3	81	5.5
14	27.1	Oct. 28, 1979	0539:36.0	88	5.4
15	28.5	Feb. 23, 1980	0551:03.5	47	6.4
16	28.5	Jan. 1, 1981	1032:13.1	53	6.2
17	29.4	Nov. 26, 1980	2348:59.9	77	5.8
18	32.7	Aug. 22, 1979	1828:55.7	128	5.5
19	28.0	Feb. 12, 1980	0320:23.2	75	5.9
20	28.0	Aug. 13, 1979	0303:47.9	88	5.8
21	28.6	May 14, 1980	1126:00.6	57	6.1
22	28.8	Sept. 28, 1980	1825:59.7	68	6.0
23	30.4	Nov. 6, 1979	1138:31.5	30	6.0
24	31.1	Oct. 23, 1979	0951:06.7	22	6.1
25	31.1	Feb. 22, 1980	2115:42.1	68	5.9

spectrums, in that the P has larger signal-to-noise ratios at lower frequencies (i.e., 1-2 Hz) than either Pn grouping (Figures 4 and 5), and the composite P is richer in lows, and weaker in highs, relative to the 26° to 33° Pn composite (Figure 5a). In comparing the composite 17° to 22° Pn spectrum to the composite 26° to 33° Pn spectrum (Figure 5b), we note that the 17° to 22° Pn is similar in character to the 26° to 33° Pn for frequencies higher than 2 Hz, but has lower signal-to-noise ratios at frequencies less than 2 Hz (i.e., values fall below the "4 dB above noise" requirement for plotting). This latter observation is also apparent in the individual spectrums (Figure 4). The fact that values for the 17° to 22° Pn spectrum fall below the 4 dB requirement for frequencies less than 2 Hz, coupled with values for the 22° to 33° P spectrum

above the 4 dB level at those frequencies, suggests that detectable normal, mantle refracted P phases may not exist in the Pn codas of events at distances of 17° to 22°.

Another important, though not surprising, observation to be made from the composite plots (Figure 5b) is that Pn phases at great distances appear to be weaker at higher frequencies (>10 Hz) than Pn phases at shorter distances.

Sn composite plots have also been made for the same events for which Pn composites have been made. These plots are shown in Figure 6. Although normal mantle-refracted P phases have been well recorded at great distances, normal mantle-refracted S phases from earthquakes have not been recorded by the Wake hydrophones. Presumably, this is due to the small pressure signal in the water resulting from S phases at

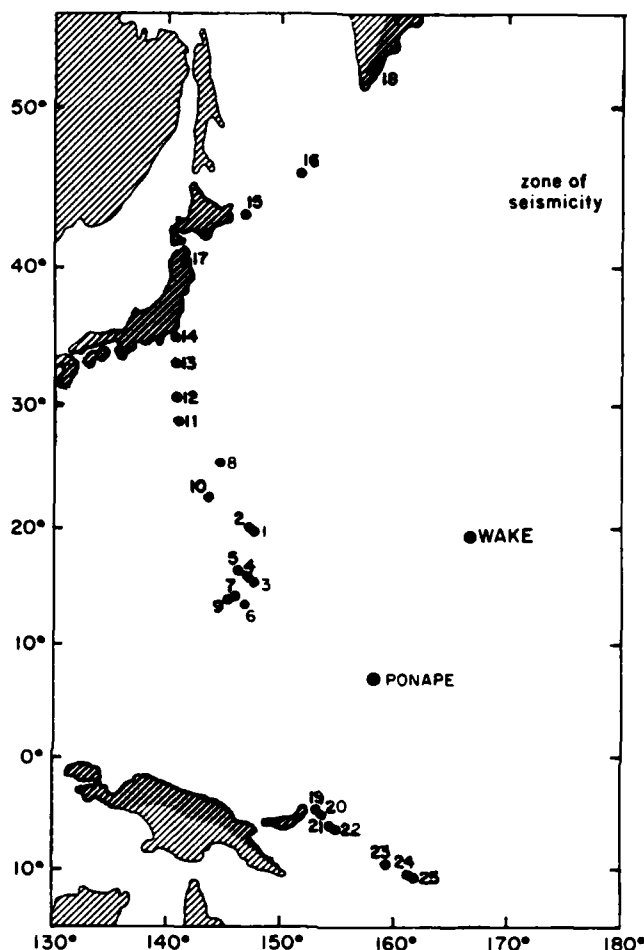


Fig. 1. Epicenter location map.

teleseismic distances. In addition, background noise levels are higher for those frequencies at which S would appear [McCreery et al., 1982].

In Figure 6a, Sn composite plots for the 17° to 22° and 26° to 33° distance ranges are compared to one another. Considering that the standard deviations of all of the composite plots presented in this paper are generally in the range of  $\pm 3$  dB, no significant differences are apparent in Figure 6a. In Figures 6b and 6c, Sn composite plots are compared to their respective Pn composite plots. Again, no statistically significant differences are indicated. In other words, Sn signal strength is generally comparable to Pn signal strength. This similarity of Pn and Sn spectrums was observed earlier for travel paths in the Western Pacific east of the Marianas [Ouchi, 1981].

Special mention should be made of the fact

that the composite Sn plot in Figure 6c is 4 dB above background noise at frequencies well above 8 Hz while the composite Pn plot is not. Also it should again be noted that the individual Pn's and Sn's used to formulate the composite plots were for the same earthquakes. These considerations suggest that Sn phases do not lose their high frequencies as rapidly as Pn phases.

It has been pointed out that some high frequencies observed elsewhere might be the result of instrumental nonlinearities [Sacks, 1980] and/or nonlinear seismic interactions in the vicinity of a receiving station [Nakamura and Koyama, 1982]. As the lower frequencies are of comparable amplitude for both Pn and Sn at both distance ranges considered (Figures 6b and 6c), it is unlikely that such nonlinearities could explain the data discussed here. We also note that P, which has higher average amplitudes than

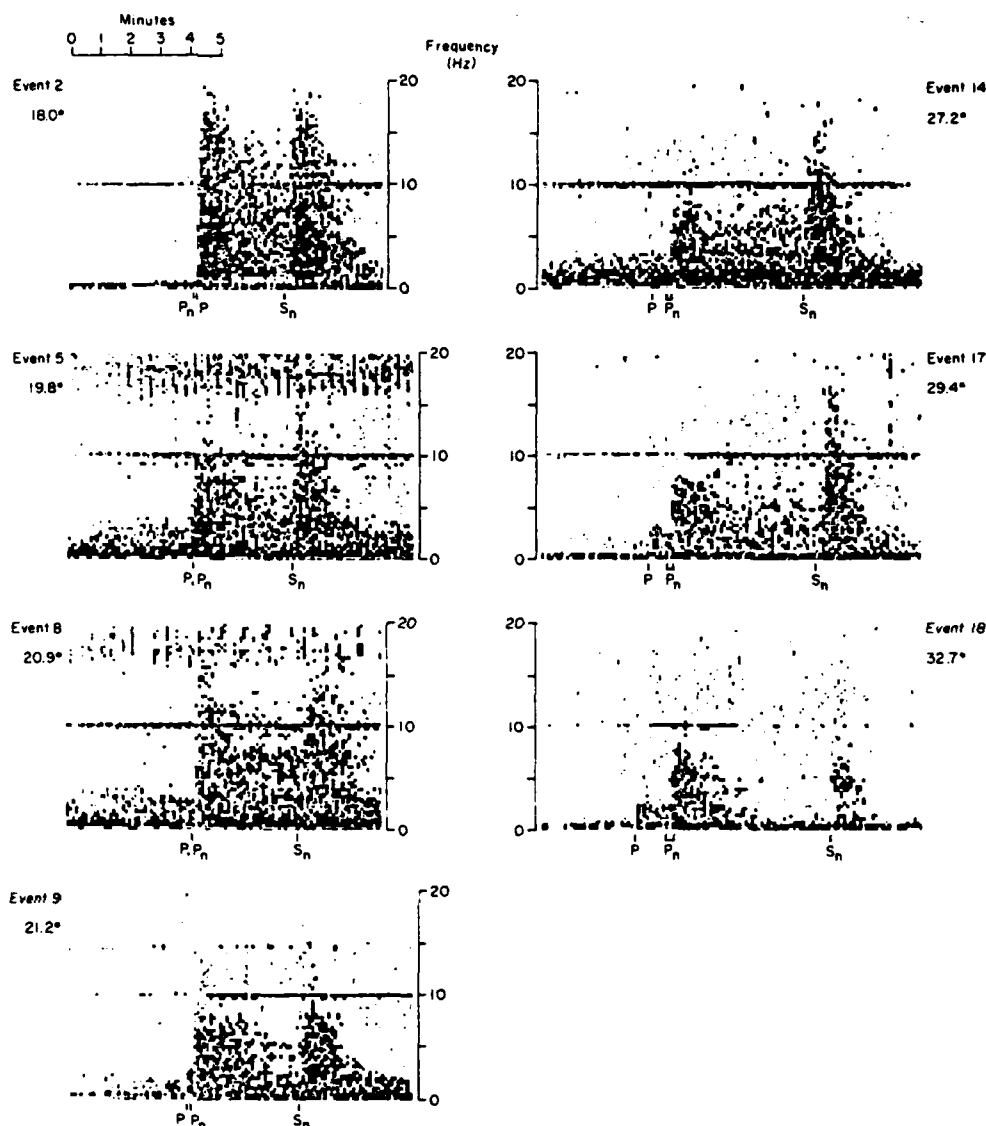


Fig. 2. Spectrograms for some earthquakes having travel paths to Wake under the Northwestern Pacific Basin. Expected times of arrivals are based on either the Jeffreys and Bullen [1958] tables for P or Pn/Sn travel time curves from Walker [1977]. These and succeeding spectrograms were made by dividing the time series into adjacent 512-point segments, Lanczos squared windowing the segments, and performing a fast Fourier transform (FFT) on each segment. In the horizontal direction, the width of each shaded block corresponds to one of the 512-point segments in the time series. In the vertical direction, each block is the average of two adjacent power spectral estimates out of the FFT. Only frequencies from 0 to  $1/2$  Nyquist are shown. The contour interval is 8 dB. The line at 10 Hz is due to time code cross talk. Instrument responses have not been removed.

Pn or Sn at the lower frequencies, has the most rapid falloff toward higher frequencies (Figure 5).

In all of these comparisons, another objection that could be made is that differences in source spectra (and/or orientation of the source

relative to the recording station) were not considered. Although all of the events occurred within the subducting margin of the Northwestern Pacific and the Pn, Sn phases used were generated by earthquakes having focal depths of 128 km or less, differences in source spectra might be

significant. We believe, however, that overall trends of the individual spectrums (Figure 4) used for the composite plots are similar (as opposed to specific details that may differ) and that such similarities could justify the general conclusions drawn from that data. We also note that source effects are minimized in those comparisons of composite Pn's and Sn's from the same earthquakes (Figures 6b and 6c).

Another interesting feature of Pn, Sn phases is that the Pn wavetrain is much longer than the Sn wavetrain (Figure 2). Spectral analyses indicate that energy is lost at all frequencies in the later arriving portions of these wavetrains, and that this loss is much greater in the Sn wavetrains than in the Pn wavetrains.

#### Ontong-Java Plateau Travel Paths

Spectrograms for some of the more interesting Pn phases with travel paths to Wake under the shallow Ontong-Java Plateau (as well as portions of the deep Northwestern Pacific Basin) are shown in Figure 7. (Refer also to Table 1, Figure 1, and Figure 8.) The most conspicuous feature of these spectrograms is that Sn phases are extremely weak, or absent, even though Pn phases are prominent.

Figure 9 compares the composite Pn spectrum for events having Ontong-Java Plateau travel paths (events 19 through 25) to the composite Pn spectrum for events at comparable distances having Northwestern Pacific Basin travel paths (events 15 through 18). The Northwestern Pacific Basin events appear to have more Pn energy at

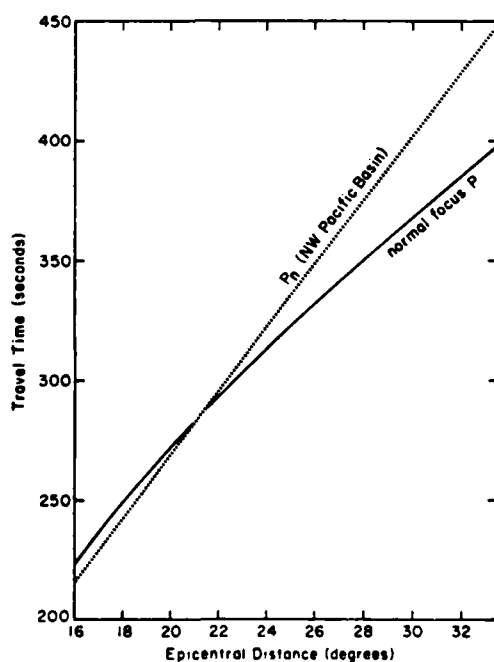


Fig. 3. Travel time curves for normal, mantle-refracted P phases and for Pn phases. P times are taken from Jeffreys and Bullen [1958], and Pn times are taken from Walker [1977].

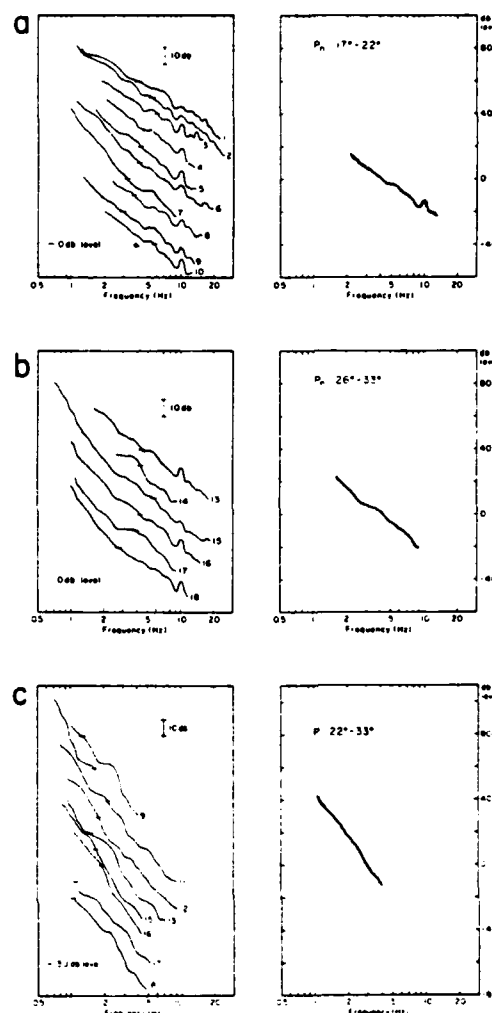


Fig. 4. Individual and composite spectrums for arrivals at Wake where (a) both Pn and P might be suspected of being present, at distances from about  $17^{\circ}$  to  $22^{\circ}$ , (b) only Pn is known to exist at distances from about  $26^{\circ}$  to  $33^{\circ}$ , and (c) only P is known to exist, at distances from about  $22^{\circ}$  to  $33^{\circ}$ . The spectrums are power level spectrums in decibels relative to one microbar peak-to-peak pressure per root hertz. Values for individual spectrums were plotted only if they were at least 4 dB above background noise. The composite curves are simply the averages for the individual curves, with the condition that composite values were used for those frequencies lacking at most only one individual curve. Standard deviations of composite values are indicated by shading. Values for standard deviations in these and succeeding spectrums are generally in the range of  $\pm 3$  dB. The peaks at 10 Hz are due to time code cross talk.

higher frequencies than the Ontong-Java Plateau events. However, because of the approximate  $\pm 3$  dB standard deviation on each of these curves, this suggestion is not statistically significant. Comparing Figures 2 and 7, the duration of the Pn

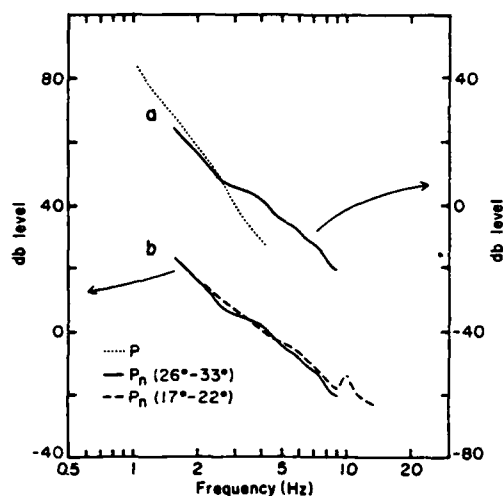


Fig. 5. Comparisons of composite spectra: (a) P and the 26° to 33° Pn, and (b) the 17° to 22° Pn and the 26° to 33° Pn. Conclusions which can be drawn from these plots are (1) P and Pn spectra are very different in character, (2) detectable P phases may not exist in the Pn codas of events at distances of 17° to 22°, and (3) Pn phases at great distances appear to be weaker at higher frequencies ( $\approx 10$  Hz) than Pn phases at shorter distances.

wavetrains appears to be greater for the Northwestern Pacific Basin events.

In such comparisons, the important question again arises of differences in source characteristics, in this instance for New Ireland-Solomon Island earthquakes and for Japan-Kuril Islands-Kamchatka earthquakes. It is not possible, however, to attribute the absence of Sn to differences in source characteristics, as Sn phases from New Ireland and the Solomons have been well recorded at Ponape on the northern margin of the Ontong-Java Plateau [Walker, 1977]. Examples of such phases are shown in Figure 10. Of the more than forty events from the New Ireland-Solomon Islands area recorded at Ponape, amplitudes of Sn phases are at least comparable to, and frequently larger than, those of their respective Pn phases.

The absence of Sn at Wake would, therefore, appear to be a result of Sn's inability to propagate efficiently across the transition zone from the shallower Ontong-Java Plateau to the deeper Northwestern Pacific Basin, and would suggest that much of the energy in Sn travels through portions of the lithosphere involved in the transition. On the other hand, Sn's that have crossed this transition zone from the other direction (i.e., from earthquakes in the Marianas, Japan, the Kuriles, and Kamchatka) are well recorded at Ponape (Figure 10). Differences in the crustal structure of the Ontong-Java Plateau and the Northwestern Pacific Basin are indicated by the section profile [Husson et al., 1979] shown in Figure 11.

Another comparison of spectra at Wake for the two differing types of travel paths

(Northwestern Pacific Basin and Ontong-Java Plateau travel paths) was made for the later arriving energy in the Pn wavetrains. For these comparisons, less energy at higher frequencies was present in those Pn's having travel paths that include the Ontong-Java Plateau. These deficiencies and the corresponding absence of Sn for paths across the transition zone from the shallow Ontong-Java Plateau to the deep Northwestern Pacific Basin suggest that the longer, stronger Pn phases observed for travel paths to Wake, primarily across the Northwestern Pacific Basin, may be the result of more efficient conversions of Pn to Sn (or Sn to Pn).

#### Concluding Remarks

The phenomenon of high-frequency Pn, Sn propagation is emerging as a major unresolved property of the oceanic crust and/or mantle. Others have described high-frequency Pn, Sn propagation as 'a challenge remaining to the theoretician' [Richards, 1979] and as 'the challenge to both explosion and earthquake

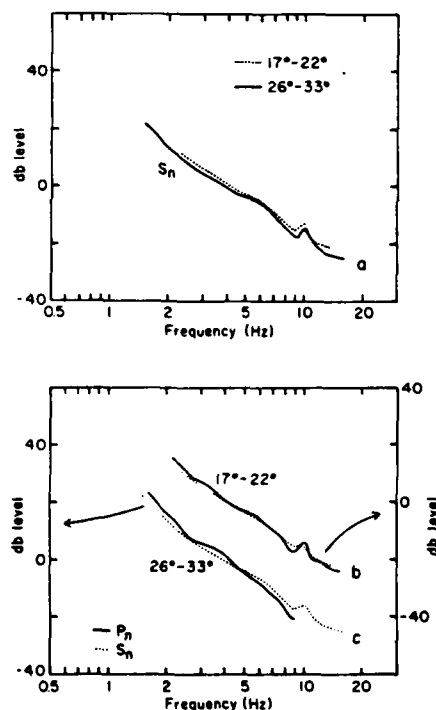


Fig. 6. Composite spectra of Sn phases for those earthquakes with their Pn phases plotted in Figures 4a and 4b. Comparisons of spectra are made (a) for the two Sn composites to one another, (b and c) and for each of the Sn composites to their respective Pn composite. A conclusion which can be drawn from these plots is that Sn signal strength is generally comparable to Pn signal strength except at high frequencies and large distances where Sn phases do not lose their energy as rapidly as Pn phases.

B7

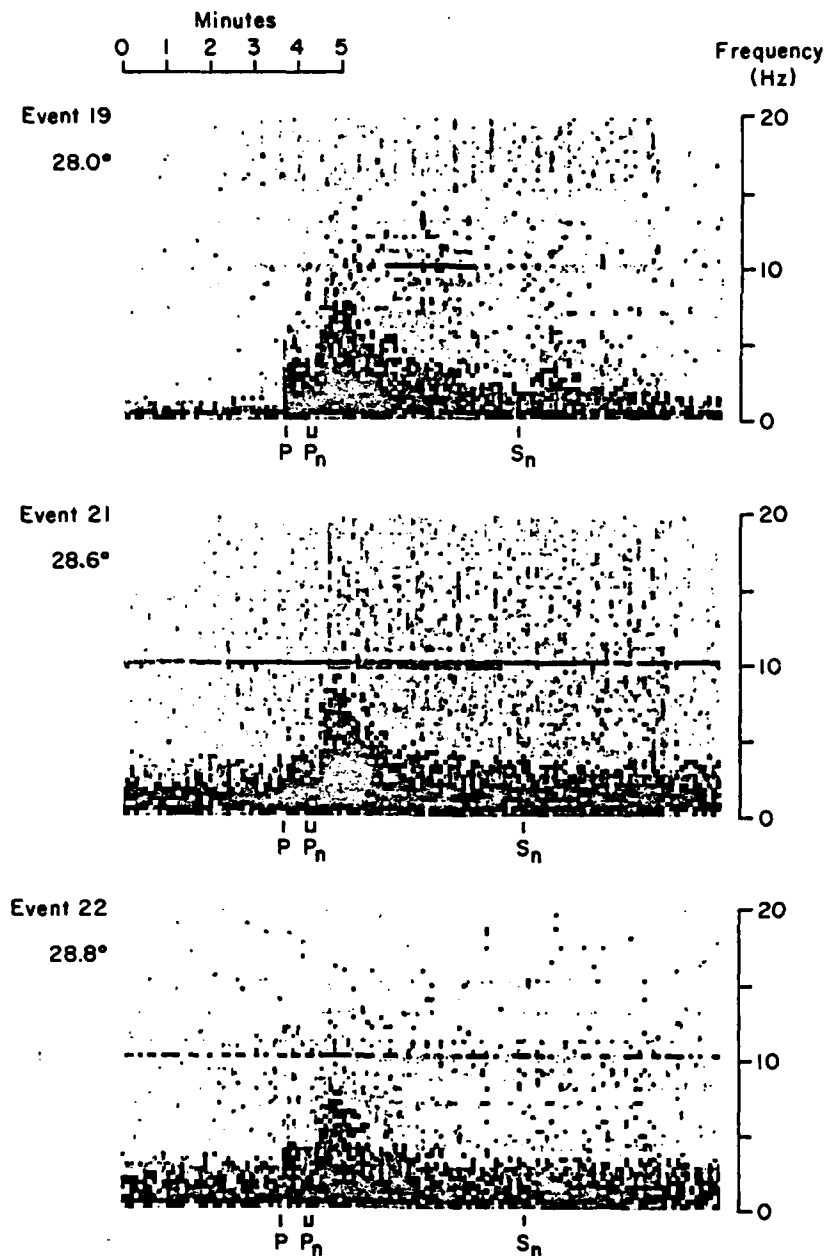


Fig. 7. Some spectrograms for earthquakes having portions of their travel paths to Wake under the Ontong-Java Plateau. In comparing these spectrograms to those of Figure 2, note the absence, or weakness, of Sn. Computational procedures are the same as used in Figure 2.

seismology for the coming decade' [Hirn et al., 1973]. These descriptions are supported not only by the unusual character of the phases but also by their probable occurrence throughout the world's oceans.

As important as recent efforts are to determine the mechanism of high-frequency Pn, Sn propagation [e.g., Stephens and Isacks, 1977; Menke and Richards, 1980; Sutton and Harvey, 1981; Gettrust and Frazer, 1981], we believe that

many essential characteristics of Pn, Sn phases (especially at very high frequencies) are not well known, and that accurate quantification of those characteristics through the acquisition of additional high-quality data is greatly needed. We hope that this report will further familiarize seismologists with high-frequency Pn, Sn propagation and will be viewed as a preliminary attempt to quantify, in a relative sense, some of the essential characteristics of these phases. A

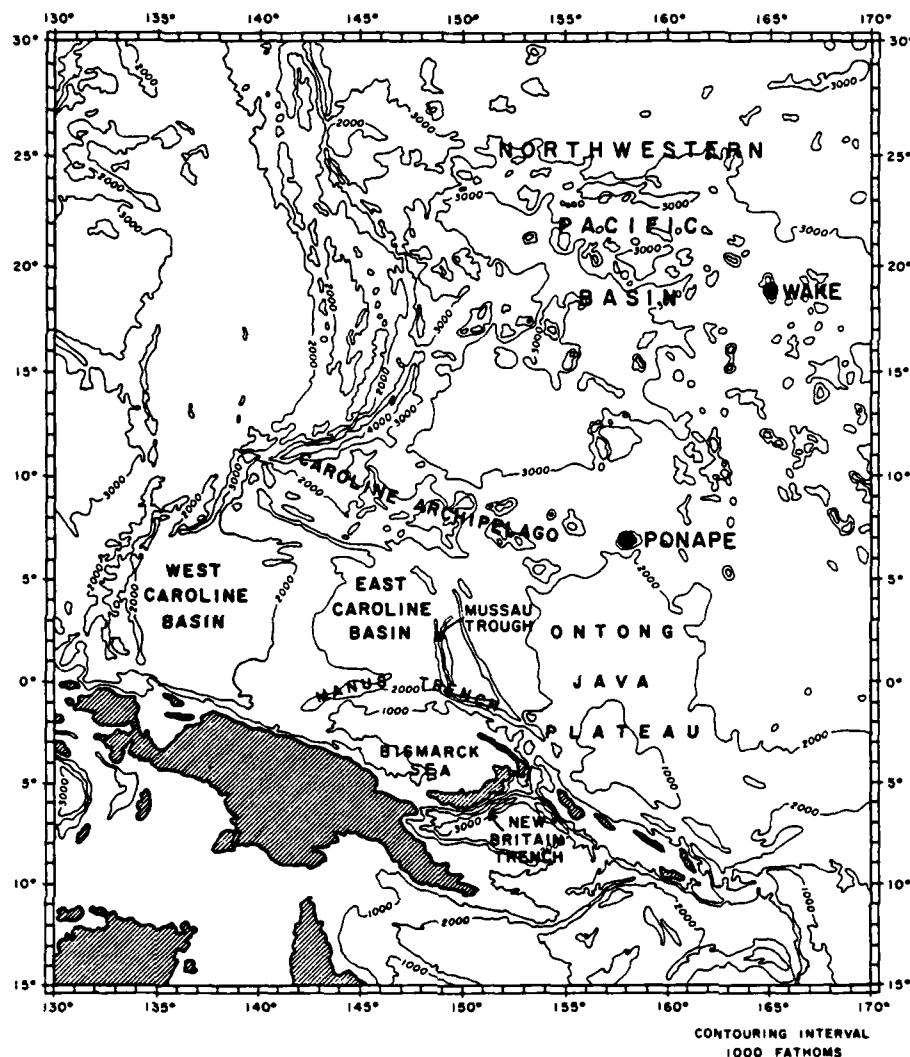


Fig. 8. Bathymetry map of the Northwestern Pacific area.

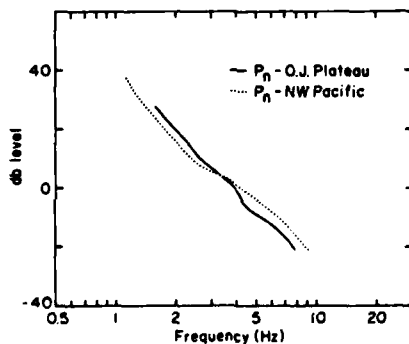


Fig. 9. Comparisons of composite Pn spectra for events having travel paths across the Ontong-Java Plateau and the Northwestern Pacific Basin.

summary of principal observations contained in this report follows.

The apparent absence of normal, mantle-refracted P phases at distances less than about  $21^\circ$  ( $\approx 2300$  km).

Frequencies as high as 30 and 35 Hz for Pn and Sn, respectively, at  $18.0^\circ$  (2000 km).

Frequencies as high as 15 and 20 Hz for Pn and Sn, respectively, at  $29.4^\circ$  (3270 km).

With increasing distance (i.e., from about  $20^\circ$  to  $30^\circ$ ), Sn phases not losing their high frequencies as rapidly as Pn phases do.

Pn wavetrains longer than Sn wavetrains.

The extreme weakness or absence of Sn phases for travel paths across the transition zone from the Ontong-Java Plateau to the Northwestern Pacific Basin and the presence of Sn phases for travel paths in the opposite direction across this transition zone.

Longer, more energetic Pn wavetrains for travel paths primarily in the Northwestern Pacific Basin than for travel paths across the transition zone from the Ontong-Java Plateau to the Northwestern Pacific Basin.



## B9

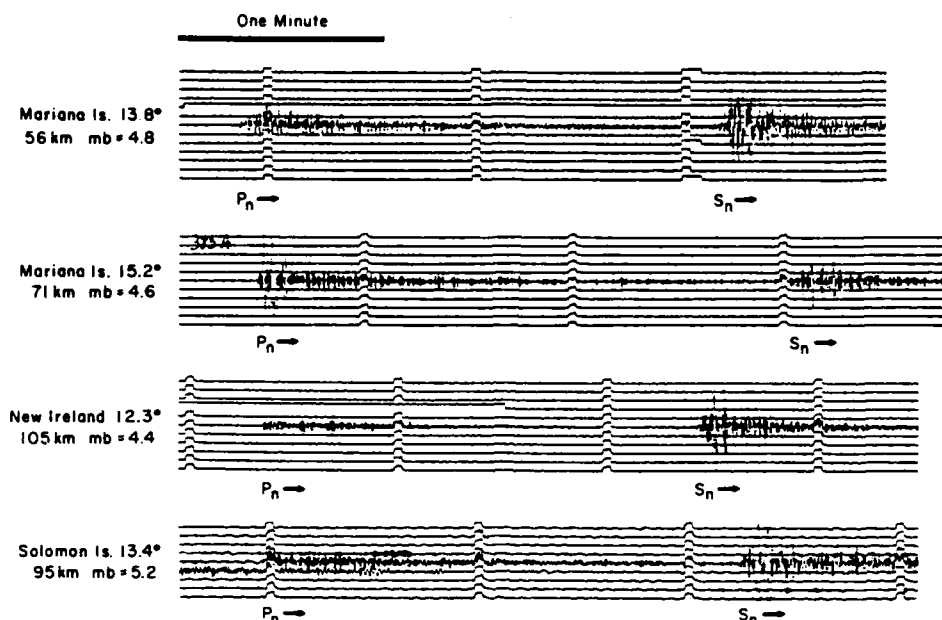


Fig. 10. Pn and Sn phases recorded at Ponape on the northern margin of the Ontong-Java Plateau.

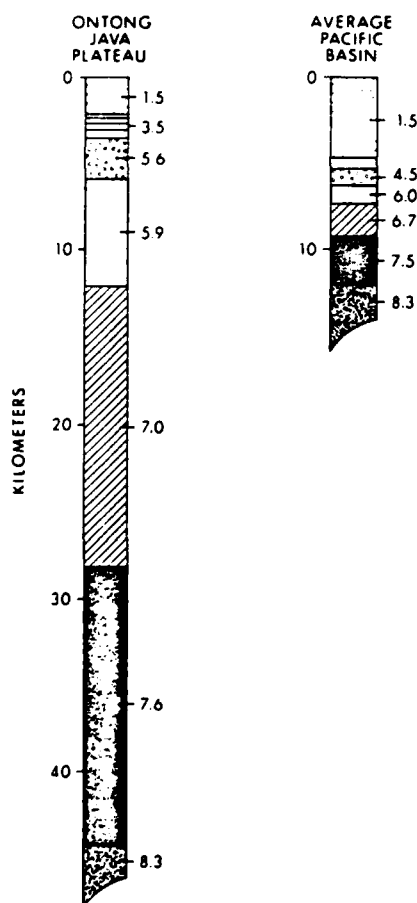


Fig. 11. Section profiles for the Ontong-Java Plateau and Pacific Basin as taken from Hussong et al. [1979].

**Acknowledgments.** This research was supported by the Advanced Research Projects Agency of the Department of Defense and was monitored by the Air Force Office of Scientific Research under contract F49620-79-C-0007. Supplementary funds were provided by the Air Force Office of Scientific Research (contract F49620-81-C-0065), the Office of Naval Research (Code 425GG), and the U.S. Arms Control and Disarmament Agency. The authors thank Fred Duennebie, Joe Gettrust, and Neil Frazer for reviewing a draft of this report. The editorial assistance of Rita Pujale is also acknowledged. Hawaii Institute of Geophysics contribution 1354.

## References

- Gettrust, J., and L. Frazer, A computer model study of the propagation of the long-range Pn phase, *Geophys. Res. Lett.*, **8**, 749-752, 1981.
- Hirn, A., L. Steinmetz, R. Kind, and K. Fuchs, Long range profiles in western Europe, II, Fine structure of the lower lithosphere in France (southern Bretagne), *Z. Geophys.*, **39**, 363-384, 1973.
- Hussong, D., L. Wipperman, and L. Kroenke, The crustal structure of the Ontong-Java and Manihiki oceanic plateaus, *J. Geophys. Res.*, **84**, 6003-6010, 1979.
- Jeffreys, H., and K. Bullen, *Seismological Tables*, Office of the British Association, Burlington House, London, 1958.
- McCreery, C., High-frequency Pn, Sn phases recorded by ocean bottom seismometers on the Cocos Plate, *Geophys. Res. Lett.*, **8**, 489-492, 1981.
- McCreery, C., D. Walker, and G. Sutton, Spectra of nuclear explosions, earthquakes, and noise from Wake Island bottom hydrophones, *Geophys. Res. Lett.*, **10**, 59-62, 1983.

- Menke, W., and P. Richards, Crust-mantle whispering gallery phases: A deterministic model of teleseismic Pn wave propagation, J. Geophys. Res., **85**, 5416-5422, 1980.
- Nakamura, Y., and J. Koyama, Seismic Q of the lunar upper mantle, J. Geophys. Res., **87**, 4855-4861, 1982.
- Ouchi, T., Spectral structure of high frequency P and S phases observed by OBS's in the Mariana Basin, J. Phys. Earth, **29**, 305-326, 1981.
- Richards, P., Theoretical seismic wave propagation, Rev. Geophys. Space Phys., **17**, 312-328, 1979.
- Sacks, I., Mantle Qs from body waves-difficulties in determining frequency dependence, (abstract), Eos Trans. AGU, **61**, 298, 1980.
- Stephens, C., and B. Isacks, Toward an understanding of Sn: Normal modes of Love waves in an oceanic structure, Bull. Seismol. Soc. Am., **67**, 69-78, 1977.
- Sutton, G., and D. Harvey, Complete synthetic seismograms to 2 Hz and 1000 km for an oceanic lithosphere (abstract), Eos Trans. AGU, **62**, 327, 1981.
- Sutton, G., C. McCreery, F. Duennebier, and D. Walker, Spectral analyses of high-frequency Pn, Sn phases recorded on ocean bottom seismographs, Geophys. Res. Lett., **5**, 745-747, 1978.
- Talandier, J., and M. Bouchon, Propagation of high frequency Pn waves at great distances in the Central and South Pacific and its implications for the structure of the lower lithosphere, J. Geophys. Res., **84**, 5613-5619, 1979.
- Walker, D., High-frequency Pn and Sn phases recorded in the Western Pacific, J. Geophys. Res., **82**, 3350-3360, 1977.
- Walker, D., C. McCreery, G. Sutton, and F. Duennebier, Spectral analyses of high-frequency Pn and Sn phases observed at great distances in the Western Pacific, Science, **199**, 1333-1335, 1978.

(Received July 14, 1982;  
revised January 5, 1983;  
accepted February 7, 1983.)

## Appendix C

NAME           scs

SYNOPSIS       scs

### DESCRIPTION

Scs is a utility program used to access the Secondary Computer Storage tape drives over the parallel interface. It is prompt line driven and therefore has no options. A description of commands follows. Most commands apply to the selected drive (see z command).

b    READ MANUFACTURERS BLOCK

The information in absolute block zero is displayed.

c    CERTIFY

You are prompted for 'beginning' and 'ending' block and then the tape blocks between these limits are certified. The results are stored in the SCS controller memory.

d    DISPLAY

You are prompted for 'where' (which block) to begin. Information previously recorded on tape is formatted and displayed. The display will continue until either the end of tape has been reached or until two quick spaces are entered. One space will force a jump to the next block.

f    FILL (DIAGNOSTIC WRITE)

The range of blocks from 'begin' to 'end' are filled with a pattern consisting of integers from 127 down to 0 and 384 zeros.

i    INITIALIZE

The controllers initialize line is strobed thus resetting the drives to their power up state. This command applies to both controllers.

k    COMMENT

The comment in block 1 is read in and displayed. Press any key to

continue.

l LOAD BAD BLOCKS

The bad block information in absolute block 8 is read in and then loaded into the controller's skip table. From then on the drive will skip over any block listed in the table.

m MEMORY

To access controller memory. For reading enter 'r' and hex location (ie. r237F). For writing enter 'w', location and value (ie. w237f a0).

p PLOT

To plot data on screen enter 'where' (block number) (0 - 2). A single character while plotting will stop the plot for viewing and a second character will return to menu. Plotting will continue from where until end of tape.

q QUIT

Return to MS-DOS.

r READ

The drive will move to the block selected with 'where' and dump 512 unsigned integers to the screen.

s STATUS

Used to report status and or clear a fault.

u UNWIND

Rewinds the selected drive.

w WRITE

Enter 'where' (block number) and 'how many'. Two byte integers from 0 to 512 will be written to each block selected.

z SELECT DRIVE

Select either controller 0 or 1. Selection will remain in effect until changed. DEFAULT 0

NAME           rai

SYNOPSIS       rai (-l drive #) (-o drive #) (-s start) (-e end)

# DESCRIPTION

Rai is an interrupt driven data collection program which is used to collect data from the Ref-Tek system and the Kinematics satellite clock and record it on two SCS data recorders. With no options, rai will check the status of both drives, load the bad block table into drive 0, load the file comment.rai into block 0, and start logging data to tape. When 65,400 blocks (approximately 38 hours) have been recorded, rai will switch to drive 1, load the bad block table and comment and record for another 400 blocks, then stop. Tapes are rewound when recording has stopped. Options are available to modify this routine.

- l Loop option. If loop is specified, the recording will start with the drive specified and shuttle back and forth as long as a tape is available. After a tape has been rewound, it can be replaced with a new one. The bad block table and comment will be loaded before use. DEFAULT=stop after recording both drives.
- o One drive. If one drive is specified, recording will start with the drive specified and will stop when end is reached on that drive. DEFAULT=use both drives.
- s Starting block number. To begin at other than the first tape block. Applies only to the first drive. DEFAULT=1.
- e Ending block number. Upon reaching ending block number, recording will stop on that drive. Depending on other options, recording may continue on the other drive. Applies to both drives. DEFAULT=65,400.

FILES           screen1.rai screen1a.rai screen2.rai screen3.rai screen4.rai  
comment.rai

### 1/4" Magnetic Tape Cartridge Format

A 1/4" tape cartridge can hold up to 67 megabytes of data which is written in 1024 byte blocks. Blocks 8 and 9 are used to store duplicate tables of bad block information and are read into the controllers ram. A header block of 1024 characters from the file "comment.rai" is written to block 0 at the beginning of the recording process and contains information manually entered about the status and/or configuration of the station. Also included at the end of this block is a 0 or 1 to indicate which tape drive was used to record the data.

Data is written to the tape in two byte words. The first word of a data block is the block number and the second is the buffer number. The next three words contain the time at the beginning of the block (Figure 1A). The clock words are followed by three dummy words after which comes the data. Four words are used for a single sample from each channel. The first three words give the channel number and mantissa and the fourth word contains the gain bits (Figure 1A). There are 126 data samples per block per channel.

## Appendix D

### Certification of 1/4" Cartridge Tapes

Certification of tapes is a simple process of writing a known bit pattern throughout the entire tape and then reading that pattern to verify that the pattern has been recorded properly. Tape blocks which do not pass this test are labeled as being bad and the locations of these bad blocks are stored in a table. When all blocks have been certified, the bad block table is written to blocks 8 and 9 at the beginning of the tape. Later, when the tape is used for recording or playback, the bad block information is read from blocks 8 or 9 and stored in the tape drive's memory. The tape drive will automatically skip the bad blocks whose addresses are stored in its memory. The maximum number of bad blocks that any single tape is allowed to have is 128; more than that and the tape should not be used.

#### Procedure

1. Load a blank tape into the tape transport not being used to record data. Tape loading will take a few minutes, be patient.
2. Plug the serial RS232 connector from the SUN into the back of the appropriate tape transport.
3. When the tape has loaded, the certification program may be invoked by typing "bad".
4. At the completion of the program (about an hour) one of two messages will appear; the bad block table or a message that more than 128 bad blocks were found and that the tape should not be used. The tape should rewind itself at the end of the program.
5. Apply a label to the tape and its box and initial the "certified" bland on the labels.

6. If for some reason the tape stops without unloading, it may be unloaded by typing "bad u". If this does not work, a) ask for help and b) go have a beer.



NAME            bad

SYNOPSIS        bad (length) (u) (debug)

DESCRIPTION

Bad is used to create a bad block table and write it to absolute tape blocks 8 and 9. Using the serial interface, a tape is certified (both data and keys) and a bad block table is created in the controller ram. This table is then written to the cartridge. With no options, bad will certify the entire tape.

length    The ending block number if less than the entire tape is to be certified (four character capital hex (i.e. 1C7F)).

u         A flag indicating bad is to just rewind the tape.

debug     Bad is normally called with one argument. If a second argument is added, the output will be more verbose.

## Data Playback

Data retrieval from the 1/4" archive tapes consists of reading the data from the tapes, demultiplexing it, converting it to a standard format and writing it to some other medium. The starting time, the number of seconds to retrieve and the destination file are all given in the command line. Digitization rate, because it is not constant, is calculated by dividing the total number of samples retrieved by the actual time they were recorded in.

### Procedure

1. Load a tape into the tape drive and wait for the tape to stop moving. This will take a minute or so, be patient.
2. Plug the RS232 from the SUN into the serial interface on the back plate of the tape drive.
3. Load the bad block information into ram by typing "read-l".
4. Type "read ddd hh mm ss nnnn wfp". The header block will be displayed along with the start time of the tape. As each tape block is read in, the start time of that block is displayed on the screen. At the completion of the program, the tape is not rewound so that different sections of data may be read from the tape without reloading after every run. Four files will have been created in the current directory; (wfp).1.w, (wfp).2.w, (wfp).3.w, and (wfp).wfdisc. The .w files are the plus vertical, north south horizontal, and east west horizontal components, respectively.
5. Unload the tape by typing "read -u".

NAME read

SYNOPSIS read (-l) (-u) (ddd hh mm ss nnn wfp)

#### DESCRIPTION

Read is a data retrieval and formatting program that is used to read data from a SCS 1/4" tape transport and format it into the structures used by the Center for Seismic Studies. Bad block information is read into the controller ram from tape blocks 8 and 9 and the header block and tape start time are displayed. If the requested time (ddd=julian day, hh=hour, mm=minute, ss=second) is on the tape, read advances the tape to the requested time and reads in nnn seconds of data. The output files are placed in the current directory with waveform prefix wfp. Three data files wfp.1.w, wfp.2.w, wfp.3.w and a parameter file wfp.wfdisc constitute the output. The tape is not rewound when all of the data has been retrieved.

- l Load option. Load the bad block information into ram from tape blocks 8 and 9.
- u Rewind and unload the tape.

The .w files consist of binary four byte integers with no headers. The timing and identification information is found in the ascii file (wfp).wfdisc. Each record of the .wfdisc file corresponds to one of the .w files.